Alma Mater Studiorum – Università di Bologna

DOTTORATO DI RICERCA IN

Fisica

Ciclo XXVIII

Settore Concorsuale di afferenza: 02/B1

Settore Scientifico disciplinare: FIS/03

Organic Bulk Heterojunction Solar Cells: Materials Properties, Device Stability And Performance

Presentata da: Marta Tessarolo

Coordinatore Dottorato

Prof. Gastone Castellani

Relatore

Prof. Beatrice Fraboni

Co-relatore

Dr. Mirko Seri

Esame finale anno 2016

A mia sorella

Contents

List of Publications Related to the Thesis **1**

Introduction **1**

1 Organic Photovoltaic: critical overview and physical processes **3**

1.1 Renewable Energy 3

1.2 Advantages and disadvantages 6

1.2.1 Low cost 7

1.2.2 Environmental impact 8

1.2.3 Power Conversion Efficiency 9

1.2.4 Lifetime 9

1.2.5 New market opportunities 10

1.3 Concepts and evolution 12

1.3.1 History of Organic Photovoltaic 13

1.3.2 Working principles of bulk heterojucntion solar cells 14

1.3.3 Buffer layers 18

2 Fabrication and characterization techniques **21**

2.1 Device Fabrication 21

2.2 Organic materials for the BHJ active layer 23

2.3 Characterization techniques 27

2.3.1 Current - Voltage characteristic 27

2.3.2 Quantum Efficiency 31

2.3.3 Mobility 33

2.3.4 Atomic Force Microscopy 34

2.3.5 Kelvin Probe Force Microscopy 37

2.3.6 Laser Scanning Confocal Microscopy 39

2.3.7 Capacitance Voltage characteristic 40

2.3.8 Impedance Spectroscopy 42

2.3.8.1 Impedance Spectroscopy applied on organic solar cells 45

3 Correlation between organic donor material structure and PV properties 51
3.1 Physics of Organic Semiconductor . . . 51
3.1.1 Organic molecules semiconductor . . . 52
3.1.2 Organic semiconductor polymers . . . 54
3.2 Charges generation in a bulk heterojunction solar cell . . . 57
3.2.1 Acceptor material for organic solar cells . . . 58
3.2.2 Donor polymer for organic solar cells . . . 60
3.3 Chemical structure and performance correlations . . . 65
3.3.1 Lowering HOMO level . . . 65
3.3.2 Side chains effect . . . 72
3.3.3 π conjugated spacers . . . 77
3.4 Conclusion . . . 85

4 Thermal degradation of the BHJ active layer 87
4.1 Overview of degradation effects on OPV . . . 87
4.2 Thermal degradation . . . 89
4.2.1 Effect of high temperature on PV parameters . . . 90
4.2.2 Influence of fullerene . . . 91
4.2.3 Influence of Glass Transition Temperature . . . 92
4.3 Fabrication and characterization of P3HT and PTB7 based solar cells . . . 94
4.3.1 Device fabrication . . . 95
4.3.2 Electrical characterization . . . 95
4.3.3 Optical characterization . . . 97
4.3.4 Morphological characterization . . . 98
4.4 Thermal degradation of P3HT and PTB7 based solar cells . . . 100
4.4.1 Electrical characterization . . . 100
4.4.2 Optical characterization . . . 102
4.4.3 Morphological characterization . . . 103
4.5 Conclusion . . . 110

5 Thermal degradation effects on operating devices 111
5.1 Influence of internal interfaces on thermal degradation . . . 111
5.1.1 Role of buffer layers . . . 111
5.1.2 Confinement effect . . . 113
5.2 How to predict the device thermal stability . . . 117
5.2.1 Devices Fabrication . . . 117
5.2.2 Standard thermal degradation test . . . 118
5.2.3 Capacitance based thermal test . . . 120
5.3 Investigation on thermal degradation mechanisms . . . 123
5.3.1 Optical characterization . . . 123
5.3.2 Mott - Schottky analysis . . . 124
5.3.3 Impedance Spectroscopy analysis . . . 127

5.4 Conclusion 131

6 Photodegradation effects on BHJ solar cells 133

6.1 Light-induced degradation 133

6.1.1 Effect of fullerene 134

6.1.2 Effect of solvent additives 135

6.2 Photodegradation of Quinoxaline based polymers 135

6.2.1 Polymers structures and characterization 136

6.2.2 Photodegrdation of neat polymer films 137

6.3 Photodegradation of polymer based solar cells 139

6.3.1 Device Fabrication 140

6.3.2 Photodegradation test and evolution of PV parameters 141

6.3.3 Optical Characterization of the Active Layer 145

6.4 Influence of the top electrode on the photodegradation 148

6.5 Influence of buffer layers on the photodegradation 149

6.5.1 ZnO characterization 150

6.5.2 Device Fabrication 153

6.5.3 Devices photodegradation 154

6.6 Conclusion 157

Conclusions and Future work 157

Bibliography 181

List of Publications Related to the Thesis

- *"2D π-conjugated benzo $[1,2-b:4,5-b']$ dithiophene-and quinoxaline-based copolymers for photovoltaic applications"*
  M. Bolognesi*, D. Gedefaw*, D. Dang, P. Henriksson, W. Zhuang, M. Tessarolo, E. Wang, M. Muccini, M. Seri, M. R. Andersson
  RSC Advances, **2013**, 3, 24543-24552

- *"Efficiency enhancement of P3HT: PCBM solar cells containing scattering Zn-Al hydrotalcite nanoparticles in the PEDOT: PSS layer"*
  M. Bolognesi, M. Tessarolo, T. Posati, M. Nocchetti, V. Benfenati, M. Seri, G. Ruani, M. Muccini
  Organic Photonics and Photovoltaics, **2013**, 1, 1-10

- *"Conjugated polymers based on benzodithiophene and fluorinated quinoxaline for bulk heterojunction solar cells: thiophene versus thieno [3, 2-b] thiophene as $\pi-$conjugated spacers"*
  D. Gedefaw, M. Tessarolo, W. Zhuang, R. Kroon, E. Wang, M. Bolognesi, M. Seri, M. Muccini, M. R. Andersson
  Polymer Chemistry, **2014**, 5, 2083-2093

- *"Structural tuning of quinoxaline-benzodithiophene copolymers via alkyl side chain manipulation: synthesis, characterization and photovoltaic properties"*
  M. Tessarolo*, D. Gedefaw*, M. Bolognesi, F. Liscio, P. Henriksson, W. Zhuang, S. Milita, M. Muccini, E. Wang, M. Seri, M. R. Andersson
  Journal of Materials Chemistry A,**2014**, 2, 11162-11170

- *"Integration of a silk fibroin based film as a luminescent down-shifting layer in ITO-free organic solar cells"*
  M. Prosa, A. Sagnella, T. Posati, M. Tessarolo, M. Bolognesi, S. Cavallini, S. Toffanin, V. Benfenati, M. Seri, G. Ruani, M. Muccini, R. Zamboni
  RSC Advances, **2014**, 4, 44815-44822

- *"Predicting thermal stability of organic solar cells through an easy and fast capacitance measurement"*
  M. Tessarolo, A. Guerrero, D. Gedefaw, M. Bolognesi, M. Prosa, X. Xu, M. Mansour, E. Wang, M. Seri, M. R. Andersson, M. Muccini, G. Garcia-Belmonte
  Solar Energy Materials and Solar Cells, **2015**, 141, 240-247

- *"Induced photodegradation of quinoxaline based copolymers for photovoltaic applications"*
  D. Gedefaw*, M. Tessarolo*, M. Prosa*, M. Bolognesi, P. Henriksson, W. Zhuang, M. Seri, M. Muccini, M. R. Andersson
  Solar Energy Materials and Solar Cells, **2016**, 144, 150-158

- *"Enhanced Ultraviolet Stability of Air-Processed Polymer Solar Cells by Al Doping of the ZnO Interlayer"*
  M. Prosa, M. Tessarolo, M. Bolognesi, O. Margeat, D. Gedefaw, M. Gaceur, C. Videlot-Ackermann, M. R. Andersson, M. Muccini, M. Seri, J. Ackermann
  ACS Applied Materials & Interfaces, **2016**

- *"Enhanced BHJ stability through environmentally friendly processing: local morphological investigations on complete solar cells using non-invasive microscopy techniques"*
  M. Bolognesi, M. Seri, M. Tessarolo, M. Prosa, G. Donati, S. Toffanin, M. Muccini
  Journal of Materials Chemistry A, submitted

Proceeding article

- *"Predicting thermal stability of organic solar cells through real-time capacitive techniques (Presentation Recording)"*
  M. Tessarolo, A. Guerrero, M. Seri, M. Prosa, M. Bolognesi, G. Garcia Belmonte
  SPIE Organic Photonics+ Electronics, **2015**

Other publication

- *"Infrared Investigations of 4-Hydroxycyanobenzene Single Crystals"*
  E. Capria, L. Benevoli, A. Perucchi, B. Fraboni, M. Tessarolo, S. Lupi, A. Fraleoni-Morgera
  The Journal of Physical Chemistry A, **2013**, 117, 6781-6788

Introduction

In the field of renewable energy sources the solar energy can potentially provide a clean, sustainable alternative to fossil fuels to meet the global growing needs for energy. Despite today the market is governed by silicon based solar cells, in the last decades alternative photovoltaic technologies, based on different materials, were investigated. This Ph.D thesis focuses the attention on the Organic Photovoltaic (OPV) and in particular on the so called bulk heterojunction (BHJ) solar cells. The interest on OPV technology comes from the specific properties of the organic materials such as: low production costs (wet processing), compatibility with flexible and transparent substrates, possibility to tune their optoelectronics proprieties by "ad hoc" structural modifications and absence of rare earth elements or precious metals reducing the environmental impact. However in order to develop competitive products, further improvements in terms of efficiency and stability are still required.

In sight of this, the present Ph.D thesis has a double goal: 1) a better understanding of the relationship between devices performance and photoactive materials structures 2) a deep investigation on device degradation processes, with particular attention to the effects induced by temperature and incident light.

To address these goals the work has been performed in collaboration with different research groups. The main part, regarding the fabrication and characterization of photovoltaic devices, has been carried out at "Consiglio Nazionale delle Ricerche - Istituto per lo Studio dei Materiali Nanostrutturati (CNR-ISMN)" in Bologna, additional morphological characterizations have been performed at "Universitá di Bologna - Dipartimento di Fisica e Astronomia", while specific investigations based on Impedance Spectroscopy have been developed at "Universitat Juam I - Photovoltaic and Optoelectronic Devices Group" in Castellon de la Plana (Spain).

The first Chapter of the thesis is focused on a critical overview of advantages and disadvantages of OPV comparing to other PV technologies and a brief introduction on the working principles of a BHJ solar cell. The second Chapter summarizes the main physical-chemical properties of the organic materials employed and briefly describes the working principles of the fabrication and characterization techniques used in the work. The third Chapter introduces the science of organic semiconductors, including the descriptions of the main characteristics/requirements of photoactive polymers applied on OPV. Then, the relationship between the photoactive materials properties and the photovoltaic performance of the resulting BHJ solar cells is investigated, demonstrating how fine structural modifications of an organic semiconductor can strongly influence the corresponding device performance. The fourth Chapter indentifies the main degradation mechanisms affecting an

organic solar cell, with particular attention to the thermal degradation. Two BHJ devices based on different polymer:fullerene blends are investigated. The morphological evolution of the active layers, induced by temperature (85^oC), has been monitored by complementary scanning probe microscopy techniques. The fifth Chapter develops the issue of the thermal stability focusing the attention on the whole working device. A new investigation tool able to predict the thermal behavior of a complete organic solar cells is presented. In addition the Impedance Spectroscopy is used as a complementary method to identify and explain the main processes occurring within the device during thermal degradation. The sixth Chapter describes a preliminary study on the photo degradation of an organic solar cell. In particular, the photostability of BHJ solar cells based on different donor polymers has been studied and compared with the intrinsic photostability of each single polymer. Moreover the role of the adjacent layers and the interfaces, on the device photo degradation is also investigated.

1

Organic Photovoltaic: critical overview and physical processes

1.1 Renewable Energy

In the modern times, the energy consumption is rising tremendously year by year due to the fast development, demands comfort, higher mobility and growing world population. At the moment fossil fuels as coal, oil and gas, joint with the nuclear energy, are playing lead role to meet the energy demand. However, the limited availability of primary exhaustible energy sources (i.e. fossil fuels and uranium) and the long-term adverse effects on the environment due to their exploitation, reflects the urgency to develop new strategies to effectively utilize other primary energy sources: the renewable ones. In the last 20 years a lot of work was done to increase the amount of energy comes from clean sources not just in terms of research and development, but also in terms of legislation and politics. A clear example is The Renewable Energy Target for Europe that consists on achieving the 20% of power produced by renewable energy by 2020.[1] Similarly, Barack Obama on the occasion of Earth Day, declared that developing renewable energy is crucial to America' s prosperity and he promised to spend $ 150 billion over the next 10 years developing alternative energy. Japan targets to develop R&D, provide incentives to install plant for renewable energy easily with lower investment costs. China's Renewable Energy law was made to increase and develop the renewable energy resources.[2] The consequence of those politics had great results as reported in the Figure 1.1, where a prospective on 2013, from the International Conference "Renewable Energy Policy Network for the 21st Century" [3] shows that almost 20% of the energy in the world comes from renewable sources. The main sources are hydropower(16,4 %), wind (2,9 %), biomass (1,8%), solar (0,7%), geothermal and tidal (0,4%).

In theory among all the renewable sources, solar energy appears to be particularly attractive. The sun bathes the earth with 92'000 TW of electromagnetic radiation, in free form, abundant, non-polluting and, on scale of our times, inexhaustible. Moreover, based on a rough calculation illustrated in the Figure 1.2, taking into account the amount of sunlight that reaches the land area of the Earth, supposing to cover just 2% of the earth surface with solar panels, and considering

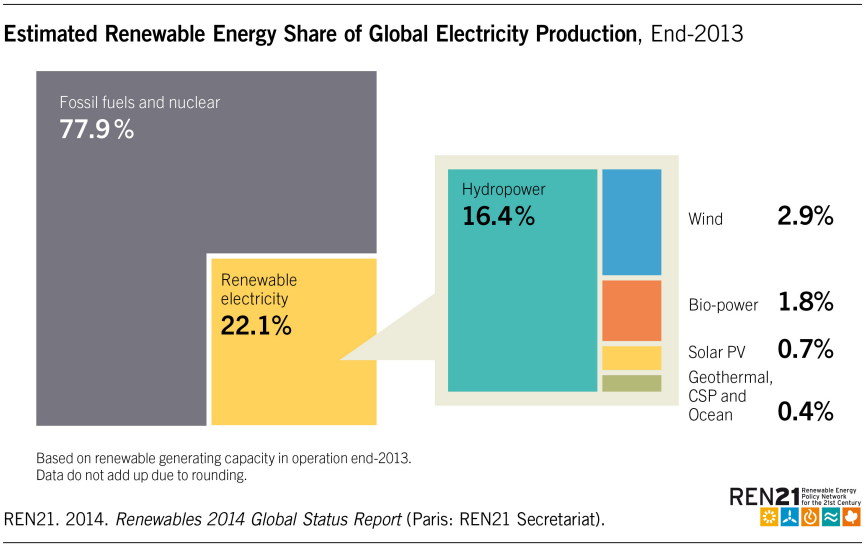

Figure 1.1: Estimation of the global energy production distribution [3]

modules with power conversion efficiency of 12%, the power produced would be 67 TW. If it is consider that the global energy demand estimate for 2050 is 30 TW, the amount produced from the Photovoltaic (PV) would be enough to meet the global demand. However the development of PV is still on going and the some intrinsic problem has to be overcome before to reach this ambitious target.[4]

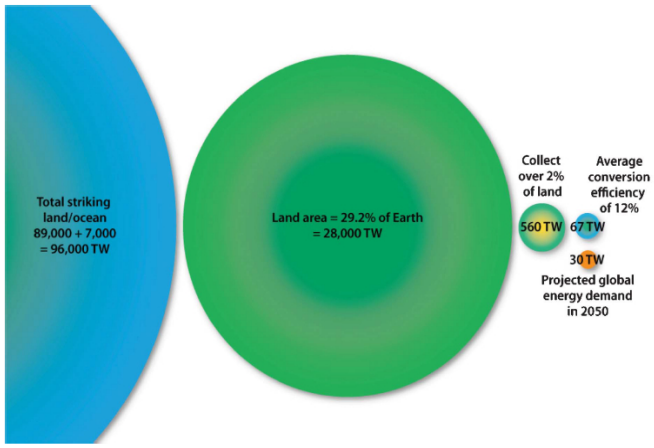

Figure 1.2: Rough approximation of technically feasible photovoltaic solar energy worldwide supply based on usage of 2% of land area and a power conversion efficiency of 12% [4]

The first generation of PV was dominated by crystalline silicon (c-Si). It is a wafer-based technologies, which benefit from high power conversion efficiencies, abundant materials, and proven manufacturability.[5] However in order to obtain high purity and crystalline materials, the fabrica-

tion process is complex and expensive. As a consequence the production costs increase, and worst, the CO_2 emissions increase [6][7] reducing the attraction to this technology. For this reason a second generation photovoltaic has developed based on thin-film cells that allow to reduce material usage, manufacturing costs and environmental impact. An overview of the main PV technologies is reported in Figure 1.3.

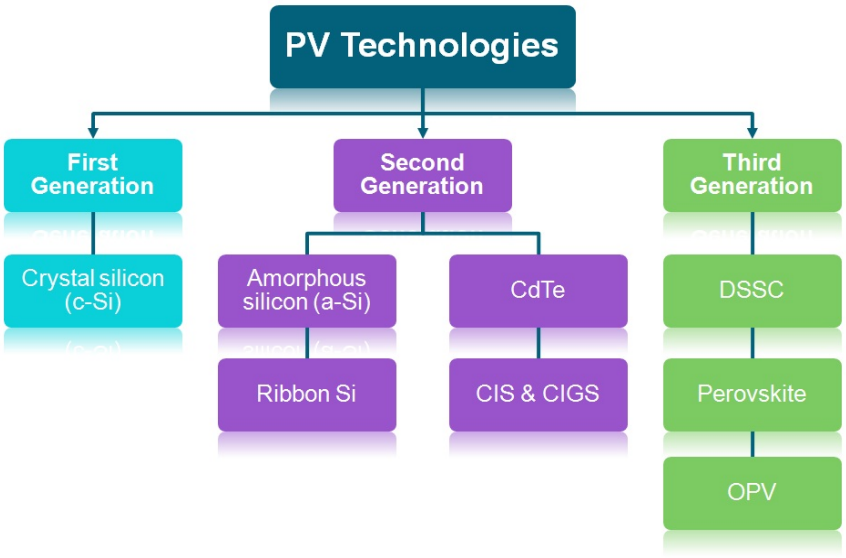

Figure 1.3: Overview of main PV technologies

The inorganic alternative are:

- **ribbon-Si**: to reduce cost for developing PV module Evergreen Solar developed a polycrystalline manufacturing technology that produced ribbons of polycrystalline silicon. However, due to their high defect density and generally higher impurity concentration its efficiency is low compared to mono-crystalline cells and other developing materials. [8]
- **a-Si**: amorphous silicon technologies has a higher band-gap(1.7eV)than crystalline silicon(1.1eV), it is compatible with lightweight and flexible solar cells[9]. Those cells are well suited for small-scale and low-power applications, however their susceptibility to light-induced degradation (the Staebler-Wronski effect [10]) and their low efficiency compared to other mature thin-film technologies limit market adoption.
- **CdTe** Cadmium telluride technology is an attractive thin film technology thanks to the deposition processes that offers low module costs. Good performance was found with sputtered CdTe layers only 0.5 mm thick, allowing low consumption materials and reduced the time processing. [11] However the main problems of this technology are the toxicity of elemental cadmium and the scarcity of tellurium.
- **CIGS** Copper indium gallium diselenide devices are based on films that can be deposited by a variety of solution- and vapor-phase techniques on flexible metal or polyimide substrates.

They shown record efficiencies of 21.7% for cells and 17.5% for modules[12]. Despite they seems a good alternative the main disadvantage is the scarcity of indium that could hinder large-scale deployment of CIGS technologies.

Summarising the key advantage of the thin-film technologies is the low materials used. Furthermore, life cycle analyses suggest that thin films produce lower greenhouse gas emissions during production and use than c-Si PV. [13] [6]. However the use of regulated, toxic elements (e.g., Cd) and reliance on rare elements (e.g., Te, In) may limit the potential for large-scale deployment.
In recent years, several new thin-film PV technologies have emerged as a result of intense R&D efforts in materials discovery and device engineering.
The third generation of thin-film PV technologies include the following:

- **DSSCs**: Dye-sensitized solar cells are photoelectrochemical cells consist of a transparent inorganic scaffold anode (typically nanoporous TiO_2) sensitized with light-absorbing dye molecules (usually ruthenium(Ru) complexes).[14] Key challenges involve limited long-term stability under illumination and high temperatures, low absorption in the near-infrared and the used of rare elements that can limited the use of this technology on large scale production.

- **Perovskite cells** Solar cells evolved from DSSCs based on a new materials called *perovskite*, it refers to the ABX_3 crystal structure. The most widely investigated is the hybrid organic-inorganic methylammonium lead halides $CH_3NH_3Pb(I, Cl, Br)_3$ that produced a certified efficiencies reaching 20.1% in less than 3 years of development.[15] Despite the great increase of the efficiency, key challenges need to be addressed, such as: to refine the control of film morphology and material properties, high sensitivity to moisture, unproven cell stability and the use of toxic lead.[16]

- **OPV** Organic PV are based on organic small molecules or polymers. These materials consist mostly of Earth-abundant elements, they can be processed by solution reducing the fabrications costs. They are compatible with roll to roll (R2R) fabrication that allow to implement the large scale production.[17] They are compatible with light weight, transparent, plastic substrates. They show the smallest ecological footprint and the shortest energy payback time possible [4]. Key challenges are: to get high efficiency at the modules scale and to increase the lifetime.

1.2 Advantages and disadvantages

Among all different photovoltaic technologies this work will focus on OPV. Conscious that the module efficiency is still not enough high for a commercial product and the lifetime still be an issue, the low cost, easy processable, portability, aesthetics freedom and low environmental impact are fundamental factors that encourage to continue the development of this technology. In this section it will be analysed in details the advantages and disadvantages of OPV.

1.2.1 Low cost

The main advantage that characterized the polymer based technologies is the low cost. In fact those materials can be processing from a liquid ink in R2R process, this can significantly reduces the costs from the expensive vacuum technologies usually required for processing other PV technologies. On 2009 Krebs *at el.* [18] reported a polymer solar cell processed by R2R on a polyethyleneterephthalate (PET) substrate with a coated layer of indium-tin-oxide (ITO) acted as transparent electrode. Recently [19], replacing the ITO electrode with high conductive - poly(3,4-ethyl-enedioxythiophene):poly(styrenesulfonate) (HC-PEDOT:PSS) was showed that all OPV layers can be process by inkjet printing directly over the encapsulation foil, further reducing costs. This manufacturing technique has many advantages as the high speed and the low energy consumption, but most important it allows a direct patterning of all the layers, including the electrodes, offering full freedom of design without the use of masks or structuring by hardware.
Saving cost doesn't concern just into a cheap fabrication process, but it involve also the post production activities. In fact OPV need low temperatures during drying and curing ($< 150^oC$) allowing to use flexible and transparent substrates. The results are light weight and mechanical flexible panels that permit to reduce transport costs and simplifying the installation. [20]
To take into account all those costs and compare OPV with other PV technologies it is introduced the "energy payback time" (EPBT), that is the time it takes for a solar cells to generate the same amount of energy invested during manufacturing, installation and maintenance. In Figure 1.4 it is reported the EPBT comparison between OPV and the commercial technologies in current, mid-term (5 years) and long-term (10 years) prevision. Currently an EPBT of ca. 90 days is possible for polymer solar cells with an efficiency of around 2% which is currently reached on flexible ITO-free modules.[21]

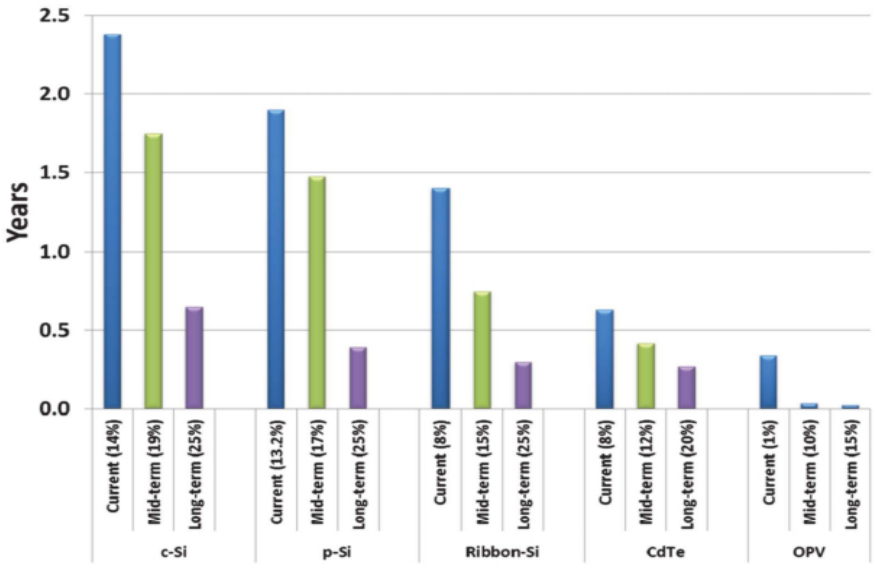

Figure 1.4: EPBT for silicon based solar cells, CdTe and OPV modules for current, mid-term (5 years) and long-term (10 years) scenarios. [4]

1.2.2 Environmental impact

The low EPBT and the used of Earth-abundant elements lead to believe that OPV is an eco-friendly technology. However some components of standard solar cells have a bad environmental impact. In the last years the research take care of this problem looking for new green materials able to replaced the toxic ones. The main toxicity arrive from PET, ITO and halogenated solvents used in the active layer ink. In the first place the PET is the most common synthetic fibre used in the world thanks to its light weight, transparency, gas-impermeability, mechanical stability, persistence, and cheap production costs. Although the high durability of PET is a requirement for commercial solar cells, it implies that its disposal has to be controlled. The immense production volumes and large amounts of PET dumped or incinerated in an uncontrolled manner represent a major environmental problem.[22] To overcome this issue different substrates have to be developed which maintain the same physical advantages joint with biodegradability. Many biopolymers such as cellulose [23], 4poly-L-lactic acid (PLA) [24] and glucose [25], have been successfully used as substrates for optoelectronic devices, but recently an interesting approach was demonstrate using silk fibroin (SF) natural protein, extracted from Bombyx mori cocoon (Figure 1.5). The main advantages is that SF can be easily processed from eco-friendly aqueous solution, it has the ability to host functional compounds such as nanoparticles (NPs) and/or optically active molecules, allows to tailor the SF properties and confer to it additional functionalities.[26].

Figure 1.5: SF-based ITO-free polymeric solar cell [26]

In second place the ITO transparent electrode is another source of pollution. The toxicity may be restricted to the nanoparticulate form, since ITO is applied as a semiconductive surface layer can be used for biological systems without adverse effects.[22] However ITO electrodes are fabricated via sputtering or e-beam processes, techniques that need high temperatures and high vacuum, thus resulting extremely expensive both in terms of costs and environmental impact. Luckily it is well demonstrated that ITO can be replaced with a conductive polymer: HC-PEDOT:PSS.[27] Many toxicity tests have been done on this material, the results indicate that PEDOT:PSS is non-toxic in its polymeric form.[22] Moreover it is water soluble processable, thus compatible with more eco-friendly coating process, in additional it is more robust than ITO during the banding and for this reason it is currently used in large area panel.[20]

In the end, the solvent used for the photoactive layer ink is another source of toxicity. Since large amounts of solution are used in the R2R printing of large-area modules, it is imperative to search for more environmentally friendly solvents. So far, most of the high-performance OPV

devices was based on acutely toxic halogenated solvents, such as chloroform, chlorobenzene or dichlorobenzene. Recently the process from non-halogenated solvents was shown to give not only the same performance. [28] [29] but also an higher thermal stability. [30]
Taking into account all those consideration OPV technology appears as a promising solution that guarantees benefits not just in terms of energy production, but also of environmental impact.

1.2.3 Power Conversion Efficiency

A disadvantages of OPV is the low efficiency under sunlight, compared with other PV techniques. However looking the Figure 1.6 the constant increase of performance in the last decades encourages the researchers to continue in this development. Different approach can be adopted to improve the performances, first, as it will be discussed in details in Chapter 3, new polymers can be designed and synthetized with better electrical and optical proprieties. Another method is to work on the device structure modifying interfacial layers, optimizing film morphologies and engineering device architectures. An example is to introduce nanocomposites on the PEDOT:PSS layer that allow to increase the incident light by scattering, inducing higher photocurrent and in consequence increasing the performance.[31] Else it possible to functionalize the substrate as Prosa *et al.* demonstrates using SF doped with a fluorofore as substrate, it acts as a luminescent down-shifting layer (LDS). This layer enhances the overall photocurrent of the solar cell by widening its spectral response in the range of absorption of the LDS. [26]
Even higher OPV efficiencies can be achieved by fabricating tandem solar cells composed of multiple active layers with different band gaps they allow to capture a greater fraction of the solar spectrum. In these devices, high energy photons are absorbed by the first layer, which has the largest band gap, and lower energy photons pass through it, and they are absorbed by a second layer of a material with a lower band gap. The theoretical best efficiency reached by a single layer cells is 15% [32] while for a tandem solar cells is over 20%.[33]

Actually the best performance is 10,1% [34] for a single layer and for a multi-junction cells 11,8%[35]; the main problems are the selection of materials with perfect absorption mismatch and the difficulty in the fabrication of a optimal interconnection layer between the two subcells.

1.2.4 Lifetime

If improving the efficiency of organic solar cells seems to be feasible, the main problem that affects those devices is the fast degradation. Different physical agents can damage the solar cells, such as water, oxygen, light and temperature.
The presence of oxygen can doped metal oxides [37], widely employed as interfacial layers between the BHJ and the cathode or can altered the photoactive polymer doping [38]. The ingress of water into the device causes fast oxidation of the low-work function metal cathode (Ca, Al) [39]. Some of these issues can be prevented with some precaution during fabrication processes and with a proper encapsulation, however other intrinsic degradation mechanism cannot be eliminated. In fact the high temperature can damage the active layer blend morphology induced separation of the polymer and fullerene phases [40], or induce the diffusion of atoms from interlayers, inside the

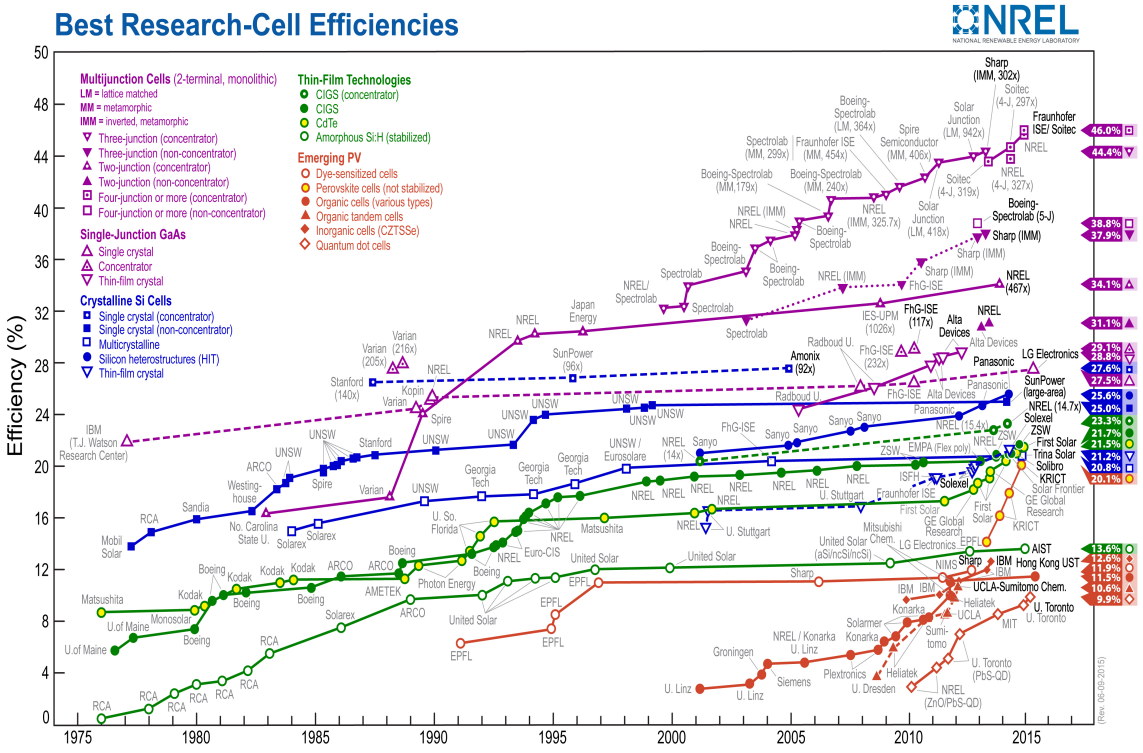

Figure 1.6: Overview of PV technologies efficiency [36]

active layer [41]. Unfortunately also the light soaking can induce photo reactions with solar cells compounds, that are usually detrimental for the device.

A deeper understanding on how the degradation mechanisms affect organic solar cells, may help the selection of stable materials, both in terms of active layer compounds, but also in terms of interlayer and electrodes [42]. In sight of this, in Chapters 4 and 5 it will be analysed in details the thermal degradation issue, while in Chapter 6 a preliminary observations on light soaking will be discussed.

1.2.5 New market opportunities

The goal of organic based optoelectronic devices is not to attain or exceed the level of performance of silicon technologies but it is to enable the fabrication of new devices with new functionalities at reduced costs (e.g., mechanical flexibility, impact resistance, and optical transparency) that are challenging to achieve with silicon.[43] The compatibility with transparent and flexible substrate, add the use of high-throughput printing techniques, allow to obtain light-weight and freedom of shape, properties that can be used in different situation. In Figure 1.7 are showed some examples of innovative applications such as active decorations on windows.

Another proprieties of OPV is to maintain the same efficiency also under un-direct or artificial light, enabling their used also in cloudy city or indoor application.[45] Furthermore, the potential for spectral selectivity through the choice of OPV materials and the semi-transparent behaviour

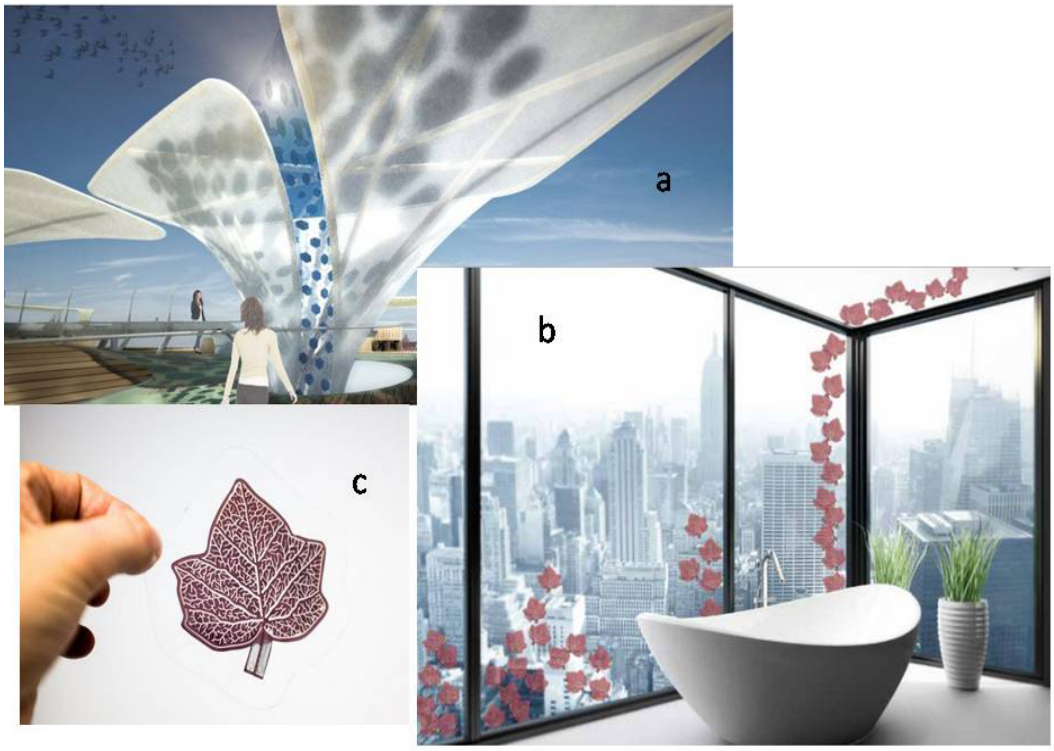

Figure 1.7: Different examples of OPV applications a) at Milano EXPO's German padillon, b) as windows decoration c) detail of a semi-transparent and light weight module [44]

induced to evaluate their use in photovoltaic greenhouse.[46]

Lastly the so called *out-off grid* energy is another market opportunities. Today more than 1 billion of people have no access to electricity. The problem is particularly acute in rapidly developing areas of Asia and Africa, where a combination of population growth and industrial development is placing huge demands on the existing electrical infrastructure. The main energy sources exploited until now are batteries, kerosene or diesel generators, all of which have a disproportionately high environmental impact as well as high costs. Traditional solar generation efforts have focused on replacing fossil fuel-based power generation but the hight weight and fragility of the traditional PV panels introduced high costs of transportation and installation. In this view OPV represents a valid alternative for the generation of *out of grid* electricity [47].

1.3 Concepts and evolution

To better understand the OPV technology it is important to start from the proprieties of organic materials. First of all, the main characteristic of an organic compound is that all molecules are based on a skeleton of carbon atoms. The most common artificial organic materials is the plastic, mainly based on polymers. Usually those materials are isolators, but in 1977, Heeger, McDiarmid and Shirakawa [48] reported the discovery of an organic semiconductor for which they received the Nobel prize in Chemistry on 2000.

At a molecular level, organic semiconductors are based on a C_2H_4 molecules, where the p_z atomic orbitals of the carbon atoms overlap to form π^+ and π^- conjugation molecular orbitals (also called π^* and π respectively) while the sp^2 form a σ^+ and σ^- planar molecular orbitals as shown in Figure 1.8a. When the number of adjacent molecules increase, the alternations of single and double bond create a conjugation that extended along all the polymer. In this way an organic semiconductor is formed and the π-electron result delocalized along the carbon backbone. From a physical point of view the system can be described with the *tight binding model*: when two atoms are closed, an orbital overlap is observed. The wave function of the two atoms Ψ_1 e Ψ_2, can combine in two different way: $\Psi_1 + \Psi_2$ or $\Psi_1 - \Psi_2$. The first case is the bonding orbital and it has a lower energy than the anti-bonding orbital (second case). When the number of atoms involved increase the number of molecular orbital increase. In the case of an organic semiconductor those correspond to π^- and π^+ orbitals. Increasing the conjugated orbitals the energy levels approach and form a continuous set of energy state forming an energy band. Also the energy separation diminish (Figure 1.8b). In comparison with the inorganic semiconductors two band can be defined: the highest occupied molecular orbital (HOMO) that corresponds to the Valence Band, and the lowest unoccupied molecular orbital (LUMO) corresponds to the Conduction Band. The difference in the energy level determines the Energy gap (E_g) of the organic semiconductor.[49] In Chapter 3 the proprieties of organic semiconductor will be explain in details.

The main difference with the inorganic semiconductor is connected with the charge transport. In a crystalline Silicon, where the atom are well ordered and the charge are free to move, the mobility is high ($10^3 cm^2 V^{-1} s^{-1}$). On the contrary an organic materials are characterized mainly by an amorphous phase alternating with crystalline regions. The charge carriers move freely in the conjugated backbone, but hopping from one molecule to the adjacent one, limiting the macroscopic charge transport. As a result, the charge mobility of organic materials is $10^{-5} - 0.1 cm^2 V^{-1} s^{-1}$. [50] Despite the low mobility, the organic materials can be efficiently used in a photovoltaic device thanks to their high absorption coefficients ($\alpha > 105 cm^{-1}$) which allow to capture most of the photons (within the absorption range) using a very thin layer($\sim$100 - 200 nm) in order to preserve a good charge transport [17]. Another main different from inorganic and organic based solar cells concern the generation of photo-charges. In inorganic semiconductors, when a photon is absorbed, at room temperature, free charges are immediately generated. Contrary in organic materials, due to their low dielectric constant ($\epsilon_r = 2 - 4$), tightly bound Frenkel excitons is observed [51]. The exciton binding energy is typically on the order of 0,3-1 eV that is considerably higher than the thermal energy at room temperature (25 meV)[52]. Therefore an additional electric fields is required to dissociate it into free charge carriers.

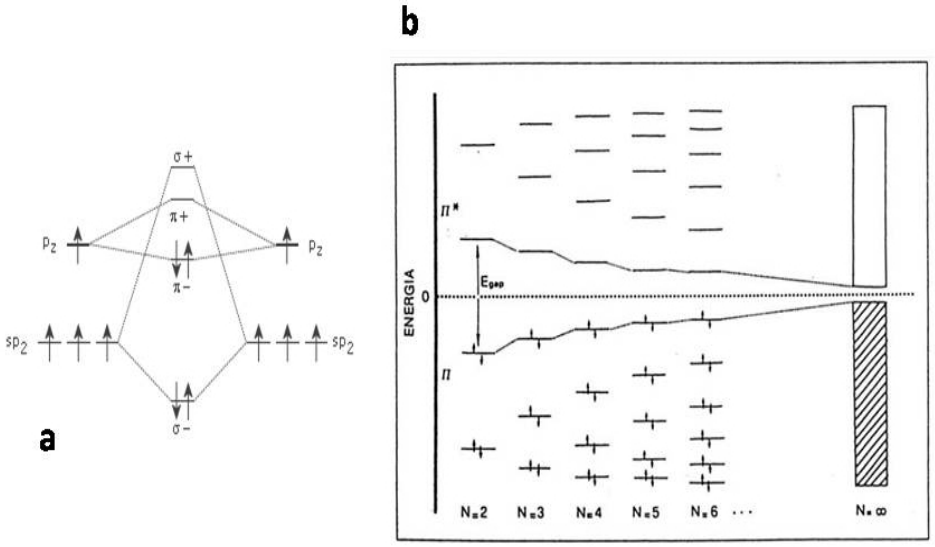

Figure 1.8: a) Scheme of orbitals overlap of two C_2H_4 molecules b) π and $\pi*$ level (correspond to π^- and π^+) increasing the C_2H_4 adjacent molecules.

1.3.1 History of Organic Photovoltaic

The first organic solar cell was based on a single organic layer sandwiched between two metal electrodes with different work functions (WF). As the organic semiconductors are mainly p-type, in the single layer structure, the semiconductor metal junctions are in one part an ohmic contact in the opposite a Schottky contact. At the interface between the organic layer and the cathode, the bands bending induces the formation of a depletion region (Figure 1.9a). The resulting electric field facilitates the dissociation of excitons generated, then the generated electrons can be collected by the low WF electrode while the holes are transported across the film to the higher WF electrode. Because of the short diffusion length (λ_D), most excitons generated outside the depletion region recombine to the ground state and do not contribute to photocurrent. Moreover, since free charges travel in the same phase, important charge losses due to recombination are also present. The combination of these factors explains the low photovoltaic performance observed in single layer OPVs in the range of $10^{-3}to10^{-2}\%$ [53].

To partially resolve the problems of a single layer solar cell, Tang *et al.* [54] introduced the bilayer structure (Figure 1.9b). The idea was to use two materials with different electron affinity and ionization potential. Between them, at the interface, the difference in potential energy is larger than the exciton binding energy provides the exciton dissociation. Then the electron is accepted by the material with the larger electron affinity (n-type) and easily collected by the cathode, while the hole is transported through the material with the lower ionization potential (p-type) and collected by the anode. In the work it was used a thin layers of p-type small molecules (copper phthalocyanine) and n-type molecules (perylene diimide derivative) thermally evaporated between a ITO and silver. The charge separation at the donor-acceptor (D-A) interface was efficient and the cells

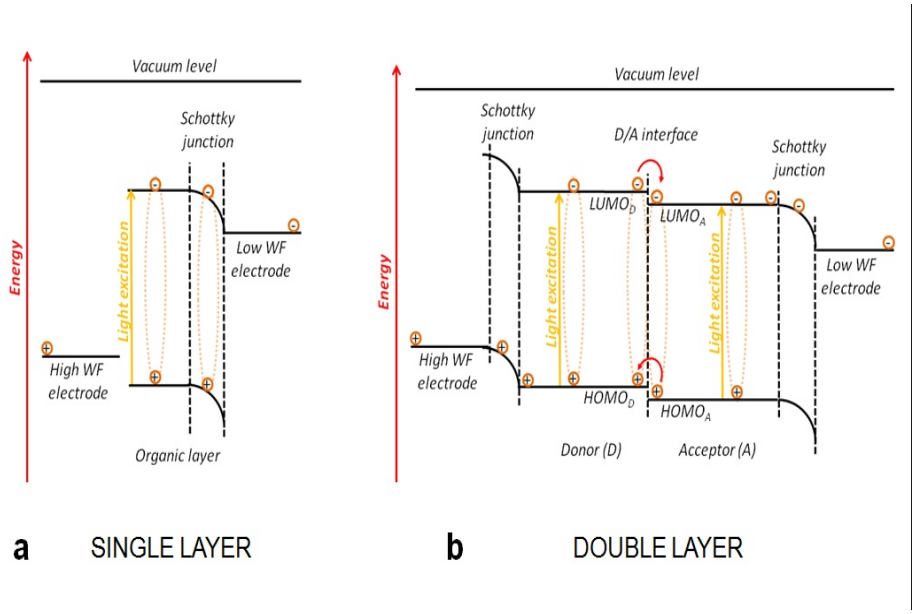

Figure 1.9: Scheme of band diagram of a single layer and bilayer structure

gives an efficiency of 1%. Beside the Schottky barrier limit was eliminated, the main limitation of this structure is correlated with the short lifetime of the exciton that has a λ_D of only $\sim 10nm$ [55]. To avoid exciton recombination, the active layer must be very thin, but such a thin film ($\sim 20nm$) is insufficient for effective optical absorption.
In this view the early 1990s were very fruitful for the OPV technology infact Heeger, Sariciftci *et al.* [56] first discovered electron transfer from polymer to fullerene. They reported ultrafast photoinduced electron transfer ($\sim 50fs$) from a conjugated polymer (MEH-PPV) to fullerene (C60). In the same year Yoshino *et al.* reported photoconductivity enhancement when polythiophene is blended with C60 [57]. Those results was very useful for Sariciftci and Heeger, that on 1992 patent the bulkheterojunction (BHJ) structure made from a solution of D and A materials [58] [59] [60]Às in the bilayer structure, the difference in electron affinities of the two materials creates a driving force at the interface between them that is strong enough to split photogenerated excitons. By blending materials on a nanostructured scale (about 10 nm), the interface is distributed throughout the device. Hence, all photogenerated excitons are likely to find an interface and split before recombining, if the charge transfer is significantly faster than competing recombination channels. Then, the separated charges can travel through the appropriate material toward the mutual contacts allowing the charge collection.
The cross-section of a standard bulk-heterojunction solar cells is depicted in Figure 1.10.

1.3.2 Working principles of bulk heterojucntion solar cells

The working principles of a BHJ solar cells is reported in Figure 1.11. The main steps are:

1. Photon absorption. The number of photons absorbed at a fixed wavelength is determined by

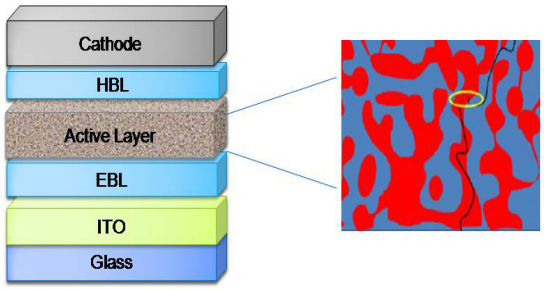

Figure 1.10: Scheme of a BHJ in standard configuration. HBL stand for Hole Blocking layer while EBL for Electron Blocking layer.

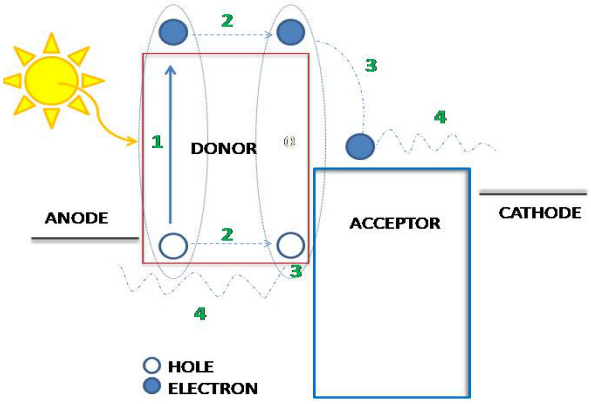

Figure 1.11: Working principles of a BHJ solar cells

the Lambert-Beer law 1.1:

$$A = log_{10}(\frac{I_0}{T_t}) = \alpha d \tag{1.1}$$

where A is the absorbance, defined as the base-10 logarithm of the ratio between the incident light (I_0) and the light transmitted by the sample (I_t). The absorbance depends, first of all, on the optical density of the film (α), which is correlated with the molar extinction coefficient (the intrinsic capacity of light absorption by a single molecule), the mass density of the layer and the orientation of absorbing molecules compared to incident light. Furthermore, absorbance is directly proportional to film thickness (d). The improvement of both α and d leads to an enhancement of absorption. However, an active layer with a significant high thickness typically affects the mobility of free charge carriers. Hence, a good balance between these two aspects is required.

When a photon is absorbed by the p-type donor material, an electron and hole with opposite spin are created, bounded by their Coulomb attraction in a singlet exciton state. Because coupling between neighbour molecules in molecular solids is low, the molecular excitations

are localized and there is no band to band transition, unlike in inorganic semiconductors. Concomitantly, the relative dielectric constant of the order of 3, as compared to 10 in inorganic semiconductors, results in strongly bound Frenkel like localized excitons [61]. The binding energy of the exciton is not well defined due to the disorder present in the conjugated polymer, but it can be determined for each single case [61]. In general the exciton binding energy is around 1- 0.3 eV. [62]

2. Exciton diffusion. Because of the high exciton binding energy the thermal energy at room temperature (25 meV) is not sufficient to dissociate a photogenerated exciton into free charge carriers. Consequently this quasi-particle diffuses inside the donor material as long as recombination processes do not take place. The exciton diffusion is an energy transfer processes, it can occur through two different types of interactions shown in Figure 1.12 i) Coulombic or Forster and ii) Exchange or Dexter interaction. Forster energy transfer represents a long range action occurring at a distance in the order of 3-7 nm. It is based on a non-radiative dipole-dipole coupling between an excited molecule, energy donor, and an exciton acceptor molecule, and it does not require physical contact of the interacting partners. On the other hand, Dexter energy transfer can be summarized with a double electron jump occurring through orbital overlap between the donor and acceptor molecules, thus it requires physical contact between the molecules involved. It is a short- range process which takes place only within distances in the order of 0.3-2 nm. [63]

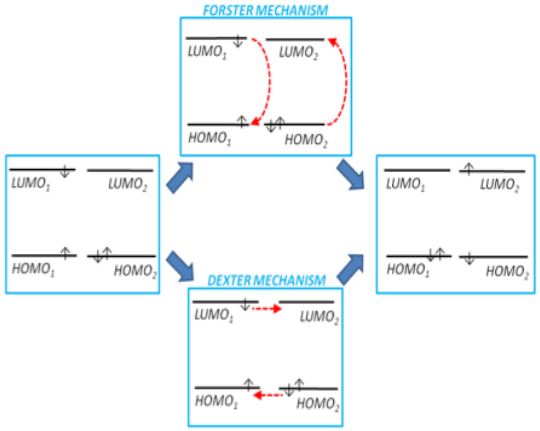

Figure 1.12: Schematic representation of the Forster and Dexter energy exchange mechanisms within two molecules 1 and 2

3. Exciton dissociation. The exciton λ_D ranging from 5 to 20 nm [61], in a BHJ solar cells the active layer morphology has to be optimized in order that the D domain size should be kept approximately in the same range of λ_D. Therefore to efficiently dissociate, the exciton has to reach an D/A interface.

   The dissociation can pass through an intermediate state called charge transfer (CT) state where the two charges are still bound by a Coulombic attractive forces. Thus an additional

force is needed to separated the charges, mainly it is determined by the different work-functions of the electrodes at the two sides of the device. This mechanism is in competition with the geminate recombination (transition from the CT state to the Ground level). [64] When the separation is efficient the two charges are free to diffuse in the respective material and to reach the electrodes.

4. Charge transport. Once the charges are separated the hole can diffuse in the p-type material, while the electron can move in the n-type material. In order to transport the charges until the respective electrodes the active layer morphologies has to be optimized to allow percolation pathways. It is clear that an ideal BHJ come from a compromise between high D/A interface and continuous pathways of the same species. When this condition is met the charge transport depends just on the conductivity of the D and A materials. However evaluate the charges mobility it is not trivial, because the intrinsic mobility can change when the two material are blended together. An useful technique that allows to reproduce the active layer device condition and measure the true mobility is the Space-Charge-Limited-Current (SCLC). In this measurement just one type of charge can be measure, by an electron- or hole- only device where, with an opportune choice of the electrode, the large injection barrier suppressed one of the type of charges. In a standard active layer composed from P3HT:PCBM (1:1 w/w) the charge mobility are for hole: $\mu_h = 10^{-4} - 10^{-3} cm^2/Vs$ [65] while for the electron: $\mu_h = 10^{-3} cm^2/Vs$ [37].

5. Charge collection. For an efficiently charge collection, following conditions must be met: the cathode Fermi level energy as to be lower then the acceptor LUMO ($(E_F)_{cathode} < (E_A^{LUMO})$) and the anode Fermi level energy has to be higher then the donor HOMO level ($(E_F)_{anode} > (E_D^{HOMO})$). Moreover another fundamental request is that one of the electrodes must be transparent to allow the light to pass through the active layer. The common electrode that satisfy this condition is a thin layer (150 nm) of highly conductive Indium Tin Oxide (ITO). ITO is a semiconductor made by In_2O_3 (90%) and SnO_2 (10%), it is transparent to visible light and partially to near UV radiation due to its bandgap (around 3.7 eV), and highly conductive due to its oxygen lacunas. The other electrode usually is a metal, such as: Al, Ca, Au, Ag, that is thermally evaporated over the active layer, if a good flatness is guarantee this electrode can acts as a mirror, reflecting part of the light that wasn't absorbed by the active layer, in order to increase the total number of photon absorbed.
   In the classical metal/insulator/metal (MIM) concept, if the semiconductor/metal is a non-ohmic contact the electrodes WF difference determine the performance of the solar cells in particular the Open Circuit Voltage V_{oc}. In case of ohmic contacts, in order to align the Fermi levels, the electrodes WF result pinned close to the LUMO/HOMO level of the semiconductor. Because of this pinning, the V_{oc} will be governed by the energetics of the LUMO of the acceptor and the HOMO of the donor. Indeed, in BHJ solar cells, a linear correlation of the V_{oc} with the reduction potential of the acceptor has been reported [66]. Moreover only a very weak variation of the V_{oc} (160 meV) has been observed when varying the work function of the negative electrode from 5.1 eV (Au) to 2.9 eV (Ca). [67]
   In the end to optimize the charge collection another factor as to be taking into account:

in a BHJ solar cell due to the intermixed active layer, both D and A are in contact with both electrode. Therefore at the semiconductor electrode interface non-geminate charge recombination processes (recombination between free charges) could take place, leading to performance losses. For this reason, a selective charge blocking layer or buffer layer is usually interposed between each electrode and the organic layer.

1.3.3 Buffer layers

In a standard structure device, the ITO is an anode and collects the holes. Usually an Electron Blocking Layer (EBL) is deposited in between the ITO and the active layer in order to prevent the charge recombination at the interface.
The most common EBL layer consists of PEDOT doped with PSS deposited as thin film onto the ITO. The PEDOT:PSS structure is reported in Figure 1.13.

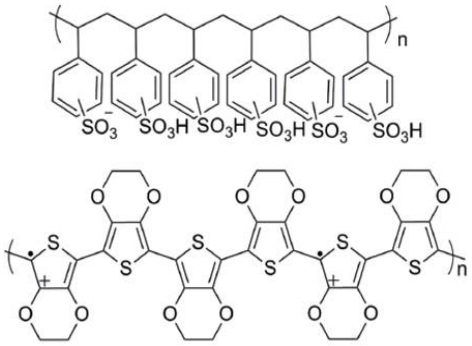

Figure 1.13: chemical structure of the PEDOT:PSS polymer

The main advantages of the PEDOT:PSS are: easily deposited by water solution/suspension, insolubility in organic solvents, relatively high conductivity ($> 200 S/cm$)[68], excellent electrochemical and thermal stability, relatively high transparency to visible light as a thin film (30 nm) [69]. In addition, an interesting feature of this material is that the Conduction Band (CB) can be tuned between -4,8 and -5,2 eV relatively easy by different ways, such as: adding oxidizing or reducing agents, adding NaOH or CsOH, or applying an electrochemical treatment to the dispersion. On the other hand, PEDOT:PSS has some negative implications due to: i) the extreme acidity of its dispersion ($pH \sim 1$), causing indium loss from the ITO contact; ii) the presence of water, both from its formulation and from humidity uptake from the ambient (PEDOT:PSS is highly hygroscopic), which could be detrimental for the device. Despite those disadvantages PEDOT:PSS results the most used EBL in the OPVs.
On the other hand in between the active layer and the top electrode (cathode), a buffer layer is often used to help the charge collection through the reduction of the barrier energy of the charge extraction process. The common material use for this purpose is Lithium Fluoride (LiF) usually combined with aluminium as electrode. The main improvement to used this buffer layer is that it induces a change in the work function or surface potential of the metal [62]. As results the V_{oc} is increased and the charge collection is improved with consequence increase also of J_{sc} and FF.

However the LiF is usually evaporated over the active layer, and this method deposition, despite it give high flatness and low roughness, it is not useful in the view of a full printed solar cells. For this reason different HBL are studied, such as $LiCoO_2$, TiO_x, ZnO, etc. deposited by solution. Moreover, when ZnO is used as HBL, in addition to its electrical and energetic advantages, it was demonstrate that it acts as an optical spacer that allow improving spatial distribution of light inside the multilayer stack of the solar cell and thus optimizing the absorption in the Active layer [70] [71].

2

Fabrication and characterization techniques

2.1 Device Fabrication

As reported in Chapter 1 a standard BHJ solar cell is composed by the structure:
glass/ITO/EBL/ActiveLayer/HBL/Cathode.
A thin film of 150 nm of ITO is generally sputtered on the glass substrate and processed in order to obtain a smooth surface, with a roughness less than 1 nm. The glass/ITO substrate is opportunely pattered compatibly with the final device geometry. After this procedure the substrate has to be properly clean before coating the next layers. The substrate is sequential sonicating (for 15 min) in baths of deionized water, acetone and isopropanol. Between each sonication step, substrate is dried with a stream of N_2 gas. After the last sonicating step it is placed in an oxygen plasma chamber for 10 min. The plasma treatment has a double scope, first it cleans the surface from any residual impurities, second it functionalized the ITO surface increasing the hydrophilic behaviour. This step is crucial for the deposition of the EBL.

A thin film ($\sim$ 35nm) of PEDOT:PSS is deposited in air condition and then annealed at 150^oC for 15 minutes in order to eliminate any residual water that can be detrimental for the solar cells. Then the active layer film has a thickness, in the order of 100 nm, is deposited over the EBL.
The main mandatory require for a full solution fabrication is that each layer has to be based on orthogonal solvent, to allow the deposition without damage the layer below. For this reason the common active layer ink is based on organic solvent that doesn't dissolved the EBL layer. The correct choice of the D:A ratio, solvent, solution concentration and different deposition parameters are crucial to optimized the morphology of the active layer, that, as explain in the Chapter 1, is fundamental for the solar cells performance.
Over the active layer usually LiF, combined with aluminium, is deposited by thermal evaporation in the same chamber where is evaporated the metal contact. Alternatively a HBL based on ZnO nanoparticles is deposited by solution over the active layer. The optimization of the ZnO layer in terms of thickness and morphology is crucial for the performance of the solar cell [71]. In the end

the negative electrode (cathode, typically, Ca/Al, or Al) is thermally deposited through a shadow mask. The geometrical overlap between the positive electrode and the negative electrode defines the active area.

The main techniques used to deposit thin film from solutions are spin coater and doctor blade (Figure 2.1 a and b respectively).

Spin coating allows to obtain uniform thin films on flat substrates via centrifugal force. Usually a small amount of coating material is applied on the center of the substrate,then the rotation spread the solution over all the substrate surface due to the centrifugal force. The affinity between the solution and the substrate, the viscosity of the solution, the boiling point of the solvent are main factors that induce different thickness and morphology. The main parameter that can be varied is the speed, increasing the rotation speed a thinner film is expected. However in a BHJ together with the thickness, also the morphology of the layer is crucial for the OPVs performance. It is possible to change the reorganization of the blend and maintain the same thickness, using different time of rotation, for example the film can remain complete dry or still wet after the spin coating. This condition implies different rearrangements of the active layer blend. The main limitation of the spin coater is correlate with the substrate dimensions. In fact to guarantee a homogeneous film the substrate has to be at least the same dimension of the rotate plate, in a common spin coater this limit is $< 25cm^2$. However is an useful technique at laboratory scale, indeed it can be easily located in a glovebox allow a base study on intrinsic proprieties in a controlled atmosphere.

A different technique used in laboratory, compatible with a R2R manufacturing technologies is the doctor blade. It is based on a blade that spread the solution over the substrate. The sample is fixed over a thermal plate, the temperature is precisely adjusted to change the proprieties of the final film. Then the ink is deposited forming a meniscus between the substrate and the blade. In the case of solution for OPVs, where the solvent can evaporate during the coating, the height of the blade and the amount of the solution are parameters crucial for the final film properties, but not direct depend with the final thickness of the layer. While the speed of the blade coating, in first approximation from experimental evidence, is direct proportional to the thickness of the final film. Obviously, as for the spin coater, [72] the quality of the layer depends also on the solution proprieties (solution concentration, solvent, viscosity etc.). Contrarily to the spin coater, the device dimensions are compatible with a commercial module ($> 100cm^2$) because the main limitations are due to the hotplate area and the blade length. In this view the doctor blade is usually placed outside the glovebox as in an industrial production line. It is important to note that not always it is possible to reproduce the quality of the film obtained via spin coater with the doctor blade, while once the layer is optimized with this blade technique the transfer to a R2R process is always guarantee. An example of a common technique used in an industrial production line is the slot die (Figure 2.1c) [73] [18] [74]. The main different with the doctor blade is that here the sample is moving and the blade is fixed. As in the previous case, the ink forms a meniscus with the substrate, then the height, the speed and the temperature can be properly change to optimized the film.

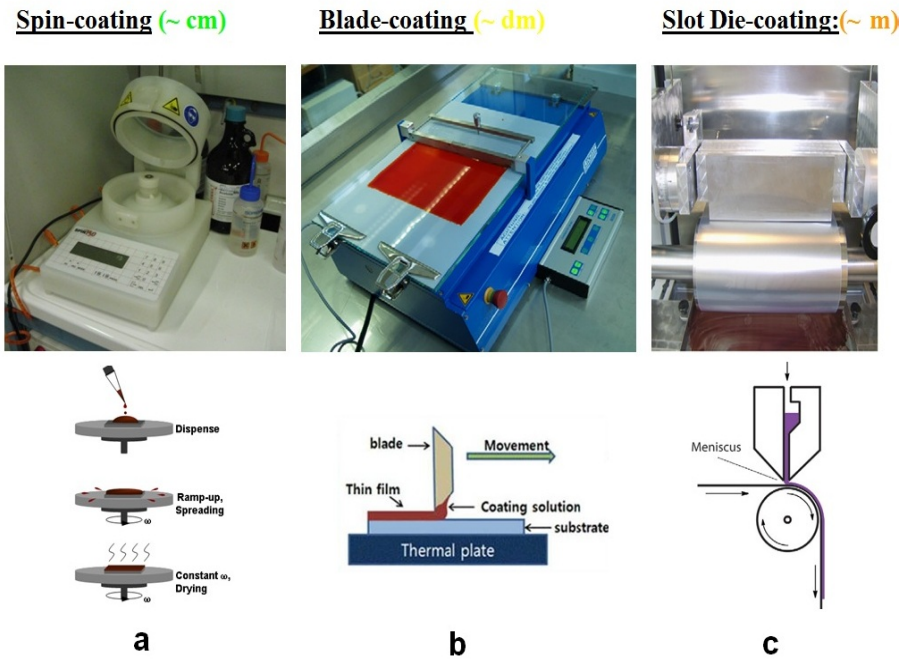

Figure 2.1: Main depositions techniques: a) spin coater b)doctor blade c) slot die coating

2.2 Organic materials for the BHJ active layer

Many different D photoactive polymers have been investigated in the present work. For facilitate good readability, each polymer has been numbered and the chemical name structure is resumed in an acronym. A part of two commercial products (P(7)-P3HT provided by Rieke Metals and P(8)-PTB7 provide by 1 Material) all the polymers are synthesized and characterised by colleagues at the "Chalmers University of Technology - Department of Chemical and Biological Engineering" in Goteborg (Sweden). The chemical structures of all D polymers are reported in Figure 2.3. In Table 2.1 main physical properties are reported: the molecular weight, the HOMO and LUMO energy and the best PV efficiency obtained in the work. Because during the thesis different batches of polymer have been investigated, for clarity it is reported also the Chapter where the specific polymer batch is used.

For the measure of the HOMO and LUMO level Square-wave voltammetry (SWV) measurements were carried out on a CH-Instruments 650A Electrochemical Workstation. The values are extrapolated from the potentials of the first oxidation and reduction peaks registered. The results are characterized by an experimental error of 5%, except the commercial products for which the data are obtained from literature and they are presented without error. Regarding the A materials, two commercial products have been used in the thesis: $PC_{61}BM$ ([6,6]- phenyl-C61-butyric acid methyl ester) and $PC_{71}BM$ ([6,6]- phenyl-C71-butyric acid methyl ester) both provided by Solenne BV. Their chemical structure is reported in Figure 2.3.

Polymer	M_n [KDa]	M_w [KDa]	E_{HOMO} (eV)	E_{LUMO} (eV)	PCE	Chapter	Ref
P(1) Q-BDT-4TR	16.3	47.4	-5.68	-3.14	3,2 %	3	[75]
P(2) FQ-BDT-4TR	18,5	46,1	-5,96	-3,20	5,3 %	3	[75]
	26	124			3,1 %	5	[76]
P(3) P-FQ-BDT-TR1	25	64	-5,89	-3,61	5,7 %	3	[77]
	37	133			5,2 %	6	[78]
P(4) P-FQ-BDT-TR2	30	66	-5,87	-3,63	3,4 %	3	[77]
P(5) P-FQ-BDT-T	101	270	-6,00	-3,63	5,3 %	3	[79]
P(6) P-FQ-BDT-TT	15	42	-5,90	-3,52	5,3 %	3;6	[79]
P(7) P3HT	18	37	-4,9	-2,7	3,0 %	4	[80]
P(8) PRB7	80	200	-5,15	-3,31	6,4 %	4;5	[81]
P(9) P-TT-MIM	91	252	–	–	3,4 %	5	[76]
P(10) P-BnDT-FTAZ	79	204	-5,36	-3,05	2,8 %	5	[82]
P(11) P-FQ-BDT-OTR	32	82	-5,74	-3,50	4,1 %	6	[78]
P(12) P-FQ-BDT-TROR	24	54	-5,84	-3,56	3,8 %	6	[78]
P(13) P-FQ-TT	19	53	-5,64	-3,45	3,8 %	6	[78]
P(14) P-FQ2T-BDT	28	66	-5,90	-3,60	4,2 %	6	[83]

Table 2.1: Summary of main physical properties of the D materials used in the thesis.

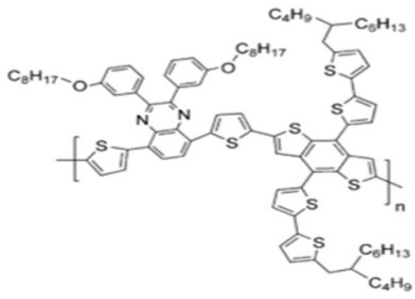

P(1) -Q-BDT-4TR

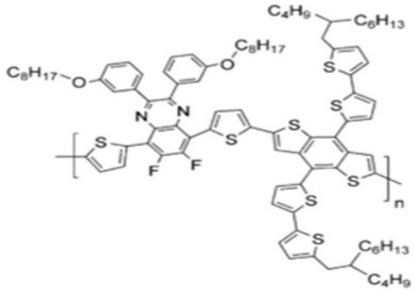

P(2) -FQ-BDT-4TR

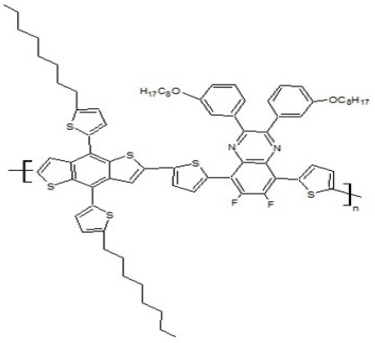

P(3)-FQ-BDT-TR1

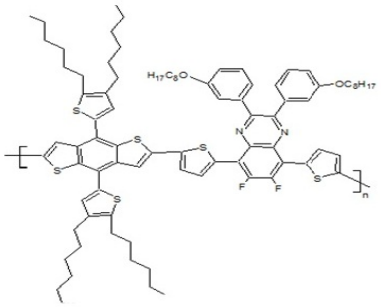

P(4)-FQ-BDT-T2R2

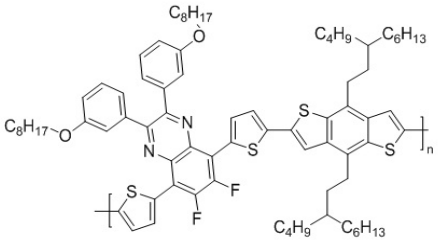

P(5) -FQ-BDT-T

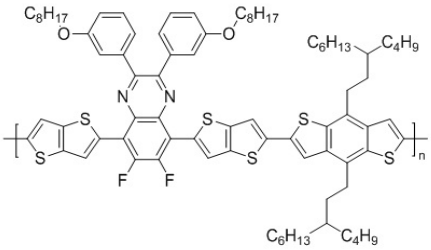

P(6)-FQ-BDT-TT

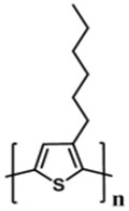

P(7) P3HT

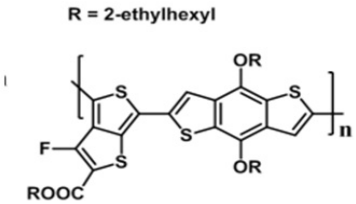

P(8) PTB7

Figure 2.2: Chemical structure of D and A materials used in the thesis

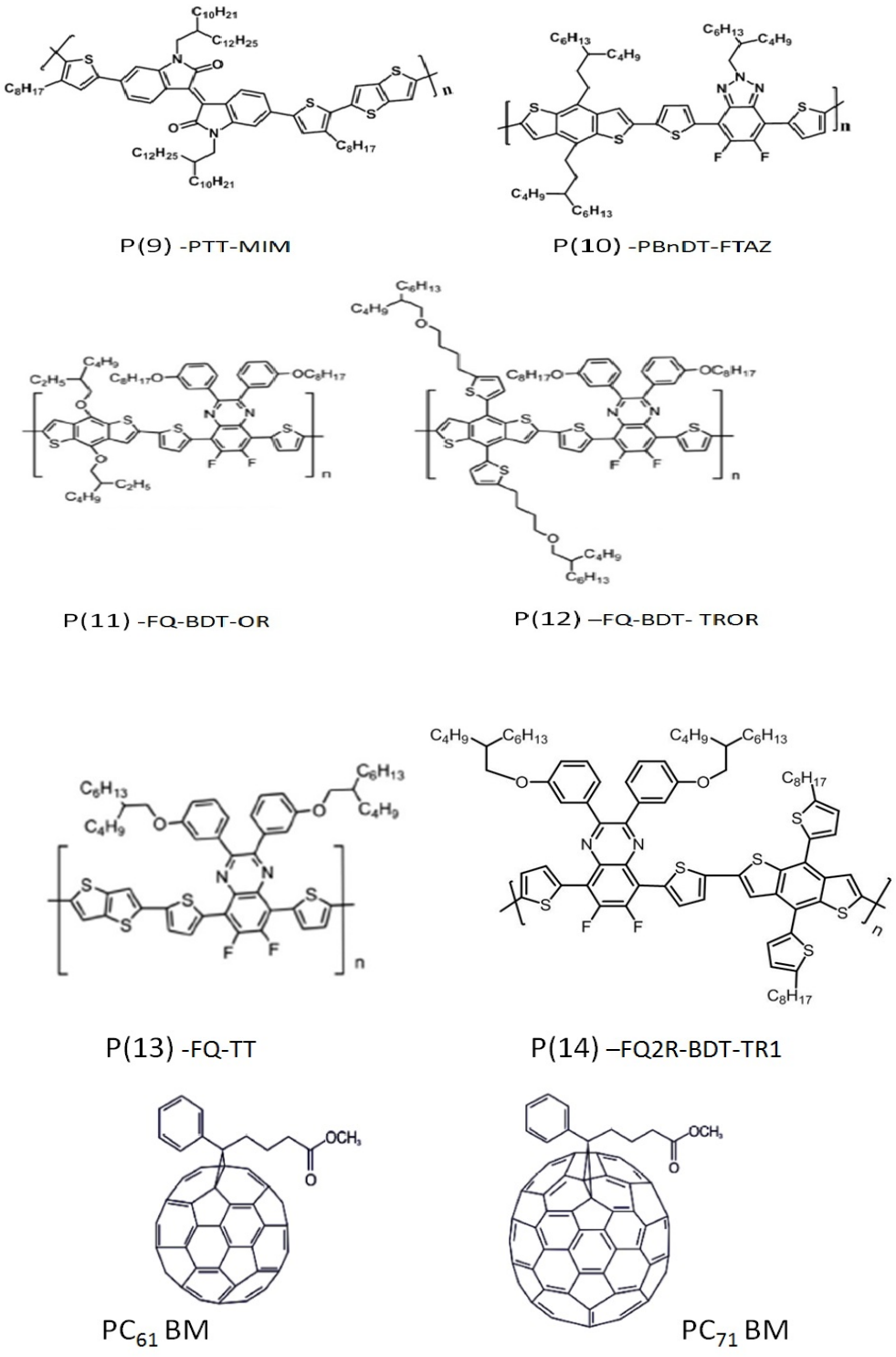

Figure 2.3: Chemical structure of D and A materials used in the thesis

2.3 Characterization techniques

2.3.1 Current - Voltage characteristic

To determinate the performance of solar cells it is necessary to know its Current - Voltage characteristic curve in dark and under illumination. This curve depends on intensity and spectrum of the incident light, for this reason it is necessary to define a standard illumination. Ideally the sun can be consider as a black body that emitted, however in a real situation part of the solar spectrum is absorbed through the gases in the atmosphere, consequently the spectrum changes as shown in Figure 2.4a. Moreover the amount of atmosphere that the sunlight must travel through to reach the Earth surface, depends on the inclination on the horizon and thus on the position in the world. To take into account this difference, it is introduced a value: Air Mass AM(x) where x is the inverse of the cosine of the zenith angle of the sun. To better clarify this idea, in Figure 2.4b different angleθ of about 48^o and 60^o are shown, that correspond of AM1.5 and AM2 respectively, while the solar spectrum emitted outside the atmosphere is defined as AM0 spectrum. For convenience, the flux of the standardized AM1.5 spectrum is called 1 Sun and it has been corrected to a fix value of $1000W/m^2 = 100mW/cm^2$; this value will used for all the experiments in this work.

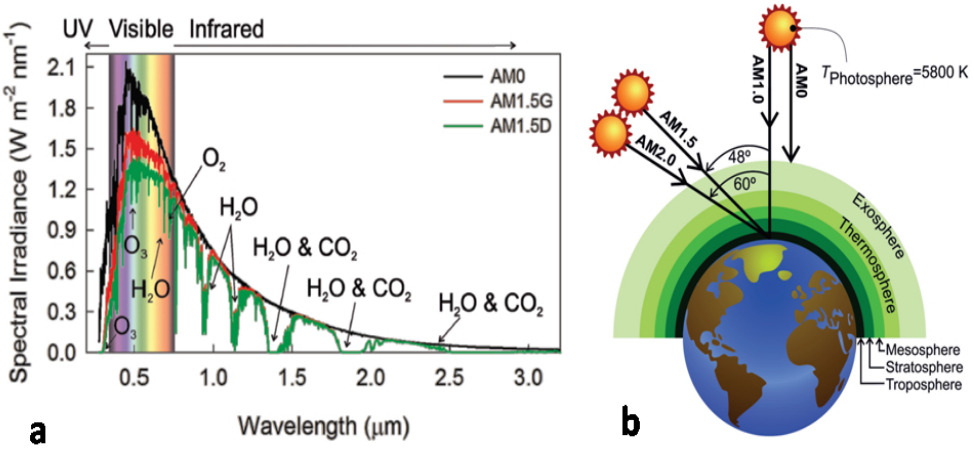

Figure 2.4: a) solar spectrum outside (black line) and trough the atmosphere at different incident angle. b) Scheme to explain the definition of the value AM(x) to identify the correct amount of sunlight reach each part of the world.

The experimental set-up used to measure the characteristic curve of a solar cells is reported in Figure 2.5. Due to the possible reactivity of the organic solar cells with the air all the I-V measurements are carried out inside a glovebox in inert atmosphere ($H_2O <$ 1ppm and $O_2 <$ 1 ppm). The sun light (1Sun AM1.5) is produced by a simulator placed under the glovebox. The correct amount of light is controlled by a reference cells. The incident light reachs the sample through a quartz window allowing an optimal transparency in the range of wavelength that are useful from an organic solar cells. During testing, each cell is carefully masked, by a calibrated mask, to pre-

vent an excess photocurrent generated from the parasitic device regions outside the overlapped electrodes area. The sample is contacted with a gold spring tips to preserve the electrodes, and then connected via BNC cable to a Keytley controlled by a Labview software.

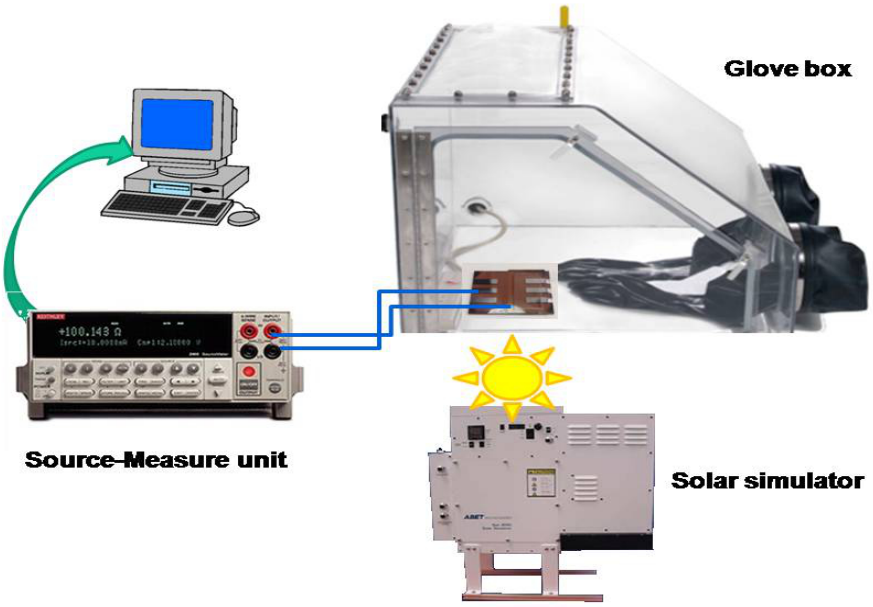

Figure 2.5: Scheme of the experimental set-up for the J-V measurement

The photocurrent generates under illumination depend on illuminated area, therefore for a properly comparison between different devices the theory will be explained based on current density instead of current. The Current density - Voltage (J-V) characteristic of an illuminated solar cell, in a first approximation, can be describe as an ideal diode p-n junction by the equation 2.1

$$J = J_s[exp(\frac{qV}{k_BT}) - 1] - J_{ph} \tag{2.1}$$

Where J_s is the saturation current density, q is the electron charge, V is the applied voltage, k_B is the Boltzmann constant and T is the temperature. Since empirically the real diode behaviour deviates from the ideal diode relation, an ideality factor n has to be introduced, leading to the Equation 2.2

$$J = J_s[exp(\frac{qV}{nk_BT}) - 1] - J_{ph} \tag{2.2}$$

The first term in equation describes the dark diode current density (J_{dk}) following the Schottky relation and the second term describes a constant photocurrent generated under illumination(J_{ph}). In the dark, there is almost no current flowing, until the contacts start to inject heavily at forward bias for voltages larger than a certain threshold voltage. While under illumination, the current flows in the opposite direction than the injected currents. However in the real solar real cells, even

in the best of cases, the ideal behaviour of the recombination diode of Equation 2.2 is never follow exactly. Indeed voltage and current are distorted with respect to this model by other elements in the device[84]. Those parameters are parasitic resistances: series resistance (R_s) and shunt resistance (in parallel) (R_{sh}). The R_s is the resistance offered by the solar cell in the path of the current flow. On the contrary, the R_{sh} is referred as the leakage path of the current in a solar cell and, therefore, it is represented in parallel with the current source. To describe the device an equivalent circuit is reported in Figure 2.6a. The current density of the dc current source corresponds to the photocurrent density J_{ph}. The diode is characterized by its reverse saturation current density J_s and ideality factor n.

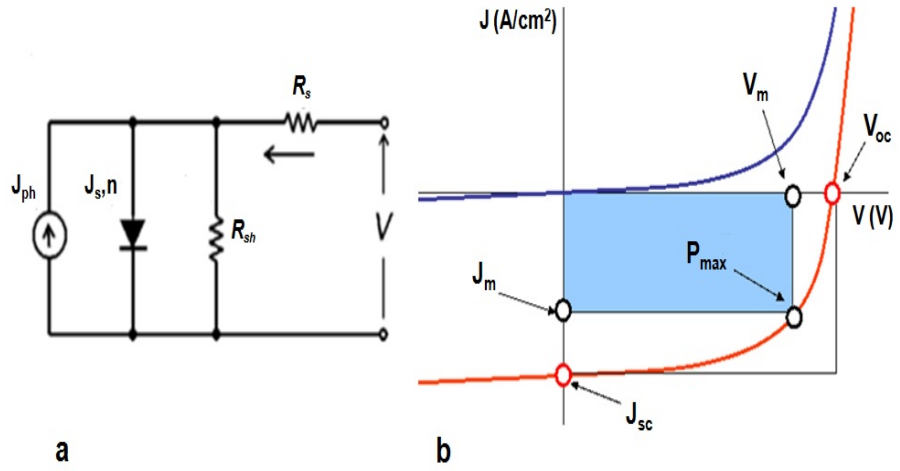

Figure 2.6: a) Equivalent circuit of an organic solar cell b)J-V curve of a solar cells where the main PV parameters are highlighted.

The electrical characteristic under illumination (IL) can be easily obtained once the functional relation of J_{ph} to IL is known. For typical inorganic pn-junction solar cells, J_{ph} vs IL is mainly linear. While in the organic solar cells the dependence is most complicated and it is not possible to fit experimental data over a range of different IL without a significant change in the diode parametersJ_s, n and R_{sh}. To take into account this fact a most complex equivalent circuit as to be introduces [63], but it is out of the aim of this work where just one light intensity will be used for all the experiments.

In the equivalent circuit model of Figure 2.6a, the current-voltage characteristic is described by equation 2.3 :

$$J = \frac{1}{1 + R_s/R_{sh}} \left\{ J_0[exp(\frac{q(V - JAR_s)}{nk_BT}) - 1] - [J_{ph} - \frac{V}{AR_{sh}}] \right\} \tag{2.3}$$

where A is the area of the solar cell. From the J-V curve can be directly evaluated the most important parameters of a photovoltaic cell: the short-circuit current (J_{sc}), the open circuit voltage

(V_{oc}), the fill factor (FF) and the power conversion efficiency (PCE).

The V_{oc} is the maximum voltage that a solar cell can deliver when no current flows through the external circuit (see Figure 2.6b). Following the classical thin-film solar cell concept, the metal-insulator-metal (MIM) model is applied to BHJ devices. In the MIM picture, V_{oc} is simply equal to the WF difference of the two metal electrodes. However in a BHJ solar cells this simple model has been found to be insufficient to justify the experimental open circuit voltage values. In fact it was shown that there is a linear relation between V_{oc} and the conjugated polymer oxidation potential [66]. Therefore, in first approximation, the open-circuit voltage of a conjugated polymer-PCBM solar cell can be estimated by the following equation:

$$V_{oc} = \frac{1}{q}(|HOMO_D| - |LUMO_A|) - 0,3V \tag{2.4}$$

Other elements, such as temperature, light intensity, active layer morphologies, nature and morphologies of interfacial layers and electrodes, can induce variation on the V_{oc}. However the equation 2.4 is considered as a starting point to evaluate the open circuit voltage.

J_{sc}, is the current flowing through the solar cell when the applied voltage V = 0V. At a certain photon flux, J_{sc} primarily depends on the ability of the Donor material to absorb light and create exciton, this is mainly determined by the absorption coefficient and the band gap. Moreover it depends on the exciton λ_D can vary with the intrinsic proprieties of the donor material, but also with the active layer morphology [85]. In the end J_{sc} depends on the carrier mobility in the D and A phases.

The power conversion efficiency (PCE) is defined as the maximum electric power (P_{max}) produced by the solar cell under illumination divided by the incident light power (P_i).

$$PCE = \frac{P_{max}}{P_i} \tag{2.5}$$

As mentioned before, the standard method to express the efficiency of a solar cells uses the conventional light intensity of 1Sun AM1.5 corresponding to $100mW/cm^2$.

In Figure 2.6b it is shown the maximum value of the output electrical power (P_{max}) in the J-V curve. At this value, the cell produces a certain current density J_m under an applied load of V_m. The ratio between the maximum power produced by the cell ($J_m \times V_m$, or P_{max}) and the theoretical maximum power that could be obtained ($J_{sc} \times V_{oc}$) is called fill factor FF, calculated as in Equation 2.6

$$FF = \frac{P_{max}}{J_{sc}V_{oc}} \tag{2.6}$$

The FF is therefore an indicator of the quality of a photovoltaic cell. In fact it represents the deviation of the J-V behaviour from ideality. These deviation is significantly affected both by the ideality factor (n) of the cell, but also from its electrical resistances (R_s and R_{sh}). For an ideal solar cell having a pronounced diode dependence of the current with voltage, R_s would be zero, and R_{sh} would be infinite. In real cases, the increase of R_s and a decrease R_{sh} determine modifications on the J-V curve shape, as shown in Figure 2.7. Indeed, a low shunt resistance implies free charges recombinations, thus current losses. As R_{sh} decrease, the J-V curve is smoother than ideality,

FF is farer from unity and V_{oc} is lower. On the other hand, a high series resistance causes ohmic losses at short circuit conditions, affecting J_{sc} and FF, while V_{oc} is not influenced. Strategies to

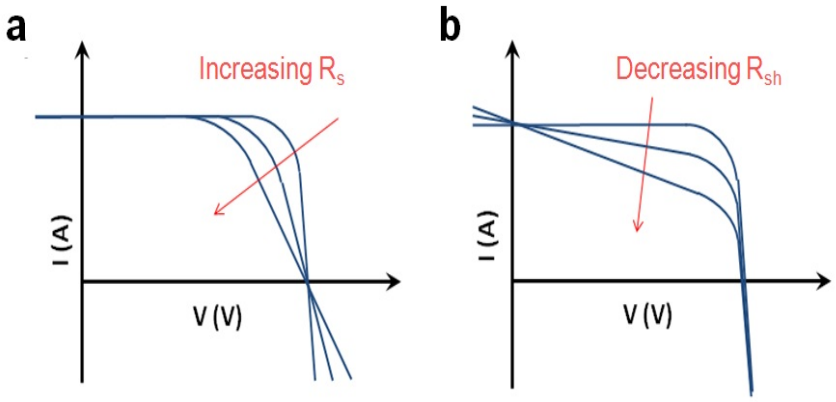

Figure 2.7: Effect of variation of R_s and R_{sh} on the ideal J-V curve.

decrease the contact resistances (thus lowering R_s) include the accurate choice and processing of the buffer layers and electrodes, while the strategies to decrease the shunt currents bypassing the D/A interface (thus increasing R_{sh}) involve the improvement of the BHJ morphology as well as the control and tuning of the energetic and kinetics involved in the charge separation process [86].

2.3.2 Quantum Efficiency

Another important photovoltaic parameter characterizing solar cells is the External Quantum Efficiency (EQE), also called incident-photon-to-current efficiency (IPCE). The EQE is defined as the ratio between the number of photogenerated electrons collected by a solar cells and the number of incident photons at specific wavelength. If the absorption spectrum of the solar cell is known, the fraction of absorbed photons can be used to calculate the internal quantum efficiency (IQE). This value gives the percentage of photons absorbed by the cell and converted into electrons as a function of wavelength. The EQE is directly correlate with the photocurrent (I_{sc}) by the equation 2.7 and it is generally measured under short-circuit conditions (V =0V) where the electric field within the device is large.

$$EQE(\lambda)\Big|_\lambda = \frac{n_{photoelectron}}{n_{incidentphoton}}\Big|_\lambda = \frac{hc}{q}\left(\frac{I_{sc}}{P\lambda}\right)\Big|_\lambda \tag{2.7}$$

where h is Planck' s constant, c is the speed of light, q is the electron charge, λ is the wavelength in meters and P is the power incident on the cell as measured by a power meter in Watts.

The experimental set-up used to measure the EQE is reported in Figure 2.8. The monochromatic light is obtained with a Xenon arc lamp from Lot-Oriel (300 Watt power) coupled with a Spectra-Pro monochromator. To evaluate properly the EQE of a functioning device an additional light simulating the Sun has to be added, to take into account the same amount of free charges than in the real device. To distinguish the photocurrent generated due to the external bias from the

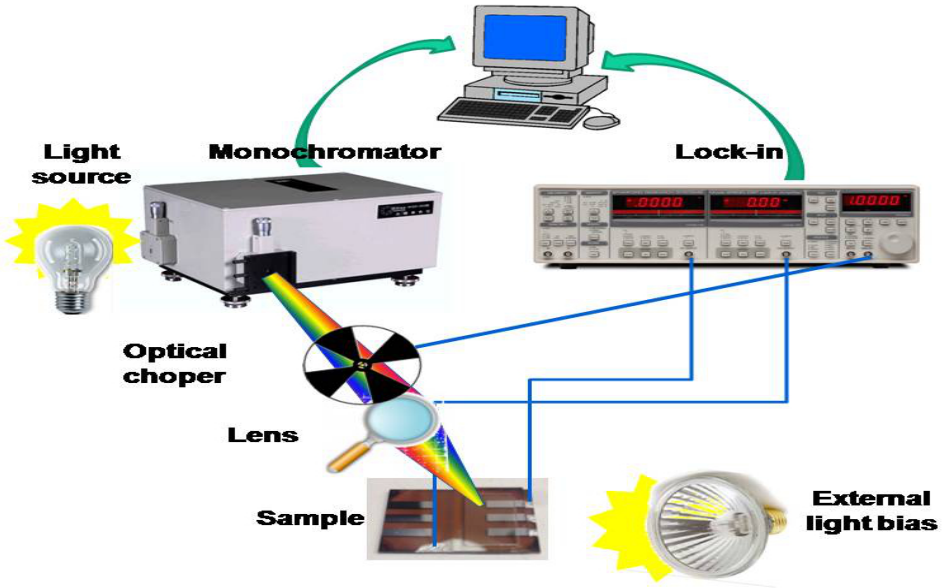

Figure 2.8: scheme of the experimental set-up for the EQE measurement

monochromator one, the last ray passes through an optical chopper connected to a Lock-In Digital Amplifier -SR830. The light, and in consequence the current signal, is pulsed with a frequency of 500Kz. To evaluate the amount of monochromatic photons that reach the sample it is used a reference Silicon UV-enhanced photodiode for which the quantum efficiency it is well known. During the measurement, the BHJ solar cells is properly encapsulated to prevent any degradation during the measurement

A simple calculation can be done to check for consistency between data obtained from EQE and J-V measurements. In fact, J_{sc} of a cell measured under solar simulator can be compared to a value calculated from the EQE data, using the expression 2.8

$$I_{sc} = \int_{\lambda_{min}}^{\lambda_{max}} P_{Sun}(\lambda) EQE(\lambda) d\lambda \tag{2.8}$$

where λ_{max} and λ_{min} are the wavelengths where the EQE vanishes.

For the operation of a organic solar cell, EQE is dependent on five major steps, each of which has some associated efficiency leading to the equation 2.9 [87]

$$EQE(\lambda) = \eta_{Abs}(\lambda) \times \eta_{Diff}(\lambda) \times \eta_{Diss}(\lambda) \times \eta_t(\lambda) \times \eta_{cc}(\lambda) \tag{2.9}$$

The absorbance efficiency parameter, η_{Abs} , describes the fraction of incident photons absorbed by the active layer which is determined by the bandgap and the absorption coefficient of the material, whilst the thickness of the active layer also affect the absorption yield. The exciton diffusion efficiency parameter, η_{Diff}, describes the ability of photogenerated excitons to diffuse through the D material and to reach a D/A interface. The dissociation efficiency parameter, η_{Diss}, is related to the separation process of bound electron-hole pair into free charge carriers. As the

electron is still bound within the exciton, the energy offset formed at the D/A interfaces provides a driving force which releases the electron and then the conduction is allowed. The transport efficiency parameter, η_t , describes the efficiency of charge carrier transport through the device. In the end, the charge collection efficiency parameter, η_{cc} , describes the ability of the charge carriers to be injected into the electrodes from the photoactive layer this parameter depends directly on the electronic composition of the device.

2.3.3 Mobility

In order to measure the correct mobility of the D polymer used in a BHJ solar cells it is fundamental to reproduce the same blend condition of the active layer of the device. Both in terms of D:A ratio, but mainly in terms of morphology. In fact, as it will better explain in Chapter 3, different organizations of the polymer in the D:A blend, lead to different device performance and often to different charge transport proprieties. A common technique used to measure the mobility of the D polymer is based on a Field Effect Transistor (FET) fabricated with the active layer. Then from the J-V characteristic of the FET it is possible to determined the hole mobility. However this approach has a disadvantage, because the charge transport under investigation is the lateral one, while in a solar cells the charges move in the vertical plane. It is well know that, due to the different spatial organization of the polymer, anisotropy in the charge transport is expected. In consequence the mobility value obtained from the FET measure is not always the relevant one. In light of this another technique is usually used to measure the hole mobility: the SCLC [88]. This technique has the unique requirement that the device has to be a hole-only device, thus the electrode has to be properly choose in order to obtain one charge injection contact and one injection-blocking contact. For example in a standard solar cells the PEDOT:PSS and the active layers are deposited in the same conditions than in the working device, while the standard LiF/Al cathode is replaced with Au. The measurement is carried out in Dark and inside the glovebox to prevent any degradation.

In Figure 2.9 is reported an ideal IV plot of a SCLC measurement.

At low voltages, the charges injected by the electrode are few and the relationship between Current and Voltage follows the Ohm law. For voltage higher than a certain threshold the charges injected increase and they generated a strong electric field, here is the region of the SCLC. In this region the J-V curve is characteristic for an insulator with traps. The J-V relationship follows the Child law or Mott-Gurney equation 2.10:

$$J = \frac{9}{8}\mu\epsilon\epsilon_0\frac{V^2}{d^3} \tag{2.10}$$

where μ is the hole mobility, ϵ is the dielectric constant of material (typically is fix at 3), ϵ_0 dielectric constant of vacuum and d is the thickness of the active layer.
Then, increasing the bias, all the trap levels are filled and an abrupt increase of current is observed. Above the trap-free voltage limit, the traps are filled and the device enters into the Traps Filled Limit.
In conclusion, the mobility value is obtained from the fitting of the SCLC region, by the equation 2.10. The main source of error is due to the correct identification of the region limits.

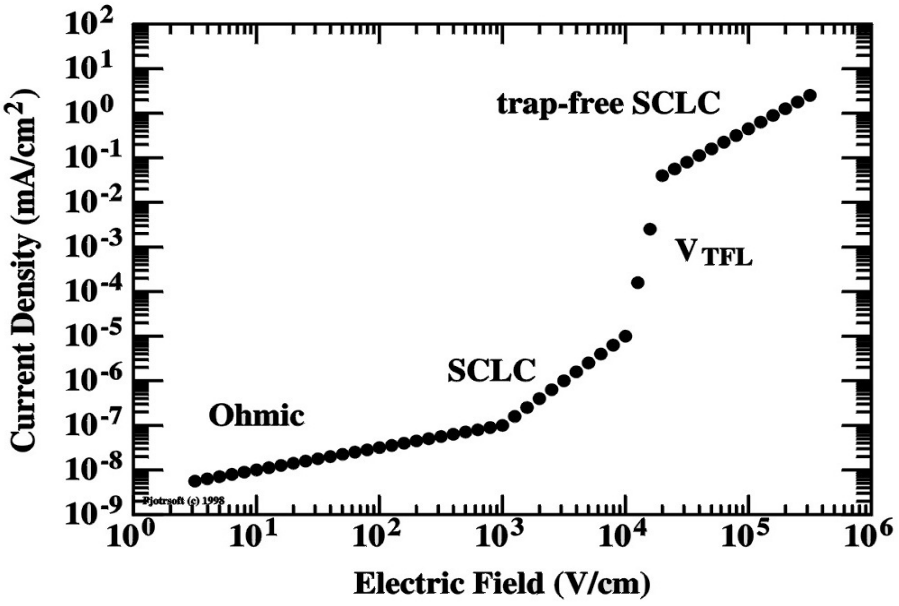

Figure 2.9: J-V curve of a hole-only device. Three main regions can be identified: Ohmic region at low voltage, the SCLC region and the Trap-Free Limit

2.3.4 Atomic Force Microscopy

The atomic force microscopy (AFM) was invented by Binnig (1986) [89]. In the AFM, the sample surface is scanned with a probe consisting of a microscopic tip situated at the end of a cantilever. The bending of the cantilever (contact mode) or damping of its oscillation amplitude (tapping mode) in response to the repulsive or attractive forces between the sample and the tip is monitored by an optical lever. A laser beam focused on the cantilever is reflected onto a four-quadrant photodetector, with the pairs of sectors arranged to detect bending deflection, bending oscillation, and torsion of the cantilever. The sample is moved in a raster pattern under the tip by the piezoelectric drive in a horizontal plane, while the vertical motion is controlled by a feedback mechanism. While scanning, the force between the tip and the sample is measured by monitoring the deflection of the cantilever. A topographic image of the sample is obtained by plotting the deflection of the cantilever versus its position on the sample. Alternatively, it is possible to plot the height position of the translation stage. This height is controlled by a feedback loop, which maintains a constant force between tip and sample. The variations of the z-position of the sample during scanning are plotted as a function of the x,y position of the tip to create the height image

Commercial cantilevers are typically made of silicon or silicon nitride. Both are covered with a native oxide layer of 1-2 nm thickness. The mechanical properties of cantilevers are characterized by the spring constant k_c and the resonance frequency ν_0. Both can in principle be calculated from the material properties and dimensions of the cantilever. For a cantilever with constant rectangular cross-section of width w, length L, and thickness t_c,the spring constant is [90]:

$$k_c = \frac{F}{Z_c} = \frac{Ewt^3}{4L^3} \tag{2.11}$$

where F is the force applied to the end of the cantilever in normal direction that induce the deflection of the cantilever Z_c, E is the Young modulus. A good cantilever should have a high sensitivity, that is achieved with low spring constants or low ratio t_c/L. Hence, in order to have a large deflection at small force cantilevers should be long and thin.

The deflection of the cantilever is usually measured using the optical lever technique. A beam from a laser diode is focused onto the end of the cantilever and the position of the reflected beam is monitored by a position sensitive detector (PSD). When a force is applied to the probe, the cantilever bends and the reflected light-beam moves through an angle equal to twice the change of the endslope dZ_c/dX. For a cantilever with a rectangular cross-section the change of the endslope Figure 2.10a is given by

$$\frac{dZ_c}{dX} = \frac{6FL^2}{Ewt_c^3} \tag{2.12}$$

The signal detected with the optical lever technique is proportional to the endslope of the cantilever. The deflection of the cantilever is given by

$$Z_c = \frac{4FL^3}{Ewt_c^3} = \frac{\Delta_{PSD}L}{3d} \tag{2.13}$$

where d is the distance between the cantilever and the detector and Δ_{PSD} is the variation in the position of the laser spot in the detector (Figure 2.10b). Hence, the deflection is proportional to the signal [90].

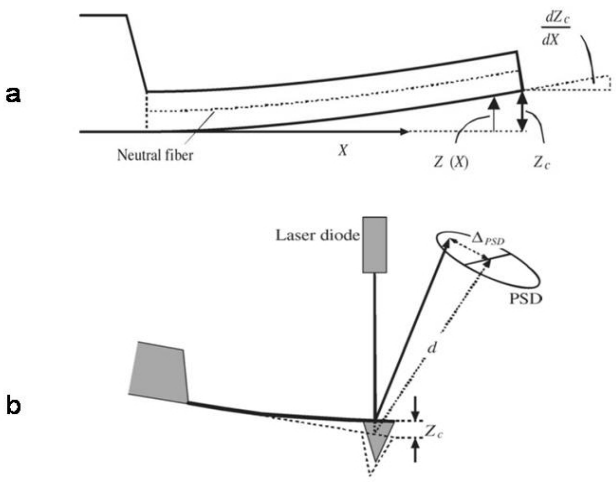

Figure 2.10: a) scheme of a cantilever with a rectangular cross-section b) scheme of optical detection of the cantilever deflection [90]

In AFM applications on soft materials, such as polymers and biological samples, it was found that high tip-to-sample forces in the contact mode often led to mechanical deformation of the surface. For this reason the no-contact mode or tapping mode is usually used for organic thin films. In tapping mode, the oscillation amplitude, which is reduced from the amplitude of the freely oscillating probe (A_0) by tip-to-sample repulsive interactions, is kept at the set-point value

(A_{sp}) by adjusting the vertical (z-axis) position of the sample with the piezoelectric drive. Such operation modes, called constant force, are the most common in AFM. Here the cantilever tip hovers about 5-15 nm above the sample surface to detect the attractive van der Waals forces acting between the tip and the sample.

The van der Waals force between atoms and/or molecules is the sum of three different forces, all proportional to $1/r^6$, where r is the distance between the atoms or molecules. The corresponding potentials are: the orientation or Keesom potential (w_K), the induction or Debye potential (w_D), and the dispersion or London potential (w_L) [91].

$$w_{VdW}(r) = w_K + w_D + w_L = \frac{C_K + C_D + C_L}{r^6} \tag{2.14}$$

In the BHJ solar cells the AFM is a useful tools in order to investigate the nanomorphologies of the active layer. In fact, in an optimized device, the morphology of D/A BHJ has to be compatible with exciton λ_D (in the order of few nanometers). Thus AFM images can give qualitative informations about the active layer morphology, two example are reported in Figure 2.11. In the first image big domains are present, suggesting a bad D/A intermixing an in consequence bad PV performance are expected. On the contrary in the second image, the fine intermixing lead to a homogeneous surface, typical of an optimized device.

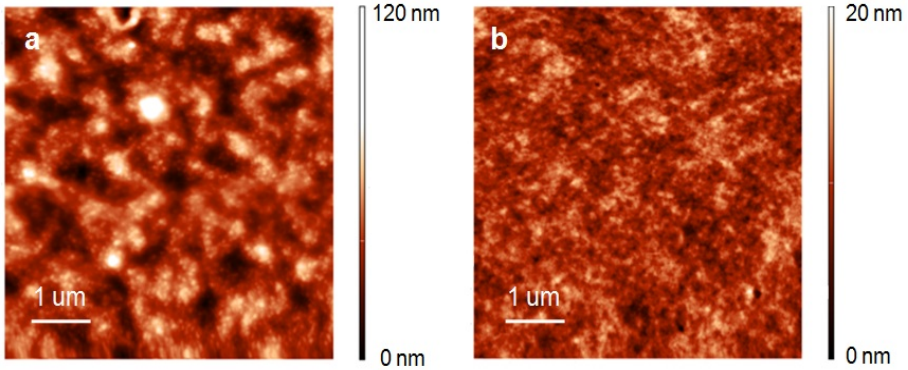

Figure 2.11: Example of active layer morphology: a) suboptimal morphology with big domains of the two species b) optimized morphology with fine intermix between D and A

Besides a qualitative analysis, a rough quantitative analysis can be carried out. The main parameter that allows to compare images of different blend is the Means Square Roughness (RMS). It is calculated as a square root of the mean of the squares of deviations from the mean [92] :

$$RMS = \sum_{i=1}^{N} \left[\frac{(z_i - \bar{z})^2}{N} \right]^{1/2} \tag{2.15}$$

where z_i represents the surface height at each data point on the surface profile, $\bar{z}$ represents the average height of the surface profile, and N is the number of data points. The average height of the surface profile is defined as:

$$\bar{z} = \frac{1}{N}\sum_{i=1}^{N} z_i \tag{2.16}$$

Basically, RMS roughness is defined in the same way as the standard deviation in statistical terms. For this reason the assumptions of having independent data samples imposed on the standard deviation would apply to the RMS roughness as well.

2.3.5 Kelvin Probe Force Microscopy

Kelvin probe force microscopy (KPFM) is sensitive to local variations in the WF of materials. In metals, the WF Φ_{WF} is considered to be the energy difference between the vacuum level and the E_F. While, in other types of materials, such as semiconductors or insulators, it can be regarded as the difference in energy between the vacuum level and the most loosely bound electron inside the sample. The WF depends on the specific material, thickness, dopant concentration, electrostatic charges, surface dipole moments and temperature. The KPFM is useful for the study of surfaces made from different materials, for example, polymer blends and composite materials [93]. The main advantages of KPFM are: i) it is quantitative, as it can measure the surface potential of nanometer scale objects with a potential resolution below 10 mV; ii) it is contact-less, and thus it does not significantly perturb the system under study and it enables in situ exploration of operating electronic devices; iii) it is versatile, as it can be employed on both conducting and insulating substrates and used to explore surfaces across a wide range of length scales, i.e., from the macro to the nanometer scale. [94]
The working principles is represented in Figure 2.12

When an AFM conducting tip is brought close to the sample surface, an electrical force is generated between the tip and sample surface, due to the differences in their Fermi energy levels. This value is called contact potential difference (CPD) and is defined as 2.17

$$V_{CPD} = \frac{\Phi_{tip} - \Phi_{sample}}{-q} \tag{2.17}$$

where Φ_{sample} and Φ_{tip} are the WF of the sample and tip, and q is the electronic charge.
During the KPFM measure it is applied an AC voltage (V_{AC}) plus a DC voltage (V_{DC}) to the AFM tip. V_{AC} generates oscillating electrical forces between the AFM tip and sample surface, and V_{DC} nullifies the oscillating electrical forces that originated from CPD between tip and sample surface. The electrostatic force between the AFM tip and sample is given by:

$$F_{es}(z) = -\frac{1}{2}\Delta V^2 \frac{dC(z)}{dz} \tag{2.18}$$

where z is the direction normal to the sample surface, ΔV is the potential difference between V_{CPD} and the voltage applied to the AFM tip, and dC/dz is the gradient of the capacitance between tip and sample surface. When $V_{AC}sin(\omega t) + V_{DC}$ is applied to the AFM tip, the voltage difference ΔV will be:

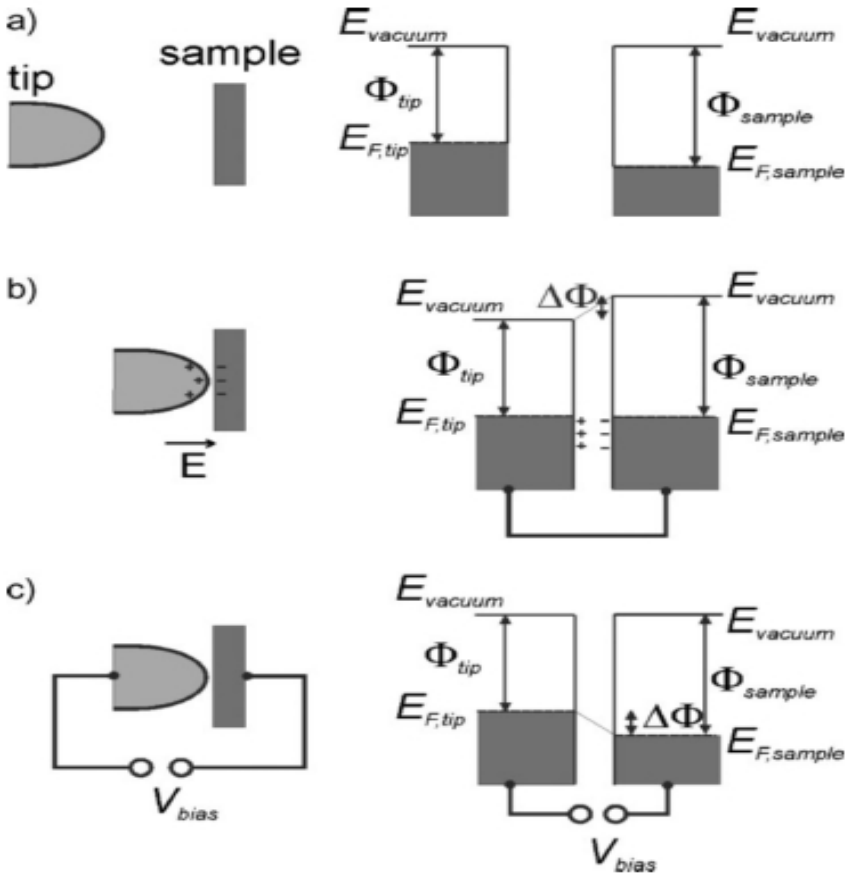

Figure 2.12: Sketch of a tip sample contact and the associated energy levels: a) tip and sample are separated, b) tip and sample are in contact ($\Delta\Phi = \Delta V = \Phi_{tip} - \Phi_{sample}$), and c) upon applying an additional external potential where $V_{bias} = V_{CPD}$ [93]

$$\Delta V = V_{tip} + V_{CPD} = (V_{DC} \pm V_{CPD}) + V_{AC} sin(\omega t) \tag{2.19}$$

Note that the $\pm$ sign depends whether the bias (V_{DC}) is applied to the sample (+) or the tip (-). Substituting equation 2.19 in equation 2.18 gives the expression of the electrostatic force applied to the AFM tip:

$$F_{es}(z) = -\frac{1}{2}\frac{dC(z)}{dz}\left[(V_{DC} \pm V_{CPD}) + V_{AC} sin(\omega t)\right]^2 \tag{2.20}$$

This equation can be divided into three parts:

$$F_{DC}(z) = \frac{dC(z)}{dz}\left[-\frac{1}{2}(V_{DC} \pm V_{CPD})\right]^2 \tag{2.21}$$

$$F_{\omega}(z) = \frac{dC(z)}{dz}(V_{DC} \pm V_{CPD})V_{AC}sin(\omega t) \tag{2.22}$$

$$F_{2\omega}(z) = \frac{dC(z)}{dz}\frac{1}{4}V_{AC}^{2}\left[cos(2\omega t) - 1\right] \tag{2.23}$$

F_{DC} (Eq. 2.21) results in a static deflection of the AFM tip. F_{ω} with frequency ω (Eq. 2.22) is used to measure the V_{CPD}, and $F_{2\omega}$ (Eq. 2.23) can be used for capacitance microscopy. When electrostatic forces are applied to the tip by V_{AC} with V_{DC}, additional oscillating components (due to the electrical force) will be superimposed to the mechanical oscillation of the AFM tip. A lock-in amplifier is employed to measure the V_{CPD}, to extract the electrical force component with frequency $\omega(F_{\omega})$, a function of V_{CPD} and V_{AC} . The output signal of the lock-in amplifier is directly proportional to the difference between V_{CPD} and V_{DC}. The V_{CPD} value can be measured by applying V_{DC} to the AFM tip, such that the output signal of the lock-in amplifier is nullified and F_{ω} equals zero. Subsequently, the value of V_{DC} is acquired for each point on the sample surface, composing a map of the WF or surface potential of the whole sample surface area.

2.3.6 Laser Scanning Confocal Microscopy

Laser scanning confocal fluorescence microscopy (LSCM) is a non-invasive technique which allows observing directly the BHJ active layer morphology inside working devices. The main advantage comparing to conventional optical microscopy is the ability to control depth of field for specimens that are thicker than the plane of focus. A representative scheme is reported in Figure 2.13 to explain the working principle. Coherent light emitted by the laser system (excitation source) passes through a pinhole aperture and it is reflected through a dicroic mirror towards an objective lens which focuses into the specimen. In confocal fluorescence microscopy , the signal detected is the emission of the excited sample, acquired at the same focus as excitation (confocal). The light emitted by the specimen (fluorescence) passes through the same objective lens, is transmitted by the dicroic mirror and passes through the second pinhole having the same focus as the first pinhole. Any light that passes the second pinhole is refocused and collected by a low-noise photomultiplier, which generates a signal related to the fluorescence intensity of the specimen. In order to build a two-dimensional map of the photoluminescence, the focused spot of light is moved in the x-y plane across the specimen (laser scanning). The final resolution achieved by the instrument is governed by the wavelength of light, the objective lenses, and the properties of the sample itself.

A standard solar cell is illuminated through the glass/ITO side under the metal electrode, and the active layer photoluminescence signal is collected in reflection mode. The device is scanned with a laser at 488 nm and the luminescence signal in the wavelength range 560-700 nm is acquired. At 488 nm light is absorbed only by the donor polymer and the observed variable is its unquenched residual luminescence from the charge generation process and from other minor energy deactivation pathways [95]. The 2D maps acquired with LSCM represent therefore a projection of the BHJ active layer morphology, where the contrast is determined, within the instrumental resolution, by the different physical and chemical nature of the photoluminescent species in the bulk: domains enriched of D would result brighter, while domains enriched of A and/or finely intermixed D:A

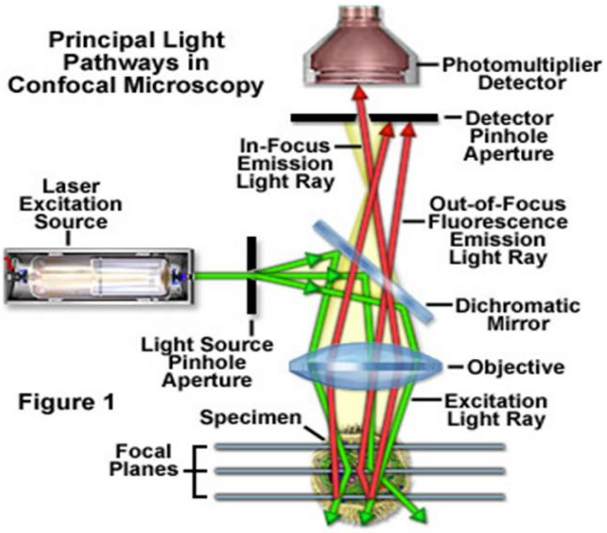

Figure 2.13: Scheme of Laser Scanning Confocal Microscopy

phases would result darker. [96]

2.3.7 Capacitance Voltage characteristic

A basic band diagram of a BHJ solar cell model is reported in Figure 2.14.

A first fundamental approximation is that the equilibrium Fermi level E_{F0} of the polymer/fullerene blend is situated close to the HOMO level of the D (in the present example P3HT). This assumption implies that the blend, at time zero, is p-doped. Possible origins of this hole majority carriers are negatively charged defects produced during exposure to air or moisture or induced during the processing. Due to this p-type behaviour, when the blend is contacted with the cathode a Schottky barrier and a depletion region is formed, while with the anode a ohmic contact is expected. The different between the cathode WF and the blend E_F gives the so called flatband potential V_{fb} (Equation 2.24).

$$V_{fb} = [E_{F0} - \phi_c]/q \tag{2.24}$$

The width of the depletion zone depends on the layer thickness the doping level and the applied voltage (V_{app}). At a low forward bias the depletion zone decreases and results confined to the cathode contact, and when the applied bias is equal to the V_{fb} it complete disappeared.

One important consideration of this model is that there is no overall electrical field in the device associated with the difference of the contact materials WFs at the two sides of the blend. Instead, each contact has its own equilibration, due to the starting number of electronic carriers in the blend. In the opposite case, if a reverse voltage is applied the width of the depletion region increase. Because the common thickness of an active layer blend is around 100 nm, at a relatively

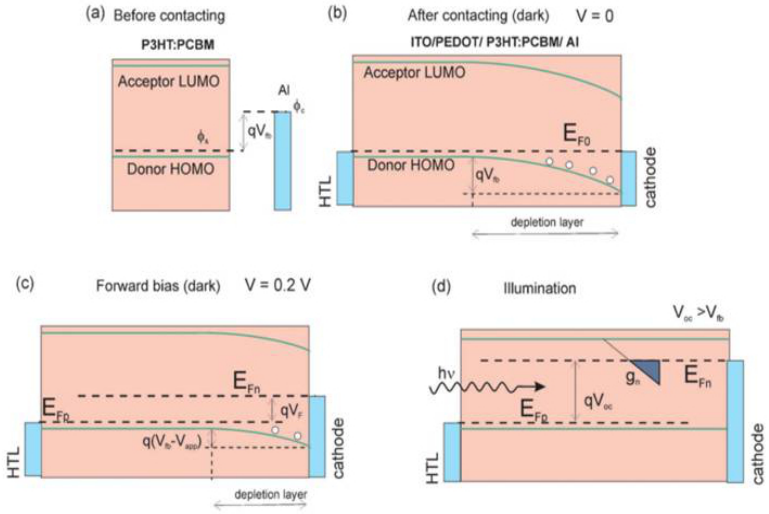

Figure 2.14: Band diagram of a BHJ solar cells before contact and under different external bias.

low reverse bias (generally $\sim 1V$) the depletion region can cover all the thickness of the active layer.

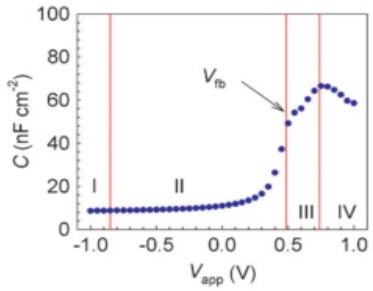

Figure 2.15: C-V plot of a P3HT:PCBM based solar cell [97]

This theoretical model is in perfect agreement with the Capacitance-Voltage (C-V) characteristic [98]. As shown in Figure 2.15 the C-V plot can be divided in 4 regions: the first region, at a large reverse bias, the sample is characterized by a constant capacitance called Geometrical Capacitance (C_g). It is connected with the dielectric proprieties (ϵ) of the active layer by the equation:

$$C_g = \frac{\epsilon\epsilon_0 A}{d} \tag{2.25}$$

where A is the area and d is the thickness of the active layer film.

The second region, at a moderate reverse and low forward bias ($V_{app} < V_{fb}$) the applied voltage modulates the width of the depletion zone following the Mott-Schottky relation explain in

the equation 2.26:

$$C^{-2} = \frac{2(V_{fb} - V_{app}))}{A^2 q \epsilon \epsilon_0 N_A} \tag{2.26}$$

The third region, at when the forward voltage excess the flat-band potential ($V_{app} \geq V_{fb}$) the depletion zone disappear, the capacitance is governed by a chemical capacitance (C_μ). This value is related, by definition, to the change of the occupancy of charge carriers in the fullerene LUMO and polymer HOMO [99] In the end, the fourth region, at a larger forward bias, usually the capacitance saturates and eventually decreases. [100]

To measure the C-V characteristic it is used using a Gamry Instruments Reference 3000 potentiostat/galvanostat/ZRA.

2.3.8 Impedance Spectroscopy

Impedance Spectroscopy (IS) is a technique allows addressing dynamic operational electric mechanisms of OPV devices which are not detectable by standard steady-state J-V characteristics. For instance, light absorption, charge separation, carrier transport (linked with series resistance), recombination losses or extraction efficiency (related to dynamic parallel resistance) and outer interface influences can be discerned, thus providing precious information in terms of device behaviour before and after thermal stress. The working principles, shown in Figure 2.16 consists on: to apply a voltage $V_{AC}(\omega) = \Delta V sin(\omega t)$ and to measure the current that will be $I(\omega) = \Delta I sin(\omega t + \phi)$. The function that correlate this two quantities is called impedance response ($Z(\omega)$). It is a complex number express by the equation 2.27:

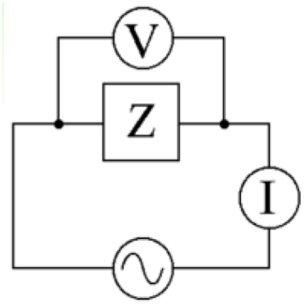

Figure 2.16: Sketch of the working principles of Impedance Spectroscopy

$$Z(\omega) = \frac{V(\omega)}{I(\omega)} = Z_0 e^{i\phi(\omega)} = Z_0[cos(\phi) - isin(\omega)] = Z_{Re} - iZ_{Im} \tag{2.27}$$

To investigate the device behaviour at different point of the characteristic I-V curve it is possible to applyed and additional V_{DC}.

Before to evaluate the $Z(\omega)$ and to guarantee a correct measurement three fundamental conditions must be met:

1. **Linearity**: the current response has to be direct proportional to the applied voltage. For this reason it is fundamental a correct choice of the amplitude of the voltage signal (ΔV) and to investigate a point in J-V characteristic where the response is linear (as in Figure

2.17a). To be sure that the linearity is maintained a Lissajous plot it usually used. As shown in Figure 2.17b the JV plot obtained during the measure, has to be symmetric to guarantee the linearity, otherwise an asymmetric curve implies a non linear response and consequently the measure cannot be interpreted correctly. The amplitude used for all the measurement presented in this thesis is 20 mV.

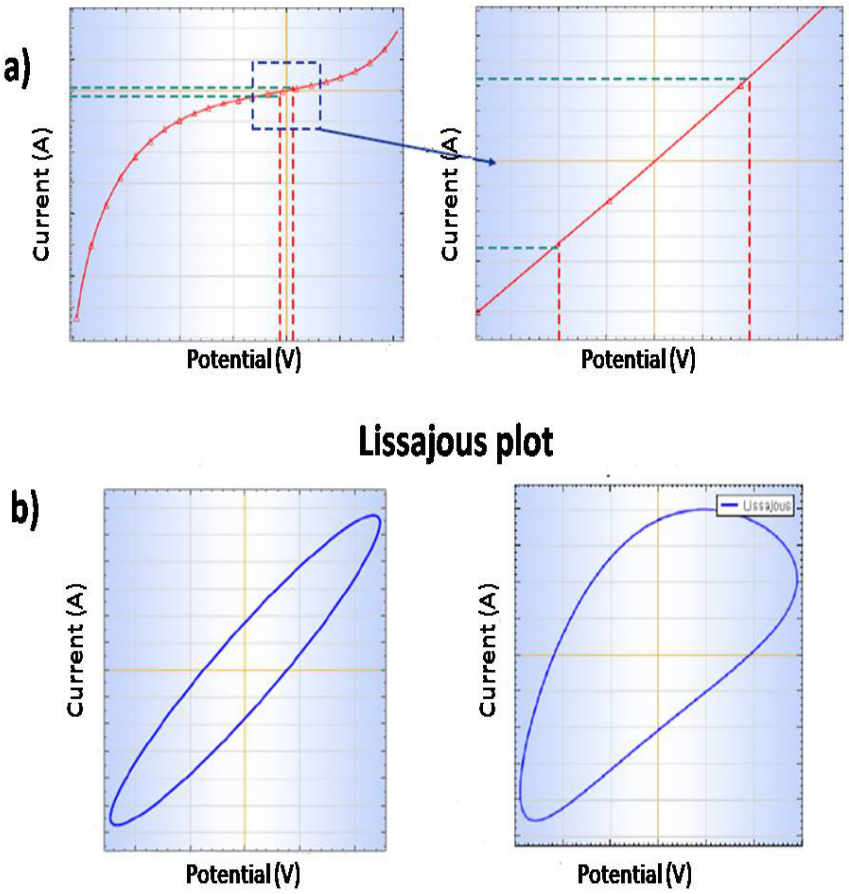

Figure 2.17: a) Condition where linearity requirement is guaranteed b)example of symmetric and asymmetric Lissajous plot useful to check the linearity of the response

2. **Stability**: the IS measurement depends on the frequency used, higher is the frequency used faster is the measure, *vice versa* lower is the ω slower is the measure, thus the lowest frequency determines the time of the measurement. To guarantee the validity of the data it is necessary that the system as to be stable along all the measurement. It is necessary to find a good compromise between the number of V_{DC} investigated and the range of frequency used. In this thesis the range used is from 1 MHz to 10 Hz.

3. **Causality**: as mentioned before, from $Z(\omega)$ response it is possible to obtain important informations of the device, so it is fundamental that the current response is induced just from the V_{app}, and not from external noise. Thus, the whole system is properly shielded with

a Faraday cage.

Once those three condition are fulfilled the data can be interpreted, but to do that a physical knowledge of the system is required. Different ways to represent the data, helping their interpretation, are : the Nyquist plot and the Bode representation. The first is obtained plotted the imaginary part of the $Z(\omega)$ versus its real part, for each frequency. While the Bode plot represents the module $|Z_c|$ and the phase ϕ against the frequency range. The interpretation consists to find an equivalent circuit that can fit both experimental curves. Some basic examples of different systems can be used to explain the IS data analysis [101].

If the sample is an ideal resistance of length d area A characterized by a conductivity σ, the impedance response, shown in the Figure 2.18a will follow the Ohm law:

$$Z(\omega) = \frac{V(\omega)}{I(\omega)} = R = \frac{L\sigma}{d} \tag{2.28}$$

No frequency depends and no different in phase ϕ are expected, so in the Nyquist plot the point at different frequency will overlap, the imaginary part will be 0Ω and the real part will have exactly the value R. In the bode representation the module $|Z_c|$ will be the resistance value R and the phase will be constantly 0^o.

If the sample is an ideal capacitor with a dielectric constant ϵ area A width d, the capacitance value is: $C = \epsilon A/d$. The impedance response, shown in the Figure 2.18b, will follow the equation:

$$Z(\omega) = \frac{V(\omega)}{I(\omega)} = \frac{-i}{\omega C} \tag{2.29}$$

In this case $Z(\omega)$ is imaginary and the current will out of phase of 90^o, so in the Nyquist plot a straight line is expected centred at 0Ω because at different frequency just the imaginary part is changed. In the bode representation the module $|Z_c|$ will change with the frequency following the Equation 2.29 while the phase will be constant at 90^o

Starting from those two basic elements it is possible to compose most complex circuits, for example they can be joined together in series or in parallel. In the first case the impedance response become:

$$Z(\omega) = Z_R(\omega) + Z_C(\omega) = R + \frac{i}{\omega C} \tag{2.30}$$

As shown in Figure 2.19, the Nyquist plot is characterized by a straight line centred at value corresponds to the resistance R. In the Bode representation at high frequency the system mostly depends on the resistance behaviour, while at low frequency the main proprieties depend on the capacitor behaviour.

Vice versa when R and C elements are put in parallel the $Z(\omega)$ becomes:

$$Z(\omega) = [\frac{1}{Z_R(\omega)} + \frac{1}{Z_C(\omega)}]^{-1} = \frac{R}{i\omega RC + 1} \tag{2.31}$$

As reported in Figure 2.20, if the axis have the same scale, the Nyquist plot presents a semicircles, the diameter correspond to the resistance R. The frequency at the maximum (ω_0)it is directly

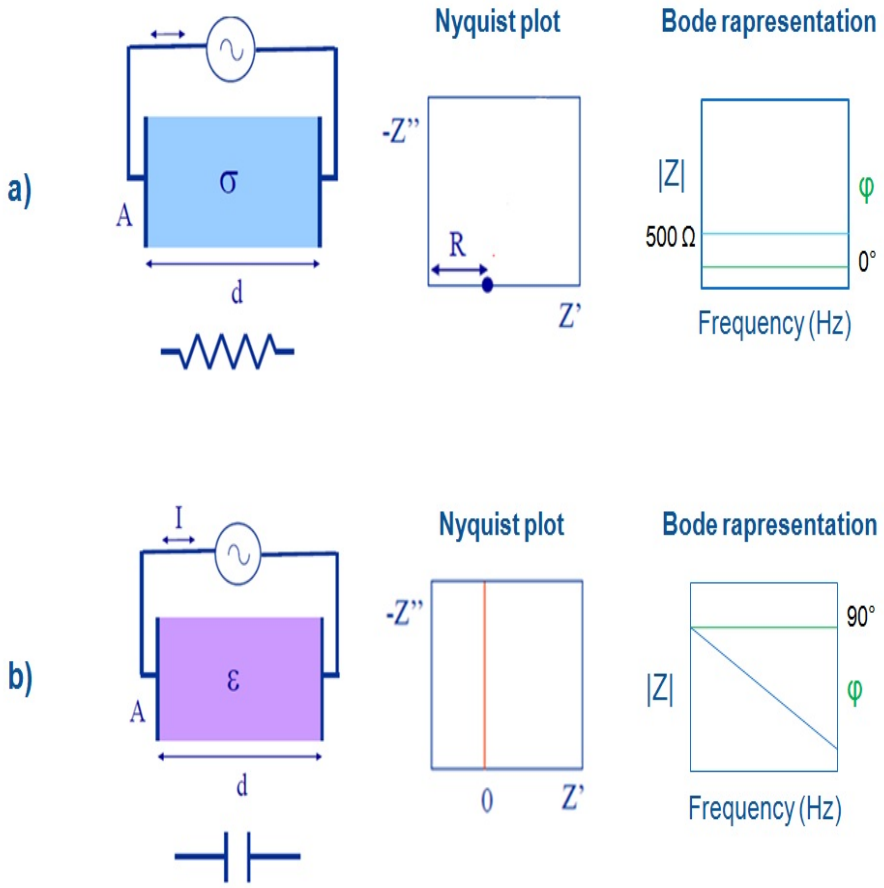

Figure 2.18: IS results of a) an ideal resistor b) an ideal capacitor

connected with the time-scale τ of the process described by the equation:

$$\frac{1}{\omega_0} = RC = \tau \tag{2.32}$$

The Bode representation contrarily than in series case, at high frequency mostly depends on the capacitor behaviour, while at low frequency depends on the resistor behaviour.

As mentioned before, the knowledge of the system in the point of view of the physical process is fundamental to interpret properly the IS data.

2.3.8.1 Impedance Spectroscopy applied on organic solar cells

To understand the IS data, it is necessary to implement experimental *ad hoc*, where just one parameter is carefully changed. For a solar cells a standard measure is done at different DC external bias both in dark and under 1 Sun. Moreover it is possible to fabricated *ad hoc* solar cells in order to enhance one effect/defect, for example, change the transport layers, the electrodes, the thickness of each layer, add impurities or insulating layers. Those experiments allow to understand the time scale of each physical processes involved in a solar cells, and identify each arc o segments

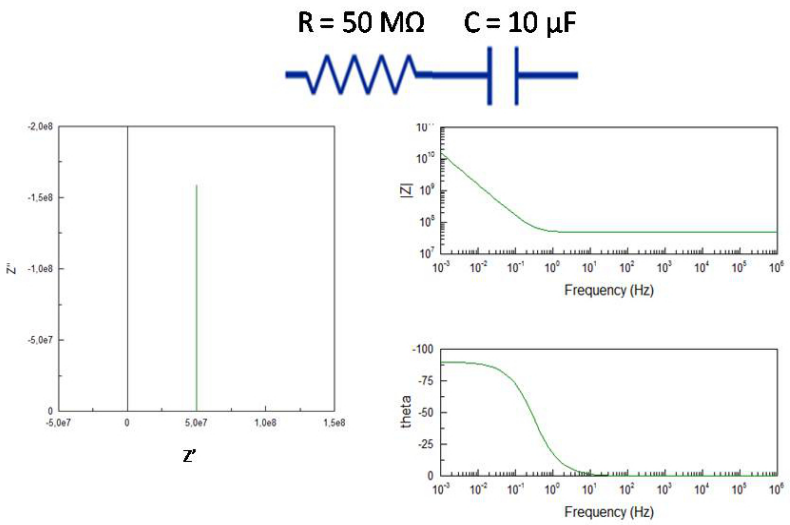

Figure 2.19: a) Example of IS results of an ideal resistor ($R = 50\Omega$) in series with an ideal capacitor ($C = 10\mu F$)

of an Nyquist spectrum.
From the physical knowledge of a standard solar cells based on a device structure: ITO/PEDOT:PSS/ActiveLayer/Al, the equivalent circuit is reported in Figure 2.21.

In first approximation the ITO/PEDOT:PSS can be consider as an ohmic contact characterized by a resistance called series resistance (R_s) connected with the conductivity of the two layers. It is important to underline that the IS measurement can investigate just the free charges, so the exciton formation and dissociation are not considered. When the charges are generated they can follow different pathways. In one case the electrons can be transported by the A and the holes by the D polymer. This process appears as an arc in the Nyquist spectrum, connected to a resistance called Transport Resistance R_t that depends on the conductivity of the blend and the dielectric proprieties of it represented by the C_g. In a BHJ solar cells those parameters depend on the active layer morphology and thickness. In opposite pathway the free charges recombine. The recombination process is characterized by a resistance called Recombination Resistance R_{rec} in parallel with the C_μ. The first has to be as higher as possible to give a high efficiency solar cell while the capacitance, as will be shown later, is direct correlated with the density of the state (DOS) of the A material. Those processes can occurs along all the active layers thickness at the different interfaces. The equivalent circuit used to describe those physical process is based on the diffusion coupled with a homogeneous reaction (recombination) with absorbing boundary condition and is represented as a transmission line model with infinite elements. In the end, the charge collection process can be represented by a Contact Resistance R_{Co} which take into account the difficulty to extract charges by the electrode, in parallel with a Contact Capacitance C_{Co} that represents accumulation of charges at the contact interface. In an optimized solar cell the R_s, R_t and R_{Co} have to be as low as possible. In consequence in a solar cell with a good transport

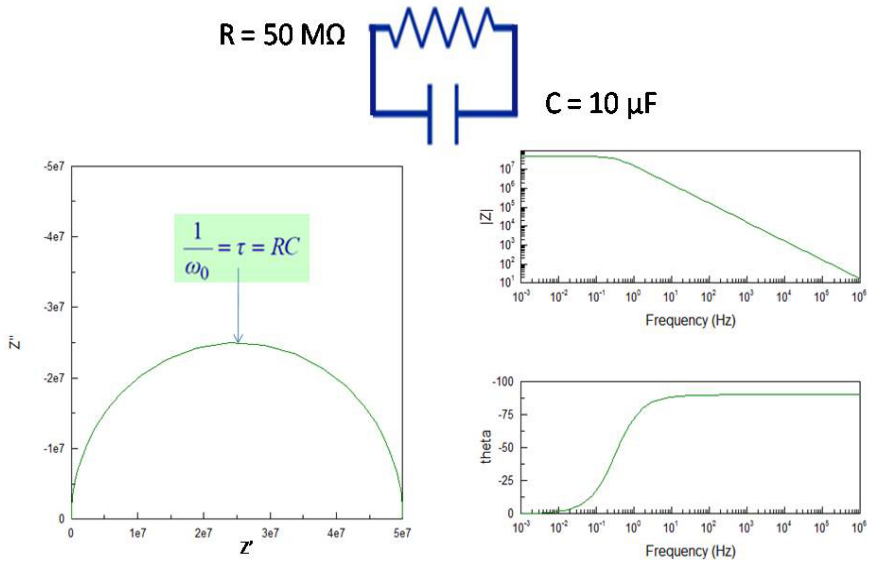

Figure 2.20: a) Example of impedance response of an ideal resistor ($R = 50\Omega$) in parallel with an ideal capacitor ($C = 10\mu F$)

and with an efficient extracting contact, in the Nyquist plot it is expected a single arc connected with the recombination process, that cannot be eliminated. In this view, the appearance of an additional arc in the Nyquist spectrum is correlated with an alteration on the solar cells. Different experiments was carried out to correlate the each arc with the processes occurred in the device.

One example concerns the study of the transport process. Guerrero *et al.* [102] demonstrated that the charge transport is connected with the response at high frequency in the Nyquist spectrum. The basic idea proposed in the work assumes that, if the transport proprieties of the blend are altered, it is expected that just R_t and R_s will change. A standard BHJ solar cell based on P3HT:ICBA is used as reference cell. Then, 0,1 % and 1 % of PCBM molecules have been incorporated into the active layer blend to altered the transport proprieties. Indeed the presence of PCBM acts as traps for the charges and limits the conductivity. As result in the high frequency part of the Nyquist spectrum an additional arc is observed (Figure 2.22b)

The data was fitted with a simple equivalent circuit (Figure 2.22a) and with the assumption that the high frequency arc correspond to the transport behaviour, while the other to the recombination process. The dependence of each parameters with the V_{app} has been found and reported in Figure 2.23. As results the resistance of the high frequency arc, increase when the number of the PCBM traps increase as shown in Figure 2.23a, while the other fitting parameters doesn't changed 2.23b,c,d confirming the hypothesis. Moreover using different cathode contacts the same behaviour is observed, confirming that high-frequency resistances only depend on the active layer blend composition, and not on the outer contact structure.

As mentioned before, another important parameters is the C_μ. In contrast with the standard dielectric capacitor, the C_μ describes a change in the electronic density that appears as a consequence of the displacement of the electrochemical potential (the Fermi level or chemical potential).

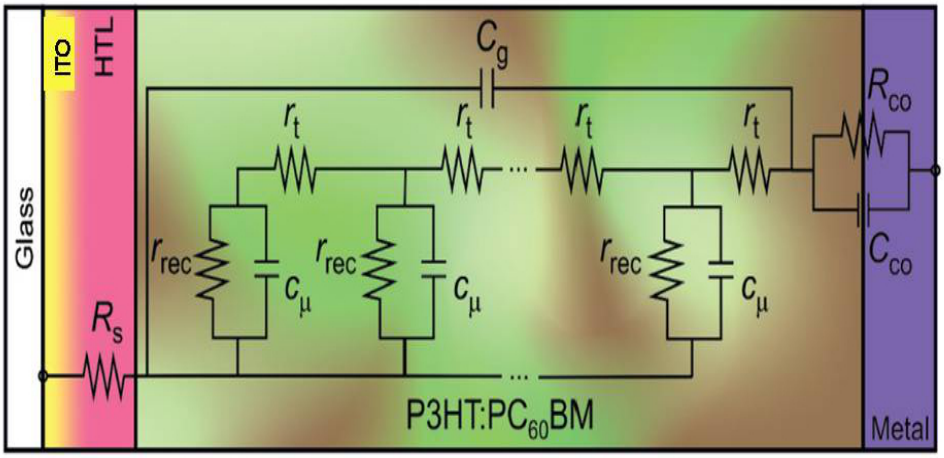

Figure 2.21: Equivalent circuit of a standard solar cells, details are described in the text.

In theory C_μ depends on the change of the occupancy of charge carriers in the both fullerene LUMO and polymer HOMO. However it was observed in a variety of polymer/fullerene blends that holes form a set of majority carriers in the active blend, and that the hole quasi Fermi level E_{Fp} correspond to the equilibrium Fermi level E_{F0} [103][99]. The D polymer results intrinsic p-doped due to oxidation upon exposure to the air or moisture. The amount of excess, photogenerated holes $\Delta p = p - p_0$ for usual illumination intensities around 1 Sun lies within the order of magnitude of the density of dopant $p_0 \sim \Delta p = 10^{16} - 10^{17} cm^{-3}$.

Therefore the downward shift of E_{Fp} by effect of illumination or V_{app} should be restricted within a few $k_B T$ (thermal energy), thus $E_{F0} - E_{Fp} \sim k_B T ln(p/p_0)$. Hence the shift of Fermi levels originated by excess carriers mainly affects the electron level E_{Fn}, which then screens a large portion of the effective band gap (Figure 2.24).

In the general mentioned conditions, assuming that the carriers follow the zero-temperature Fermi distribution, it can be shown that the C_μ is proportional to the DOS, g(E), at a given position of the Fermi level by the equation 2.33.

$$C_\mu = q^2 g(E_{Fn}) \tag{2.33}$$

The DOS in disordered organic conductors usually exhibits a Gaussian distribution following the equation 2.34

$$g(E) = \frac{N}{\sqrt{2\pi\sigma}} exp\Big[-\frac{E - E_0)^2}{2\sigma^2}\Big] \tag{2.34}$$

Here N is the total DOS with mean energy E_0 and width σ. Experimentally in was found for different D:A materials an exponential increment of the type

$$C_\mu = C_0 exp(\frac{\alpha q V_F}{k_B T}) \tag{2.35}$$

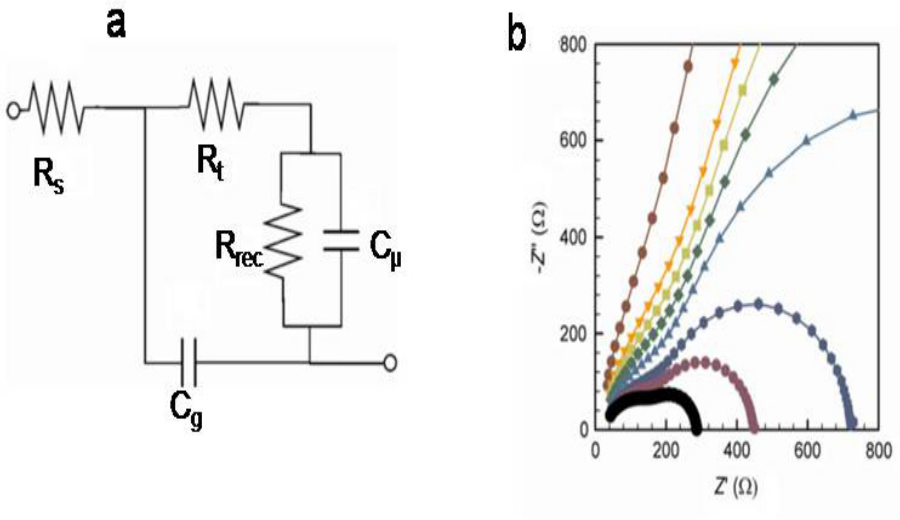

Figure 2.22: a) equivalent circuit used to fit the IS data b)Nyquist spectra of device with transport properties altered, each line correspond on different external bias. [102]

with $\alpha \sim 0.3 - 0.4$ according to an exponential bandgap DOS.

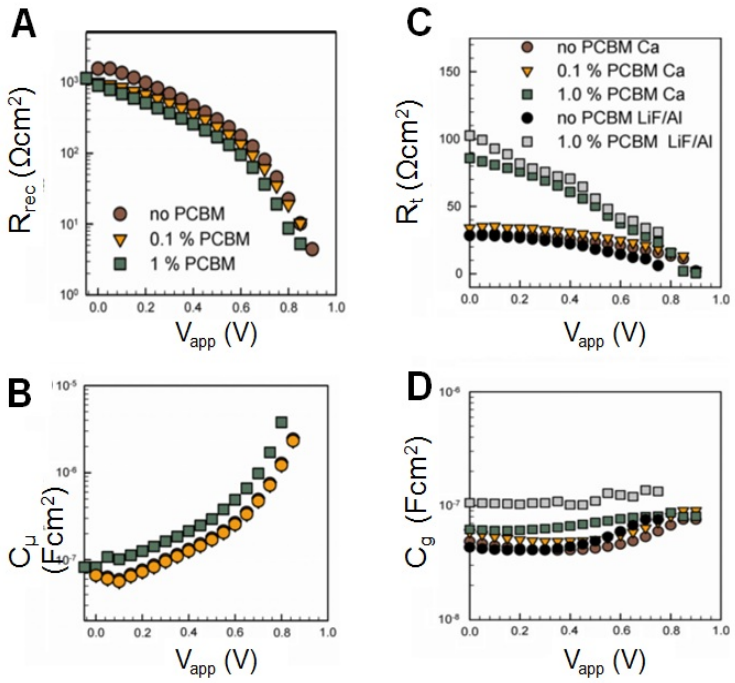

Figure 2.23: Dependence with the applied voltage of: A) Resistance of low frequency arc: R_{rec} B)Capacitance of low frequency arc: C_μ C)Resistance of high frequency arc: R_t D) capacitance of high frequency arc: C_g. [102]

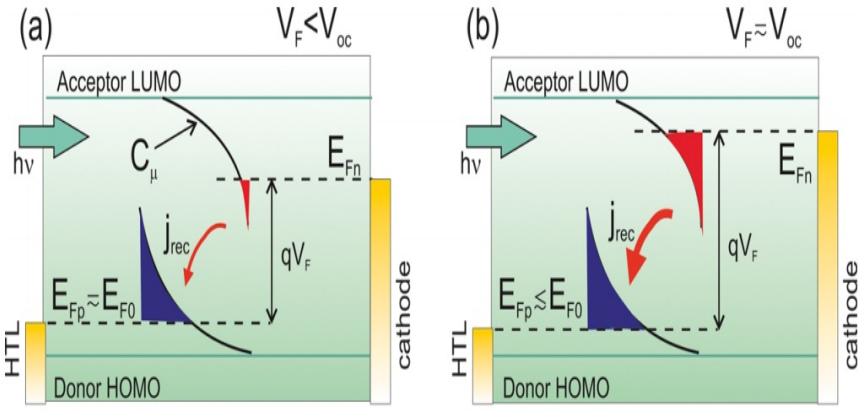

Figure 2.24: Mechanisms governing the Fermi level location within the effective band gap established between $HOMO_D$ and $LUMO_A$ levels [99]

3

Correlation between organic donor material structure and PV properties

3.1 Physics of Organic Semiconductor

As introduced in Chapter 1, organic materials are, by definition, compounds of Carbon. The main ability of this atom is to build complex molecules and macromolecules, the infinite possibilities to modify chemical structures lead to materials with endless different proprieties. Indeed from the knowledge of the structure-proprieties relationship, it is possible to synthesized material that meet any requirement. Organic materials can be distinguished in two categories: molecules and polymers. A polymer is composed by many identical bulding blocks called monomers. A metaphorical way to describe a polymer is to picture the monomer as a pearl and the polymer as the necklace composed by the pearls. When the repeat unit is a single monomer the result is called homopolymer, but more often the monomers are two different unit and the result is called copolymer. The different way to combined the based unit defines four different categories of copolymer (Figure 3.1):

- **Alternatic copolymer**: regularly alternating monomers [ABAB...]n
- **Statistical copolymer**: monomer arranged according to a known statistical rule or random.
- **Block polymer**: have two or more homopolymer subunits linked by covalent bonds
- **Graft copolymer**: side chains whit a different composition than the main chain

The different type of polymers are responsible of materials behaviour, in terms of morphological, mechanical, thermal, optical and electrical properties. Among all the different capability of polymers, this thesis will concentrate on the electrical proprieties, in particular on the semiconductor polymer.

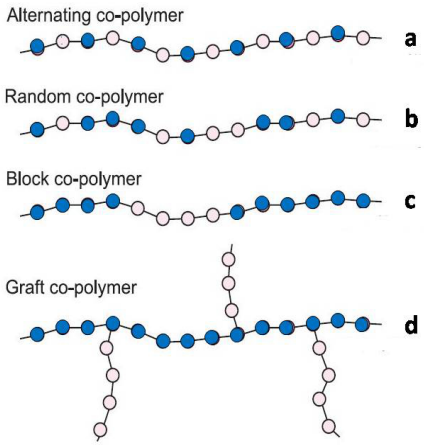

Figure 3.1: Different categories of copolymer: a) alternatic b) statistical/random c) block and d) graft polymer

3.1.1 Organic molecules semiconductor

The main proprieties of an organic semiconductor is the ability to transport charges, here the delocalization of the charge is obtained from the conjugated π molecular orbitals. Indeed an alternation of single and double bond creates a conjugation that extended along all the macromolecule. To understand the physics of polymeric semiconductor is better to start from a simplest system as the semiconductor molecules. The aromatic molecule benzene (C_6H_6) is a prototypical planar conjugated molecule with an extended π electron system. The π electrons reside in the molecular orbital that are delocalized over the molecule forming a negatively charged π clouds, while in the core σ orbital the positive charged lead to a neutral molecule. As reported in Figure 3.2, in comparison with the inorganic semiconductor it is possible to identify two band: the π-bond energy is the HOMO and correspond to the Valence Band, while the π^*-bond is the LUMO and correspond to the Conductive Band.

This particular arrangement of charges corresponds to a quadrupole which can also be seen as two dipoles μ pointing toward each other. A molecular solid can thus be represented as an assembly of many such quadrupole charge distributions [104].
To describe the energetic proprieties of a molecules it is useful to define two value: the Ionization Energy (I_E) is the energy required to remove an electron from the sample into infinite distance, vice versa the Electron Affinity (E_A) is the energy need to attach an electron to the sample from infinite distance. For a single isolated molecule those values correspond to: $I_E \sim -HOMO$ and $E_A \sim -LUMO$. Despite in single molecules those value are well define, in ordered assembly, different value of I_E and E_A are founded. Moreover the molecular orientation has profound consequence on energetic distribution. A relevant case is the pentacene, (chemical structure reported in the insert in Figure 3.3). [105]
The molecule can arrange in two different configurations: the “lying” and the “standing”, depend-

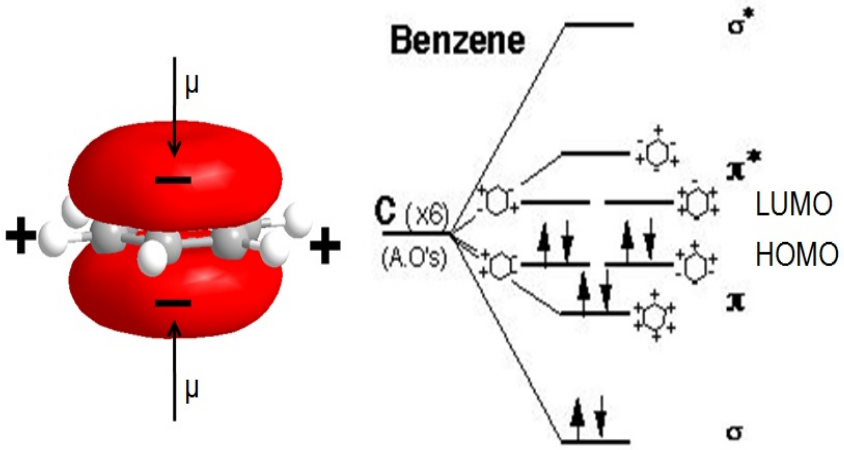

Figure 3.2: Orbital distribution of a benzene molecule

ing on the substrate where it growths. Figure 3.3 shown the Ultraviolet Photoelectron Spectroscopy (UPS) data of the two cases: in the Au substrate the molecules lying on the surface, a distinct peak, which corresponds to the molecular HOMO, is observed. The low binding-energy onset of the HOMO is chosen to determine the Ionization Energy of I_E= 5.35 eV.
In contrast, on silicon oxide, most rod-like organic semiconductors growth with their long molecular axis close to perpendicular to the surface. In this case the corresponding UPS spectrum yields a significantly lower I_E of 4.80 eV.
The substantial I_E difference between lying and standing orientations, clearly demonstrates the collective effect of the intra-molecular interactions.

As the energetic level are strongly dependent on the molecular aggregation, it is obviously that also the charge transport is effected from the packing mode of the molecules.
Indeed the efficient motion of charge from one molecule to another is intimately related to the electron cloud splitting with its neighbour molecules. Two parameters can be describe the system: the Transfer Integral that depends on the overlap of wave function between adjacent molecules, and the Reorganization Energy, that is the energy loss when a charge carrier passes through a molecule and is dependent on the conjugation length, degree, and packing [106].

The main mechanism that is involved in the transport of charges between two molecules is based on a hopping process, described by the Marcus theory [107]. The equation 3.1 gives the rate of the electron transfer from molecule i to j as a process of reduction followed by oxidation of the participating molecules.

$$\nu_{ij} = \frac{|I_{ij}|^2}{\hbar}\sqrt{\frac{\pi}{\lambda k_B T}}\left(-\frac{(\Delta G_{ij}+\lambda)^2}{4\lambda k_B T}\right) \tag{3.1}$$

where I_{ij} is the Transfer Integral between the two molecules i and j, λ is the Reorganization Energy, ΔG_{ij} is difference in energy between the two sites, k_B is the Boltzman constant and T the temperature.

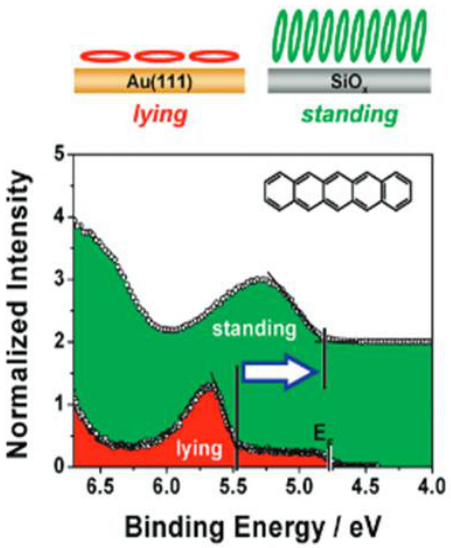

Figure 3.3: Pentacene orientations and corresponding energy levels.[105]

The molecules can arrange in infinite way, but when the structure is well order four main kinds of packing motifs are identified. Summarized in Figure 3.4, they are: (1) herringbone packing (face-to-edge) without $\pi - \pi$ overlap between adjacent molecules; (2) herringbone packing with $\pi - \pi$overlap between adjacent molecules, also called slipped π stacking (3) lamellar packing, one-dimension (1-D) π stacking, and (4) lamellar packing, two-dimension (2-D) π stacking [108].

It is common to consider that 2-D π stacking has the larger the Transfer Integral and the smaller the Reorganization Energy, that give highest charge mobility.

3.1.2 Organic semiconductor polymers

If the orientation is important for an organic molecule, for the polymer this aspect is even more crucial and complex. In fact the polymeric conformation in the solid state depends not only to its chemical structure but also on its chain length, more precisely on the molecular weight.

In general for a polymer is better to talk about the molecular weight distribution, that describes the relationship between the number of moles of each polymer species (N_i) and the molar mass (M_i) of that species. Different average values can be defined to describe the distribution:
number average molar mass or M_n define as:

$$M_n = \frac{\sum M_i N_i}{\sum N_i} \tag{3.2}$$

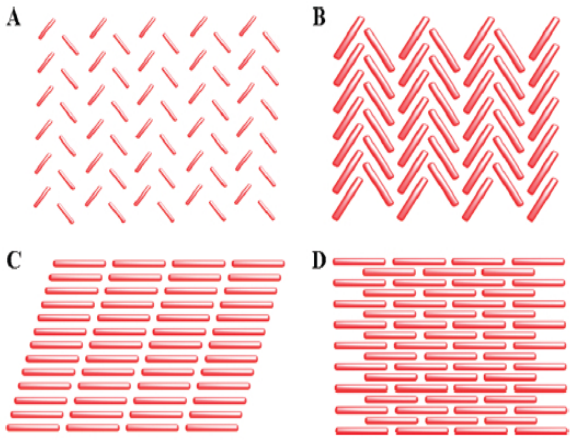

Figure 3.4: Molecular packing motifs in crystals. A) Herringbone packing without $\pi - \pi$ overlap B) herringbone packing with $\pi - \pi$ overlap between adjacent molecules; c) lamellar motif, 1-D π stacking , D) lamellar motif, 2-D π stacking [108]

and mass average molar mass or M_w define as:

$$M_w = \frac{\sum M_i^2 N_i}{\sum M_i N_i} \tag{3.3}$$

with this two value is defined the Polidispersivity PDI index as:

$$PDI = \frac{M_w}{M_n} \tag{3.4}$$

Larger it's PDI index, broader it's the molecular weight distribution.
A simple representation, reported in Figure 3.5, shows how increasing molecular weight (i.e., chain length), polymers in their solid state are organized from a highly ordered extended chain conformation to a structure consisting of alternating crystalline and amorphous (largely unordered) regions.

In general, the charge transport in a semiconductor polymer has to be distinguish in two contributes: the intra-chain and the inter-chain transport.
The first one is defined by the conjugation length of a polymer segment. In comparison with the inorganic materials, in a first approximation, it can be describe by a band transport model. The distribution of electronic states in an organic disordered semiconductor is often described to be Gaussian Density of States distribution (GDOS), which also accounts for the random distribution of the molecular sites [110]. Experimentally, this is observed as an inhomogeneous broadening of the optical spectra such as absorption, fluorescence, and phosphorescence spectra. Unlike the inorganic semiconductor the electronic interactions between the molecular orbitals of adjacent lattice sites are weak and the resulting bands are narrow, with bandwidth below 500 meV [111]. Another different is that in a polymer it is difficult to define free charges due to the strong electron-phonon

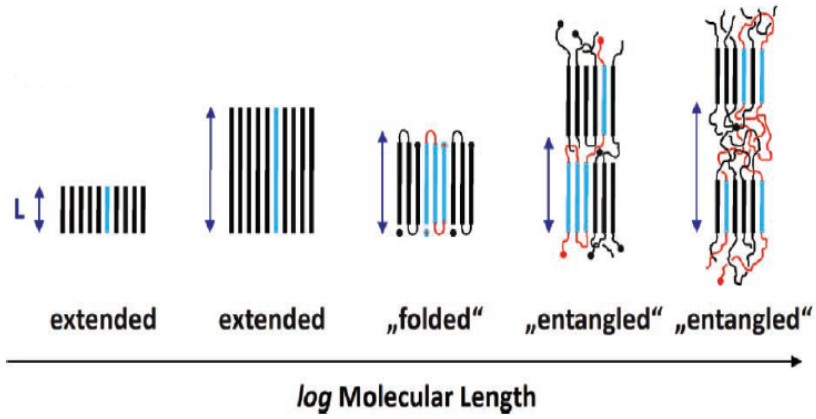

Figure 3.5: Representation of different polymer configuration in function of increasing molecular weight [109]

interaction. Indeed the presence of a charge in the polymer segment, induced a deformation of the latter called "polaron". When a polaron moves, it carries the charge associated with a structural deformation. It appears clear that the band model used to describe the intra-chain transport is a simple model, but it is useful to define the Energy gap and compare the energetic proprieties of different polymers.

The second process, inter-chain transport, is mainly based on hopping between neighbour or multiple trapping and realise mechanism. Looking the Figure 3.5, it is clear that the inter-chain transport is direct correlated with the morphology of the polymer solid state, and thus on M_w. Kline *et al.* [112] showed that the charge carrier mobility of the most popular semiconductor polymer, the P3HT, could be varied by several orders of magnitude by changing the M_w. The drop in very low M_w films is attributed to poor connectivity between well-defined, highly crystalline grains. In general low M_w materials can form highly ordered structures, but if those crystalline region are not electrically connected between each other, the charge transport is not allowed.[113] In opposite, long chains (high M_w) provide electrical connectivity between more ordered regions, allowing efficient charge transport, but also result in higher structural disorder. This disorder gives rise to energetic distribution in the π stacks, that affects intermolecular charge Transfer Integrals [114].

Salleo *et al.* [115] describe the structural disorder in an imperfect crystal by a paracrystallinity model as a random fluctuations in lattice spacings. In this region is observed a coexistence of localized and delocalized states, indicating that in paracrystalline aggregates, the transport is based on a mechanism where the charge is temporarily trapped in localized states, akin to multiple trapping and release. The short-range order of the aggregates is sufficient to support efficient intermolecular CT, because charges have a short scattering mean free path in the π polymers. The intermolecular Transfer Integral (I_{ij}) between two molecules (i and j) placed at a distance x_{ij} has an exponential decay:

$$I_{ij} = I_0 e^{-\beta x_{ij}} \tag{3.5}$$

where I_0 is Transfer Integral at the minimum distance and $1/\beta$ is the wavefunction overlap decay length. Those parameters govern the extent to which lattice disorder affects charge transport. For example, I_0 can be increased by reducing the $\pi - \pi$ stacking distance. In this way, transport in paracrystallinity aggregates is less sensitive to large amounts of disorder. Similarly, it is possible to reduce β by designing materials with orbitals having large overlaps or that pack in symmetric way in order to minimize the disorder.
Those considerations separate polymeric semiconductors into two classes. One class composed by truly amorphous materials, lacking any long-range order, charge transport is limited by hopping between localized states in a broad GDOS. In the second class are materials that can form interconnected aggregates exhibiting at least short-range order, with transport described by a multiple trapping and release mechanism.

3.2 Charges generation in a bulk heterojunction solar cell

In theory the class of the materials that forms order aggregates, seems to have better electrical proprieties, and in consequence appears to be a better choice for a device. However in the BHJ solar cells, the active layer is based on two different material intermixed in a blend. The two species are electron-D, usually a π-conjugated polymer, and an electron-A, commonly a fullerene derivatives. In this complex system many factor can determine the morphology of the final blend, in Figure 3.6 are reported main different intermixing.

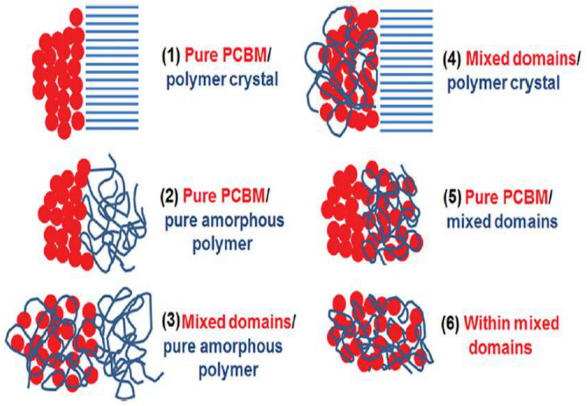

Figure 3.6: 6 possible morphologies of polymer:fullerene active layers [116]

Depending on the material proprieties, the D polymer can partially crystalline or not, and in both case it can form pure polymer region, well separated from fullerene reach domains, or vice versa, forms intermix area with both species. The optimal morphology for a BHJ solar cell should result in a fine intermix of the D and A domains, with sizes that meet the compromise between the D and A exciton λ_D and a high D/A interfacial area, together with the need of bicontinuous percolation pathways for charges transport at the electrodes. It is difficult to define a priori which is the best morphology, because big crystal regions can compromise the percolation pathways to

the electrodes, in opposite high disorder areas can act as traps and limit the charge transport.
Focusing on the photogeneration of charges, in principle, both photoactive constituents of the BHJ solar cell, can absorb light. But fullerene derivatives, usually have lower absorption coefficients than the D conjugated polymers. For this reason the description of the charge photogeneration is mainly related to the D point of view [104].

In Figure 3.7 is reported the diagram of the photogeneration of charges in a BHJ solar cell. Only photons with energy above polymer's optical bandgap (E_{gap}^{opt}), can be absorbed. This limit value can be extracted from the absorption spectrum of the polymer, from the onset wavelength ($E_{gap}^{opt} = hc/\lambda_{onset}$). When the photon is absorbed a singlet photo-exciton is generated. As mentioned before, due to the low dielectric constant ($\epsilon \sim 3$) of organic material, the exciton binding energy (E_b^{exc}) results considerably high $\sim$ 0.3-1 eV and cannot be dissociate without and additional force [52]. However, when the exciton is in the vicinity of a D/A interface, the energetic difference between the two species allow the dissociation. Note that the E_{gap}^{opt} differs from the effective Energy gap by the E_b^{exc}.

After successful singlet exciton dissociation, two scenarios are possible: the first one is characterized by an intermediate state between the photo-exciton and the separated charges, namely the CT state, where the charges still Coulomb interact among them. In the opposite, the generation of free charges is faster then the thermalization of the CT state (<100 fs [117]), and the resulting charges don't interact between each other. The charge generation is a fast process (femtosecond) where the exceed energy came from the exciton dissociation is completely converted to kinetic energy of the two free charges [118]. Those process are in competition with the geminate and non-geminate recombination illustrated in Figure 3.7 with blue arrows. The geminate recombination occurs when an electron and hole of the exciton, recombine; while the non-geminate recombination occurs when two free opposite charges recombine.

To identify which of this two processes are involved in the BHJ solar cell, time-resolved photoluminescence (PL) technique can be used. In fact the CT state can partly coupled radiatively to the ground state. Emissive CT states have been shown to be characterized by a broad, red-shifted PL band, with a long radiative lifetime, that occurs only in the blend and cannot be assigned to PL from either of the individual components.[118] When the PL emission of the CT state is too weak, the electroluminescence (EL) technique can be used [115]. The charge carrier are injected into the solar cell device and EL spectra is recorded. The electron-hole recombination comes from the lowest energy excited state of the blend system, which is the CT state.
It was shown that the formation of the CT state is detrimental to the efficiency of solar cells. Several strategies, such as increasing the mobility or the crystallinity of the polymer, have beneficial effects on the suppression of the CT state. [118]

3.2.1 Acceptor material for organic solar cells

As illustrated in the previous paragraph, in the active layer of a BHJ solar cells, the D material is the main absorber of solar photon flux. An efficient A counterpart has high E_A, a proper LUMO level and a good electron mobility. Those aspect are satisfy from the fullerene derivates, that, for

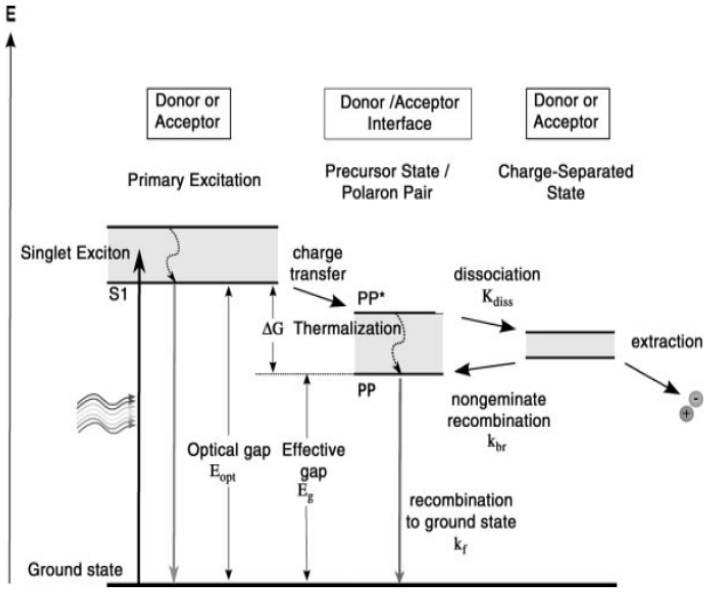

Figure 3.7: Diagram of the photogeneration of charges in a BHJ solar cell

this reason, are currently considered to be the ideal acceptors in OPV. The fullerene is a molecule based on 60 Carbon that form a sphere, the structure is reported in Figure 3.8a. Increasing the number of the Carbon involved, the distorted sphere results in the C70 (Figure 3.8b). Those molecules are usually growth via evaporation, because they have a low solubility. To improve it Wudl *et al.* [119] synthesized one of the most important derivative of C60 called $PC_{61}BM$ (Figure 3.8c). This fullerene derivative represents a milestone in the development of OPV acceptors and is still widely used today due to its solubility, strong electronegativity, high electron mobility and crystal packing. Another fullerene derivates that show an enhanced absorption in the visible with respect to $PC_{61}BM$ is the $PC_{71}BM$ (Figure 3.8d). When it is used as A counterpart in a BHJ solar cell, usually yields larger photocurrents. Those material show a LUMO level located at - 4,03 and -4,3 eV for $PC_{61}BM$ and $PC_{71}BM$ respectively [66] [120], which considerably limit the V_{oc} of operating devices. In order to increase the LUMO level other fullerene derivates was synthetiezed, one of the most impressive examples of these new novel materials is C60 molecule with an indene bisadduct: ICBA (Figure 3.8e) [121]. Adding symmetrically such electron-rich indene units to C60 molecule, the LUMO energy level of the ICBA (-3,74 eV) is up shifted compared with $PC_{61}BM$. This acceptor combine with P3HT, shows higher V_{oc} and in consequence higher efficiency (V_{oc}=0,84V and PCE=5,44% compare to V_{oc}=0,58V and PCE = 3,88% obtained with $PC_{61}BM$).

However, due to the different proprieties in aggregate, mixing ICBA with other D material not always improves the device performance. The study of new acceptor material is out of the aim of this thesis, for this reason in the following section the main acceptor material used is the $PC_{61}BM$.

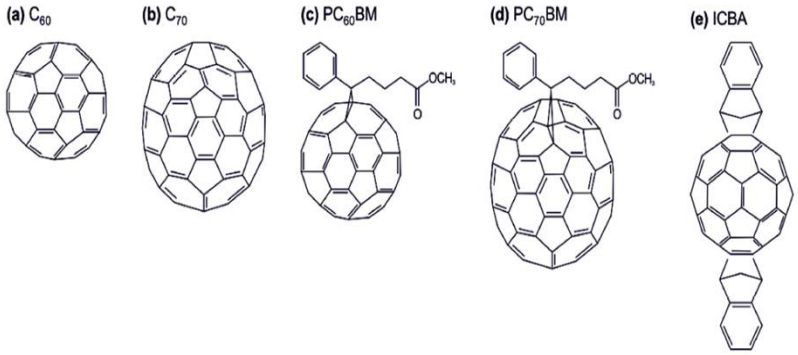

Figure 3.8: Chemical structure of a) C60 b)C70 c) $PC_{61}BM$ d) $PC_{71}BM$ e) ICBA

3.2.2 Donor polymer for organic solar cells

In order to reach high performance solar cells many efforts was done to optimized the chemical structure of the D polymer. The ideal D materials have to fulfil some fundamentals requirements:[108]

1. high solubility to allow a good processability by solution
2. broad absorption spectrum with high absorption coefficient to absorbed efficiently the sunlight.
3. high mobility
4. a good energetic alignment of the HOMO and LUMO energy levels to ideally provide large V_{oc}, increased environmental stability and efficient exciton dissociation at the D-A interface.

Those goals can be reach when the D polymer has two essential structural features: i) an highly π-conjugated backbone to guarantee optimal charge transport and optical absorption; ii) a functionalization of the polymer core with solubilizing substituents, to allow the good solubility and processability [122].

Traditional π-conjugated polymers used as donor semiconductors in OPV cells are Polythiophenes due to the good optical and electrical properties and good thermal and chemical stability that they present [123]. Polythiophenes are based on repeating units of thiophenes (Figure 3.9) where different side chains can be added in order to tune the resulting properties and increase the solubility [124]. The most popular example of this type of semiconductor is the P3HT reported in Figure 3.9a. When P3HT is combined with $PC_{61}BM$ in a BHJ solar cells the resulting device gives an efficiency around 3% - 4% [80]. The organization of the D strongly influences the device performance, and it mainly dependent on the nature of the side chains. Different poly-thiophene and poly-benzene derivates was synthetized to improve the reorganization(some example are reported in Figure 3.9 [60] [125]). However the resulting devices showed lower efficiency than P3HT.

The main drawback of those kind of material is the low V_{oc} and their restricted absorption to below 600 nm, that limits their efficiency below 5%. [124] However studies on the above-

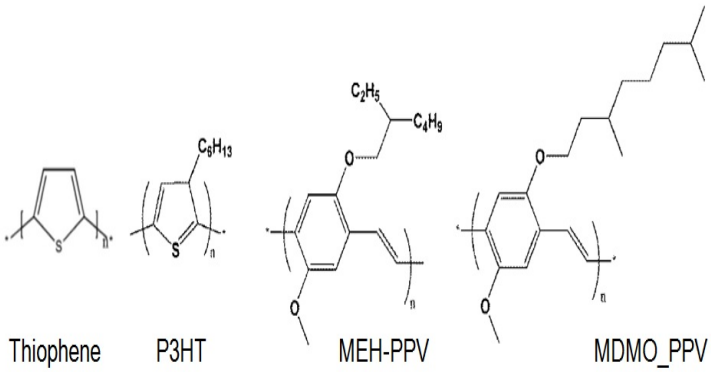

Figure 3.9: Chemical structure of different poly-thiophenes and benzene derivates [123]

mentioned polymers paved the way to understanding the basic working principles of BHJ solar cell an to identify the critical parameters affecting efficiency and stability. The main targets for a new generation donor polymer are to enlarge their optical absorption to better match the solar terrestrial radiation, enhance (bulk) hole mobility, and improve energy alignment with the A to enhance the V_{oc}. An effective strategies that allows to reduce the bandgap and broaden the optical absorption is to realize the combination of alternated electron rich and electron poor units in so called *push-pull* or donor-acceptor structures [126].

Some example of donor and acceptor groups are reported in Figure 3.10. In details, in the donating groups there are dithiophene, cyclopentadithiophene, carbazole, benzodithiophene, whereas the acceptors are benzothiadiazole, quinoxaline, thienopyrroledione and diketo-pyrrolo-pyrrole (DPP) [122].

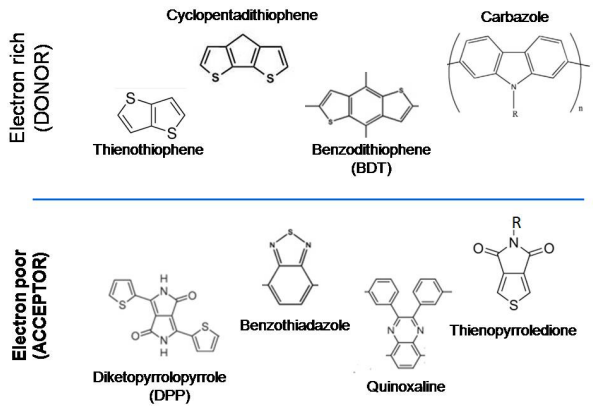

Figure 3.10: Chemical structure of different donor and acceptor groups that form *push-pull* polymers

Among all the possible combinations of those basic units,some examples of the most performing polymer are reported.

The PCDTBT [127] is a poly(2,7-carbazole) derivative, the chemical structure is reported in Figure 3.11. Cho *et al.* [128] investigated the PCDTBT in blend with $PC_{71}BM$. They observed that the nanoscale morphology is strongly affected by processing parameters such as choice of solvents, D:A blend ratio, thermal annealing etc. The best performance was obtained by a D:A ratio of (1:4) in a orthodichlorobenzene (ODCB) solvent. The main advantage of this blend is that it shows and IQE that approaches 100% around 450 nm and stays near or even above 90% throughout the entire absorption spectrum (400-650 nm). Such a high IQE is remarkable, indicating that nearly every absorbed photon leads to a separated pair of charge carriers and that all photogenerated carriers are collected at the electrodes. As a result the device shows a PCE=6,1% with a J_{sc}=10,6 mA/cm^2, V_{oc}=0,88V and FF=66%. Then, with a further optimization of the nanoscale morphology with the addition of dimethyl sulfoxide (DMSO) to the ODCB solution, higher peformance was obtained. The device showed a PCE = 6,7%, J_{sc}=11,4 mA/cm^2, V_{oc}=0,91V and FF=65% [127].
Another interest example of different donor-acceptor polymer is based on the combination between benzodithiophene (BDT) unit and quinoxaline (Q) acceptor, that give the polymer PBDT-TFQ reported in Figure 3.11 that shows a PCE up to 8% [129]. It is a medium band gap polymer, with an excellent photon harvesting and efficient photogeneration when it is blended with $PC_{71}BM$. The HOMO and LUMO energy levels of PBDT-TFQ are -5.52 and -3.30 eV, respectively. Different molecular weights were investigated and it was found that the charge-carrier mobility and the nanoscale morphology of the BHJ film are strongly influenced by this parameter. In fact the hole mobility of PBDT-TFQ:$PC_{71}BM$ (1:1) based devices varied from $3,8 \times 10^{-4} cm^2/Vs$ to $2,3 \times 10^{-3} cm^2/Vs$ as the molecular weight of PBDT-TFQ increased. In addition,with the low molecular weight batch, when different D:A ratio are used, the AFM images show unevenly polymer and $PC_{71}BM$ domains, forming large isolated islands that are detrimental for the device performance. Changing D:A ratio and adding additive in the active layer solution allowed to optimized the solar cell. In the opposite using the high molecular weight PBDT-TFQ, the best device shows an average PCE=7.8% Voc = 0.76 V, Jsc = 17,9 mA/cm^2, and FF = 57,6%. The good performance are justified from a high IPCE that show a maximum value of 85.5% at 425 nm, and exhibits a broad photoresponse of over 75% in the 400-640 nm range.
Going on with examples, an relevant case is the high performing polymer based on a copolymers of Benzodithiophene and Thienopyrroledione: the PBDTTPD [130][131]. An interesting aspect of this polymer, is that with a proper choice of the side chains, it is possible to increase the corresponding device performance. In fact by replacing short ethylhexyl chains with longer octyl side chains, broader and red-shifted absorption spectrum, with more defined vibronic structure, is obtained. As a result, when the polymers is combined with $PC_{61}BM$, the performance of the devices pass from PCE= 3,9% to a maximum PCE value of 6.8% [131]. Moreover, it is interesting to note that usually a possible approach to increase the device performance is to blend the polymer with the $PC_{71}BM$ instead of $PC_{61}BM$ in order to increase the absorption. However, after a proper optimization of the blend morphology, the best performing device based on PBDTTPD:$PC_{71}BM$ has a PCE=4,2% considerably lower than the previous one[130]. This result show that not always the same approach used with different polymer, leads higher device performance.

In the end, an evolution of the previous polymer is represented by tthieno[3,4-b]thiophene/ benzodithiophene (PTB7), the chemical structure is reported in Figure 3.11. The introduction of a fluorine atom in the TT unit, thanks to its strong electron withdrawing character, determines the lowering of the HOMO polymer, leading to an improved V_{oc} of the resulting device. When PTB7 is combine with $PC_{71}BM$ the film exhibits a strong absorption covering a range from 300 to about 800nm. With a proper choice of solvent of the active layer solution, the corresponding device performance shows a PCE=7,4% with a J_{sc}= 14,5 mA/cm^2 V_{oc}=0,74V and FF=69%. The good perfromance are in agreement with the high IQE spectrum that shows and average higher than 90% in a wide range from 420 to 660 nm [81]. This interesting material was used as a reference in many following works. For example it was used to demonstrate a simultaneous enhancement in the J_{sc} and V_{oc} when the common buffer layer is replaced with the alcohol/water-soluble conjugated polymer (PFN). As result the new device showed a higher PCE of 8,37% with J_{sc}=15,75mA/cm^2, V_{oc}=0,76V and FF=70% [132]. Then it was demonstrated the powerful of the inverted structure. In a standard structure ITO is used an anode and top metal electrode as cathode, while in the inverted structure, with a proper choice of blocking layers and electrode, ITO can be used as a cathode and the top electrode as anode. . When this new configuration has been used for a PTB7 based device, a high average PCE of 8,97% (with a maximum of 9.15%) was achieved [133]. The improvement in the efficiency is mainly due to the higher J_{sc} = 17,2 mA/cm^2 while the V_{OC} and FF substantially unchanged in comparison to the previous cases. Additionally, with a proper light manipulation approach based on the substrate nano patterning, the light harvesting of the active layer can be further enhanced, without sacrificing the charge transport properties. As result a PTB7 based solar cells exhibit highest J_{sc} of 19,47 mA/cm^2 and a final maximum PCE=10,1%, with a V_{oc}=0,78V and FF=67%. [134]

To date, a PCE of 10,1% represents the world record for a single organic solar cells. More information about the relationship between donor polymer structure and device performance is crucial to generate improved polymers for efficient BHJ devices.

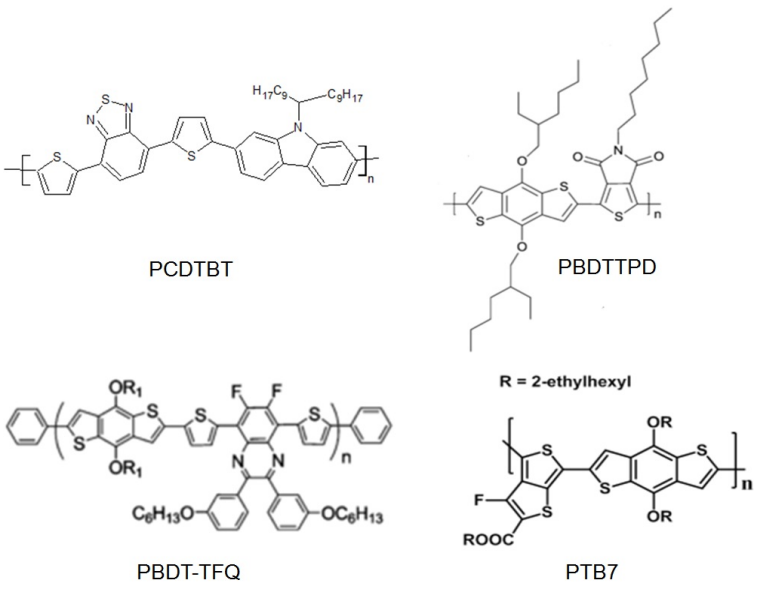

Figure 3.11: Chemical structure of different *push-pull* polymers

3.3 Chemical structure and performance correlations

Over a wide variety of *push-pull* polymers, this part of the work is focused on the study of novel semiconducting quinoxaline(Q)-benzodithiophene (BDT) based copolymers. The first electron-acceptor unit (Q) is widely used as building block for optoelectronic applications, since it can be easily modified and side substituted to finely tune the optoelectronic properties of the resulting polymer [135]. On the other hand, BDT is a commonly used electron-donating moiety with additional desirables peculiarities such as structural rigidity and planarity leading to extended π-conjugation length and favourable inter-chain $\pi - \pi$ stacking, other than the presence of additional substitution sites for the incorporation of side chains. In the next sections, will be investigated the effect different substituted on both the Q and BDT units. In particular the effect of the fluorine atoms substituted in the Q unit, and different side chains in the BDT unit will be investigated. Energetic, optical and transport proprieties of the polymers are expected to change, leading to different OPV performances. Moreover different processing conditions such as the effect of annealing and active layer solution additives, will be examined.

3.3.1 Lowering HOMO level

An interesting approach to increase the performance of a BHJ solar cells consists of lowering the HOMO level, to increase the V_{oc} following the equation 2.4 already reported in Chapter 2, where the V_{oc} depends on the different on the $HOMO_D$ level and the $LUMO_A$ level.

A possible method to modulate the HOMO level of a semiconducting polymers is based on a modification of side substitution of the π-conjugated co-monomers. For instance, the introduction of strong electron withdrawing halogen atoms (e.g. fluorine) on the polymer backbone allows to tune its electronic properties such lowering the HOMO level [136] but doesn't increase the optical bandgap and the LUMO level. Thus an increase in the V_{oc} is expected in the correspondent solar cells, without sacrificing the J_{sc}. In addition, it is reported that the introduction of fluorine atoms increases the polymer charge carrier mobility by promoting stronger inter-chain interactions.[82]

In particular this effect is clear when two p-type copolymers P(1)-Q-BDT-4TR and P(2)-FQ-BDT-4TR are compared (their chemical structure presented in Chapter 2 is recalled in Figure 3.12).

The BDT monomer is substituted with alkyl-dithiophene side groups (4TR) to form a 2D-conjugated unit in order to obtain a broader absorption, a higher hole mobility and a low HOMO energy level of the resulting polymer. It is combined with an unsubstituted or fluorinated quinoxaline moiety (Q and FQ, respectively) sandwiched with a thiophene spacer to limit the inter-monomers steric hindrance,.

In the Table 3.1 are recalled the main physical properties of the two polymer (already reported in Chapter 2 Table 2.1).

Note that the similar values of the Molecular weight distribution allow to compare correctly the two polymers. The lowering of the HOMO of P(2) comparing to the HOMO of P(1) by 0,28 eV confirms the strong effect played by the electron withdrawing fluorine atoms. As expected, the influence of fluorine on the frontier orbital energies is more pronounced for the HOMO than for

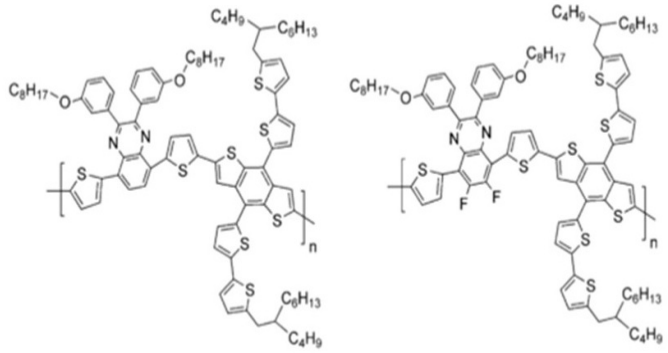

Figure 3.12: Chemical structure of P(1)- Q-BDT-4TR and P(2)-FQ-BDT-4TR. [75]

Polymer	M_n (KDa)	M_w (KDa)	PDI	E_{HOMO} (eV)	E_{LUMO} (eV)
P(1)- Q-BDT-4TR	16.3	47.4	2.9	-5.68	-3.14
P(2)- FQ-BDT-4TR	18.5	46.1	2.5	-5.96	-3.20

Table 3.1: Molecular weight and Energy proprieties of the two polymer P(1)- Q-BDT-4TR and P(2)-FQ-BDT-4TR

the LUMO, the latter differing only by 0,06 eV between the two polymers. P(1)- and P(2)-based devices could reasonably give devices with a high V_{oc}, in agreement with the experimental relation 2.1: $V_{oc} = 1/q(HOMO_{donor} - LUMO_{acceptor}) - 0,3V$
Moreover, the measured HOMO energies are in an ideal range to ensure good polymer air stability (being the oxidation threshold from air around -5,2 eV [137]). In addition, considering that the LUMO level of the typical electron acceptor $PC_{61}BM$ is located at -4,03 eV [66], the offset between the excited state of the D polymer and of the molecular A should provide the driving force for an efficient exciton dissociation, ensuring energetically favourable electron transfer [49].

Optical characterization of the two polymer was carried out. In Figure 3.13 are reported the UV-visible absorption spectra of P(1) and P(2), both in solution and in the solid state deposited as thin films on glass. The two polymers show similar behaviour both in solution and in thin film, with broad absorption spectra with a onset above 700nm. In diluted solution a first absorption band centred around 400 nm is observed for both polymers, attributable $\pi - \pi$ transitions localized on the 2D π-conjugated units, as confirmed by the good overlap of this absorption band with the spectrum of the BDT monomer in solution, also shown in Figure 3.13 in green line. Between the 500 and 700 nm, a structured peak is observed for both polymer indicates the probable presence of molecular aggregates also in solution. In agreement with the tendency of the polymers to aggregate promoted by their 2D highly π-conjugated structure- In particular the intra-molecular charge-transfer-like interactions between the electron-rich (BDT) and electron-poor(Q) could be

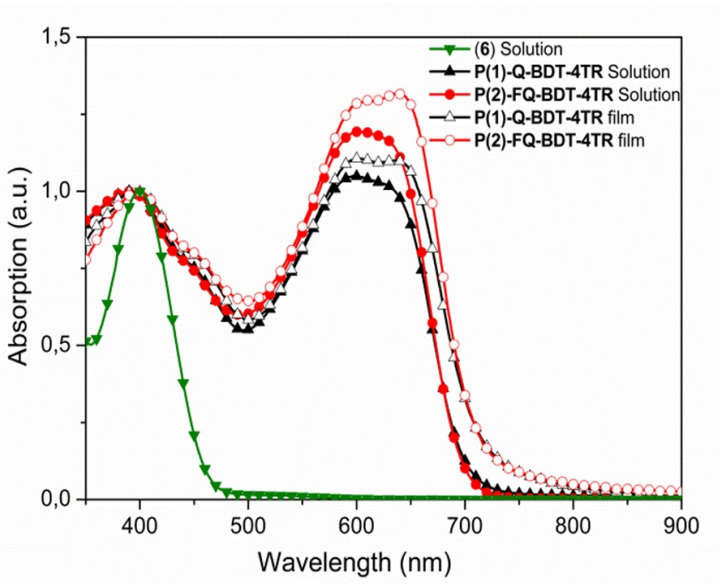

Figure 3.13: Absorption spectra of P(1)- Q-BDT-4TR and P(2)-FQ-BDT-4TR both in solution and in thin film. In green line is reported the spectrum of the BDT monomeric precursor in solution. [75]

responsable for the peak at 600nm, while the more red-shifted shoulder at 650 nm could be mainly due to inter-chain interaction [138]. Note that the relative intensity of the charge-transfer-like band versus the $\pi - \pi^*$ one is higher for P(2) than for P(1), this indicating the stronger *push-pull* character of the fluorine substituted polymer comparing to the other, due to the superior electron-with-drawing strength of the fluorine. A red shift of the low energy bands absorption maxima and onsets is registered for both P(1) and P(2) when passing from solution to thin film. An intensity increase of the absorption shoulder at 650 nm relative to the shoulder around 600 nm indicates a high aggregation tendency of the two polymers in the solid state comparing to solution.

In order to evaluate the positive effect on increase the V_{oc} as expected from the presence of the fluorine, P(1) and P(2) was used as D material combine with $PC_{61}BM$ as A. The photovoltaic performance was investigated by fabricating conventional BHJ solar cells having the following the standard structure: ITO/PEDOT:PSS/active layer/LiF/Al. The active layers were prepared by spin-casting with different D:A (wt/wt) ratios, from ODCB solutions. The thickness of the active layers has been optimized for each D:A ratio. The effect of the post deposition annealing was also investigated. In Table 3.2 are reported the best cells for each D:A ratio with and without thermal annealing. The results are an average on 6 devices, the error of each parameters is obtained from the standard deviation.

Devices based on the fluorinated polymer P(2) in general shown improved photovoltaic performance with respect to P(1). For P(1) based device the best performances are obtain whit a D:A ratio of 1:1 (wt/wt) with 5 minutes of annealing at 110^oC. The average PV parameters are J_{sc} = 7,3% mA/cm^2, V_{oc}= 0,74V, FF=58% and PCE=3,2%. Analogous conditions, but without the annealing, give the best performance also for the P(2) based solar cell, with a J_{sc}=10.2 mA/cm^2,

Polymer	D:A ratio (wt/wt)	$T_{ANN}[^oC]$	V_{OC} [V]	J_{SC} $[mA/cm^2]$	FF [%]	PCE [%]
P(1)	(1:2)	-	0.70 ± 0,03	5.8 ± 0,3	42 ± 3	1.7 ± 0,3
	(1:2)	110 / 5'	0.73 ± 0,01	6.3 ± 0,1	61 ± 1	2.8 ± 0,1
	(1:1)	-	0.78 ± 0,01	6.5 ± 0,2	34 ± 1	1.7 ± 0,1
	(1:1)	110 /5'	0.74 ± 0,01	7.3 ± 0,02	58 ± 2	3.2 ± 0,1
	(2:1)	-	0.80 ± 0,01	3.6 ± 0,4	28 ± 4	0.8 ± 0,2
	(2:1)	110 /5'	0.75 ± 0,01	6.0 ±0,3	35 ± 3	1.6 ± 0,1
P(2)	(1:2)	-	0.87 ± 0,01	7.9 ± 0,1	56 ± 3	3.8 ± 0,1
	(1:2)	110 / 5'	0.86 ± 0,01	6.1 ±0,3	65 ± 2	3.4 ± 0,2
	(1:1)	-	0.90 ± 0,01	10.2 ± 0,5	58 ± 2	5.3 ± 0,3
	(1:1)	110 / 5'	0.86 ± 0,01	9.4 ± 0,2	65 ± 1	5.2 ± 0,2
	(2:1)	-	0.91 ± 0,01	6.9 ± 0,3	33 ± 2	2.1 ± 0,1
	(2:1)	110 / 5'	0.89 ± 0,01	8.7 ± 0,5	41 ± 2	3.1 ± 0,2

Table 3.2: Photovoltaic performance of P(1)- Q-BDT-4TR and P(2)-FQ-BDT-4TR based solar cells

a V_{oc} = 0,90 V, a FF = 58% and a PCE of 5,3%. As expected, passing from P(1) to P(2) based device an increase in V_{OC} by 0,13 V is observed, due to the discussed effect of the F atoms in lowering the polymer HOMO level. Moreover by comparing the other photovoltaic parameters, the higher efficiency can be ascribed, other than to the higher V_{oc}, to enhanced J_{sc} and FF. This could be due to the $\pi - \pi$ polymer chains interactions that, even is already promoted by the high 2D π-conjugation, it is stronger in presence in the fluorinated polymer. This strong interaction enhances the polymer light absorption and most importantly its charge carrier mobility.

To confirm this hypothesis the hole mobility (μ_h) measurement of the two optimized active layers, was carried out by the SCLC technique describe in Chapter 2. The plots are reported in Figure 3.14.

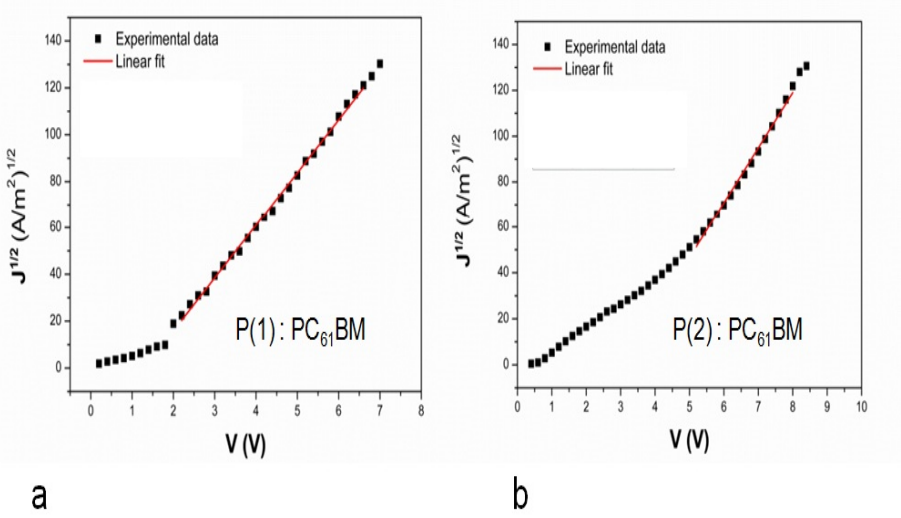

Figure 3.14: SCLC plots of P(1)- Q-BDT-4TR and P(2)-FQ-BDT-4TR based devices [75]

For the optimized P(1):$PC_{61}BM$ blend the mobility results $\mu_h = (2,4 \pm 0,2) \times 10^{-4} cm^2/Vs$ while for the optimized P(2): $PC_{61}BM$ blend $\mu_h = (8 \pm 1) \times 10^{-5} cm^2/Vs$. The difference of three times between the two blends, confirms the strong $\pi - \pi$ intermolecular interactions of P(2), and justify a higher J_{sc}. In fact the good mobility allows to increase the thickness of the active layer increasing the absorption. As reported in Figure 3.15a the absorbance of the $P2 : PC_{61}BM$ blend is considerably higher than the $P(1) : PC_{61}BM$ blend. Moreover, as noticed before, for P(2) the absorption maximum at 650 nm is higher than the relative maximum at 600 nm, in opposite of P(1) absorption, indicates a stronger $\pi - \pi$ inter-chain interaction. Similar spectra features are observed in the EQE spectra of P(1) and P(2) based devices. In particular the positive effect in the OPV performance appears clear, at the relative polymers absorption maxima wavelength, where the EQE of P(2) based device result to be 52%, considerably higher than the 43% for the P(1) based device.

In the end, in order to understand the different effect of the annealing on the morphology of the two polymer based solar cell and on the corresponding devices performance, morphological analysis was carried out. In Figure 3.16 are reported the Atomic Force Microscopy (AFM)images

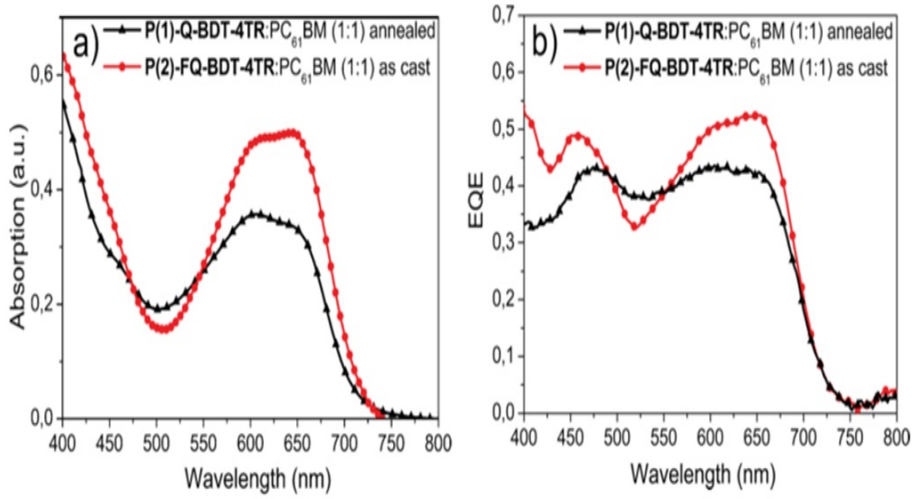

Figure 3.15: a) Absorbance and b) EQE spectra of P(1): $PC_{61}BM$ and P(2): $PC_{61}BM$ based devices [75]

of the two polymer:$PC_{61}BM$ (1:1 wt/wt) blend both as-cast and annealed.

Roughness was calculated as Root Mean Square deviation (RMS). Similar RMS ¡ 1nm was registered for P(1):$PC_{61}BM$ films (RMS equal to 0,8 nm and 0,9 nm for as-cast and annealed films respectively). On the opposite, an evident increase in roughness is found when passing from P(2):$PC_{61}BM$ as cast film to the annealed one, with RMS going from 1,3 nm to 3,4 nm.

In particular the P(2):$PC_{61}BM$ blend annealed film (Figure 3.26c) exhibits a less structured surface with relatively larger domains comparing to the analogous as-cast film (Figure 3.26c). As result, the annealing in the P(2) based devices causes a slightly decrease in PCE (Table 3.2). Probably the strong inter-chain interactions of P(2), due to the presence of the F atoms in the polymer backbone, leads to a well defined and finer polymer self-organization in as-cast blend films, that allow to have the best performance without the needed of additional step of annealing.

An opposite trend is observed comparing the two P(1) based blends. The P(1):$PC_{61}BM$ annealed film (Figure 3.26b) exhibits a superficial morphology with slightly reduced domain size and finer nanostructures comparing to as-cast film (Figure 3.26a). For this reason the thermal annealing leads to an increase in J_{sc} and in FF for the P(1):$PC_{61}BM$-based devices (Table 3.2). The finer reorganization of the active layer surface despite the identical surface roughness suggests a better packaging/ordering of the P(1) polymer chains, which improves the polymer electrical and optical properties.

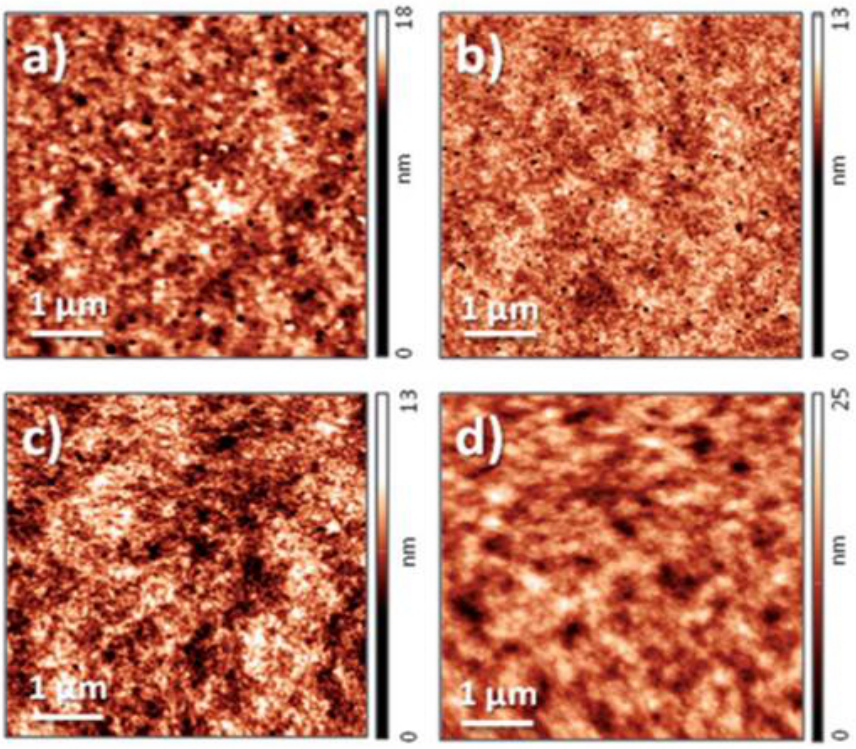

Figure 3.16: AFM images (size: 5 x 5 mm) of blend films on ITO/PEDOT:PSS of: a) P(1):$PC_{61}BM$ as cast, RMS = 0,8 nm; b) P(1):$PC_{61}BM$ annealed, RMS = 0,9 nm; c) P(2):$PC_{61}BM$ as cast, RMS = 1,3 nm; d) P(2):$PC_{61}BM$ annealed, RMS = 3,4 nm. [75]

3.3.2 Side chains effect

Once determined the positive effect of the fluorine atoms in the quinoxaline unit, in the next sections FQ is adopted as electron acceptor part of the *push-pull* polymers. Then, the effect of different side chains on electrical, optical proprieties, is investigated. Therefore two polymer with same backbone but different substituted are studied. Alkyl substituted aromatic side groups are used, for their demonstrated contribution to both enhance the solubility of the macromolecule and to extend the π-conjugation from the backbone to the lateral substituents, leading to a more extended or 2D π-conjugated system. For instance, Li *et al.* [139] reported the synthesis and characterization of a 2D-conjugated polymer with alkyl-thiophene π-conjugated side chains, which showed improved optical, electronic and electrical properties with enhanced photovoltaic responses compared to the corresponding alkoxy-substituted copolymer(PCEs of 6% compare to 3%). It is well know that extending the lateral π-conjugation of 2D-polymers, the nature, length, conformation (linear or branched), position and number of alkyl side chains in the side groups strongly influence the main properties of the resulting polymers, such as: (i) solubility, (ii) miscibility with the A counterpart and, (iii) structural conformation by favouring planarity or torsion angles on the backbone, thus promoting or hindering intra- and inter-molecular interactions. As a result, the optical, morphological and electrical properties of the polymer films can be controlled and optimized.

A representative case is given from the two polymer P(3)- PFQ-BDT-TR_1 and P(4)-PFQ-BDT-T2R_2, in which the BDT core unit was substituted with either 2-octylthienyl (-TR_1)or 2,3-dihexylthienyl (-T2R_2), respectively, as side groups. The chemical structures, already reported in Chapter 2, are recalled on Figure 3.17

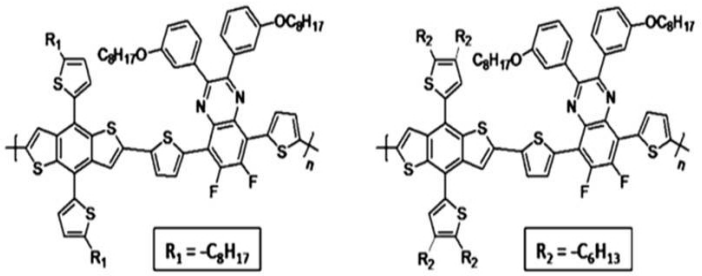

Figure 3.17: Chemical structure of P(3)- PFQ-BDT-TR_1 and P(4)-PFQ-BDT-T2R_2 [77].

The main physical properties of the two polymers are reported in Chpater 2 and recalled in Table 3.3 to facilitate the comparison. The different in the side chains is not expected to influence the energetic level of the two polymer. In fact HOMO and LUMO energy levels of the two polymer are very similar. In addition the deep HOMO levels, comparable to the previous P(2)-FQ-BDT-4TR polymer, suggest a high V_{oc} for the correspondent devices, a good air stability of the two polymers

Polymer	M_n (KDa)	M_w (KDa)	E_{HOMO} (eV)	E_{LUMO} (eV)
P(3)- PFQ-BDT-TR_1	25	64	-5,89	-3,61
P(4)- PFQ-BDT-T2R_2	30	66	-5,87	3,63

Table 3.3: Molecular weight and Energy proprieties of the two polymer P(3)- FQ-BDT-TR_l and P(4)-PFQ-BDT-T2R_2

and when combined with the typical A $PC_{61}BM$ provide an efficient exciton dissociation. Note that the similar values of the Molecular weight allow to compare the two polymers.

Despite the two polymer show similar behaviour from energetic point of view, the different aggregation tendency induces different optical proprieties. In fact in Figure 3.18 are reported the polymer dilute in chloroform solutions that appears complete different in colour, (i.e. violet and blue), reflecting the strong influence of the alkyl side chains on the intra- and inter-molecular interactions and aggregation tendency. To better investigate this aspect, the optical absorption spectra of the pristine polymers P(3)-PFQ-BDT-TR_1 and P(4)-PFQ-BDT-T2R_2 both in solutions and thin-films are carried out and displayed in Figure 3.19a and3.19b respectively. Both materials exhibit two high energy absorption bands between 400nm ans 500nm, due to the $\pi - \pi^*$ transition and a low-energy band arising from the intra-molecular *push-pull* interactions and from the inter-molecular interactions between the polymer chains. The main parameters of the absorption spectra are reported in Table 3.4

Figure 3.18: Chloroform solution of P(3)- Q-BDT-TR_1 and P(4)-FQ-BDT-T2R_2

In the solution absorption spectra, it is observed an evident red shift (by 52 nm) of the maximum wavelength λ_{max} of P(3) versus that of P(4) (615 nm versus 563 nm, respectively), indicates a different aggregation tendency. It suggesting that the presence of two alkyl side chain substitution on the thiophene rings decreases the intra- and inter-molecular interactions in solution. On the other hand, more similar λ_{max} are observed in the solid state spectra of the two polymers. A broader spectrum is registered for P(3) compared to P(4), in the longer wavelength region ($\sim$700 nm). As a result, the absorption onset values (λ_{onset}) are 730 nm and 700 nm for P(3) and P(4) respectively, from which the resulting optical gaps E_{gap}^{opt} are estimated to be 1.70eV and 1.77 eV,

	Solution		Thin Film		
Polymer	λ_{max} (nm)	λ_{onset} (nm)	λ_{max} (nm)	λ_{onset} (nm)	E_{gap}^{opt} (eV)
P(3)	615	714	610	730	1,70
P(4)	563	640	623	700	1,77

Table 3.4: Main optical value parameters of P(3)- FQ-BDT-TR_l and P(4)-PFQ-BDT-T2R_2 absorption spectra, both in solution and in thin film. An experimental error of 2 nm for each wavelength due to the spectrum resolution is considered.

respectively.

Observing the chemical structure reported in Figure 3.17, P(3) has a linear octyl (C_8H_{17}) side chain linked to the thiophene side group, which improves the solubility of the polymer, without determining a significant steric hindrance or side chain congestion with the adjacent octyloxy (OC_8H_{17}) substituent of the quinoxaline unit. As a consequence, it is assumed that P(3) adopts a more favourable planar conformation, which could be responsible for a partial pre-aggregation of the polymer backbone in solution, in agreement with the relatively small λ_{onset} ((16 ± 4) nm) passing from solution to thin-film. Diversely, in P(4) the two n-hexyl side chains linked to the thiophene side groups could sterically interact with the adjacent octyloxy chains of the quinoxaline units. It is supposed that P(4) adopts a conformation where the side chains are placed away from each other, probably determining a partial twisting of the polymer backbone. This twisting, as expected, is stronger in solution, where the inter- molecular interactions are relatively low, while in the solid state the polymer chains will be forced to adopt a more planar conformation. As a result, the partial planarization of the P(4) backbone in the thin-film is reflected in a drastically red-shifted onset ($\Delta\lambda_{onset}$= (62 ± 4) nm).

The OPV responses of P(3) and P(4) based solar was investigated tuning the D/A blend ratios to reach the best BHJ morphology. As reported on Table 3.5 the optimal D:A ratio was found to be 1 : 1 (wt/wt) for P(3) and 1 : 2 (wt/wt) for P(4). Upon increasing or decreasing the donor content in the active blends, a significant drop in J_{sc} and V_{oc} or FF was observed, resulting in lower PCEs

In particular, the best P(3) based solar cell exhibits in average: J_{sc} = 11,1 mA/cm^2, V_{oc} = 0,84 V and FF =61% with a resulting PCE = 5,7%, while the P(4) based device shows J_{sc} = 6,5 mA/cm^2, V_{oc} = 0,96 V and FF =54% with a resulting PCE = 3,4%. By comparing the resulting OPV characteristic, the main difference is represented by the J_{sc} and V_{oc} values, which exhibit an opposite trend passing from P(3) to P(4).

Note that, as for the previous case, for each D/A ratio the proprieties of the active layer was optimized in terms of thickness, annealing, additives, deposition conditions in order to obtain the best morphology. The best resulting thickness are reported in Table 3.5, exactly for the best device based on P(3) is 110 nm, while for P(4) is just 65 nm. In general, the optimized thickness is due to the best compromise between high mobility and good absorption. In this case the value almost double of P(3) based blend indicate a better morphology that improve both proprieties. To

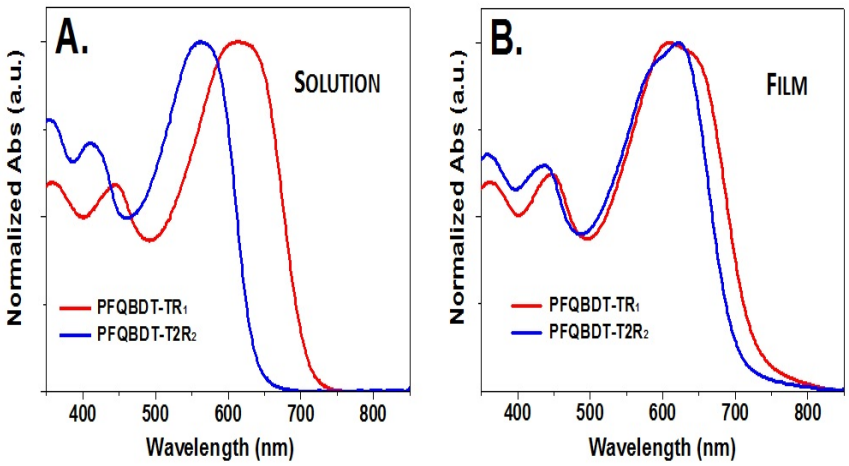

Figure 3.19: Absorption spectra of P(3)- Q-BDT-TR_1 and P(4)-FQ-BDT-T2R_2 a) in solution and b) in thin film. [77]

confirm this, the hole mobility for both polymer based blend was estimated by the SCLC method, reported in Figure 3.20. The mobility of the optimized P(3):$PC_{61}BM$ 1 : 1 (wt/wt) film resulted to be one order of magnitude higher compared to that of the P(4) :PC61BM blend 1 : 2 (wt/wt)($2,0\pm0,2\times10^{-4} and 4\pm1\times10^{-5} cm^2/Vs$ respectively). Indicate a closer $\pi-\pi$ stacking and ordering of P(3) polymer backbones the allow a better charge transport.

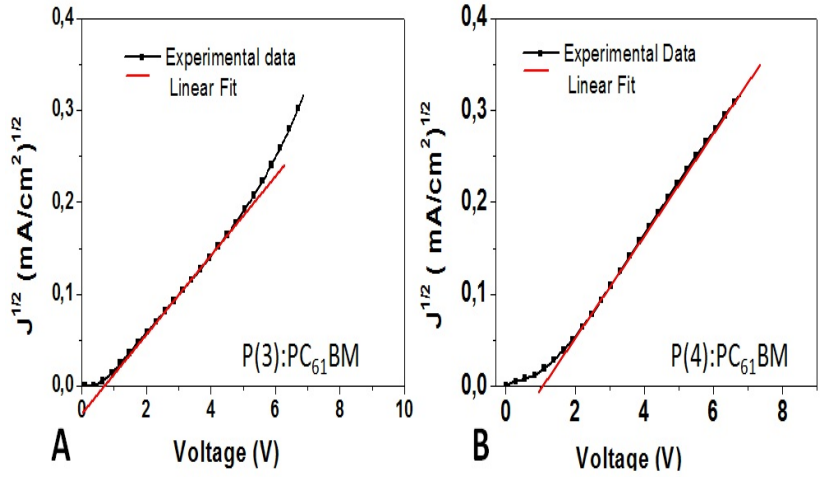

Figure 3.20: SCLC plots of P(3)- PFQ-BDT-TR_1 and P(4)-FQ-BDT-T2R_2 based devices [77]

In addition to the highest mobility, a better absorption proprieties are expected. In Figure 3.21a are reported the optimal blend absorption spectra of the best devices. Due to the different thickness, to be able to compare the shape of the spectra, the normalized spectra in the range

Polymer	D:A ratio (wt/wt)	Thickness (nm)	V_{OC} [V]	J_{SC} $[mA/cm^2]$	FF [%]	PCE [%]
P(3)	(2:1)	105 ± 6	0,78 ± 0,01	7,7 ± 0,3	39 ± 2	2,3 ± 0,2
	(1:1)	110 ± 4	0,84 ± 0,01	11,1 ± 0,5	61 ± 2	5,7 ± 0,2
	(1:2)	120 ± 5	0,79 ± 0,01	8,9 ± 0,3	67 ± 2	4,7 ± 0,2
P(4)	(2:1)	80 ± 5	0,97± 0,01	3,1 ±0,5	30 ±2	0,9 ± 0,1
	(1:1)	80 ± 4	0,96 ± 0,01	6,9 ± 0,2	47 ± 1	3,1 ± 0,1
	(1:2)	65 ± 4	0,96 ± 0,01	6,5 ± 0,1	54 ± 1	3,4 ±0,1

Table 3.5: Main PV parameters of P(3)- FQ-BDT-TR_l and P(4)-PFQ-BDT-T2R_2

between 650nm and 750nm, of both blend, are reported in the inset. The P(3):$PC_{61}BM$ blend exhibits a broader and more defined absorption profile in the red portion of the spectrum, suggesting enhanced $\pi - \pi$ inter- chain interactions, in agreement with improved charge mobility. Those aspects lead to a substancial different EQE spectra of the best devices reported in Figure 3.21b. The spectral features are consistent with the corresponding blend absorption spectra, with a higher value for the P(3) based blend compared to the P(4) based one. In particular, the maximum values of the EQE at the relative absorption maxima of the blend, are 65% (at 600 nm) for P(3)based device and 50% (at 435 nm) for P(4) based device. Convolution of these spectra with the AM1.5 solar spectrum gives calculated J_{sc} in good agreement, within a 5% experimental error, with that obtained in the J-V measurement. The best mobility, highest thickness and best EQE spectrum justify the highest value of the J_{sc} of P(3) based device (11,1 mA/cm^2 versus 6,5 mA/cm^2).

Different trend is observed for the V_{oc}. By comparing the average value of V_{oc} (V_{oc}^{av}) for each polymer:$PC_{61}BM$ based solar cell, estimated from the open-circuit voltages observed at different D/A w/w ratios (Table 3.5), an increase in V_{oc}^{av} by 0,15 V is observed passing from P(3) to P(4). In particular, the best performing P(3) and P(4) based solar cells exhibit a V_{oc} of 0,84 V and 0,96 V, respectively. This variation, despite the nearly identical electrochemically derived HOMO and LUMO energy levels (Table 3.3), could be ascribed to the effect of the side-chain architecture on the film-forming properties of the blend. Different blend organization could influence the exciton stabilization and dissociation, the D:A aggregation and interfacial energetics, all factors that are known to strongly affect the V_{oc} [140] [141]. This, correlates well with our hypothesis that P(3), compared to P(4), adopts a more planar conformation which promotes the generation of different and relatively more ordered and well-organized domains, in perfect agreement with the highest mobility and more define absorption profile.

In order to gain a deeper understanding on how the side chain architecture of polymers P(3) and P(4) affects the solar cell output parameters, the morphological differences of optimized P(3):$PC_{61}BM$ (1:1) and P(4):$PC_{61}BM$ (1:2) blend films by tapping-mode AFM, reported in Figure 3.22. The surface morphology of the resulting films are significantly different with morphological features that correlate well with the previous results. In particular, the topographic image

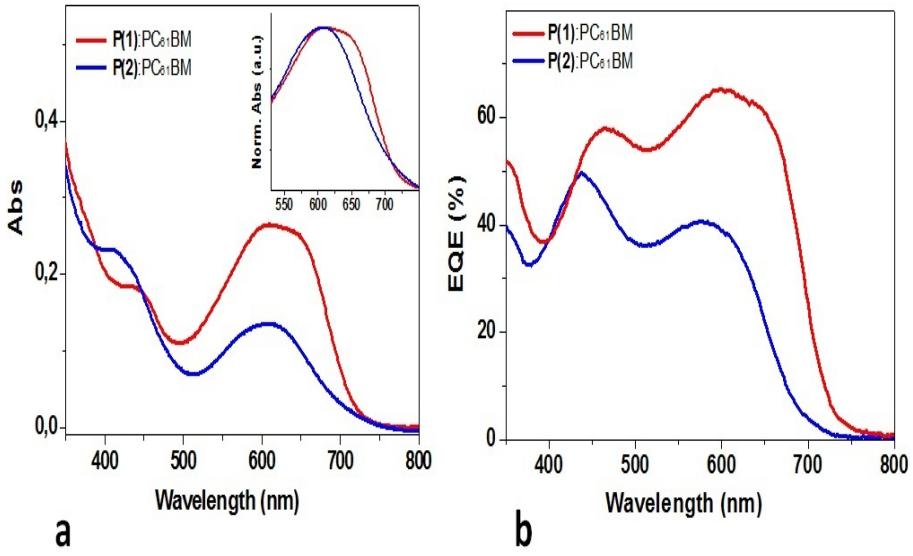

Figure 3.21: a) Absorbance and b) EQE spectra of P(3): $PC_{61}BM$ and P(4): $PC_{61}BM$ based devices. In the inset there are reported the absorption spectra normalized by the thickness [77]

of as-cast P(3):$PC_{61}BM$ (1:1) film is characterized by a well defined and structured surface (RMS, of $\sim$ 5 nm) with the presence of more ordered and aggregated polymer domains, and an optimal phase separation with the fullerene. Diversely, the AFM image P(4):$PC_{61}BM$ (1:2) exhibits a smooth and almost featureless surface (RMS of $\sim$ 1 nm) with poorly defined domains indicating an bad phase segregation of the D/A blend. Thus, limited percolation pathways are expected that suggest a bad charge transport both in terms of mobility and charge collection. This in good agreeement with the low charge mobility,J_{sc}, FF, and PCEs obtained from the corresponding BHJ device. This result correlates well with the above mentioned hypothesis on the twisting of P(3) backbone which might partially hinder $\pi - \pi$ interchain interactions, resulting in relatively more disordered and disaggregated domains.

3.3.3 π conjugated spacers

In the *push-pull* architectures, a part the side chains, also the connection spacer between the donor and acceptor unit can plays a fundamental role in the proprieties of the resulting polymer. Indeed, the presence of a conjugated π-bridges strongly affect the electronic structure, and consequently optical and electrical properties [142]. The main effect is to mediated the electronic interaction between the push and pull moieties, thus affect the spatial distribution of the molecular orbitals over the polymer backbone [143]. In addition, π-bridges also influence the structural conformation of the polymer chains, by introducing rigidity and planarity or torsion angles on the backbone and by favouring or hindering inter-chain interactions. Many kind of π-conjugated spacers are studied, from vinylenes [144], ethylenes [145], to aromatic rings such as thiophenes, furans and selenophenes [146] [147]. Among them, the introduction of fused aromatic units, such as thieno[3,2-b]thiophene

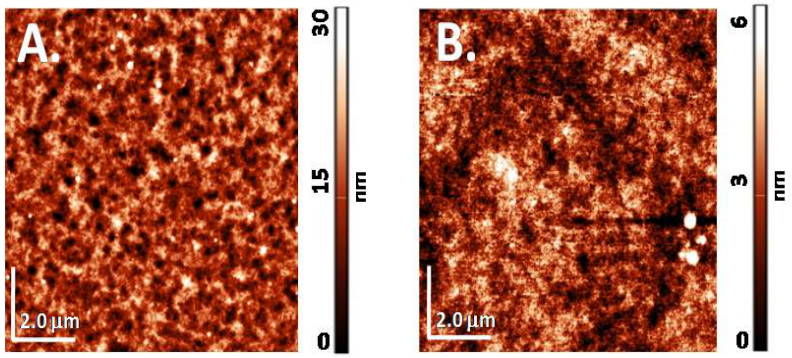

Figure 3.22: AFM images (size: 5 x 5 mm) of blend films on ITO/PEDOT:PSS of a) P(3):$PC_{61}BM$ (1:1) with a RMS= 5 nm b)P(4):$PC_{61}BM$ (1:1) with a RMS= 1 nm

(TT) has recently attracted much interest.

In fact, the centrosymmetric, rigid and coplanar structure of TT ensures a high delocalization of the π-electrons over the polymer backbone and also favours intermolecular $\pi - \pi$ stacking, resulting in red-shifted absorption, reduced band gap and enhanced charge mobility [148]. TT has already been applied successfully as a π-bridging group in carbazole-benzothiadiazole[149] and BDT-benzothiadiazole polymer systems [150]. The comparative studies with analogous polymers containing a single thiophene ring, indicate a red-shifted light absorption spectra and higher charge carrier mobility (by two orders of magnitude) of the TT containing polymer compared to the analogous with thiophene. A band gap narrowing (by 0.1 eV) and stronger intermolecular interactions favoured by the structural rigidity, planarity and linearity of the polymer backbone are observed. However, a disadvantage to use the TT spacer is a decrease in the solubility of the corresponding polymer.

Following the same approach, the thiophene (T) or thieno[3,2-b]thiophene (TT) groups are used as π-bridging units between FQ and BDT. The results are the polymers P(5) PFQ-BDT-T and P(6) PFQ-BDT-TT. Their chemical structures, already reported in Chapter 2, are recalled in Figure 3.23

The main physical properties of the two polymers are reported in Chpater 2 and recalled in Table 3.3 to facilitate the comparison. In order to compare the properties of the two polymers on the basis of the different π spacer nature, exactly the same chemical structure of the donor and acceptor building blocks, including side chains was maintain. An unavoidable drawback of this choice is the big difference in the solubility of the two corresponding monomers and of polymers during polymerization, affecting the relative molecular masses of the final products.Thus the TT spacer, despite the optical and electrical positive effect, it affect the solubility lead a polymer with a low molecular weight (Table 3.6).

As for the previous investigated polymers, the deep HOMO energy levels,ensure devices with a high V_{oc}, good air stability and, in blend with $PC_{61}BM$, provides a driving force to ensure an

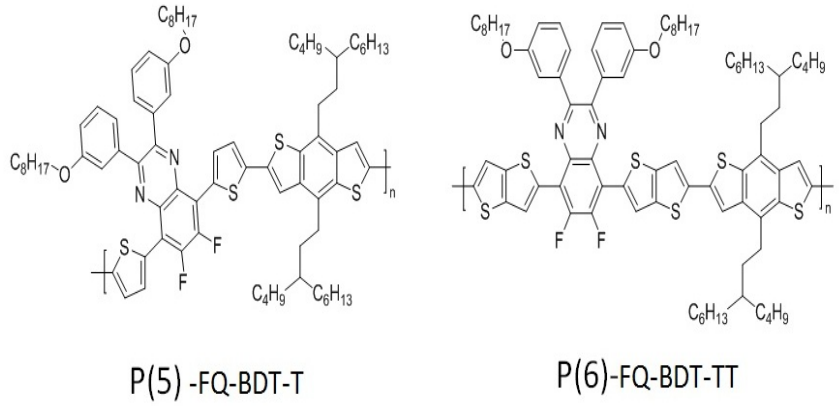

Figure 3.23: Chemical structure of P(5) PFQ-BDT-T and P(6) PFQ-BDT-TT. [79]

Polymer	M_n [KDa]	M_w [KDa]	E_{HOMO}[eV]	E_{LUMO}[eV]
P(5)- PFQ-BDT-T	101	270	-6,00	-3,63
P(6)- PFQ-BDT-TT	15	42	-5,90	-3,52

Table 3.6: Molecular weight and Energy proprieties of the two polymer P(5)- FQ-BDT-T and P(6)-PFQ-BDT-TT

efficient exciton dissociation. The slightly higher lying HOMO energy of P(6) compared to P(5) (by $\sim$ 0,10 eV) is in agreement with the other cases of T and TT bridged *push-pull* polymers reported in the literature [149]. In fact, the relatively higher electron density of the TT spacer compared to the T one attenuates the *push-pull* character of the polymer and slightly raises its molecular energy levels. From the optical point of view a discussed red-shifted of the TT based polymer is expected. Therefore the Absorption spectra of both solution and thin film of the two polymer are carried out and reported on Figure 3.24.

The UV-vis absorption spectra of both P(5) and P(6) show the same features: a higher-energy absorption band between 380-480 nm, which can be assigned to localized $\pi - \pi^*$ transitions, and a lower-energy band between 500-700 nm, arising from the intramolecular charge-transfer-like interactions between the electron-rich BDT and electron-poor FQ units and from the intermolecular interactions between the polymer chains. As expected the a red shift both in solution and in thin film is observed for P(6) (TT spacer). Indeed, the resulting optical gap (E_{gap}^{opt}) of P(6) is slightly lower (1.71 eV) compared to P(5) (1.77 eV). For polymer P(5), a red shift of the spectrum when passing from solution to the thin film is observed, indicating that $\pi - \pi$ intermolecular interactions occur in the solid state. In addition, the main peak is structured and it displays vibronic features both in solution and in thin film, implying the presence of ordered $\pi - \pi$ stacks likely due to polymeric chains entanglements, difficult to dissolve even in diluted solutions owing to the high molecular mass of the polymer. In comparison, P(6) shows a smaller red shift of the absorption

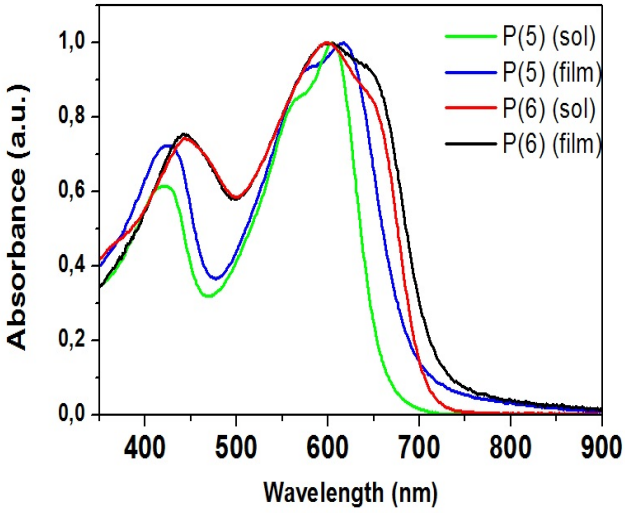

Figure 3.24: Absorption spectra of P(5)- PFQ-BDT-T and P(6)-FQ-BDT-TT in solution and in thin film. [79]

onset, when passing from solution to film. This could be due to the low molecular mass, which renders easier the polymer solubilization and chains disentanglements, and to the higher rigidity and linear geometry of the TT spacer which imparts to the polymer a higher stability in a linear conformation.

To investigate the effects of π-conjugated bridges on the photovoltaic properties of P(5) and P(6), they have been employed as D materials in BHJ solar cells, with $PC_{61}BM$ as A counterpart, in the conventional device configuration glass/ITO/PEDOT:PSS/Active Layer/LiF/Al. For each D:A ratio, different processing conditions are investigated. As reported in Table 3.7 the presence of additive in the P(5) blend is beneficial for the OPV performance, while for P(6) based device is detrimental. The results are an average on 6 devices, the error of each parameters is obtained from the standard deviation.

For both materials the optimal D:A ratio is 1:1 (wt/wt), upon increasing or decreasing it lower OPV responses are observed. By comparing the performances of devices prepared in the same conditions, the one based on P(5) showed a low PCE (2,2%), mainly due to a low J_{sc} (5,5 mA/cm^2) and FF (46%). On the other hand, the device based on P(6) showed more than doubled PCE, as high as 5,3%, with V_{oc} = 0,82 V, J_{sc} = 10,9 mA/cm^2 and FF = 59%. The doubled J_{sc} is explicable through the effect of the TT spacer which favours a linear polymer backbone and promotes inter-chain packing lead to an higher hole mobility. In fact the mobility, measured through the SCLC method, of the blend processing in the same condition (without additive) of the mentioned devices, result: for P(5): $PC_{61}BM$ $\mu_h = (1,1 \pm 0,1) \times 10^{-4} cm^2/Vs$ while for P(6): $PC_{61}BM$ $\mu_h = (3,7 \pm 0,2) \times 10^{-4} cm^2/Vs$.

However in order to enhance the photovoltaic performances of P(5) based solar cell, through the optimization of its blend nanomorphology, a 3% (v/v) of 1,8-diiodooctane (DIO) was added to the active layer solution. As a result, the J_{sc} of the P(5) based device results almost doubled (9,3 mA/cm^2) and FF grew up to 68%, resulting in a PCE of 5,3% comparable with the best

Polymer	D:A ratio (wt/wt)	Additive	V_{oc} [V]	J_{scC} $[mA/cm^2]$	FF [%]	PCE [%]
P(5)	(1,5:1)	/	0,85 ± 0,01	1,9 ± 0,1	36 ± 1	0,6 ± 0,1
	(1,5:1)	3%	0,85 ± 0,01	8,6 ± 0,03	67 ± 2	4,9 ± 0,2
	(1:1)	/	0,87 ±0,01	5,5 ± 0,2	46 ± 1	2,2 ± 0,1
	(1:1)	3%	0,84 ± 0,01	9,2 ± 0,5	67 ± 2	5,3 ± 0,3
	(1:1,5)	/	0,88 ± 0,01	5,1 ± 0,3	65 ± 2	2,9 ± 0,2
	(1:1,5)	3%	0,81 ± 0,01	9,3 ± 0,3	68 ± 2	5,1 ± 0,1
P(6)	(1,5:1)	/	0,83 ± 0,01	10,5 ± 0,3	58 ± 2	5,1 ± 0,3
	(1,5:1)	3 %	0,77 ± 0,01	10,9 ± 0,8	51 ± 2	4,3 ± 0,2
	(1:1)	/	0,82 ± 0,01	10,9 ± 0,5	59 ± 3	5,3 ± 0,3
	(1:1)	3%	0,75 ± 0,01	9,5 ± 0,2	45 ± 4	3,2 ± 0,3
	(1:1,5)	/	0,81 ± 0,01	9,3 ± 0,5	62 ± 4	4,6 ± 0,3
	(1:1,5)	3%	0,75 ± 0,01	10,1 ± 0,2	53 ± 2	4,0 ± 0,1

Table 3.7: Main OPV parameters of P(5)- FQ-BDT-T and P(6)-PFQ-BDT-TT

P(6) based device. To add an additive in the blend solution, is a well know strategy to increase the PCE [151]. In fact the presence of a high boiling point additive (i.e. DIO has a boiling point of 325^{o}C at 1 atm) in the P(5):$PC_{61}BM$ blend allows a slow film forming process with an easier macromolecules disentanglement and ordering, inducing an overall blend film morphology with optimal phases intermixing. The rearrangement of the blend has consequence, as expected, also in the charge mobility, in fact, in the blend processing as for the last device has a mobility $\mu_h = (3,7 \pm 0,2) \times 10^{-4} cm^2/Vs$, very similar the once found for the optimized P(6):$PC_{61}BM$ blend. On the contrary, the addition of 3% of DIO to the P(6):$PC_{61}BM$ based blend lead to a drastic drop in PCE (3,19%), due to a decrease in V_{oc} (0,75 V), FF (45%) and J_{sc} (9,5 mA/cm^2).

From the optical point of view it is interesting to compare the absorption spectra of the devices, processing with and without the additive; the spectra are reported in Figure 3.25a. A variation in the spectral shape in the red-range of the spectra is expected due to the different reorganization of the polymer in the blend. However, interesting, the use of DIO in the blend does not induce any relevant spectral shift. The absorption measure results thus less sensitive to the nanomorphological variations in the active layer, that induce relevant changes clearly observed in mobility and photovoltaic response. Taking into account both electrical and optical aspect of the device, the EQE measurement results more sensitive. Thus the EQE spectra of the based devices processing with and without the additive was carried out and reported in Figure 3.25. The EQE have spectral features consistent with the corresponding blend absorption spectra, main in terms of onset. As expected the P(5) based device processing without the additive show the lower EQE spectrum, with a maximum value of 30%. When P(5) is processing with the presence of DIO, the EQE spectrum reflects the highest mobility and optimal morphology of the active layer that lead to a high $J_{sc} = 9,3 mA/cm^2$. In the opposite, the P(6) based device show a similar shape in the spectra, but with different intensity. In particular, at 622nm (correspond to the relative absorption maxima of the polymer), the EQE is 48% when the blend is processing with DIO, while 54% without DIO. This fact, in perfect agreement with the OPV devices performance, suggest that the blend reorganization due to the presence of the additive, is detrimental

In order to deeper investigate the difference influence of the additive in the blend morphology, tapping-mode AFM images of the active layers of optimized cells, prepared with and without DIO additive, were registered and reported in Figure 3.26 The AFM topography of the P(5) based blend prepared without DIO shows finer and regular unconnected grains, or small circular islands, accompanied by a low roughness (RMS = 1.3 nm) (Figure3.26a). The addition of DIO to the P(5)-based blend leads to an improved morphology by generating more organized nanostructures and promoting an optimal D:A intermixing (Figure3.26c) with a similar roughness (RMS=1,5nm). This is in agreement with the trend evidenced for the J_{sc} and hole mobility of the corresponding devices and indicates that the use of the additive promotes both the phase separation between the BHJ components and also the formation of more ordered and aggregated polymeric domains. Similar optimal morphology is observed for the P(6) based blend prepared without DIO (Figure 3.26b). The structured topography is characterized by a slightly higher roughness (RMS = 2.2 nm) even higher when is added the additive (RMS=2,5nm). In Figure 3.26d is observed the formation of evident aggregates which suggest a probable higher phase separation between polymer and fullerene. This kind of morphology is expected to result in inefficient exciton separation and lacks

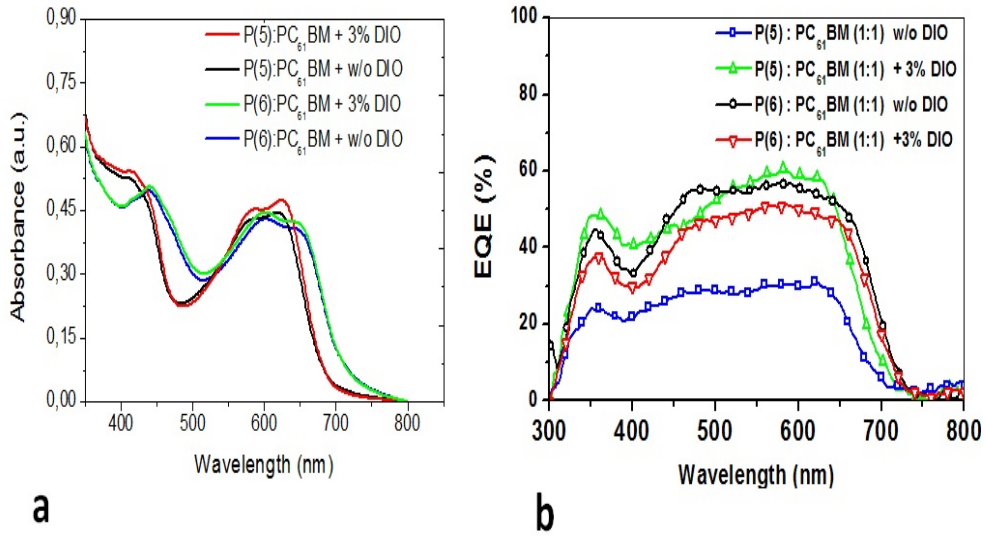

Figure 3.25: a) Absorbance and b) EQE spectra of P(5): $PC_{61}BM$ and P(6): $PC_{61}BM$ based devices [79]

the bicontinuous interpenetrating pathways necessary for the charge transport, in agreement with the relatively low OPV performance.

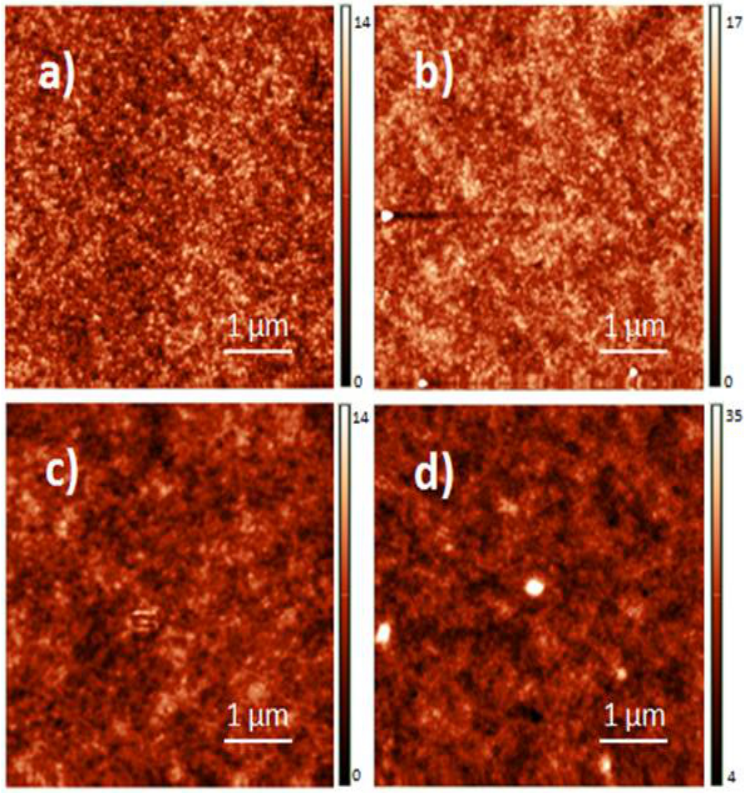

Figure 3.26: AFM images (size: 5 x 5 mm) of blend films on ITO/PEDOT:PSS of a) P(5):$PC_{61}BM$ w/o DIO b) P(6):$PC_{61}BM$ w/o DIO c) P(5):$PC_{61}BM$ with DIO and d) P(6):$PC_{61}BM$ with DIO.

3.4 Conclusion

In conclusion 6 different *push-pull* donor polymers based on the same D and A units, precisely Quinoxaline group as electron acceptor and Benzodithiophene as electron-rich group, have been investigated.. Different strategies to improve the photovoltaic performance of the devices based on those polymer, were investigated in order to highlight the complexity of the OPV. The infinite possibilities in terms of synthesis and process are, in the same time, the best and the worst aspects of the OPV technology. A summary of the previous results can justify this sentence. As demonstrated, the presence of a strong electron withdrawing atoms, as the case of fluorine, has a clear positive effect in terms of energetic properties of the polymer and in consequence enhancing the performance of the corresponding device. However the presence of the FQ unit in the donor polymer backbone is not sufficient to have a high performing device, this aspect becomes evident when P(1) and P(4) based devices are compared. Despite P(4) is based on the FQ unit and P(1) on simple Q unit, the PCE of the correspondent devices are 3,4% for P(4), slightly lower than 3,7% of P(1) based device (OPV parameters are reported in Table 3.5 and Table 3.2 respectively). In fact, a different in the side chains in the BDT unit, induce different structural organization of the polymer. For instance the presence of two side chains in BDT unit can induced a twisting of the polymer backbone that hinder the $\pi - \pi$ interactions, leading to a bad charge transport and consequence worst photovoltaic performance. In this case is evident that the morphological, structural behaviour of the polymer is more important than the energetic proprieties. Another example of complexity is observed in the case of P(5) and P(6) where the T spacer is substituted with a TT spacer. Despite in literature the clear positive effect on used TT spacer instead of T is often reported, here, in this particular case, it was shown that with proper optimization of the processing condition of the P(5) (T spacer) based device, it can reach the same PCE of the P(6) (TT spacer) based device (Table 3.7). In fact, the presence of an additive in the active layer solution, allow to a reorganization of the blend morphology. In the case of P(5) based blend, the presence of high boiling point solvent increases the formation of order domains with a good intermixing with the A counterpart increasing the charge transport and the resulting PV performance.

These examples suggest, in one hand that it is difficult to predict *a priori* which donor polymer structure will reach the best PV performance, but, on the other hand, the infinite strategies that can be adopted to improve PV proprieties, guarantee the possibility to reach the target of high efficient organic solar cells.

4

Thermal degradation of the BHJ active layer

4.1 Overview of degradation effects on OPV

The long-term stability of organic solar cells is a fundamental issue that has to be achieved in order to fabricate a commercial product. For this reason, to understand and prevent the degradation processes is crucial for the success of the OPV technology. The main problem concerning the stability is that, unlike the inorganic device, the organic solar cells can be prepared with different architectures, using many different materials and combinations and processed by many different methods. All these variables enter as parameters that influence the overall stability performance of the final device. For this reason in 2011 Reese *et al.* [152] define guidelines for standard procedures to testing the organic solar cells stability in order to compare data and claims obtained by different laboratories. The main degradation sources considered are oxygen, water, light and temperature plus their combination. To illustrate the complexity of the stability issue a scheme of the main phenomena is reported in Figure 4.1 [153]. The main part of the device that influences the stability is the active layer. In fact, many agents can modify the blend morphology or induce chemical reactions that can corrupt the polymer conjugation, affecting the electrical and energetic proprieties of the D and/or A materials. These chemical degradation processes can be induced from oxygen [153] [154], water [155] or atoms that percolate into the active layer from adjacent layers [156] [157], moreover they can be accelerated in presence of light and/or high temperature [158].

The mechanisms governed by oxygen can be reversible and recover with a proper annealing treatments [38], or irreversible. For example Guerrero *et al.*[154] show that when an active layer solution, based on P3HT:$PC_{61}BM$ is exposed to oxygen, the complex $P3HT^{+} : O_2^{-}$ can be formed. This species can be identified by the formation of an additional absorption band in the UV-Visible absorption spectrum of the blend. This process, highly reversible, leads to a decrease in the active layer absorption that induces a reduction in the J_{sc} of the resulting solar cells. At the same time an irreversible reaction with oxygen alters the electrical proprieties of P3HT, increasing the p-doping.

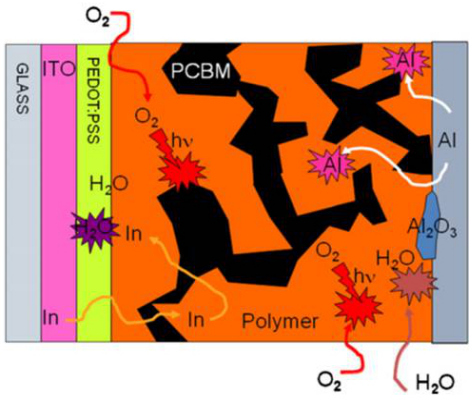

Figure 4.1: Different degradation agents that can affect the performance of an organic solar cell: water, oxygen, atoms percolation and light [153]

Indeed the photochemical oxidation leads to the formation of traps for electrons increasing hole concentrations and reducing charge carrier mobility [38]. In addition, also the electrodes can suffer from the presence of oxygen, when Ca or Al is used as cathode, aregiona of CaO or AlO_2 can be formed at the interface with the active layer. This region is insulating and detrimental for the charges extraction [154].

Another element that can damage the solar cells is the moisture [155]. The main source of water in organic PV devices comes from PEDOT:PSS, in fact due to his high hydrophilic behaviour it can absorb water from the atmosphere during the fabrication process. Kawano *et al.* [159] demonstrated that the main effect of water is to increase the resistivity of the PEDOT:PSS/active layer interface. Moreover Bulle-Lieuwma *et al.* [157] showed that the presence of water can catalyse the diffusion of Indium from the ITO electrode into the active layer inducing chemical reactions with the polymer. To prevent this problem the PEDOT:PSS layer is annealed at 150^oC to eliminate residual water, however, if the following layers are deposited in air the moisture can still be an issue. Finally, the third degradation source is the diffusion of the atoms from the adjacent layers into the active layer. As just mentioned, Indium can diffuse from the ITO, but also metal atoms can diffuse into the active layer during the thermal evaporation process, causing shunting or electrical shorting of the device.[41] Moreover Al or LiF atoms can diffuse into the organic layer also during the annealing processes. In the case of P3HT based solar cell the presence of Al atoms can disturb the alignment of the P3HT crystals and limiting the charge transport. [158] On the other hand, when LiF is used as buffer layer, the post-annealing induces the formation of PCBM:LiF complex at the interface, which reduces the PV performance [156].

In general it is difficult to discriminate the degradation mechanisms induced by one agent at time, however a few of them can be neglected with some precautions, such as: thermal treatment of the PEDOT:PSS to eliminate residual water, deposition the active layer inside the glovebox in inert atmosphere in order to prevent doping, pre annealing of the active layer and evaporation of the top electrode with a slow rate in order to prevent the atoms percolation. Moreover a proper

encapsulation, or the control of the atmosphere in which the device sare tested/stored, allows to prevent detrimental interactions with oxygen and/or water.
The remaining degradation processes that cannot be eliminated with these precautions, can be distinguished in three main categories: i) long term ii) thermal and iii) light-induced degradation. The first category is characterized by a slow and linear decay degradation [160] which becomes predominant after an initial loss in performance induced by light and/or temperature. A long time test allows to predict the lifetime of the solar cells. For example Peters *et al.* [161] showed that, after an initial burn-in loss in efficiency, PCDTBT:$PC_{70}BM$ based solar cells have lifetime approaching seven years, which is the longest reported lifetime for a polymer-based solar cell and approximately twice than the well-studied P3HT:$PC_{60}BM$ system. It is clear that in view of a commercial product the investigation of the long term degradation is crucial, however to also guarantee high performance during the time, a deep understanding on how to prevent or limit the initial PCE loss is equally important. For this reason the other two categories will be investigated more in details in the next Chapters. In particular the thermal degradation of the active layer will be investigated in the following sections while the whole device thermal stability will be discussed in Chapter 5. Then a preliminary study on the photodegradation will be presented and analysed in Chapter 6.

4.2 Thermal degradation

A working device, during a sunny day in a warm region, can reach a temperature of 65/85 ^oC [152]. The high temperature can induce different processes into the device, for example: a reorganization of the active layer [162], agglomeration of fullerene[163][40], crystallization of D polymer [40], chemical changes of both species [164], percolation of atoms from adjacent layers [158][156] or formation of defects limiting the charge transport. All of those processes mainly concern the BHJ active layer. In fact the D/A blend morphology is crucial for the long-term operation of solar cells. An optimal intermixing is the result of trade-off the compromise between a high density of D/A interfaces compatible with the exciton λ_D and high number of percolation pathways. A little variation of the BHJ organization can partially hinder these conditions becoming detrimental for the functioning of the solar cell.

All these processes have in common that they have to overcome a certain activation energy (E_a). Thus, the kinetics of these processes is strongly temperature dependent. The model that can describe this process is the Arrhenius one [165], in which the degradation constant (k_{deg}) is defined as follows:

$$k_{deg} = Aexp\left(\frac{-E_a}{k_B T}\right) \tag{4.1}$$

where k_B is the Boltzmann constant,T is the temperature (K), and A is a constant dependent on the degradation mechanisms and experimental conditions. However, in real conditions, where additional factors, besides the temperature, influence the degradation, more complex models should be considered (e.g. Eyring model) [153] [166]. Nevertheless, in this thesis one source of degradation at time is investigated, for example the thermal tests were performed in dark and in

inert atmosphere, allowing to consider the simplest model.

4.2.1 Effect of high temperature on PV parameters

As above mentioned, one of the main effects of the thermal stress on OPV devices is the modification of their BHJ morphology. Usually, the main consequence is the reduction of D/A interfaces and/or the percolation pathway towards the electrode, which is reflected in the performance of the solar cells mainly as a drop of the J_{sc} [167]. The example of MDMO-PPV : $PC_{61}BM$ is representative of this process. Conings *et al.* [165] show that at temperatures above the glass transition temperature (Tg) of MDMO-PPV (45 ^oC), the polymer becomes softer, allowing the fullerene molecules to move and start forming clusters. What it is supposed to occur, confirming by TEM images, is that after a short annealing time, small nuclei of $PC_{61}BM$ are formed. Then increasing the annealing time, the fullerene molecules dispersed throughout the polymer, move to the nuclei to form clusters, until saturation. As this process needs an activation energy to form the first nuclei and then the process reach a plateau, it can be described by the Arrhenius model (Equation 4.1). In Figure 4.2 the current decay of solar cells based on MDMO-PPV annealed at different temperatures is reported.

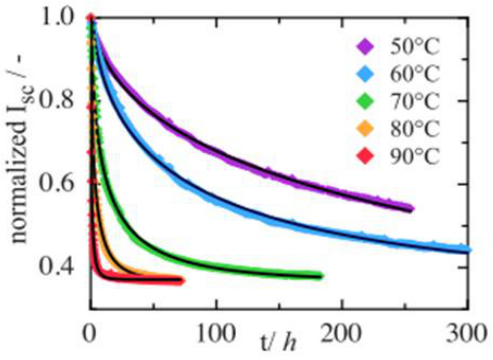

Figure 4.2: I_{sc} decay of MDMO-PPV based solar cells at different annealing temperatures [165]

The I_{sc} trend is an exponential decay that follow the law:

$$I_{sc} = I_{sc}(\infty) + I_{sc}(0)exp(-k_{deg}t) \tag{4.2}$$

where $I_{sc}(0)$ is the initial photocurrent value while $I_{sc}(\infty)$ is the value of the photocurrent at infinite time that seems to be independent from the temperature.

In this example the main phenomenon that occurs is the agglomeration of the fullerene, which limits the J_{sc}. However, also the FF can suffer from the blend reorganization, in fact a high FF can be expected from an optimal BHJ morphology, in which a proper D:A phase segregation and bicontinuous inter penetrating pathways are generated. Diversely, under thermal stress, the D:A intermixing and the number of percolation paths can be drastically modified/reduced, leading to

an increase of the series resistance which limits the FF [167].

In the end, also the V_{oc} can be influenced by a D/A reorganization. In fact, as discussed in Chapter 3, the V_{oc} directly depends on the energy of the CT state, that corresponds, in a first approximation, to the difference of the $HOMO_D$ and the $LUMO_A$. However it was demonstrated that the CT state depends also on the blend organization, indeed D-A interactions/distances as well as molecular orientation and packing can drastically deviate the CT state energy from the simple approximation [141]. Those variations can be induced by a thermal stress, thus leading to significant changes in V_{oc}.
In specific cases, thermal degradation can alter just the interfaces with the active layer and the electrodes, leaving the BHJ unchanged. The main process involved is the migration of the D or A compounds close to the electrode, generating very thin barriers or selective transport regions as a function of the device architecture. The mainly unaltered BHJ morphology guarantees a good charge generation and a constant J_{sc}, while the barriers regions represent a shunt resistance that can affect both the FF and V_{oc}.

4.2.2 Influence of fullerene

In inert atmosphere, fullerene derivatives are expected to be thermally stable at the operating temperature of OPV cells according to TGA measurements performed in inert atmosphere and in air[168]. Therefore the main process involved with the fullerene in a BHJ solar cells under thermal stress is connected with its agglomeration tendency [169].

The presence of fullerene can induce different organization of the D polymer. For instance when the D polymer is mainly crystalline, as the case of P3HT, the presence of $PC_{61}BM$ in P3HT:$PC_{61}BM$ films casted from CB reduces the crystallinity of P3HT. The P3HT crystalline domains can be recovered with a proper annealing step, but it is demonstrated that when the D:A ratio is 1:4 (wt/wt) the crystallization is completely inhibited [163]. Indeed when a blend of P3HT:$PC_{61}BM$ with a ratio of 1:4 (wt/wt) is annealed at 110^oC a strong phase separation is observed, with the formation of fullerene clusters which almost cover the entire surface of the film [163]. Diversely with a standard ratio of 1:1 wt/wt the phenomena is less intense. Note that, despite the optimal morphology of the active layer has a resolution of nm, $PC_{61}BM$ crystals can reach dimension of the order of μm and appear evident with optical microscopy. Interesting, when the annealing is performed during a simultaneous illumination of the films, the phase separation is almost totally prevented, with only a few isolated clusters of $PC_{61}BM$ formed [163]. This behaviour was observed for other blend based on different polymer such as: DPP-TT-T, PTB7 and PCDTBT [170]. In particular, studying the optical microscopy images of PCDTBT: $PC_{61}BM$ (1:2) blend film under thermal stress, it has been estimated the temperature dependence of the nucleation and growth rates, both in dark and in light conditions, as reported in Figure 4.3. Clearly, the nucleation rates for illuminated blends are significantly suppressed across all temperatures investigated. On the other hand, the growth rate exhibits a monotonic increase, increasing the annealing temperature. The photo-oligomerisation process appears thus to affect the nucleation process but not the crystal growth [170].

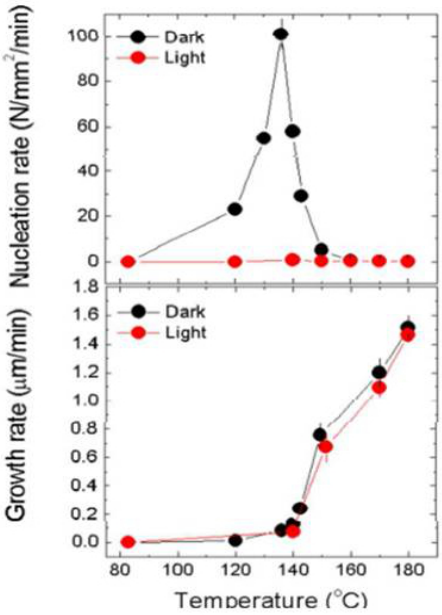

Figure 4.3: Nuclearization of PCBM in blend with PCDTBT [170]

4.2.3 Influence of Glass Transition Temperature

The T_g is a crucial parameter that governs the reorganization of a polymer in the solid state. It corresponds on a second order state transition from a hard and relatively brittle state into a molten or rubber-like state. However this important value is not an absolute constant related to a particular chemical structure, in fact, it is necessary to consider the technique and experimental parameters that were used to determine a particular T_g value as well as the processing history of the sample [164]. It should also be noted that only the amorphous and disordered fraction of a polymeric material displays a glass transition and, hence, the signal strength of any T_g measurement depends on the polymer crystallinity. From the chemical point of view the T_g strongly depends on a number of structural factors such as: the molecular weight, the constitution of chain segments, the side-chains length and grafting density and the interchain interactions that can reduce the molecular mobility of polymer segments. Many techniques can be used to determine the T_g, however the most common is the Differential Scanning Calorimetry (DSC). The DSC measures the difference in heat flow to/from a sample compared to a reference system as a function of temperature. The heat can be absorbed or released during phase transitions such as melting or crystallization and they appear as peaks in the DSC graph, while the glass transition temperature appears as a inflection point. The main advantage of this technique is that just few milligrams of material (in powder)are required for the measurement. However, the main limitation is that some crucial factors that can affect the T_g ,such as the polymer organization/cristallinity and eventual interactions with the substrate, are not taken into account.

An alternative technique used to measure the T_g is the Ellipsometry that provides information

about the evolution of the film thickness (d) with temperature. In fact phase changes manifests themselves as a change in volumetric expansion coefficient α, which is directly proportional to variations in the rate of change of the volume (hence d due to the substrate confinement), with temperature T, according to $\alpha = \frac{1}{d}\delta d/\delta T$. Contrarily to DSC here the sample is a thin film of polymer. With this technique it has been clearly demonstrated how the confinement effects interactions with the substrate [171] and the thickness of the layer, can affect the T_g [172]. An example is reported in Figure 4.4.

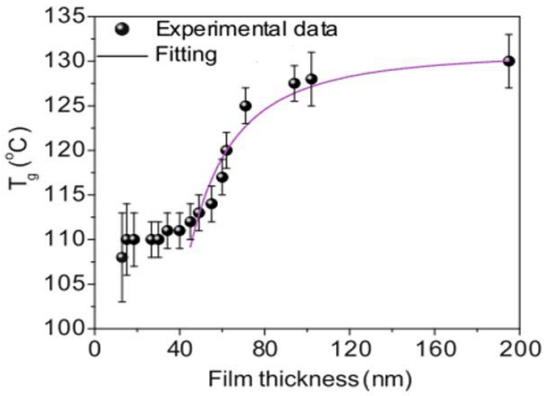

Figure 4.4: Variation of the T_g with the thickness of the PDCTBT layer measured with Ellipsometry [172].

The knowledge of the T_g of a D polymer is expected to be a fundamental parameters in order to determine the thermal stability of the BHJ solar cells. In fact, the main hypothesis on the thermal degradation process asserts that at temperature above the T_g the polymer matrix become more soft and the fullerene molecules start to form crystal, with consequent losses in the PV performance [173]. In the opposite at temperature lower the T_g the blend morphology is unaffected and thus thermally stable. This hypothesis is well demonstrated from Bertho *et al.* [40] comparing two D polymers: MDMO-PPV ($T_g \sim 45^oC$) and "high Tg PPV" ($T_g \sim 138^oC$). As a result, the solar cells based on the "high Tg PPV" show an enhanced thermal stability, compared to the analogous system based on MDMO-PPV [40]. However when the P3HT ($T_g \sim 6^oC$) is added in the comparison, an intermediate behaviour of the corresponding solar cell was observed, despite the T_g of P3HT is lower than that of MDMO-PPV [173]. This unexpected result reflects the more complex mechanism involved in the P3HT:$PC_{61}BM$, where simultaneous processes take place. The first one occurs at temperature up to 110^oC promoting the crystallization of P3HT resulting in a higher J_{sc}. While, increasing the annealing time or increasing the temperature to 150 ^oC, the fullerene starts to cluster as in blends with MDMO-PPV, resulting in a decreased J_{sc}.
As a consequence the knowledge of the T_g of the pristine D polymer is not enough to predict the thermal behaviour of the corresponding solar cell, mainly because this value can also vary when the D is blended with the fullerene. A clear example is observed in Figure 4.5 where different value of T_g is observed as a function of different P3HT:$PC_{61}BM$ ratio [164].

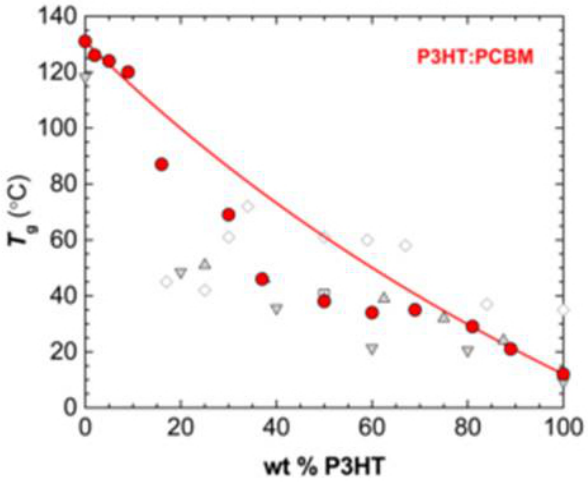

Figure 4.5: Variation of the T_g of the P3HT:$PC_{61}BM$ blend in function of the D:A ratio. Data are collected from different references [164]

In conclusion, the T_g of the active blend (T_g^{blend}), which can be significantly differs form the T_g of the D polymer, is the more appropriate parameter to predict the thermal behaviour of a solar cell. However, despite an high polymer's T_g is expected to give high T_g^{blend}, the determination of the T_g^{blend} is not trivial.

4.3 Fabrication and characterization of P3HT and PTB7 based solar cells

In order to evaluate how the thermal degradation can affect the active layer, two representative polymers are used as D materials to fabricate BHJ solar cells: P3HT and PTB7. Their chemical structures are reported in Chapter 2 Figure 2.2, coded as P(7) and P(8). As discusses in the previous Chapter, the P3HT is one of the most famous organic semiconductor polymer, based on the repetition of thiophene rings. The best performance can be obtained when it is combined with $PC_{61}BM$ using a D:A ratio of 1:1 wt/wt [174]. The main characteristic of this material is that it forms crystalline domains with a high mobility allowing to increase the thickness of the active layer (∼300nm). A common strategy to enhance the cristallinity of P3HT blends is based on a slow drying process, following by a thermal annealing at high temperatures ($110^oC - 140^oC$). On the opposite, PTB7 is a commercial D polymer commonly used for high performing BHJ solar cells, which, contrarily to P3HT, has an amorphous character [175]. Based on this polymer, different innovations on the device structure were demonstrated to lead to high efficiency solar cells [133]. However in the standard structure the best performing device gives an efficiency of 7,4% when PTB7 is combined with $PC_{71}BM$ with a ratio 1:1,5 wt/wt [81]. Note that, the main challenge

was to optimized the morphology of the active layer, this goal was reached adding to the initial CB solution a small percentage of solvent additive (3% v/v of DIO) [176].

4.3.1 Device fabrication

To compare the thermal behaviour of the active layer, the same device structure is used for the two polymers based solar cells. The stack selected is: ITO/PEDOT:PSS/Active Layer/ZnO/Ag. The cathode (ZnO/Ag) is chosen to prevent degradation processes, such as oxidation and diffusion, that can occur at the active layer/electrode interface when other common materials such as Ca/Al[42] or LiF/Al [156] are used.
For both devices the glass/ITO substrate is cleaned following the procedure reported in Chapter 2. Then a thin layer ($\sim 35nm$)of PEDOT:PSS is deposited by spin coater in air and annealed for 15 minutes at 150^oC to eliminate residual water.
Then, the samples are immediately transferred inside the glovebox (inert atmosphere) for the active layer deposition. The active layer of P3HT is based on a solution of P3HT:$PC_{61}BM$ (1:1 wt/wt), dissolved in ODCB:CB (1:1 v/v) with a polymer concentration of 30 mg/ml. In parallel, PTB7 is mixed with $PC_{71}BM$ (1:1,5 wt/wt) and dissolved in CB solution with 3% (v/v) of DIO as additive (the total concentration is 25 mg/ml). Both solutions are formulated in glove-box to avoid oxygen/water contamination and stirred overnight at 60^oC. The P3HT:$PC_{61}BM$ solution is spin-coated on the top of the PEDOT:PSS layer (1000 rpm for 10 seconds) and the resulting wet film is slowly dried (30 min) in glove-box. Before the ZnO deposition, the stack is annealed at 110^oC for 10 minutes. The PTB7: $PC_{71}BM$ solution is spin coated at 700 rpm for 120 seconds allowing the complete drying of the resulting film. No additional post treatments were carried out. Next, a solution of ZnO nanoparticles (provided by Genes-Ink, Lab-Ink Jet ZnO) is spin coated on the top of the active layers. The ZnO layer has a thickness around 50 nm. To complete the device fabrication, 100 nm of Ag are deposited using a thermal evaporator directly connected to the glovebox at 10^{-6} mbar at a rate of 1 nm/s to inhibit any atoms percolation.

4.3.2 Electrical characterization

The PV parameters of the best performing P3HT and PTB7 based solar cells are reported in Table 4.1 and the corresponding JV curves are reported in Figure 4.6.

Active Layer	$J_{sc}[mA/cm^2]$	V_{oc} [V]	FF [%]	PCE [%]
P3HT:$PC_{61}BM$	8,6	0,60	57	3,0
PTB7:$PC_{71}BM$	13,4	0,72	66	6,4

Table 4.1: PV parameters of the best P3HT and PTB7 based solar cells with the structure ITO/PEDOT:PSS/ActiveLayer/ZnO/Ag

From the literature, BHJ solar cells based on blends of P3HT: $PC_{61}BM$ typically show efficiencies in the range of 2-4% [113]. The variability of the PCE is a consequence of the role of the

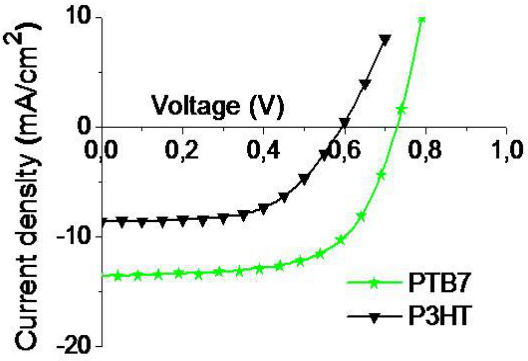

Figure 4.6: JV curve of PTB7 (green) and P3HT (black) based solar cells.

organization of P3HT films are strongly dependent on the polymer packaging in the solid state. For example, the highest mobility ($\mu_h = 0,1 - 0,3 cm^2/Vs$) is obtained with a regioregular P3HT able to generate thin films with a high degree of crystallinity. *Vice versa*, when the P3HT film is amorphous, the resulting mobility drop to 10^{-3} - $10^{-4} cm^2/Vs$ [113]. In general, when $PC_{61}BM$ is blended with P3HT, polymer crystallization is partially hindered. However when P3HT has time to crystallize, either by using casting techniques with slow evaporation of solvent or by using solvents with high boiling points, the charge mobility of the resulting films is typically improved [113]. In addition, a proper post-deposition thermal annealing helps to improve the crystallinity of the P3HT leading to higher PV performance [177]. In this context, another crucial parameter, that influence the morphology and electrical properties of the resulting blend, is the molecular weight (M_w) of P3HT. It is well known that M_w strongly affects the conformation, packing and interactions of the polymer chains [178] [179]. The P3HT M_w can range over 10kDa to 120kDA and the higher performance are obtained from the highest M_w. In this thesis the P3HT has a relatively low M_w of 37kDa, thus the performance obtained in this work are in well agreement with the literature confirming the optimized morphology of the active layer.

On the other hand, the PTB7:$PC_{71}BM$ solar cells exhibit high performance which are strongly dependent on the processing conditions. It was shown that, in order to increase the nanoscale phase separation, chemical additives, such as DIO, have to be added in PTB7:$PC_{71}BM$ blend solution [180]. In fact without additive, $PC_{71}BM$ molecules tend to aggregate, while with the correct amount of DIO (3% v/v) the aggregation is limited and an optimal BHJ morphology can be obtained[176].

As a result, standard solar cells with a PCE of 7,4%, V_{oc} 0,74V, J_{sc} 14,5 mA/cm^2 and FF 69 % have been reported in literature [81]. In this thesis PTB7 based solar cells show a slightly lower PCE (6,4%) likely due to the different cathode used, in fact it is well know that the energy matching between the interfacial layers (or electrodes) and the PTB7 layer, plays an crucial role in optimizing the charge transport and collection processes [134]. Here, ZnO/Ag is used as top electrode, while in literature reference devices are capped with Ca/Al. However, as mentioned

before, the Ca/Al electrode is extremely sensitive to the ambient conditions (even in glove-box) and is usually not recommended for thermal degradation tests. In conclusion, despite the different cathodes, responsible for different charge extraction processes, the obtained OPV results are comparable.

4.3.3 Optical characterization

The absorption spectra of the two active layers based on P3HT and PTB7 are reported in Figure 4.7. The P3HT:$PC_{61}BM$ blend spectrum shows an intense absorption between 400 nm - 650 nm, with three vibronic shoulders. It is well established that the position of the P3HT peak absorbance band (at around 500 nm) provides information on the degree of conjugation of the polymer chains, while the P3HT vibronic shoulders (at around 600 nm) provides information on the degree of interchain order/interactions [181]. Thus the peaks indicate strong intermolecular interactions among the P3HT chains, also suggesting a high ordering of the polymer chains in the solid state. From the absorption spectrum is evident that the main limitation of the P3HT as D material, despite the good degree of crystallinity which in principle favours high charge mobilities, is represented by the relatively narrow absorption band, up to 650 nm, which limits the light harvesting and thus the resulting photocurrent generation.
On the opposite the PTB7 : $PC_{71}BM$ blend spectrum shows a broader absorption from 300 nm to 750 nm. The absorption between 550 nm and 750 nm is mainly due to the PTB7, while its relatively weak absorption from 300 nm to 500 nm is compensated by the presence of $PC_{71}BM$. The amorphous character of the PTB7 film is confirmed by the absorption spectrum where no vibronic shoulders are observed. As result the broader absorption of PTB7 based devices is one of the main reason for the higher J_{sc} (13,4 mA/cm^2) compared to the analogous cells based on P3HT (8,6 mA/cm^2).

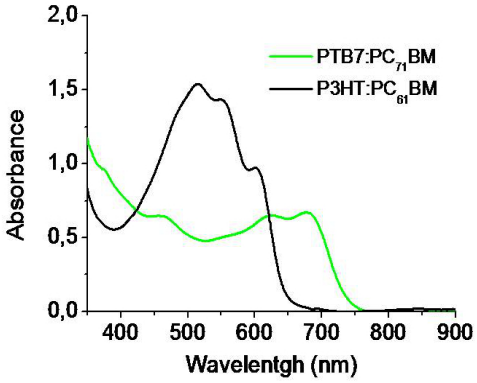

Figure 4.7: Absorption spectra of PTB7:$PC_{71}BM$ (1:1,5) (green) and P3HT:$PC_{61}BM$ (1:1) (black).

4.3.4 Morphological characterization

The AFM is a powerful tool that allows to characterize the surface nanomorphology of a BHJ active layer, with a resolution on the order of nanometers. The AFM images, topography and phase, of P3HT based blend are reported in Figure 4.8. In a relatively large area of $5\mu m \times 5\mu m$ the morphology is characterized by a finely structured blend organization (Figure 4.8a and b). The heights average is 36 nm and the RMS is 14,4 nm in agreement with values reported in literature [174]. Indeed a rough surface indicates the presence of ordered structure in the film, while smoother films are observed when crystalline domains of P3HT are not formed (without the annealing step or due to a fast dry). When a relatively small area of $1\mu m \times 1\mu m$ is considered, reported in Figure 4.8c and d, ordered domains of dozens of nm well dispersed in the background are observed. This fine intermixing is compatible with the exciton λ_D of P3HT in blend with $PC_{61}BM$ (4,6 - 9 nm) [55] thus promoting an efficient exciton dissociation and charge generation.

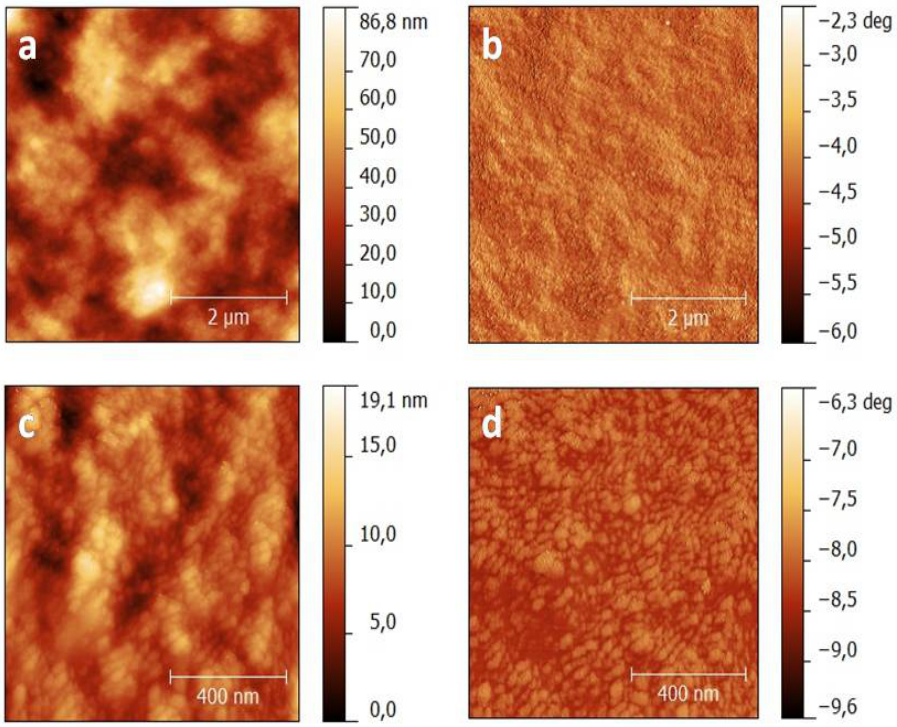

Figure 4.8: AFM images, topography and phase, of P3HT:$PC_{61}BM$ (1:1) thin film. a,b) area $5\mu m \times 5\mu m$ and c,d) $1\mu m \times 1\mu m$

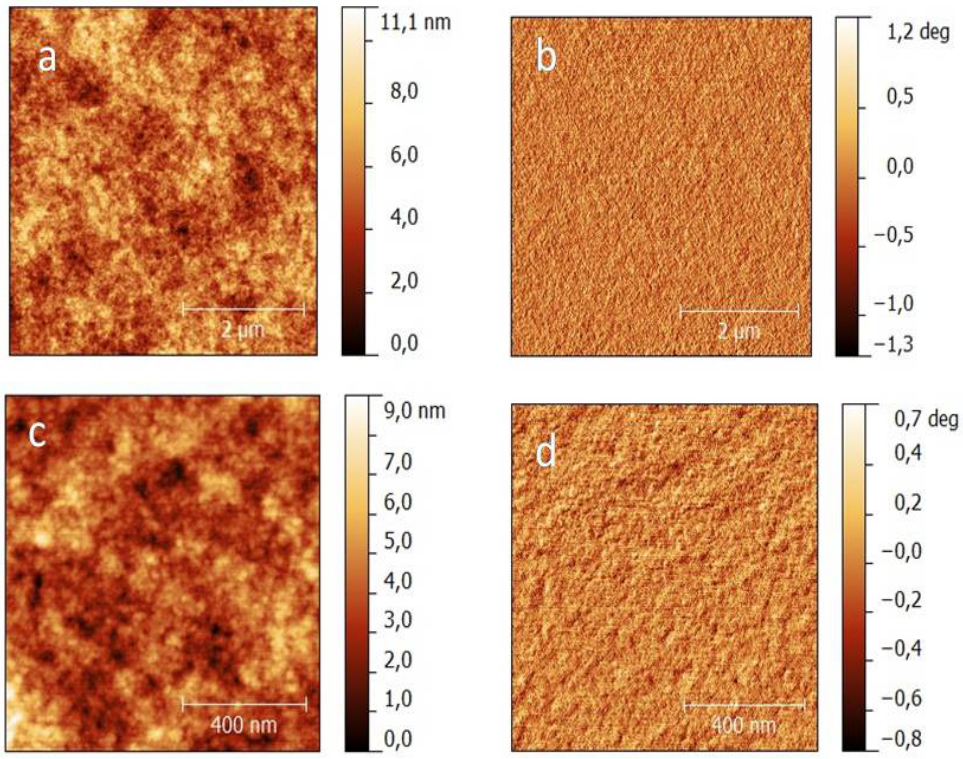

Figure 4.9: AFM images, topography and phase, of PTB7:$PC_{71}BM$ (1:1,5) thin film. a,b) area $5\mu m \times 5\mu m$ and c,d) area $1\mu m \times 1\mu m$

Diversely, the PTB7 has an amorphous character and the resulting BHJ morphology is expected to be smooth and almost featureless [182]. In Figure 4.9a and b are reported AFM images, topography and phase, of an area $5\mu m \times 5\mu m$ of the active layer based on PTB7. The morphology, indeed, appears smoother in comparison with to the P3HT case, the RMS is 1,1 nm and the height average is 4,2 nm. In addition, the solvent additive (DIO) acts as a good solvent for $PC_{71}BM$, further hindering the $PC_{71}BM$ aggregation and promoting a fine intermixing with the polymer chains, in agreement the featureless and smooth surface of the resulting film [176]. Chen *et al.* [182] describe the multiple-length-scale structural features of PTB7:$PC_{61}BM$ by means grazing incidence wide-angle X-ray scattering. It was shown that the films could form hierarchical nanomorphologies at with several nanometers of PTB7 nanocrystallites within hundreds of nanometers of intermixed amorphous PTB7-rich or $PC_{61}BM$-rich domains. This hierarchical nanomorphology is coupled to significantly enhanced exciton dissociation, which consequently contribute to photocurrent. Despite the fullerene used in this work is $PC_{71}BM$ instead of $PC_{61}BM$ a similar hierarchical behaviour of the morphology seems evident in smaller AFM images (Figure 4.9c), in good accordance with the high J_{sc} measured for the solar cells.

4.4 Thermal degradation of P3HT and PTB7 based solar cells

In order to study the effect of the high temperature and avoiding other sources of degradation, the thermal tests are carried out in dark and inert atmosphere. Following the standard protocols for testing the thermal stability of organic solar cells [152] the temperature of the test is fixed at 85^oC. The PV performances are monitored at certain interval times for a total period of 24h. After the test, the aged devices are characterized and compared with the fresh ones. The reported PV data are an average among 15 different cells obtained in two different laboratories. The errors are obtained for each single parameters from the standard deviation. The absolute error of 7%-10% in the PCEs reflects the reproducibility of the organic devices. Despite the error, the results are well consistent with the thermal degradation processes proposed.

4.4.1 Electrical characterization

The PV parameters of fresh and aged devices based on P3HT and PTB7 are reported in Table 4.2.

Active Layer	condition	$J_{sc}[mA/cm^2]$	V_{oc} [V]	FF [%]	PCE [%]
P3HT:$PC_{61}BM$	fresh	8,3 ± 0,5	0,59 ± 0,01	60 ± 4	2,9 ± 0,2
P3HT:$PC_{61}BM$	aged	7,9 ± 0,5	0,56 ± 0,01	52 ± 4	2,4 ± 0,2
PTB7:$PC_{71}BM$	fresh	14 ± 1	0,72 ± 0,01	59 ± 7	6,0 ± 0,4
PTB7:$PC_{71}BM$	aged	13 ± 1	0,64 ± 0,02	36 ± 5	3,0 ± 0,3

Table 4.2: PV parameters of P3HT and PTB7 based solar cells both fresh and aged for 24h at 85^oC in inert atmosphere

The P3HT solar cell shows a loss in PCE of just 17%, thus the active layer morphology can be considered thermal stable following the standard directives [152]. The main parameter affected by the high temperature is the FF, also the V_{oc} slightly decay while the J_{sc} is substantially unchanged, inside the error, during the thermal test. It is reasonable to supposed that charge collection process is altered affecting the shunt resistance but not the J_{sc}.
In the opposite aged PTB7 based solar cells shows relevant losses in the PCEs (50%). It is known that the thermal treatment of BHJ solar cells based on low energy-gap amorphous-type polymers yielding high power conversion efficiency, such as PTB7, causes serious deterioration of their photovoltaic performance [28], likely a suboptimal reorganization of the active layer.
To better understand the electrical behaviour of the BHJ devices under thermal stress, the evolution of the normalized PV parameters, as a function of the ageing time, is reported in Figure4.10

P3HT based solar cells show an initial increase of the J_{sc} and FF in the first 5 hours followed by a slight decrease. This behavior is in perfect agreement with the work of Bertho *et al.* [173] where they observed an increase in J_{sc} when the cells is annealed at 90^oC. Indeed, they suggest

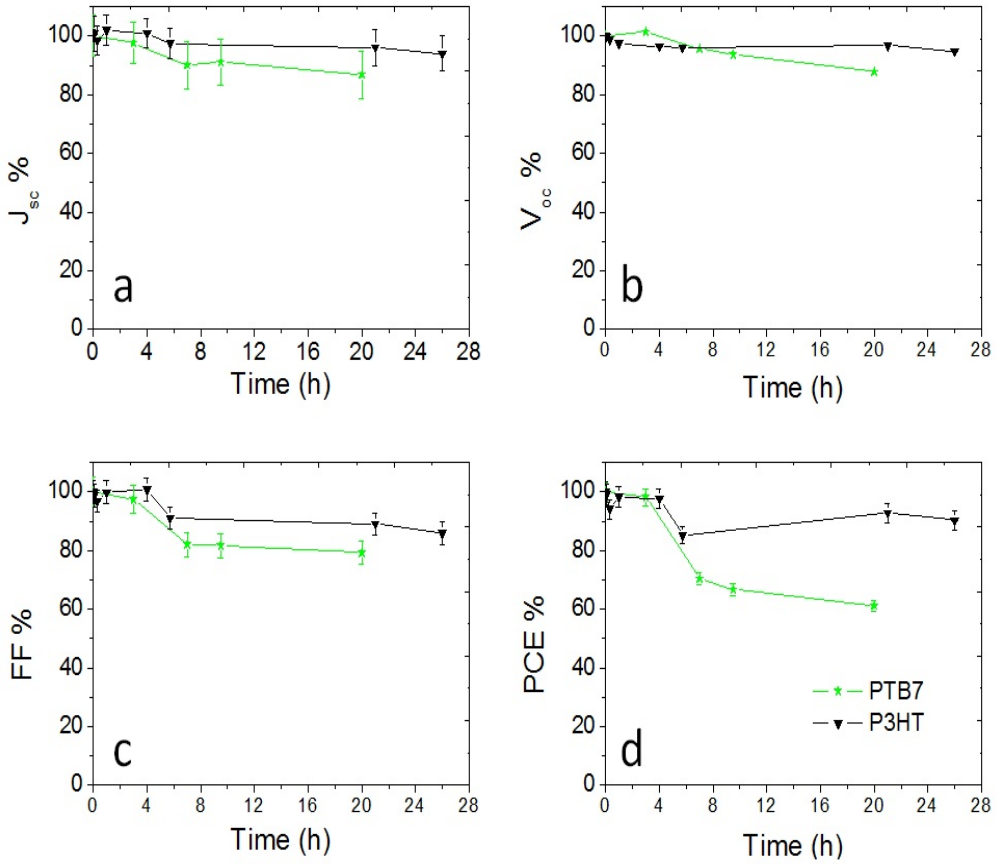

Figure 4.10: PV parameters decay during the thermal stress for both PTB7 (green) and P3HT (black) based solar cells.

a morphological reorganization of the P3HT domains into fiber-like structures, which enhance the charge transport properties and thus the J_{sc} of the corresponding BHJ blends. However the drop in PCE is mainly due to the V_{oc} and FF. What it is expected to occur is well described by Sachs-Quintana *et al.* [160], they observed a similar behaviour with a P3HT:$PC_{61}BM$ solar cells aged at 60^oC for 50h. They claimed that during the thermal stress a thin polymer layer is formed at the back contact, creating an electron blocking layer between the BHJ and the electron extracting electrode that, in a standard structure, can disturb the charge diffusion and collection.
On the contrary, the thermal degradation of PTB7 based solar cells is quite controversial. Tada [28] observed that, when PTB7:$PC_{71}BM$ processed without DIO is annealed at 80^oC in inert atmosphere, the PCE drops from 2,97% to 1,33% mainly due to a drop in J_{sc} and FF. The hypothesis, confirmed by transmission electron microscopy, affirms that the thermal annealing induces enlarged nearly- pure domains of the fullerene as well as the polymer, causing an increase of recombination of photocarriers yielding approximately 50% reduction in the PCE. However, when $PC_{71}BM$ is substituted whit C_{71} an improvement on the thermal stability was obtained. The C_{71} seems to suppress the aggregation of fullerenes and thus hinder the enlargement of nearly-

pure domains.

On the other hand Chun-Guey Wu *et al.*[183] reports that PTB7:$PC_{71}BM$ blended film processed with DIO is thermally sensitive. When the device is annealed at 100^oC for 30 minutes a drop in PCE of 20% is observed mainly due to a significantly decrease on the J_{sc}. The additive has a higher boiling point (T_b= 325^oC) compared to the CB (T_b = 131^oC) and it is a good solvent for fullerene, therefore during the film drying process, it allow PCBM to reorganize, resulting in better nanophase segregated structures[184]. Indeed, residual traces of additive can remain in the active layer and, under thermal stress, they can evaporate inducing a BHJ reorganization. Interesting, changing the solvent additive (DIO) with a solid compounds (2,3-pyridinediol) the thermal stability considerably increases with a loss in performance of just 3%. Its melting temperature is 245^oC, thus, neither under high temperatures of thermal stress, it will evaporate guaranteeing no changes in the active layer morphology.

The results obtained for the PTB7:$PC_{71}BM$ in the present work are partially in agreement with the literature. In fact in the first 8 hours is registered a drop in the performance that could be ascribed to a partial segregation between the D and the A phases within the active layer. The change in the D/A reorganization can also justify the decreased V_{oc} [141]. After the 8 hours the J_{sc} remains substantially constant, while the V_{oc} continue to decrease. As in the case of the P3HT a degradation at the interface between the electrode and the active layer is expected to occur.

4.4.2 Optical characterization

In order to understand the origin of the PV parameters decay for both devices the UV-visible absorption spectra of the active layers is registered before and after thermal degradation. The plots are reported in Figure 4.11

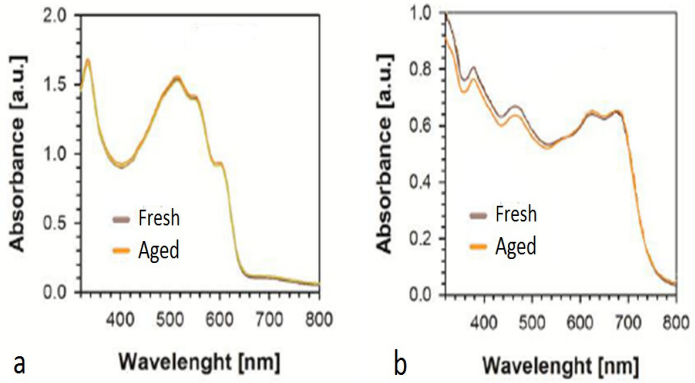

Figure 4.11: Absorption spectra of the active layers based on a) P3HT and b) PTB7 before and after thermal stress.

From the PV parameters decay of P3HT based solar cells no relevant variations in the optical proprieties of the active layer are expected. In fact, before and after the thermal test, the absorption spectra of the P3HT:$PC_{61}BM$ blend perfectly overlap. The annealing step at 110^oC after the

active layer deposition allows to form P3HT crystalline phase and improves the active layer thermal stability.
In the opposite the PTB7 based blend shows a slight variation on the absorption spectra suggests a reorganization in the blend morphology [141] [185] in agreement with the decay of the PV parameters. The main variation is localized in the high energy portion of the spectrum, while the tails of the absorption doesn't change. This suggests that the PTB7 remain mainly in an amorphous conformation, while the fullerene molecules probably start to aggregate.
Despite the absorption measurement is an interesting tool that gives qualitative information about relevant variations in the bulk of the active layer, it is not enough sensitive to reveal surface modifications and/or slight morphological changes.

4.4.3 Morphological characterization

To validate the hypothesis formulated from the electrical (Table 4.2 and Figure4.10) and the optical characterization, the AFM and KPFM techniques have been employed, to explore the surface morphology of both polymer based blends, before and after degradation. Despite the high resolution of the AFM technique which allows to observe morphological features at nanoscale level, it doesn't provide information about the phase segregation of the BHJ components. However, using a conductive tip it is possible to overcome this kind of limitation. In fact the KPFM images obtained at the same time and in the same region of the AFM images give information about the surface potential which is expected to be different for D and A domains [186].
Note that, the absolute value of the surface potential obtained from the KPFM cannot be used for a quantitative analysis. However the scale of colours are adjust to the same interval allowing to compare images for a qualitative analysis.

The AFM images of fresh and aged P3HT based blends are reported in Figure 4.12. As expected slight changes of BHJ morphology are observed. The RMS passes from 14,4 nm for the fresh active layer to 15,6 nm for the aged device (Table 4.3). This result correlates well with the optical characterization and the J_{sc} decay, while it does not give information about the variation of the other PV parameters. In this view the KPFM images (Figure 4.13) help to further clarify the degradation processes occurred in the P3HT based blend. For the fresh device the KPFM image (Figure 4.13b) shows the same morphology of the AFM image (Figure 4.13a). The different potential of the BHJ components clearly identifies the two species: the red regions, with a high surface potential, corresponds to polymer-rich domains, while the blue ones, with a low surface potential, are based on fullerene-rich areas [186]. Note that the green area likely represents an intermix between the two species that exhibits an intermediate value of surface potential.
Diversely, the KPFM and AFM images of aged P3HT based device are quite different (Figure 4.13c and d). The distribution of the potential does not reflect the AFM image, indeed the domains are poorly defined, while in the AFM images large aggregates can be identified. This result suggests that most of the domains are based on the same material (polymer), which could be in agreement with the formation of a skin layer of P3HT at the top of the active blend during thermal degradation [160].

Active Layer	Conditions	Heights average [nm]	RMS [nm]
P3HT:$PC_{61}BM$	Fresh	36	14,4
P3HT:$PC_{61}BM$	Aged	38,6	15,6

Table 4.3: Morphological parameters of P3HT based solar cells both fresh and aged for 24h at 85^oC in inert atmosphere

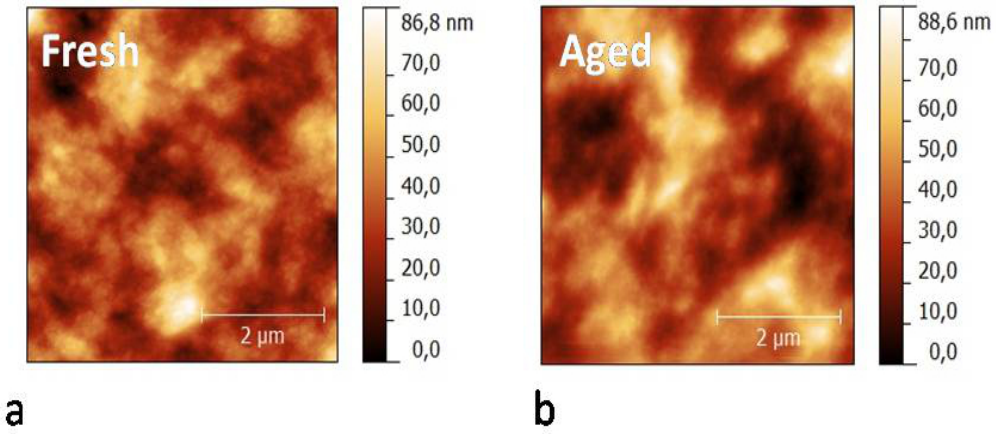

Figure 4.12: AFM images of the P3HT based solar cells a) fresh and b) aged

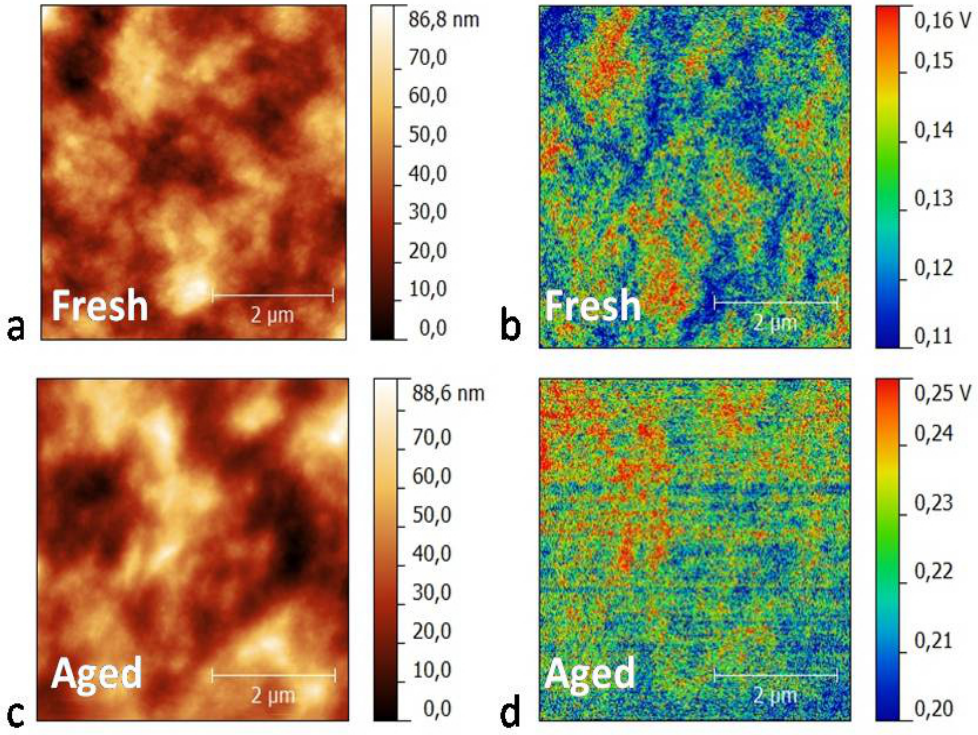

Figure 4.13: AFM images $5\mu m \times 5\mu m$ of P3HT active layer a) fresh and c) aged. Corresponding KPFM images b) fresh and d) aged.

On the other hand, during thermal degradation a modification of the D A intermixing is expected for the PTB7 based active layer. Figure 4.14a and b show the AFM images (size: $5\mu m \times 5\mu m$)of the fresh and aged PTB7 based device, which seem do not reveal evident changes of the nanoscale morphology. However, reducing the area of the scanning (Figure 4.14 c and d, size: $1\mu m \times 1\mu m$) clear variations of the BHJ film become evident.
As discussed, what it is expected that the annealing induces the formation of D and A rich-domains mainly due to the agglomeration of $PC_{71}BM$. From the AFM it is difficult to discriminate this behaviour. Interestingly, when the KPFM images are compared to the corresponding AFM images, the complementary information allow a better understanding of the involved processes. Similarly to the AFM, the KPFM images of fresh and aged device on a relatively large area, does not reveal evident changes or specific features of the active layer (Figure 4.15a and b respectively). Even in this case, KPFM images on a smaller scale exhibits appreciable differences (Figure 4.16). Despite the absolute value cannot be used to compare the results, the same width in the potential distribution was used for the color scale. This allows to discriminate the D rich domains (red) to the A rich domains (blue). Interestingly, in the aged device more separated phases appear evident in good accordance with the previous hypothesis.

Active Layer	Conditions	Heights average [nm]	RMS [nm]
PTB7:$PC_{71}BM$	Fresh	4,2	1,1
PTB7:$PC_{71}BM$	Aged	5,3	1,2

Table 4.4: Morphological parameters of PTB7 based solar cells both fresh and aged for 24h at 85^oC in inert atmosphere

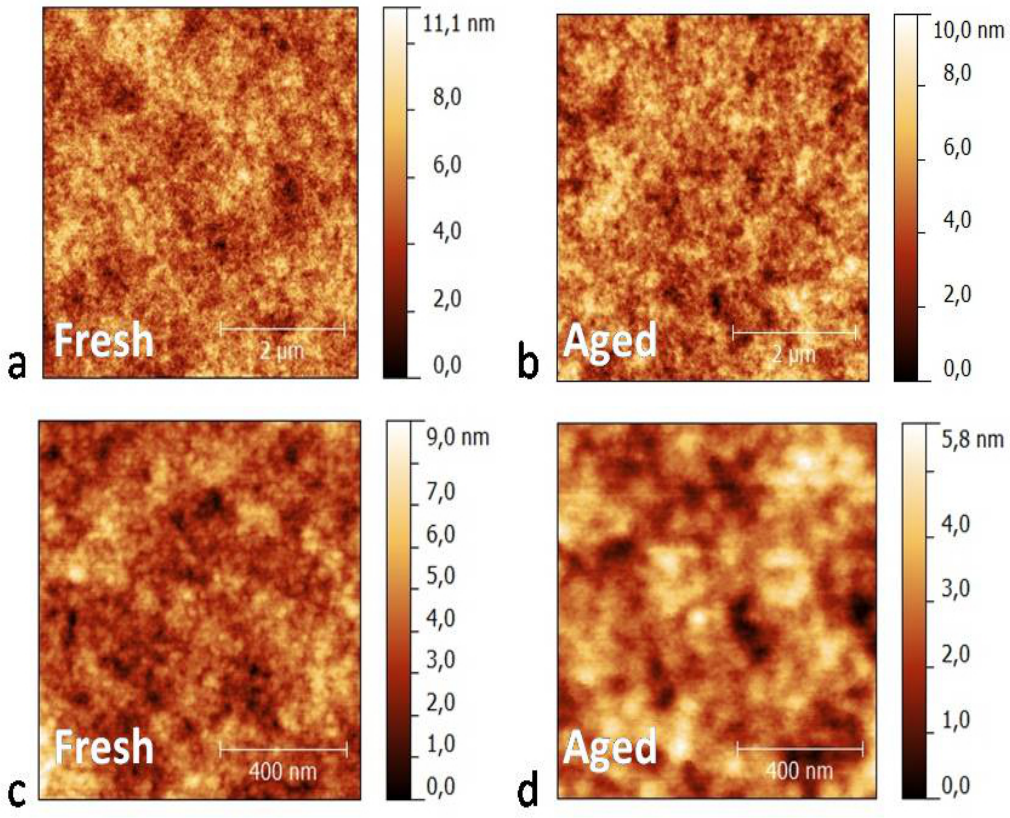

Figure 4.14: AFM images of PTB7 based solar cells on the right fresh active layer while on the left aged .

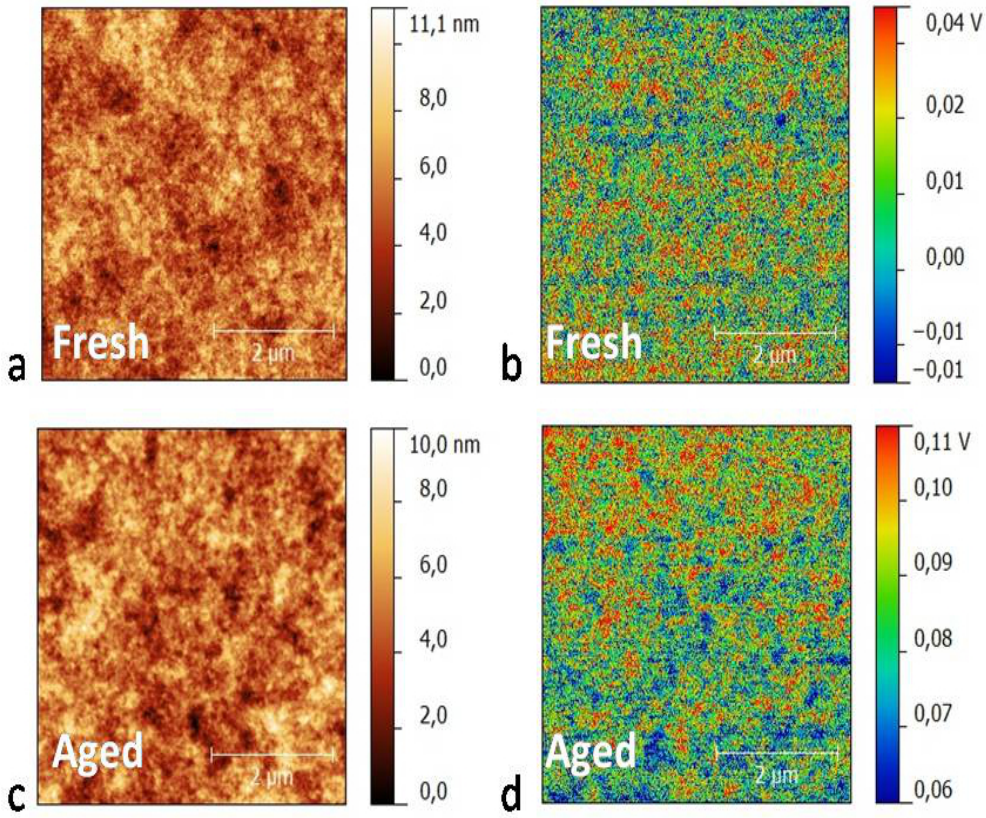

Figure 4.15: $5\mu m \times 5\mu m$ AFM images of PTB7 active layer a) fresh and c) aged. Corresponding KPFM images b) fresh and d) aged.

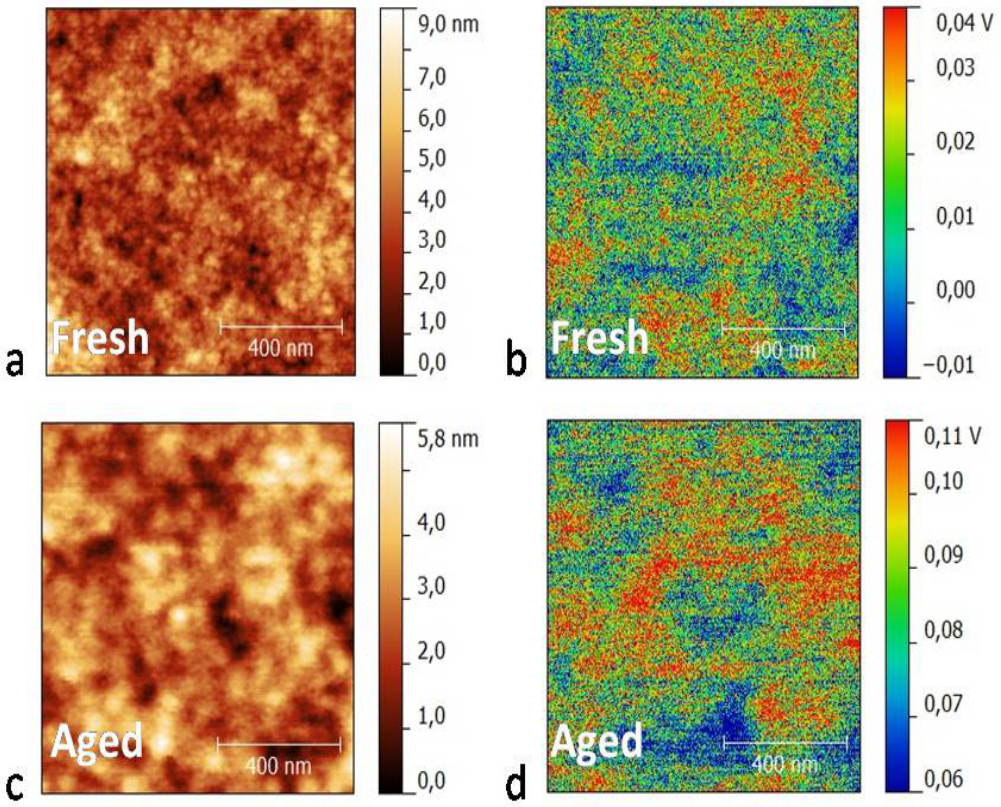

Figure 4.16: $1\mu m \times 1\mu m$ AFM images of PTB7 active layer a) fresh and c) aged. Corresponding KPFM images b) fresh and d) aged.

4.5 Conclusion

In conclusion the thermal degradation of P3HT and PTB7 based solar cells have been studied. The highly crystalline polymer shows a better thermal stability mainly because the best active layer morphology is obtained with an annealing step during the process fabrication. This step not only leads to high performance but also to a more thermally stable morphology at temperature stress of 85^oC. Note that when the film morphology is not well optimized both the performance and the thermal stability can be affected [76].

On the other hand the best performing PTB7 based solar cell shows a poor thermal stability. The amorphous behaviour of the PTB7 leads to a less stable active layer morphology. Moreover the use of the additive in the fabrication process has a positive effect in the initial performance, but it results detrimental for the thermal stability. The main degradation process involved is the fullerene aggregation, which is likely facilitated in a soft matrix of an amorphous polymer. Note that after a certain time (8-10hours) the reorganization reaches a thermally stable morphology that leads to a final PCE of 3,0% considerably lower than the initial one, but comparable with the P3HT based solar cells.

In conclusion, the highly efficient solar cells are not necessarily thermally stable. In view of a commercial product a correct compromise between stability and efficiency has to be reached before getting into the market.

5

Thermal degradation effects on operating devices

5.1 Influence of internal interfaces on thermal degradation

In the previous Chapter was showed how the thermal behaviour of the active layer is a crucial aspect for the thermal stability of the corresponding solar cells. The main degradation mechanism is the reorganization of the blend morphology. The process can involve the surface and thus the interfaces with the electrodes, or it can be a bulk reorganization. In both cases the main parameters responsible for the degradation is the solid state organization: crystalline against amorphous. In general this behaviour is connected with the T_g^{blend} [164]. However it is difficult to determine this value, being related to many factors. Recent studies have demonstrated that the different active layer morphology and thickness can have impact on the T_g^{blend}, however this value can be influenced also from the nature of the underlying substrate. For example Liu *et al.* [187] observed different T_g of an amorphous conjugated polymer when is deposited on Si-SiOx substrates with respect to the same films coated on the top of the PEDOT:PSS surface. Moreover, different values of T_g^{blend} were observed at the surface with respect to the bulk, confirming that the interactions occurring at the interface are crucial for thermal degradation processes. The influence of the adjacent layers on the thermal behaviour of a solar cells becomes evident when a standard structure is compared to an inverted one. Devices based on the same active layer (P3HT or PCDTBT) were used to demonstrate that the inverted structures result more thermally stable than the standard (Figure 5.1) [160]. In fact, for both active layers the thermal degradation induces a vertical segregation and a thin polymer layer is formed at the back contact, creating an electron blocking layer that is detrimental for the standard structure, but not harmful for the inverted device.

5.1.1 Role of buffer layers

The effects of thermal degradation on an operating device don't concern just the active layer but can involve also buffers layers. A clear example is obtained comparing the thermal stability, at 85^oC for 150 hours in dark and in inert atmosphere, of three different solar cells based on the same

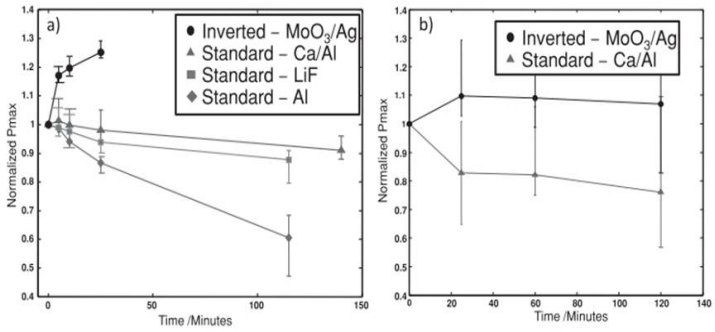

Figure 5.1: Thermal degradation at 65^oC of a) P3HT:$PC_{61}BM$ and b) PCDTBT:$PC_{71}BM$ devices with different back contacts [160]

active layer.

The device structure used is ITO/PEDOT:PSS/P(3):$PC_{61}BM$/HBL/Al. The devices differ only in the HBL while the other layers are identical. The HBLs chosen are LiF and two formulation of ZnO nanoparticles (ZnO^A and ZnO^B). The details of ZnO formulation are confidential, they differ on the solvent used for the nanoparticles dispersion and on the stabilizing additive, while the nature of the nanoparticles and their dimensions are the same. In Table 5.1 are reported the PV parameters of fresh and aged devices. The results are an average of 6 devices and the error is calculated from the standard deviation. Note that the initial performance of the different devices are comparable between them, thus allowing a good comparison.

HBL	Conditions	$J_{sc}[mA/cm^2]$	V_{oc} [V]	FF [%]	PCE [%]	ΔPCE
LiF	Fresh	9,5 ± 1	0,815 ± 0,005	56 ± 3	4,3 ± 0,3	
	Aged	4,4 ± 0,4	0,670 ± 0,003	50 ± 1	1,5 ± 0,2	- 65%
ZnO^A	Fresh	10,3 ± 0,5	0,805 ± 0,005	49 ± 5	4,1 ± 0,4	
	Aged	10,2 ± 0,4	0,765 ± 0,005	45 ± 4	3,4 ± 0,2	- 15%
ZnO^B	Fresh	10,5 ± 0,1	0,805 ± 0,005	51 ± 1	4,3 ± 0,2	
	Aged	6,8 ± 0,5	0,770 ± 0,005	42 ± 1	2,2 ± 0,1	- 49%

Table 5.1: PV parameters of the solar cells based on different HBLs before and after thermal test

When LiF is used as HBL a loss in PCE of 65% is observed after the thermal test. The main parameter affected is the J_{sc} passing from 9,6 mA/cm^2 to 4,4 mA/cm^2. As expected, the high temperature likely induce the LiF dissociation, the Li^+ atoms percolate into the active layer and form the complex $PC_{61}BM^- : LiF^+$ causing the performance degradation [156]. Diversely, when ZnO NPs are used as HBL, a different thermal degradation mechanism is expected. Interestingly,

despite the ZnO^A and ZnO^B formulations are based on the same nature and dimensions of the nanoparticles their thermal behaviours are very different. The solar cells based on the first formulation ZnO^A shows good thermal stability with a loss of PCE of just 15%, while devices based on ZnO^B show a loss in PCE of almost 50%. The V_{oc} of both devices has the same drop, the values pass from 0,81V to 0,77V. This reduction can be correlated with the same aspect: it was found that high temperature can increases the WF and decrease the conductivity of ZnO films [188] in agreement with the observed variation in V_{oc}. Note that the energetic properties of the ZnO are correlated with the nature of NPs, thus, as the two formulation are based on the same material, the same behaviour is expected. However, observing all PV parameters, in particular the J_{sc}, the two devices present a different thermal degradation. In the device based of ZnO^A the J_{sc} doesn't change after degradation, suggesting that the active layer morphology and the ZnO^A are thermally stable. On the opposite when ZnO^B is used as HBL the J_{sc} decreases from 10,5 mA/cm^2 to 6,8 mA/cm^2. These results clearly suggest that the ZnO layers (A and B formulations) are the main responsible for the thermal degradation of the corresponding devices, since the active layers of both devices have been processed using identical conditions. It is reasonable to assume that during the heating process, residual traces of additive/solvents/dopants in the ZnO^B layer, diffuse into the adjacent BHJ layer likely determining the reduction of the performance. Additional tests to clarify the involved mechanisms are currently underway.
In conclusion, despite the active layer was demonstrated to be thermally stable, the stability of the different operating devices is strongly influenced by the nature/intrinsic properties of the HBL. Thus, in addition to the T_g^{blend}, the thermal behaviour of the buffer layers is another essential parameters to evaluate the device stability.

5.1.2 Confinement effect

As above mentioned it is clear that the thermal behaviour of a solar cell depends on the contribution of each layer and interface. To this end, in order to properly evaluate the thermal stability of a working solar cell, it is mandatory to analyse the whole device. However common techniques used to study aged devices not always are able to give a complete description of the mechanisms induced by the temperature. A clear example is represented by AFM and KPFM techniques. As showed in Chapter 4, the changes on the surface morphology of the active layer give important information on the occurring degradation processes, however not always the investigated areas is representative of the device behaviour. In fact, for solar cells the crucial regions of the active layer are located under the electrode, not accessible from AFM measurement. To clarify this concept, a representative example is reported.
A solar cell based on a Merck's D polymer (chemical structure is confidential) shows a good thermal stability after an annealing at 85^oC in dark in inert atmosphere for 150 hours (Table 5.2).
The device structure used is ITO/ZnO/Active Layer/MoO_3/Ag. The PV parameters and the JV curves for the fresh and aged are reported in the Table 5.2 and Figure 5.2.

The PCE loss is less than 20%, the J_{sc} passes from 11,7 mA/cm^2 to 11,0 mA/cm^2 suggesting that no relevant morphological changes of the active layer are expected. However using a standard morphological characterization unexpected results are found. The AFM images of the fresh and

Condition	$J_{sc}[mA/cm^2]$	V_{oc} [V]	FF [%]	PCE [%]
Fresh	11,7 ± 0,3	0,780 ± 0,005	68 ± 2	6,2 ± 0,1
Aged	11,0 ± 0,04	0,73 ± 0,01	62 ± 2	5,0 ± 0,2

Table 5.2: PV parameters of the representative solar cells before and after the thermal test

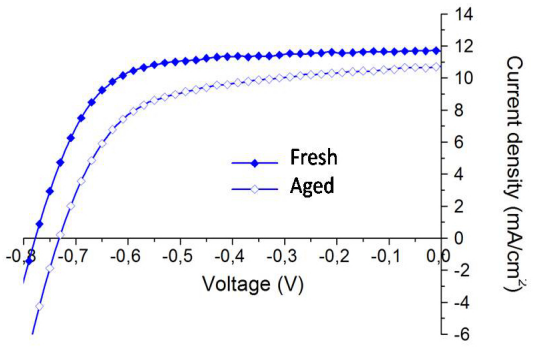

Figure 5.2: JV curve of the representative solar cell before and after the thermal stress.

aged device, reported in Figure 5.3, show that after the thermal ageing the morphology of the active layer is drastically changed. Large domains on the order of few μm are formed, the optimal intermix between D and A interface observed in the fresh active layer, is completely loss in the aged device. In light of this results, it may be surprising that such drastic morphological changes (in the area outside the top metal electrode) occurring with thermal ageing do not correspond to drastically reduced OPV performance of the solar cells.

In order to justify this apparent incongruence an alternative technique is used to map the active layer morphology: the Laser Scanning Confocal Microscopy (LSCM). The main limitation of this technique is that the resolution is limited by the wavelength of the laser used, in this case the resolution is around 200 nm. In a fresh device the LSCM image cannot resolved the D and A domains typically in the range of nm, but in the aged device, when the domains become much bigger, they can be appreciated. Despite the resolution, the main advantage of this technique is the possibility to investigate the active layer in the operating device. The LSCM images of the aged solar cells both outside and under the electrode are reported in Figure 5.4 a and b respectively. The two images are very different between them: outside the electrode the same big crystal observed in the AFM image are presented, while under the electrode the morphology appears homogeneous and almost featureless correlating well with the PV parameters of the aged device.

This result is a clear example of the so called "confinement effect": the interactions at the organic/electrode interface could strongly stabilize the active layer morphology and influence the reorganization of the BHJ blend in the device during ageing [169]. In this sample this interaction

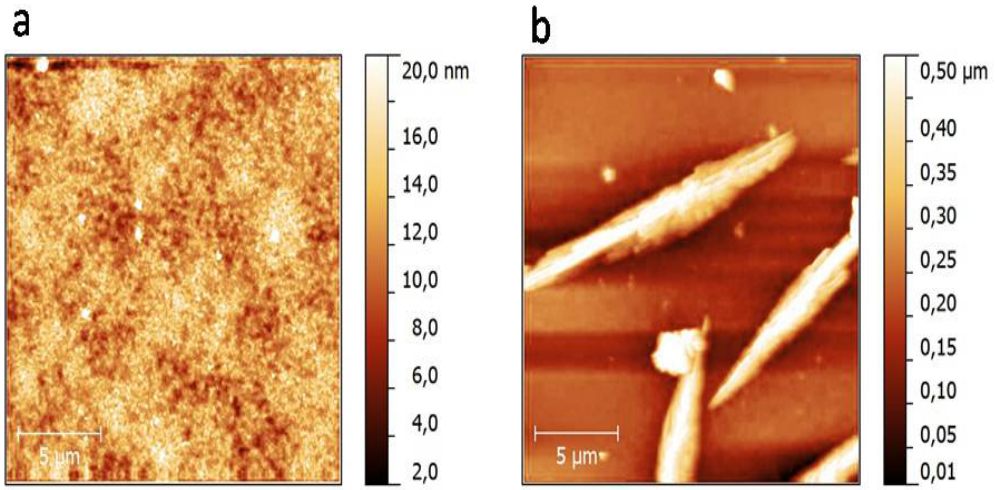

Figure 5.3: AFM images of the representative solar cell a) before and b) after the thermal stress.

seems to be stronger than the polymer interchain ones, thus hindering the formation of the rod-like aggregates which would be otherwise favoured.

In conclusion the thermal stability of a solar cells strongly depends both from the active and the buffer layers, as well as from the interface between them and the electrode. For this reason, in-line techniques, able to investigate the whole operating device, are essential to properly characterize the effect of temperature on operating devices.

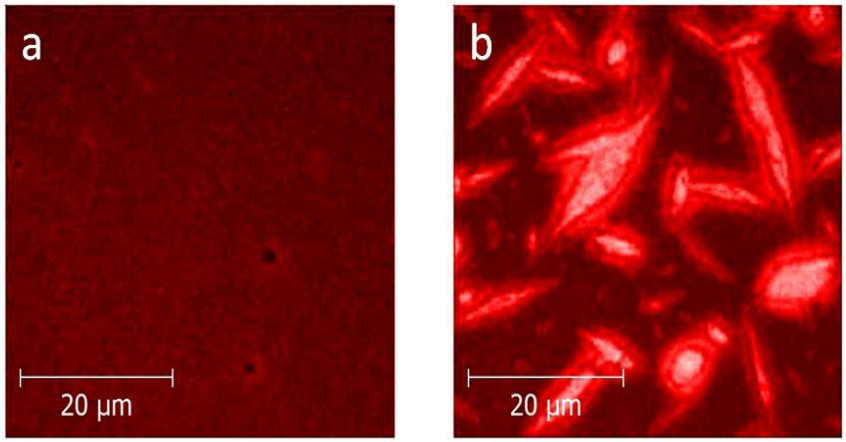

Figure 5.4: LSCM images of the representative solar cell after the thermal stress, a) outside and b) under the electrode

5.2 How to predict the device thermal stability

An innovative technique, based on a capacitance measurement on a working device, allows to predict the maximum limit temperature for a stable solar cell [76].

Four different BHJ solar cells with different thermal behaviour were selected from the work of Tessarolo *et al.* [76]. The thermal test is based on monitoring the performance decay during an annealing at 85^oC for 24 hours in dark and inert atmosphere. The solar cells differ just in the D polymer used, their polymer structures, reported in Chapter 2 Figure XX, are also depicted in Figure 5.5. In details P(2) FQ-BDT-4TR is a D polymer already reported in Chapter 3, P(8) is the PTB7 studied in the previous Chapter, while P(9)PTT-MIM and P(10) PBnDT-FTAZ are two new D polymer based on different backbone.

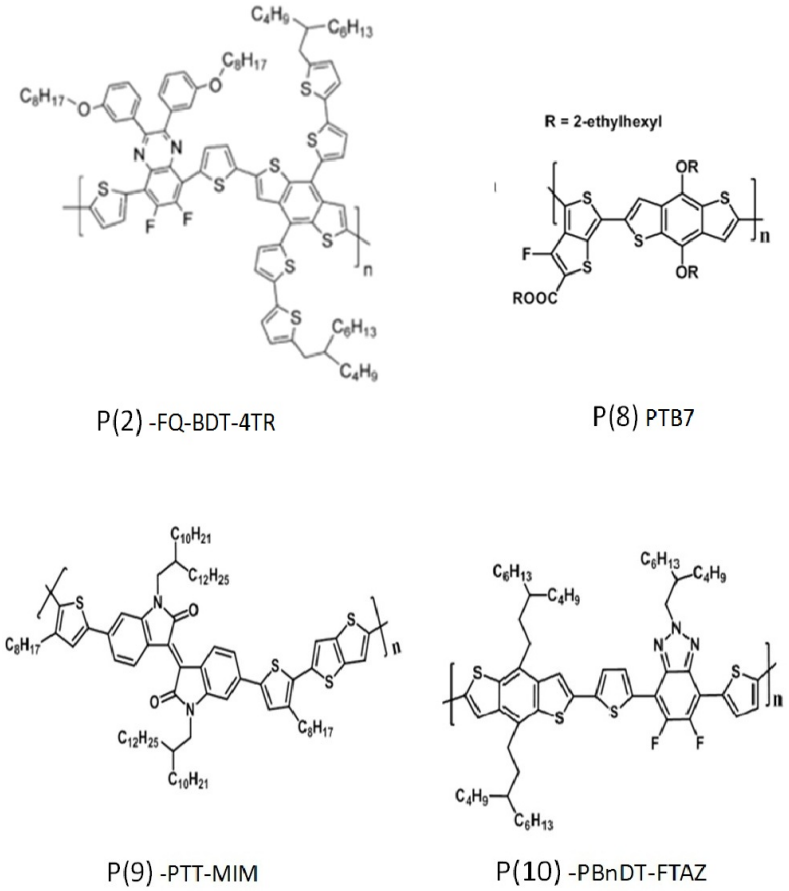

Figure 5.5: Chemical structure of P(2) FQ-BDT-4TR, P(8)-PTB7, P(9)PTT-MIM and P(10) PBnDT-FTAZ used as D polymer in the solar cells.

5.2.1 Devices Fabrication

The device stack used for all devices is ITO/PEDOT:PSS/ActiveLayer/ZnO/Ag. The PEDOT:PSS is spin coated over the ITO surface to form a thin layer ($\sim 35nm$) and annealed at 150^oC for 15

minutes to eliminate any residual water, then the devices are moved into the glovebox to deposit the other layers. The active layer of the first device is based on a solution of P(2):$PC_{61}BM$ in ratio 1:1 wt/wt dissolved in ODCB. The layer is deposited with spin coater following the procedure reported in literature [75] without an additional annealing. The Active layer of the second device is based on PTB7:$PC_{71}BM$ in ratio 1:1,5 wt/wt. The deposition conditions are described in the previous Chapter. The device based on the P(9) is obtained from a solution of P(9):$PC_{61}BM$ in ratio 1:1,5 wt/wt dissolved in a mixture of ODCB and DIO (98:2 v/v). The layer is deposited via spin coater at 700 rpm for 120 seconds, without any addition annealing. In the end the last device is based on active layer of P(10):$PC_{61}BM$ in ratio 1:2 wt/wt dissolved in ODCB deposited at 1500 rpm for 10 seconds. The resulting film is still wet and it is leaved to dry in a petri dish without cover for 30 minutes. Then it is annealed at 110^oC for 10 minutes. Over the active layers, a film of 50 nm of ZnO is deposited via spin coater inside the glovebox. In the end the cells are moved into the metal evaporator directly connected to the glovebox, then 100 nm of Silver were evaporated at 10^{-6} mbar at a rate of 1 nm/s to inhibit any atoms percolation. The PV parameters of fresh devices are reported in Table 5.3. The results obtained for P(2),P(9) and P(10) based solar cells are an average on 6 devices, while P(8) based device was investigated in more details, thus the values, obtained from an average on 15 devices, are slightly different, but still consistent, from the reference paper [76]. It should be noted that the initial PCEs of P(2) and P(10) based solar cell are considerably lower than the corresponding values reported in literature (5,3% and $\sim$ 6% [189] respectively). The main reason of this discordance is that different batches with different M_w were used, moreover the replacement of LiF with ZnO as buffer layer, can altered the PV performance. However the achievement of "hero" efficiency is out of the aim of this work, while it was preferred to selected different thermal behaviour in order to cover all the possible cases, from completely unstable to highly stable devices.

5.2.2 Standard thermal degradation test

The standard thermal test is performed at 85^oC following the procedure reported in literature [152]. The test is carried out inside the glove-box to prevent interactions of devices with oxygen and/or moisture. The test runs for 20 hours and the solar cells are illuminated to monitor the OPV performance for a total period shorter than 30 minutes, allowing to neglect the initial burn-in light induced degradation [190].

Table 5.3 summarizes the OPV response data, before and after thermal degradation, of the different polymer based BHJ solar cells. To better analyse the trend of the OPV performance of each device, normalized PCE, V_{oc}, J_{sc} and FF, as function of time are reported in Figure 5.6. Fitting of the PCE data was carried out using an exponential decay: $PCE = PCE_f + (1 - PCE_f)exp(-t/\tau)$, where t represents the experiment time, PCE_f is the final value attained by the efficiency and accounts for the percentage of the initial efficiency preserved after thermal degradation, while the time constant τ is the lifetime at which the efficiency value is decreased by a factor e, and allows to compare the kinetic of the PCE decay of each samples. The PCE_f and τ values are reported in Table 5.4.

The most stable device is based on the polymer P(2) as shown in Figure 5.6. The drop in normalized

Active Layer	Conditions	$J_{sc}[mA/cm^2]$	V_{oc} [V]	FF [%]	PCE [%]
P(2):$PC_{61}BM$	Fresh	7,3 ± 0,3	0,890 ± 0,005	47 ± 2	3,1 ± 0,2
	Aged	7,5 ± 0,3	0,82 ± 0,02	46 ± 3	2,9 ± 0,2
P(8):$PC_{71}BM$	Fresh	14 ± 1	0,72 ± 0,01	59 ± 7	6,0 ± 0,4
	Aged	13 ± 0,4	0,64 ± 0,02	36 ± 5	3,0 ± 0,3
P(9):$PC_{61}BM$	Fresh	8,8 ± 0,2	0,76 ± 0,01	50 ± 1	3,4 ± 0,2
	Aged	7,8 ± 0,3	0,51 ± 0,04	37 ± 3	1,5 ± 0,2
P(10):$PC_{61}BM$	Fresh	8,3 ± 0,7	0,78 ± 0,01	44 ± 1	2,8 ± 0,3
	Aged	/	/	/	/

Table 5.3: PV parameters of the solar cells based on different BHJ before and after thermal test

PCE is only of 7% after 20 hours at 85^oC. For this polymer all the photovoltaic parameters remain constant during the experiment time, negligible thermally-induced morphological changes are expected to occur. In the other extreme, devices fabricated with P(10) degraded very fast: after 1 minute of thermal stress PCE drops to 65% of the initial value by the fast initial decay in J_{sc} and FF, leading to a very low efficiency after only 15 minutes, no photovoltaic response was obtained after the 20 hours. For P(10) based solar cell important morphological reorganization are supposed, but the drastically drop in performance not allows to investigate properly the mechanism occurred.

Devices fabricated with the D polymers P(8) and P(9) show an intermediate behaviour between these two border cases. As already discussed in Chapter 4 the P(8) (PTB7) based device shows a drop in PCE from an initial value of 6% to a value of 3% after 20 h. The main factor influencing the degradation trend is FF, which drastically decreases due to an increased series resistance in the device, which could be ascribed to a partial segregation between the D and the A phases within the active layer.

In the end, the P(9) based solar cells shows a drop in PCE from 3,4% to 1,5% mainly due to a decrease in FF and V_{oc}. In particular seems that two degradation processes are taking place: one occurred in the first 5 hours which affects FF due to an increase in the series resistance in the device, and a second, with a slower kinetic, mostly affecting V_{oc}.

5.2.3 Capacitance based thermal test

The four solar cells are a representative group of device with different thermal behaviour. They can be used to demonstrate the working principles and the reliability of the innovative thermal test based proposed [76]. The new method consists on the detection of the whole device capacitance variation as a function of temperature (C-T). This approach is based on the model proposed by

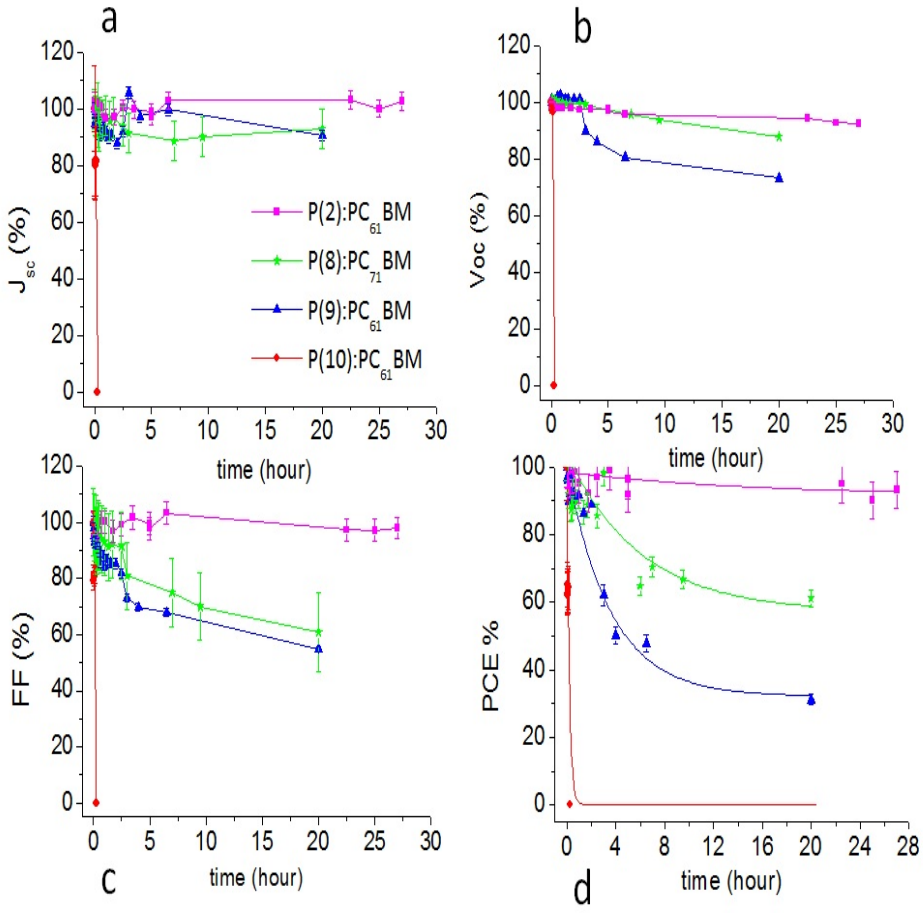

Figure 5.6: PV parameters decay of the 4 BHJ solar cells based on P(2) (magenta), P(8) (green), P(9) (blue), P(10) (red).

Lungenschmied *et al.* [191] where the C_g is used to monitor morphological changes in operating devices. C_g can be expressed by the equation $C_g = \epsilon\epsilon_0 A/d$ where A is the area of the device, d is the thickness of the active layer, ϵ_0 the dielectric constant of vacuum and ϵ the static permittivity of the active layer. When the temperature is increased two phenomena can influence C_g due to significant morphological modifications of the active layer: i) variation of the active layer thickness (d) [192] [171], and ii) change in the dielectric properties of the blend (ϵ) [193][194]. The correct conditions to measure the C_g are obtained from the MS analysis (Section 5.3.2). Once selected the correct frequency and applied voltage, devices are introduced in an oven with a heating ramp of 1 ^oC/min and capacitance is monitored every 10 seconds. The variation of capacitance with respect to temperature for all P(2)-P(10) based devices is reported in Figure 5.7. All the curves have been smoothed and normalized at their maximum to simplify their comparison.

For all devices, except the specific case of P(10) based solar cell, the C-T curves show an initial rise after which capacitance reaches a maximum value, in correspondence to a temperature defined

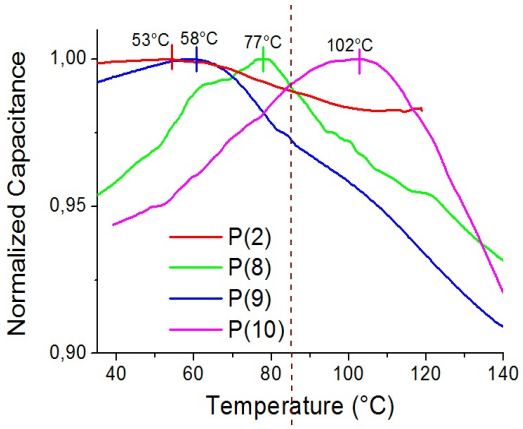

Figure 5.7: C-T curve for P(2)(magenta), P(8) (green),P(9) (blue) and P(10) (red) based devices. The brown dash line indicates the temperature of the thermal life test (85^oC). The maximum of the Capacitance-Temperature (T_{MAX}) is indicated in the graph for each system [76].

as T_{MAX} (Table 5.4), and then capacitance starts to decrease. The initial rise is in agreement with previous work on P3HT [192] and PCDTBT [171] based solar cells, where, increasing the annealing temperature, a reduction of the active layer thickness is observed as a consequence of an increased phase-separation of the BHJ components and possibly to residual solvent loss, resulting in an overall reduction of the free volume of the BHJ films. Moreover Pearson *at al.* [195] observed that the PEDOT:PSS layer has a thickness contraction in the low temperature range up to 70^oC, which can partially contribute to the initial rise of C_g. A further increase in the temperature above the T_{MAX} gives rise to a capacitance decrease. This fact could be attributed to additional physical or chemical processes occurring in the active layer and/or at the active layer/electrode interface which could modify the dielectric permittivity of the layer and/or the thickness of the active layer. Regardless the degradation process involved the presence of this maximum indicates that significant morphological rearrangements occur in the active blend in relation with the onset of the thermal stability.

The T_{MAX} values extracted from the C-T measurements correlates well with the thermal degradation behaviour of the devices observed during the performance thermal tests. Indeed, by plotting the PCE_f and τ values, calculated from the PCE decays during the thermal stress at 85^oC, versus the corresponding T_{MAX} obtained from the C-T measurements (Figure 5.8) for all devices, a clear and direct correlation is found. In conclusion devices show to be thermal stable when the temperature of the thermal stress is below the T_{MAX}, while above the T_{MAX} PV performance start to worsen.

Active Layer	PCE_f (%)	τ (hours)	$T_{MAX}(^oC)$
P(2):$PC_{61}BM$	92 ± 6	15 ± 3	102 ± 5
P(8):$PC_{71}BM$	46 ± 12	9 ± 3	77 ± 3
P(9):$PC_{61}BM$	32 ± 4	3,5 ± 1	58 ± 5
P(10):$PC_{61}BM$	0	0,2	53 ± 7

Table 5.4: PCE_f and τ parameters calculated from the exponential fitting of the PCE decay and T_{max} obtained from the C-T curve. The errors are derived from the fitting, while the error of T_{MAX} is higher for the broader peaks.

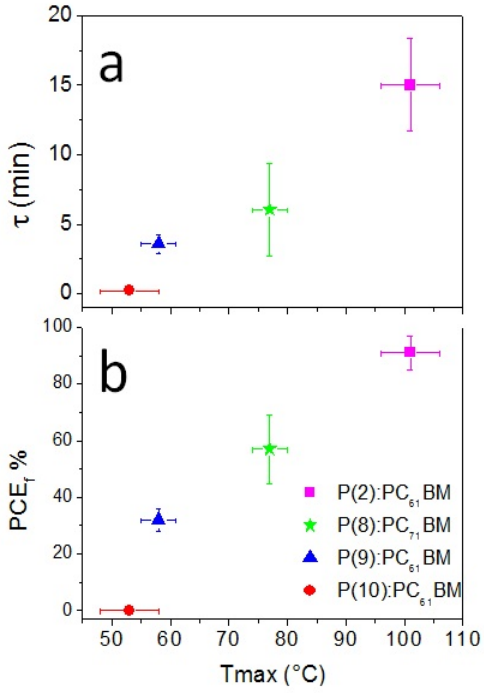

Figure 5.8: Correlation between T_{MAX} and parameters extracted from life test at 85^oC: a) Proportion of initial efficiency preservation (PCE_f) after thermal degradation and b) time constant τ calculated from the PCE decay [76].

5.3 Investigation on thermal degradation mechanisms

The innovative thermal test based on a capacitance value is an interesting tools able to predict the limit temperature for a stable solar cell. However it doesn't give accurate information about the mechanisms involved into the degradation process. To have a reliable description about the phenomena, additional measurements, based on specific technique able to analysed the whole device in operating conditions, are needed. A preliminary study on the thermal degradation occurred on the devices under investigation is reported in the followed sections.

5.3.1 Optical characterization

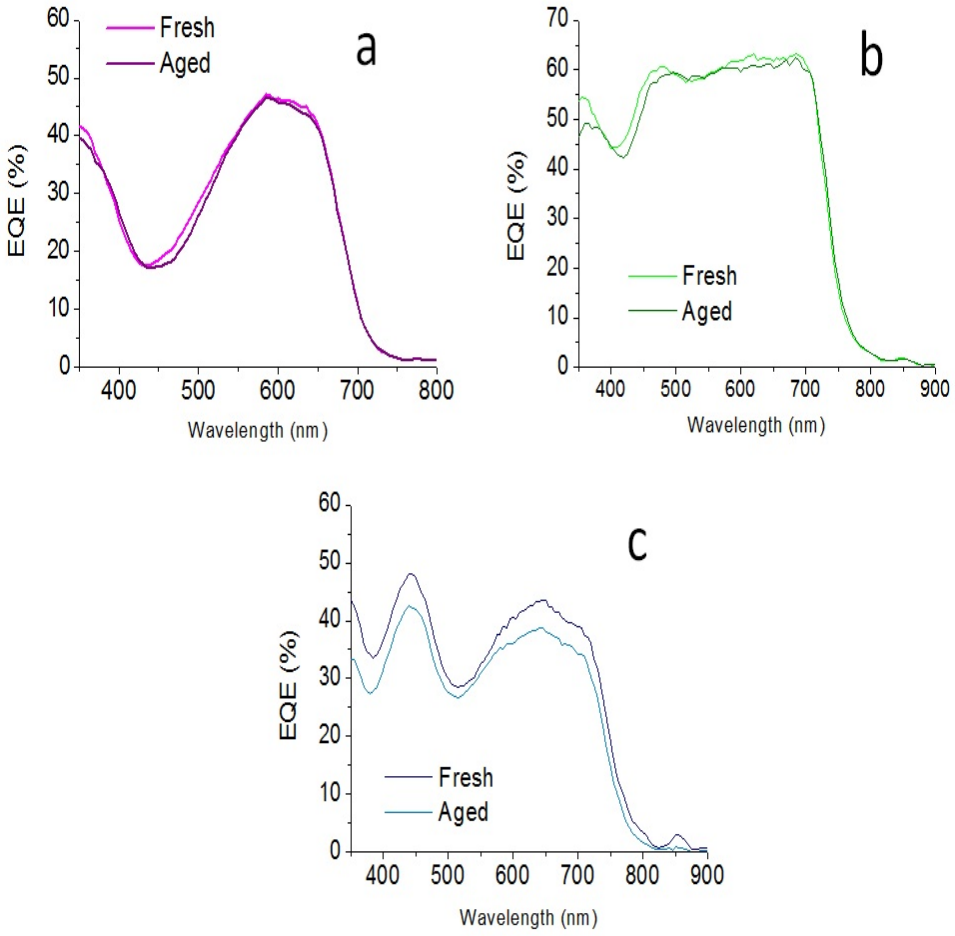

Figure 5.9: EQE plots of the fresh and aged devices based on a) P(2), b)P(8) and c) P(9).

The EQE is a common technique used to analyze a complete solar cell. In contrast to the Absorption measurements that give information just about the active layer, the EQE takes into account simultaneously several factors such as the absorption of the active layer, the charge generation and the collection processes in short circuit conditions, thus providing information about

the photocurrent generated at specific wavelengths, which can be directly correlated to the corresponding J_{sc}.
The EQE of the P(2), P(8) and P(9) of fresh and aged devices are reported in Figure 5.9, unfortunately the P(10) aged device did not give any PV response. The P(2) based solar cell represents the more stable device and no relevant changes in terms of EQE spectrum have been observed. The P(8) based device shows a slight variation of the EQE spectrum in particular in the range between 400 nm and 500 nm where the absorption is mainly due to the $PC_{71}BM$ confirming the reorganization of the fullerene domains supposed to occur after thermal degradation. At wavelengths $>$ 500 nm the EQE profiles are nearly identical, in agreement with the small drop in J_{sc}. Analogously, the EQE spectra of the P(9) based device reflects the modest reduction in J_{sc} that passes from 8,8 mA/cm^2 to 7,8 mA/cm^2. For both cases, it is reasonable to suppose a morphological reorganization of the active layer which likely determines an increase of the series resistance within the devices. As a result, the charge diffusion/collection processes and thus the resulting EQE values are partially affected.

5.3.2 Mott - Schottky analysis

The MS analysis is based on the C-V characteristic described in Chapter 2. The frequency is fixed at 1 kHz, the capacitance of the encapsulated devices is measured in dark in function of an external bias ranging from -1 V to 1,5V.
Recalling the theory reported in Chapter 2, the standard C-V characteristic scans a Schottky junctions between a doped semiconductors and a metal. The analysis is based on the depletion approximation, which implies that there are no free carriers in the space charge region at the junction under investigation. The CV characteristic it is expected to follow the MS relation [97]:

$$C^{-2} = \frac{2(V_{fb} - V)}{A^2 \epsilon \epsilon_0 N_A} \tag{5.1}$$

Where V_{fb} is the potential at which the band become flat, A is the area of the device, ϵ the dielectric constant of the active layer, ϵ_0 the vacuum permittivity and N_A the doping density. If the depletion approximation is satisfied, the charge in the space charge region is entirely due to dopant atoms or molecules. Thus, the width ω of the depletion region is modulate from an external bias by the follow relation[97]:

$$\omega = \sqrt{\frac{2\epsilon\epsilon_0(V_{fb} - V)}{qN_A}} \tag{5.2}$$

Note that in intrinsic or lowly dopant materials, the capacitance is no longer dominated by the charge of the doping atoms, but instead it is dominated by the charge carriers injected from the contact [98] and the MS analysis cannot be considered reliable. Those consideration, assumed for a single carrier devices, can be used for a bipolar device with some precautions. Simulation study [98] demonstrated for thin film ($\sim 100nm$) that: if the doping density obtained from the MS analysis is higher than ($10^{16}cm^{-3}$) the results are reliable, otherwise the assumptions are not satisfy and the results inconsistent.

Moreover, the V_{fb} is even more sensitive to the validity of the depletion approximation than the determination of the doping density. In fact in principle at V= V_{fb} no electric field is present inside the semiconductor, no current flows inside the device and thus, in a JV of a solar cells, this bias correspond to the V_{oc}. In the real device recombination process at the internal D-A interface or nonselective contacts can violate the depletion approximation, in this case the V_{bi} obtained can differ from the V_{oc} [98]. The origin of this different is due an accumulation of charges at the interface between the active layer and the electrode that induce a variation in the V_{fb} value [196]. In particular it was shown that, in a standard structure, when the fullerene molecules move close to the top electrode a better charge selectivity is obtained induce a V_{fb} that can be lower than V_{oc}. *Vice versa* when excess of polymer is present at the top active layer surface, the recombination at the contact increase and the V_{fb} becomes higher than V_{oc}[197]. Then the V_{fb} measured in the Mott-Schottky analysis in a BHJ solar cells, give information not mainly on the V_{oc} but rather about the content of fullerene at the cathode interface.
The MS plot of fresh and aged devices are reported in Figure 5.10. The aged P(10) based device is not reported because the measure results meaningless. From the linear part of the spectrum, assuming $\epsilon = 3$ for all devices, it is possible to calculate N_A from the slope and the V_{fb} from the intercept, those values are reported in Table 5.5 for all devices. A relative error of 10% is consider for all the values calculated from the fitting.

Active Layer	conditions	$N_d(cm^{-3}$	V_{fb} (V)	V_{oc} (V)
P(2):$PC_{61}BM$	Fresh	(2,5 ± 0,3) $\times 10^{16}$	1,0 ± 0,1	0,890 ± 0,005
	Aged	(5,8 ± 0,6) $\times 10^{16}$	0,95 ± 0,09	0,82 ± 0,01
P(8):$PC_{71}BM$	Fresh	(2,9 ± 0,3) $\times 10^{16}$	0,68 ± 0,07	0,72 ± 0,01
	Aged	(2,5 ± 0,3) $\times 10^{16}$	0,73 ± 0,07	0,64 ± 0,02
P(9):$PC_{61}BM$	Fresh	(5,2 ± 0,5) $\times 10^{16}$	0,97 ± 0,08	0,76 ± 0,01
	Aged	(8,2 ± 0,8) $\times 10^{15}$	0,65 ± 0,06	0,51 ± 0,04
P(10):$PC_{61}BM$	Fresh	(5,2 ± 0,5) $\times 10^{15}$	0,97 ± 0,09	0,78 ± 0,01

Table 5.5: N_A and V_{fb} parameters calculated from the MS plots. V_oc values are recalled for an easy comparison. The relative error for each value is around 10 % mainly derived from experimental noise and calculated from the fitting.

From the MS analysis on P(2) based solar cell the N_A doubles, within the measurement uncertainty, in accordance with the great value of J_{sc} after the thermal test (Table 5.2). V_{fb} results higher than the V_{oc} indicating that a non-selective contact was obtained from the beginning, in accordance with the low FF. However this morphological organization, despite the low performance, is highly thermal stable.
For the P(8) based device the N_A , calculated from the MS analysis, remains constant suggesting

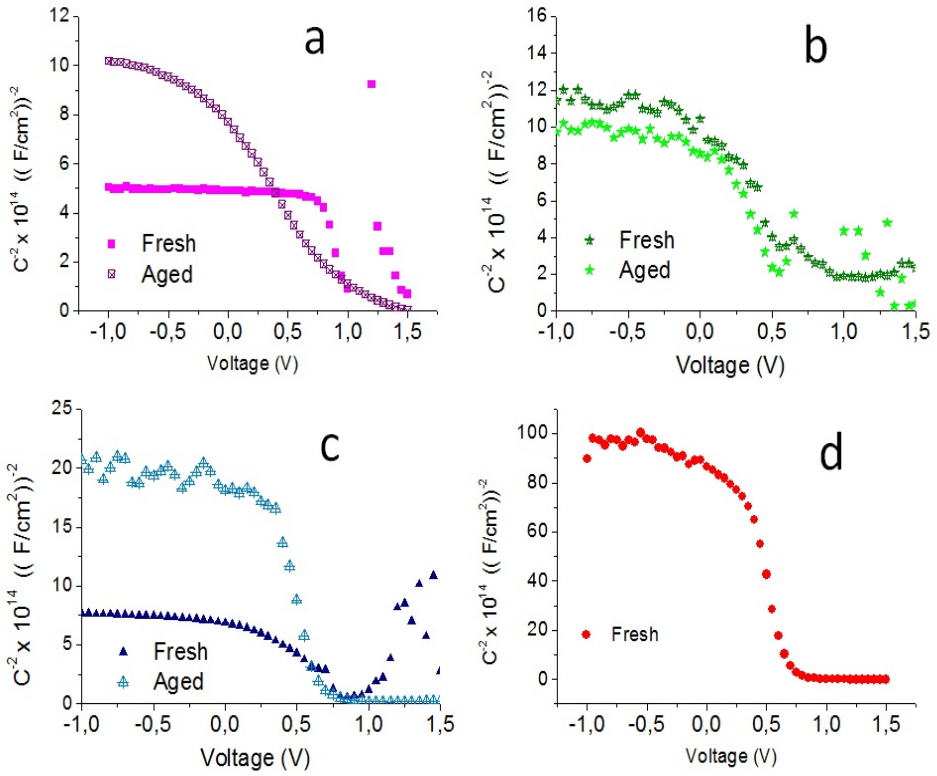

Figure 5.10: Mott-Schottky plots of the fresh and aged devices based on a) P(2),b) P(8) c) P(9) and d) P(10)

that any morphological changes occurred into the active layer doesn't affect the D polymer doping level. As supposed the reorganization is mainly due to the fullerene agglomeration. The V_{fb} value obtained for the fresh device is in perfect agreement with the literature [198] and close to the V_{oc} suggesting that at the initial conditions the device is optimized. However after thermal degradation, V_{fb} pass from 0,68V to 0,73V in an opposite trend respect the V_{oc} that diminishes from 0,72 V to 0,64 V. Also the reduction of the FF indicates the presence of recombination pathway. As supposed in the previous Chapter the thermal degradation induces a agglomeration of fullerene that can affect the intermixing of D and A, and thus increase the non germinate recombination. The fresh P(9) based device has a high doping density $N_A = 5,2 \times 10^{16} cm^{-3}$ that drastically decreases after the thermal test to $8,2 \times 10^{15} cm^{-3}$. The drop suggests a strong reorganization of the active layer and an increase of the defect states. As a consequence, recombination processes increase affecting both the FF and the J_{sc}. The V_{fb} of the fresh device is higher than the V_{oc} suggesting that an excess of polymer is present close to the cathode even on the fresh device, justifying the low PV performance. Then, after the thermal test, the V_{fb} decrease from 0,97V to 0,65V following the trend of the V_{oc}, however the low value of $N_A < 10^{16} cm^{-3}$ calculated for the aged device suggests that the depletion approximation is not valid and the last value of V_{fb} cannot be considered reliable. [98].

Similarly for the fresh P(10) based device a low doping concentration of $5,2 \times 10^{15} cm^{-3}$ is calculated, thus no consideration on the V_{fb} can be done. Moreover the low N_A is in accordance with the low PV performance.

5.3.3 Impedance Spectroscopy analysis

In order to confirm the suppositions obtained from the MS analysis a deeper investigation of the impedance device response can be done by IS. The range of frequency used is from 1 MHz to 100 Hz. The measurement were carried out for encapsulated devices under 1 Sun and the external bias is varied from -0,05V to 0,8V with a step of 0,05V. The range of frequency and voltage is selected to guarantee the stability of the solar cells during the measurement. Despite these precaution the P(10) based solar cells wasn't stable during the measurement and for this reason the IS analysis wasn't reliable and it is not reported. The curves obtained for all devices are fitted with the equivalent circuits shown in Figure 5.11. As explained in details in Chapter 2, in the Nyquist plot of an optimized solar cells is expected to be a single arc shifted from the origin of a value R_s which corresponds to the series resistance of the ITO/PEDOT:PSS contact. The arc is the result of a recombination resistance R_{rec}, that has to be higher as possible to inhibit recombination processes, in parallel with a chemical capacitance C_μ correlate with the DOS of the fullerene (Figure 5.11a). When an additional arc (in the high frequency range) appears might be the signal of charge transport limitations within the active layer. This additional arc can be fitted with a transport resistance R_t in parallel with the C_{geo} that take into account the dielectric proprieties of the active layer. The equivalent circuit used to fit those Nyquist plots is reported in Figure 5.11b. An eventually contact problem can be detected in the low frequency part of the spectrum, but the low number of data recorder in this region not allows a correct fit. Note that the R_s calculated for all devices results $< 5\Omega/cm^2$, as expected the ITO/PEDOT:PSS electrode has the same behaviour for each device and its degradation is neglected in this conditions.

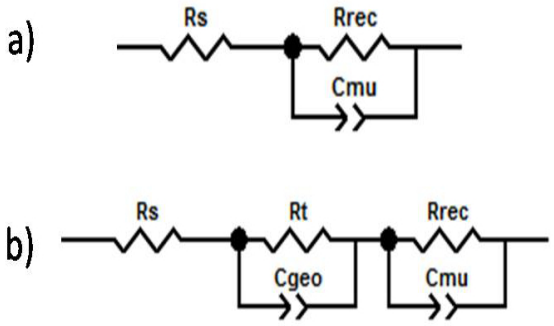

Figure 5.11: Equivalent circuit used to fitting the IS data: a) case of one arc b) case of two distinct arcs.

The fitting parameters obtained for the P(2)based devices are reported in the Figure 5.12.

Both the fresh and the aged devices present a unique arc in the IS spectra which has been fitted with the equivalent circuit reported in Figure 5.11a. From the previous results it is supposed that a contact problem is present from the beginning, however from the IS spectra the arc formed at low frequency can be observed, but not properly fitted. The R_{rec} of the aged devices is slightly lower than the R_{rec} of the fresh devices, indicating that the phenomena of recombination slightly increase, in good accordance with the modest decrease in PCE (-7%) registered after the thermal test (Table 5.2). The variation of R_{rec} and C_μ well describe the loss in the V_{oc} that passes from 0,89V to 0,82V. In fact C_μ is correlated with the DOS of the fullerene [103], different distribution of the energy level of the fullerene can induce a variation in the recombination process and thus in V_{oc} [199]. In the end the presence of a single arc in the IS spectrum of the aged devices indicates that the charge transport properties of the system are not affected by the thermal test, highlighting a good thermal stability of the solar cell.

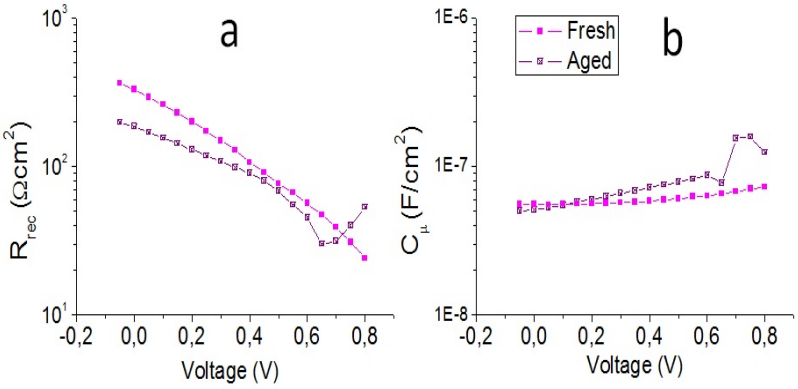

Figure 5.12: Parameters obtained from the fitting of the IS spectra by the equivalent circuit reported in Figure 5.11a of P(2) based solar cells

Concerning the P(8) based device, the previous results suggested that the temperature induces an active layer reorganization which favours charge recombination processes. The IS analysis confirms this hypothesis, the fitting parameters obtained for the P(8) based device are reported in the Figure 5.13. The IS spectrum of the fresh device presents a single arc, confirming that the initial device was optimized, thus neither contact nor transport problems are expected. On the opposite, the aged device shows a second arc at high frequency indicating an alteration of the transport process induced by the thermal degradation. The R_{rec} parameter it diminishes of one order of magnitude from the fresh to the aged device, in perfect accordance with the assumptions and in particular with the drop in FF from 59% to 36%. Analogously to the previous case also the C_μ is in good agreement with the PV results, an evident variation in the shape indicates a reorganization of the energy level of the fullerene and justifies the loss in V_{oc}. Finally, the R_t calculated for the aged device is higher at low bias, when higher current circulate into the solar cells. Despite the presence of the new arc indicates a limitation on charge transport, the low value of the $R_t < 20\Omega/cm^2$ correlates well with the slightly decrease of J_{sc} that passes from $14mA/cm^2$

to $13mA/cm^2$.

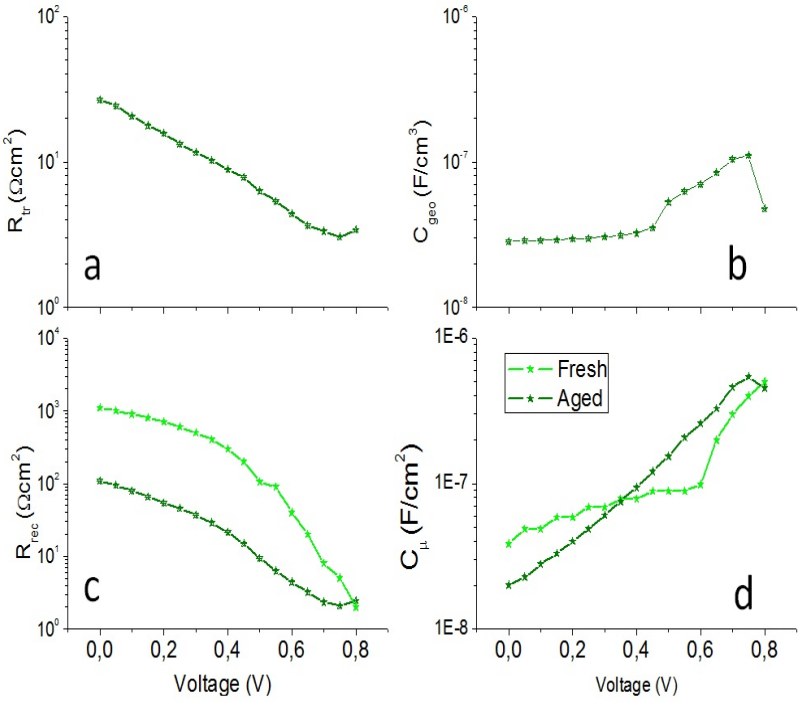

Figure 5.13: Parameters obtained from the fitting of the IS spectra by the equivalent circuit reported in Figure 5.11 of P(8) based solar cells

In the end for the P(9) based device an increase of the defect state is supposed from the MS analysis. The parameters obtained from the fitting of the IS spectra of the fresh and aged devices are reported in Figure 5.14. Interestingly the fresh device shows an unoptimised charge transport that worsens under thermal stress. The R_t clearly increases from the fresh to the aged device justifying the drop in J_{sc} from $8,8mA/cm^2$ to $7,8mA/cm^2$. The reorganization of the active layer concern mainly the A material, the C_μ proves that the energetic distribution of the fullerene drastically change after the thermal annealing in agreement with the loss in the V_{oc} from 0,76V to 0,51V. On the contrary to the P(8) based device, the variation in the R_{rec} cannot justify the big drop in the FF from 50% to 36%. However from the MS analysis a migration of D polymer close to the top electrode is supposed. This process in a standard configuration is detrimental for the PV performance in particular for the FF. As consequence, in the IS spectrum of the aged device an additional arc at low frequency it is expected, in fact it can be appreciate but not properly fitted.

In conclusion, the hypotheses obtained from the previous measurements are confirmed by the IS measurement underling the power and the efficacy of this technique to discriminate all the process involved in a solar cell. Note that increasing the data at low frequency can help to have a quantitative analysis of the contact problem, but implies a longer time of measure that can affect the stability condition, fundamental for reliable IS data.

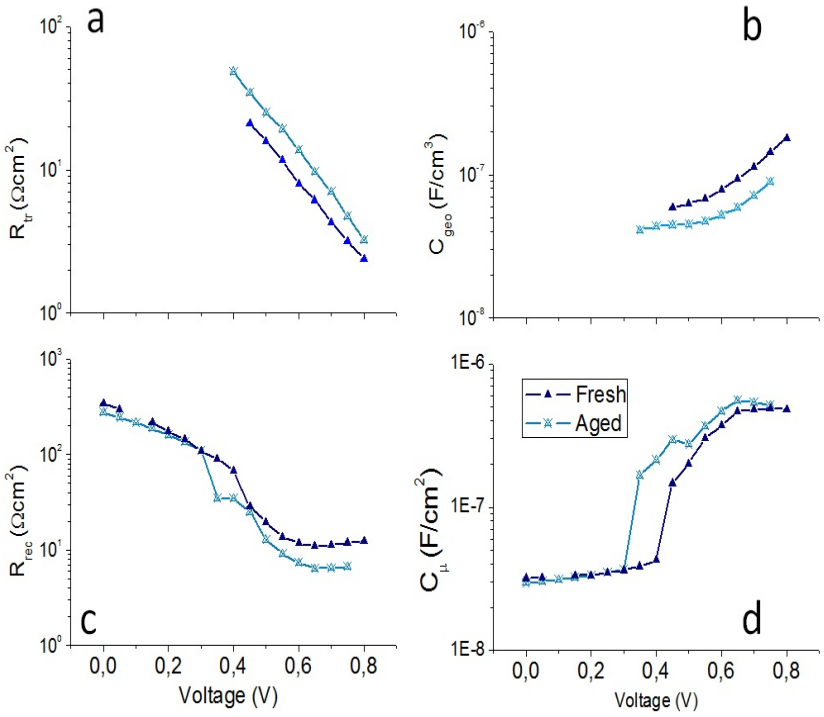

Figure 5.14: Parameters obtained from the fitting of the IS spectra by the equivalent circuit reported in Figure 5.11 of P(9) based solar cells

5.4 Conclusion

In conclusion, the techniques used to study the thermal degradation effects give a complete description of the phenomena involved. In fact both minimal and strong reorganizations of the active layer, for P(8) and P(9) based devices respectively, can be detected following the proposed analysis. For example, despite FF for P(8) and P(9) devices follow the same trend during the thermal test, the causes of their decay are different. In the case of P(8) based devices an increase of the charge recombination in the bulk of the active layer, caused by the thermal degradation, justifies the drop in FF, while for P(9) based devices the contact problem, worsen in the aged device, results predominant with respect to the FF variation. In view of a commercial product, both the efficiency and lifetime are crucial parameters that have to be simultaneously optimized. Thus an high efficiency is not enough if the thermal stability is not guaranteed. A representative case is the comparison between the P(2) and P(8) based devices: despite the initial PCE of P(8) was higher than the one of P(2) based devices (6% against 3%) after the thermal test the performance resulted comparable, indicating that in principle both materials can be chosen for as active materials for commercial applications.

In this context, it is difficult to select *a priori* the best device without performing any thermal test. Here we demonstrate that the long standard test procedures routinely used to establish the lifetime of OPV devices (150 hours) can be easily replaced with the new fast capacitance based thermal test proposed (2 hours). The new approach not only identifies the stable device at a particular test temperature, but also it gives an additional information: the value T_{MAX} suggests the limit operating temperature above which the device becomes thermally unstable. Thus, this new method results to be an interesting tools in view of an industrial production. For the future work it will be interesting to investigate the effects of thermal degradation for different configurations based on the same active layer in order to identify optimal devices in terms of efficiency and stability.

6

Photodegradation effects on BHJ solar cells

6.1 Light-induced degradation

Summarizing from the previous Chapters, the stability of an encapsulated organic solar cells can be affected from incident light and high operating temperature. The degradation involves mainly the active layer properties, but it can affects also the other layers and interfaces that composed the device. Focusing the attention on photostability, it is well know that organic materials, in particular photoactive materials are vulnerable to photodegradation under UV-visible light irradiation, in presence or in absence of oxygen [200][201]. In most cases, the degradation induces modifications in the chemical structure of the macromolecular chains [202][203]. These structural changes provoke variations of the physical and chemical properties of the polymer, mainly in terms of loss of π-conjugation with the consequent deterioration of the performance of the system in which the material is used [204]. The mechanisms by which most polymers degrade when submitted to UV-visible light irradiation in ambient air are well understood [200][201]. The first step of the oxidative reactions is always a hydrogen abstraction on the polymeric backbone (PH) by a free radical ($r^{\bullet}$) formed by photonic excitation of a chromophoric species:

$$PH + r^{\bullet} \rightarrow P^{\bullet} + rH \tag{6.1}$$

Then the macroradical produced $P^{\bullet}$ can reacts with oxygen and induce a chain reaction [200]. Thus hydrogen abstraction can be significant for modifications of the polymer properties. This reaction strongly depends on the chemical structure of the polymer, moreover many study shown that the hydrogen abstraction most likely occurs at the side-chains. However them are fundamental to tune several properties such as: i) solubility and processability, ii) position of the HOMO and LUMO levels, iii) structural conformation and iv) intra- and inter-chain interactions of the polymer chains. Thus their nature, length and position has to be properly choose to satisfy the compromise between good processability, performance and stability.

Despite the chain reaction is governed by the O_2, it is important to observe that also in total absence of oxygen the polymer can degrade under light soaking [153][203]. Indeed, absorption of the UV - visible radiation range contained in the solar spectrum can induce photochemical processes such as rearrangements, chain scissions and crosslinking reactions. The main consequence of these reactions is a decreases of the UV-visible absorbance in the domain of visible light[200] due to the partial interruption of the π - conjugation[204][138].
Some general considerations can be resumed from literature and used as guide lines for the synthesis of new materials. First, the stability ranking of the side chains from the lowest to the highest is as follows: $CO_2R < OR < H$ [203]. Second, moieties containing a quaternary site are very unstable (e.g. fluorene, cyclopentadithiophene) because of the oxidability of this site. Third, the presence of readily cleavable bonds (such as C-N or C-O) also limits stability. In the end aromatic polycyclic units generally exhibit a good photochemical stability [203].

6.1.1 Effect of fullerene

The intrinsic photostability of a D polymer is fundamental aspect for the resulting device stability, however its behaviour can be influenced when mixed with fullerene derivatives [153][205][206]. In fact $PC_{61}BM$ has been observed to stabilize many π-conjugated polymers used in the active layer by reducing the photodegradation rate. Three mechanisms are usually invoked for the stabilizing effect of $PC_{61}BM$: screening from UV light, exciton quenching and radical scavenging.
To quantify the benefit due to UV inner filter effect, Distler *et al.* [206] compared the stability of 3 similar system: a P3HT film deposited on a glass substrate, an analogous films with an additional layer of $PC_{61}BM$ deposited on the opposite site, and then P3HT:$PC_{61}BM$ blend film. All system were irradiated and the corresponding absorption decay was recorded. Comparing the degradation rate of the three films appears that the optical screening effect of $PC_{61}BM$ seems to contribute 30% to the observed reduction of the P3HT degradation rate.
Another mechanism that limits the polymer degradation is the exciton quenching by electron transfer to $PC_{61}BM$, in fact this process reduces the lifetime of the excited singlet state and thus reduces the population of all reaction-inducing states (e.g., triplet states) (Figure 6.1b). Triplet states are notorious for their reactivity, due to their relatively long lifetime, which favours bimolecular reactions [205].
In the end, in many study it is reported the radical scavenging ability of fullerenes, mainly due to the stabilization of radicals by their addition to the extended π -system [207] .
Nevertheless, despite most of D polymers show an enhancement on their photostability when mixed with fullerene, sometimes the presence of $PC_{61}BM$ can be detrimental for the device. An example is the PCPDTBT based active layer. In this blend the presence of fullerene enhances the generation of triplets via the CT state (Figure 6.1a). In presence of oxygen, the triplet state may sensitize the formation of chemically active oxygen species (e.g., singlet oxygen), which then would act as oxidants for the polymer [206].

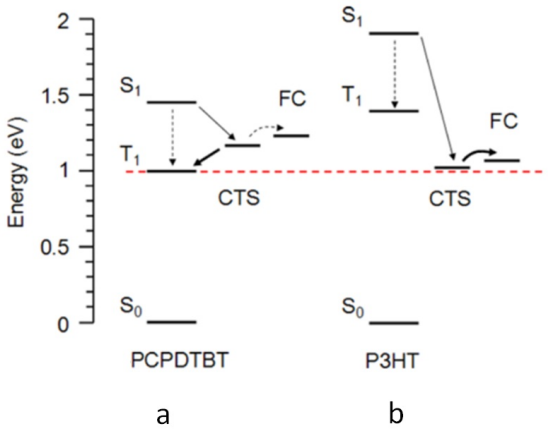

Figure 6.1: State diagram of the PCPDTBT:$PC_{61}BM$ and P3HT:$PC_{61}BM$ blends. CTS is the energetic level of the CT state between the polymer and fullerene; FC is the energetic level of free charge carriers, T is the triplet state and S is the singlet state. The oxygen singlet energy is indicated by the dashed red line across the graph. [206]

6.1.2 Effect of solvent additives

The use of solvent additive in the D:A blend solution is a common strategy to optimize the morphology of the active layer [151] taking advantages from two main aspects: a selective solubility of the fullerene derivatives and a higher T_b than the host solvent. The selective solubility is necessary to perform D:A domains in solution and the different T_b to preserve the domains during the drying process [184]. The most common additive that meets these requirements is the DIO, however, despite the benefits in terms of photovoltaic performance[151], recently it was found to have a detrimental impact on device stability during UV-light exposure [208]. In fact DIO molecules are highly sensitive to light, and the radicals formed are susceptible to saturate instantaneously the neighbour π-conjugated systems and/or to be trapped by the fullerene. Moreover when the BHJ is confined by a top layer, residual additives, or more precisely the photoproducts issued from their degradation, cannot migrate out of the film and they can react with the polymer and fullerene molecules, determining their degradation [176].

As a result, the photostability of a D polymer can be related to its chemical structure both in terms of backbone and number, size and nature of the side chains. However, when the polymer is used into an active layer of a solar cells, additional factors should be taken into account to rule the photochemical behaviour of a complete BHJ device.

6.2 Photodegradation of Quinoxaline based polymers

In order to further elucidate the relationship between the intrinsic photostability of different donor polymers and the corresponding impact in terms of device photodegradation, a series of quinoxaline based polymers have been concretely studied. The intrinsic stability of each polymer is investi-

gated by monitoring the UV-vis absorption decay of the corresponding neat films under 1 Sun illumination, as a function of ageing time. Next, the corresponding BHJ solar cells are fabricated and tested during prolonged light exposure in order to evaluate and compare the photostability responses of more complex systems such as complete device,under working conditions.

6.2.1 Polymers structures and characterization

The studied D polymers are based on a fluorinated quinoxaline (FQ) acceptor unit either with a differently substituted benzodithiophene (BDT) or an unsubstituted thieno[3,2-b]thiophene (TT). In details: P(3)-PFQBDT-TR (already investigate in Chapter 3) containing alkyl-thienyl side chains, P(11)-PFQBDT-OR containing alkoxy side chains, P(12)-PFQBDT-TROR containing alky-oxy-alkyl-thienyl side chain and P(13)-PFQTT has an unsubstituted TT. The chemical structure of the polymer reported in Chapter 2 Figure 2.2, are recalled in Figure 6.2.

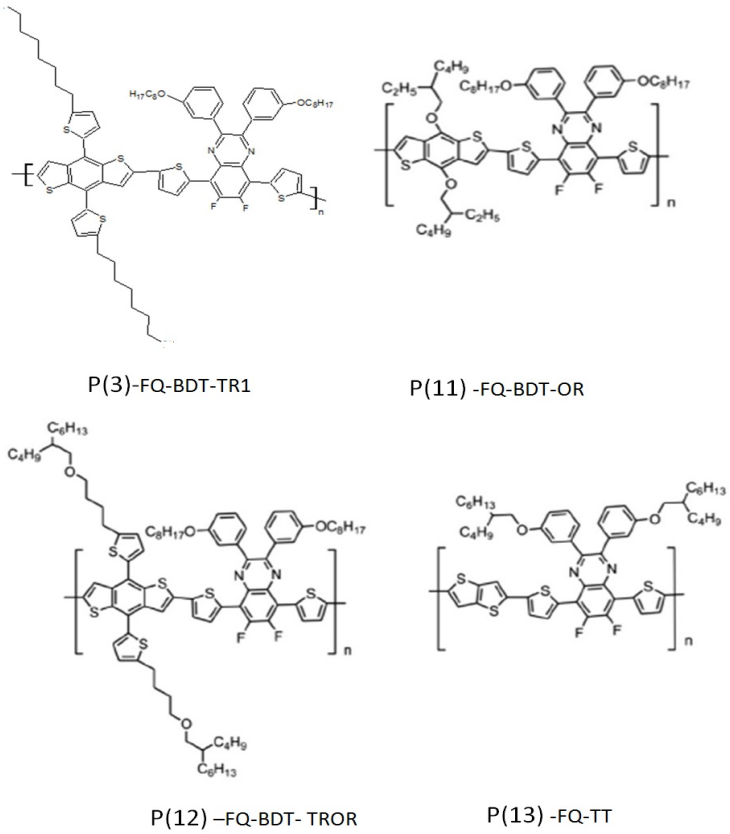

Figure 6.2: Chemical structure of P(3)-PFQBDT-TR, P(11)-PFQBDT-OR, P(12)-PFQBDT-TROR and P(13)-PFQTT [78]

SWV have been employed to investigate the electrochemical properties of the polymers and estimate the HOMO and LUMO energy levels (Table 6.1). The different in the side chains have an effect on the E_{HOMO} and E_{LUMO} . Polymers P(3) and P(12) present similar HOMO and LUMO

energies while the analogous polymer P(11) shows a slightly higher HOMO level likely due to the stronger electron-donating effect of the alkoxy side chains linked to the BDT unit. Moreover the TT polymer P(13) exhibits further raised HOMO and LUMO energy levels mainly because the relatively high electron density of the TT unit, compared to other D moieties, increases the push-pull character of the polymer. Interestingly, all polymers exhibit relatively deep HOMO energy levels, which would result in devices with a high V_{oc} and ensure good air stability [137] [49].

D	M_n (kDa)	M_w (kDa)	λ_{max} (nm)	λ_{onset} (nm)	E_{gap}^{opt} (eV)	E_{HOMO} (eV)	E_{LUMO} (eV)
P(3)	37	133	610	726	1,71	-5,89	-3,61
P(11)	32	82	595	702	1,77	-5,74	-3,50
P(12)	24	54	617	720	1,72	-5,84	-3,56
P(13)	19	53	629; 676	750	1,65	-5,64	-3,45

Table 6.1: Molecular weight, optical and energetic proprieties of P(3), P(11),P(12), (13) D polymer. An error of 2 nm is considered for each wavelentgh due to the spectrum resolution.

For the optical characterization of the polymers, the absorption spectra of the thin films are reported in Figure 6.3.

The UV-vis spectra of all polymers exhibit similar main features: a higher-energy absorption band, between 380 and 480 nm, which can be assigned to localized $\pi - \pi^*$ transitions and a lower energy band, between 500 and 700 nm (up to 750 nm for P(13)), arising from the intra-molecular charge-transfer-like interactions between the electron-rich (BDT or TT) and electron-poor (FQ) moieties, and from the inter-chain interactions between the polymer chains. For P(13) the vibrational structure of the low energy band is well resolved showing two peaks at 630 nm and 670 nm, respectively, while for P(3), P(11) and P(12) the two vibrational peaks are partially overlapped. The replacement of the alkoxy chains on the BDT unit (P(11)) with thiophene based side groups (P(3) and P(12)) is known to extend the π-conjugation (2D-conjugated polymer) resulting in a red-shifted absorption profile [209]. Then, the use of an electron-rich TT comonomer, instead of the weaker electron donating BDT unit, leads to a further significant red-shift (50 nm) of the absorption spectrum of the corresponding polymer P(13)

6.2.2 Photodegrdation of neat polymer films

In order to investigate the photochemical stability of P(3),P(11),P(12) and P(13), a set of neat polymer films deposited on glass substrates were prepared and illuminated in air at 1 Sun for 72 hours. Then, the absorption spectrum of each films is recorded at certain interval time.
Figure 6.4 shows the evolution of the UV-vis absorption profiles of P(3),P(11), P(12) and P(13) as a function of the irradiation time (after 0, 5, 30, 45 and 72 h). As expected, the general tendency, similar for all polymers, is a decrease of the peaks magnitude over time due the photo-bleaching[138][200]. Despite the different rate of the photodegradation as a function of the polymer

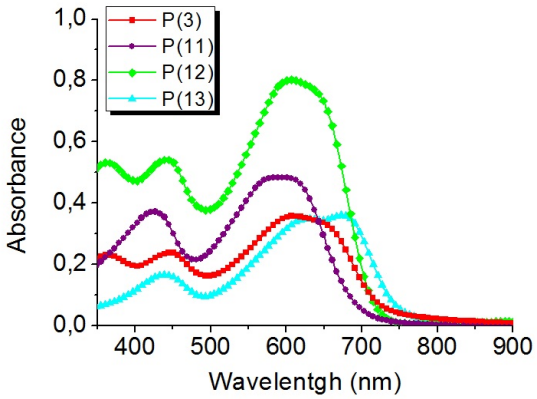

Figure 6.3: Absorption spectra of P(3)(red), P(11) (purple), P(12) (green), P(13) (light blue).

structure, it is evident that for all polymers the low energy peak decreases faster than the high-energy peak, resulting in a change of the relative absorption peak ratio. It has been demonstrated that the relative ratio of these peaks varies with the polymer chain length, suggesting that the π-conjugation length of polymers could be reduced when the they are subjected to photo-induced oxidation, likely due to saturation/opening of π-conjugated units or chain scission reactions [210][211]. To evaluate the photodegradation of the four polymers, the decrease in the intensity of the absorption peaks, relative to the same electronic and vibrational transition, are compared. Thus the absolute absorption maximum (λ_{max} reported in Table 6.1) have been used for P(3), P(11) and P(12), while for P(13) it is considered the relative absorption maximum at 629 nm related to the first vibration peak of the electronic transition. Then, to quantify the photodegradation, it is calculated the remaining peak absorbance (Rm_{Abs}) define as:

$$Rm_{Abs} = \frac{A_{max}(t)}{A_{max}(0)} \times 100 \tag{6.2}$$

where $A_{max}(t)$ is the residual absorbance after a specific time t (5, 30, 45 and 72 h, extrapolated from the UV-vis spectra in Figure 6.4), while $A_{max}(0)$ is the initial absorbance (at t=0 h). Figure 6.5 exhibits the trend of Rm_{Abs} plotted against the irradiation time for all polymers.

The P(11) shows the worst photostability , Rm_{Abs} decreases quickly to 85% after 5 h of illumination, and then follows a degradation rate similar to the other materials reaching a final value of 45%, after 72 h. In the opposite polymers P(3), P(12) and P(13) exhibit a relatively similar and constant decay during illumination indicating an improved resistance towards photodegradation as suggested by the relatively high values of Rm_{Abs} after 72 h (65%, 58% and 74%, respectively for P(3), P(12) and P(13)). As above mentioned, the polymer structure and in particular the number, length and nature of the side chains linked to the polymer backbone strongly influence the photochemical stability of the resulting polymers. Looking at the structural differences of the present polymers, P(11) contains alkoxy side chains with the oxygen atoms linked to the BDT comonomer which can be readily cleaved under illumination, thus starting the polymer degradation [200]. Indeed, the resonance stabilizing effect of the oxygen atom is known to weaken the

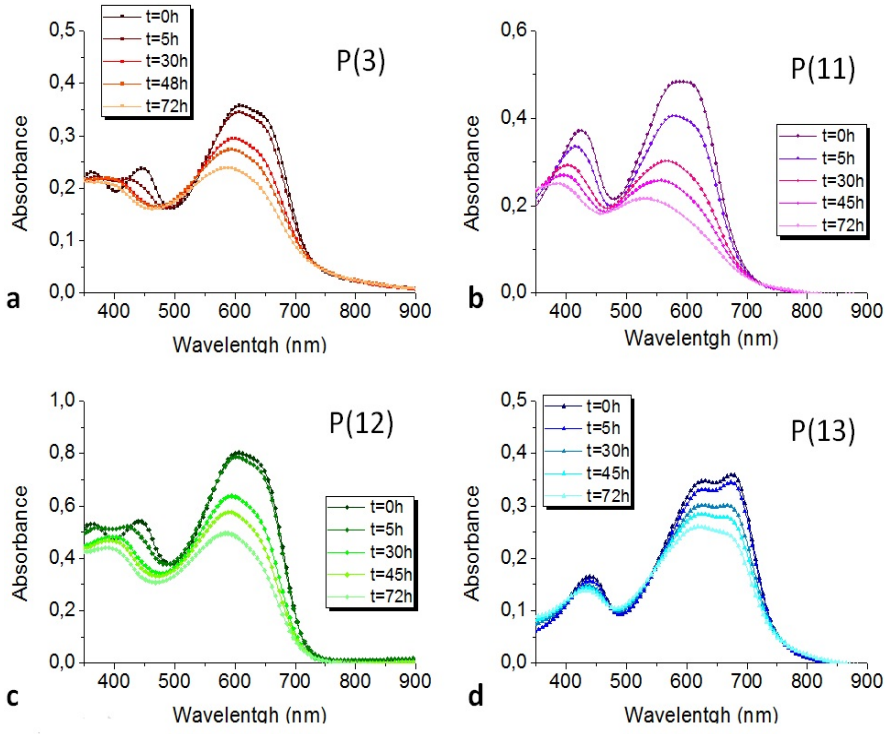

Figure 6.4: Absorption spectra decay of a) P(3)(red), b) P(11) (purple), c) P(12) (green), d) P(13) (blue) D polymers.

energy of the C-H bond of the adjacent CH_2 group thus favoring the hydrogen extraction (by a free radical) leading first to side chain oxidation and then to the subsequent stepwise oxidations [200].

For P(3) and P(12), the replacement of the oxygen atoms with aromatic units (thiophene) significantly improves the resulting photochemical stability. Interestingly, the nature of the residual portion of the side chain linked to the thiophene ring (alkyl or alkyl-oxyalkyl , respectively for P(3) and P(12)) has a negligible impact on the photodegradation rate of the corresponding polymer films. In the end, polymer P(13), in which the BDT unit has been replaced with an unsubstituted fused bithiophene (TT) comonomer, is the most photochemically stable material of the series. In general, these findings are fully consistent with the literature and confirm that the use of unsubstituted aromatic units enhances the photochemical stability of the resulting polymer films, while the presence of the oxygen close to the backbone is detrimental[206].

6.3 Photodegradation of polymer based solar cells

As previously mentioned, once analysed the photodegradation of the neat polymer it is interesting to investigate the photostability of the corresponding BHJ solar cells. To this end, working devices were exposed to prolonged illumination in inert atmosphere and the evolution of their PV performance were periodically monitored.

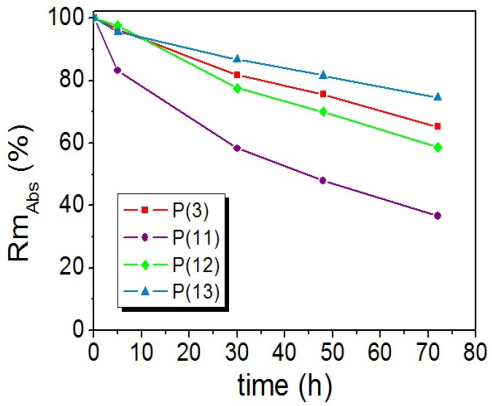

Figure 6.5: Rm_{Abs} decay of P(3)(red), P(11) (purple), P(12) (green), P(13) (blue).

To take into account the increase of the temperature during light exposure (thermal degradation), all BHJ devices are fabricated in duplicate: the first group of devices is exposed to heat stress (named "Heat") and a second group of samples is exposed to light stress (named "Light").
The device structures used, identical for all polymers, is glass/ITO/PEDOT:PSS/active layer/LiF/Al therefore the differences between the devices can be mainly related to the different stability of the active blends, since the internal interfaces and/or buffer layers are the same in all cases. Moreover, the stack was demonstrated to be relatively stable and compatible with light soaking tests [212].

6.3.1 Device Fabrication

After the cleaning process of the ITO-glass substrates, a thin layer of PEDOT:PSS was deposited by blade-coating, following the procedure already reported in Chapter 2. The active layer solutions of P(3) and P(11) are based on ODCB, while in the case of P(12) and P(13), 3% v/v of DIO is added to the ODCB solution. All polymers are blended with $PC_{61}BM$ with a weight ratio of 1:1. The active blend solutions were processed by blade-coating in air, without the need of additional thermal treatments. The PV parameters of the best solar cells are reported in Table 6.2.

Active Layer	Additive	$J_{sc}(mA/cm^2)$	V_{oc} (V)	FF (%)	PCE (%)
P(3):$PC_{61}BM$ (1:1)	/	10,2	0,81	63	5,2
P(11):$PC_{61}BM$ (1:1)	/	7,7	0,77	68	4,1
P(12):$PC_{61}BM$ (1:1)	3 %	7,6	0,85	58	3,8
P(13):$PC_{61}BM$ (1:1)	3%	9,2	0,65	64	3,8

Table 6.2: PV parameters of devices based on P(3), P(11),P(12), (13) as D polymer

All OPV devices exhibit remarkable photovoltaic responses, with the maximum PCE of 5,2%

for the P(3):$PC_{61}BM$ active layer, in agreement with previous results (Chapter 3). The V_{oc} of all BHJ devices correlates well with the difference between the HOMO level of the D and the LUMO level of the A. The low-lying HOMO levels (-5,8 eV) of BDT based polymers P(3) P(11) and P(12) result in higher V_{oc} (0,8 V) compared to that obtained by using the TT-Q polymer P(13) (0,65 V), having a relatively higher HOMO level(-5,64 eV). The FF values seem to depend on the structural complexity of the side chains linked to the BDT moiety, which strongly affects the polymer:fullerene self-organization in the solid state. Fill factors (FF) of 68%, 63% and 58% are obtained, respectively, for BHJ cells based on P(11) (containing alkoxy side chains), P(3) (containing alkyl-thienyl side chains) and P(12) (containing longer alky-oxy-alkyl-thienyl side chains). On the other hand, the P(13) based blend exhibits a FF of 64% suggesting a proper phase segregation and inter-chain interactions likely promoted by the presence of the planar TT unit. The J_{sc} varies between 7,6 mA/cm^2 (for P(11) and P(12)based devices) and 10,2 mA/cm^2 (for P(3) based device). Since the three polymers exhibit UV-vis absorption spectra with very similar profiles in the same spectral ranges (Figure 6.3) the observed variations may be ascribed to the different charge transport properties of the polymers due to their different morphological organization in film. Similarly, despite the red-shifted absorption spectrum of P(13) compared to the other ones, the corresponding OPV device generates a comparable $J_{sc}(9,2mA/cm^2)$, likely due to the relatively low molecular weight of the polymer (Table 6.1).

6.3.2 Photodegradation test and evolution of PV parameters

The light soaking test is carried out by illuminating the cells at 1 Sun for 72h in inert atmosphere and monitoring the PV performance at different interval time: 24h, 48h and 72h ("Light"). In parallel, an identical set of devices, processed in the same experiment, are entirely masked with black tape, and kept under illumination("Heat"). On Figure 6.6 and 6.7 are reported the trend of the normalized PV parameters of the solar cells in function of the ageing time for the "Heat" of the "Light" groups respectively. To summarize the results, the initial (PCE_i) and final (PCE_f) PCE values and their percentage variation are reported in Table 6.3. The results are an average of 6 devices. The errors are calculated from the standard deviation. Note that, despite the devices are fabricated in the same conditions and in the same experiment, the typical reproducibility of organic device determines slightly different on the initial performance.

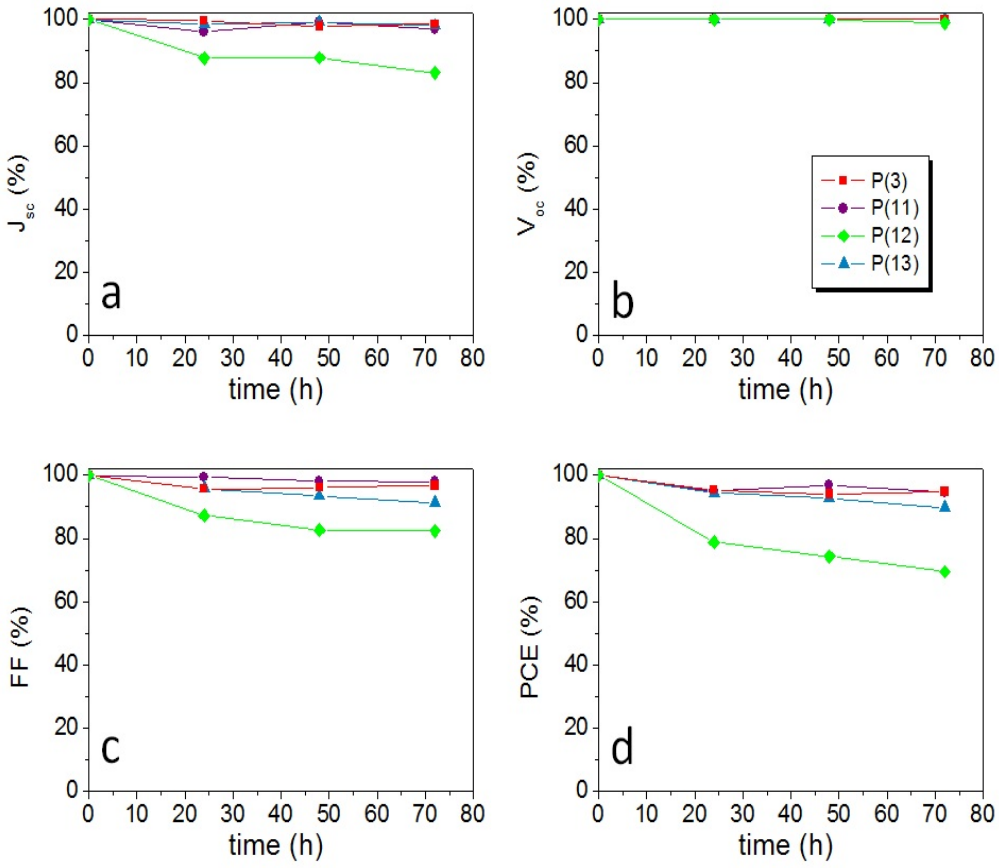

Figure 6.6: PV parameters decay of devices based on a) P(3)(red), b) P(11) (purple), c) P(12) (green), d) P(13) (blue) heat in Dark in inert atmosphere.

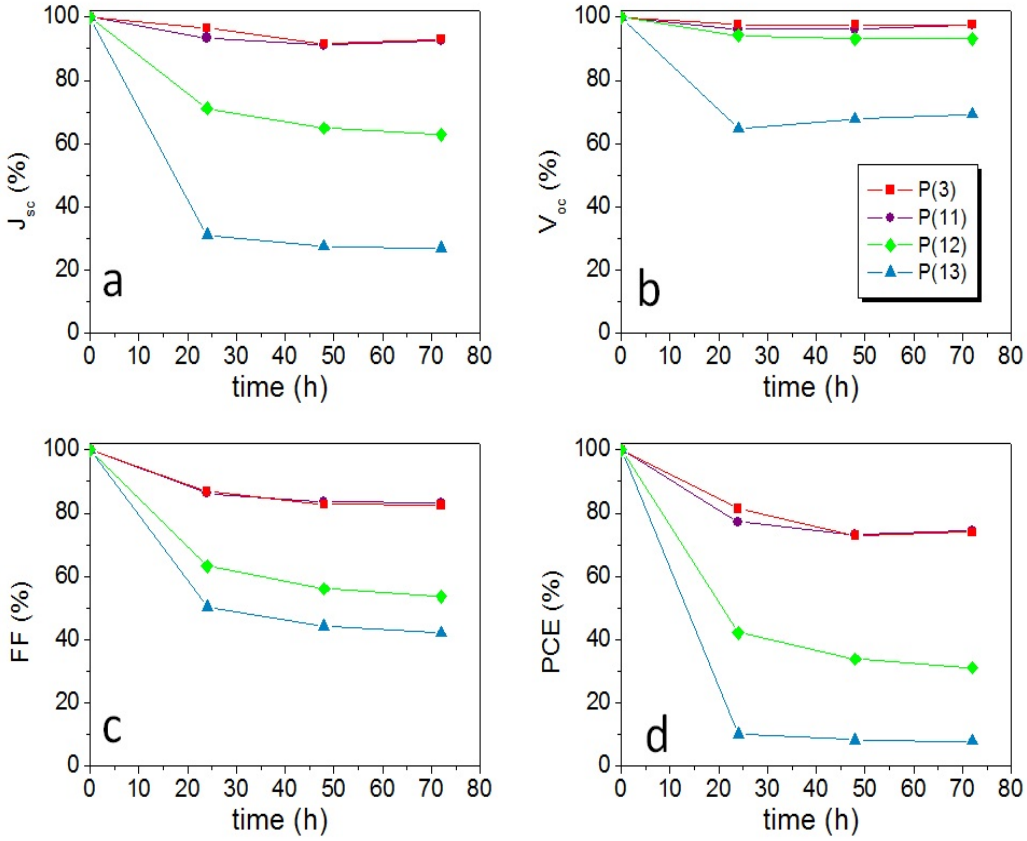

Figure 6.7: PV parameters decay of devices based on a) P(3)(red), b) P(11) (purple), c) P(12) (green), d) P(13) (blue) under 1 Sun in inert atmosphere.

Active Layer	Ageing	PCE_i (%)	PCE_f (%)	Δ PCE
P(3):$PC_{61}BM$ (1:1)	Heat	4,1 ± 0,2	3,8 ± 0,1	-7%
	Light	4,9 ± 0,3	3,6 ± 0,2	-27%
P(11):$PC_{61}BM$ (1:1)	Heat	3,6 ± 0,2	3,4 ± 0,1	-6%
	Light	4,0 ± 0,1	2,9 ± 0,1	-28%
P(12):$PC_{61}BM$ (1:1)	Heat	3,5 ± 0,3	2,4 ± 0,1	-31%
	Light	3,7 ± 0,1	1,1 ± 0,1	-70%
P(13):$PC_{61}BM$ (1:1)	Heat	3,2 ± 0,1	2,7 ± 0,1	-15%
	Light	3,7 ± 0,1	0,3 ± 0,1	-92%

Table 6.3: Initial PCE_i and final PCE_f and relative variation of the devices based on P(3), P(11),P(12) and P(13)

The OPV devices exposed to Heat stress retain most of their initial performance ($\Delta PCE <$ 15%), except the case of the P(12) based cell which shows a reduction in PCE of -31%, likely due to thermally induced morphological rearrangements of the D:A blend as suggested by the decrease in J_{sc} and FF. Indeed, the presence of relatively long and branched side-chains causes steric hindrance in solid films which might increase the $\pi-\pi$ stacking distances and in turn increase the void fraction and therefore the $PC_{61}BM$ diffusion rate, promoting the generation of aggregates/clusters in the BHJ blend which might limit the OPV performance [40][167].
During Light soaking the performance of the BHJ solar cells gradually decreases with the irradiation time and it is reasonable to assume that the contribution of the thermal degradation is not substantial, except the case of the P(12) cell. As shown in Figure 6.7, the degree of photodegradation is considerably different among the polymers. The decrease of the PCE is generally caused by a decrease in FF and J_{sc}, whereas the V_{oc} remains constant during the 72 h of measurement, except the case of P(13) based cells. Note that, the V_{oc} loss during photoinduced degradation has been demonstrated to become relevant in amorphous materials as a result of a redistribution of the charges in a broader density of states [213]. The amorphous character of the P(13) based blend might be related to the relatively low molecular weight of the polymer (M_n=19 KDa, PDI=2,8 Table 6.1).
As a result, the photodegradation of the solar cells exhibits a different trend in comparison to the behaviour of the corresponding neat films.
Indeed, P(3) and P(11) based devices are the most stable, preserving more than 70% of their initial performance, with a reduction in PCEs mainly due to a decrease in FF values. Diversely, P(12) and P(13) based devices exhibit the largest degradation during the light soaking, showing a decrease in PCE of 70% and 92% respectively. Note that, both cells (P(13) and P(12)) have been processed using DIO as solvent additive. Probably, residual amounts of additive remain in the film, contributing to device degradation [176][200]. This aspect combined with the poor thermal stability of P(12) based device can justify the drastic loss in PCE of 70%. Surprisingly the solar cell based on the most photostable polymer P(13) (in neat film) totally degrades losing its initial performance after 24 h under 1 Sun, in absence of oxygen (Figure 6.7). Analogously, for P(13) the presence of DIO in the blend solution can partially explain the loss in performance, in addition it is reasonable to assume that the absence of side chain in the TT unit implies that the site of the degradation involve the polymer backbone thus determining a drastic effect on the $\pi-$ conjugation.

6.3.3 Optical Characterization of the Active Layer

In order to evaluate the effects of the light soaking on the optical properties of blend films, the absorption spectra of the solar cells before and after ageing are carried out (Figure 6.8). Note that, despite the devices are fabricated using the same conditions, the ageing can induce slight variation on the thickness of the active layers. A small difference (<20 nm) can affect the light absorption. In order to take into account this variation, the absorption spectra are normalized by the thickness of the active layer. Following the law of Lambert-Beer the resulting value is called "Linear absorption coefficient" [214].
Observing Figure 6.8 it is evident that the photodegradation of the active layers is considerably

reduced with respect to the pristine polymers (Figure 6.4). The main reasons can be traced to the absence of oxygen that slow the photodegradation [202][211], but also the presence of fullerene that, as observed for many D polymer [202] [206], stabilizes the active layer. Comparing the polymer with the thiophene based side chains, both the absorption spectra of P(3) P(12) based active layer show a decrease of the linear absorption coefficient under "Heat" condition, suggesting a variation of the BHJ morphology. Apparently this reorganization is beneficial for the solar cells based on P(3), indeed the PCE and J_{sc} remain constant under this stress conditions (Figure 6.6), while seems to be detrimental for the P(12) based device which shows a loss in PCE of $\sim 30\%$. On the opposite, under "Light" condition, an additional variation of the morphology is supposed, that further decrease the absorptions, in this case it induces a loss in PCE for both devices. Additional interfacial effects can affect the performance, but they cannot be appreciated by the absorption measurement.

Interestingly, an unexpected behaviour is observed for the P(11) based active layer. The Absorption increase upon stress in the same way for "Heat" and "Light" conditions in contrast with the behaviour of pristine film (Figure 6.4). Probably the high temperature induces a reorganization of the active layer that is beneficial for the optical properties. Under "Heat" conditions this beneficial effect can guarantee a good stability reflecting the unaltered PCE before and after stress. While the loss in performance registered under "Light" cannot be correlated with the optical absorption, but it probably depends on interfacial defects that limit the FF and then the PCE.

In the end, the P(13) blend presents the biggest difference between the absorption spectra passing from the fresh to aged devices. A strong reorganization of the active layer is expected to occur. As mentioned before, the presence of residual traces of DIO can also induce the degradation of the polymer by hindering the $\pi-$ conjugation and thus the resulting optical absorption. Further investigations should be carried out to discriminate the reasons of the loss in performance, however it is interesting note that the active layer based on the most photostable polymer (in neat film), results to be the less stable in blend.

Again, as for the thermal degradation, the information on the stability behaviour of the D polymer are not sufficient to predict the stability of the corresponding solar cell, in which other factors play simultaneously a role during degradation.

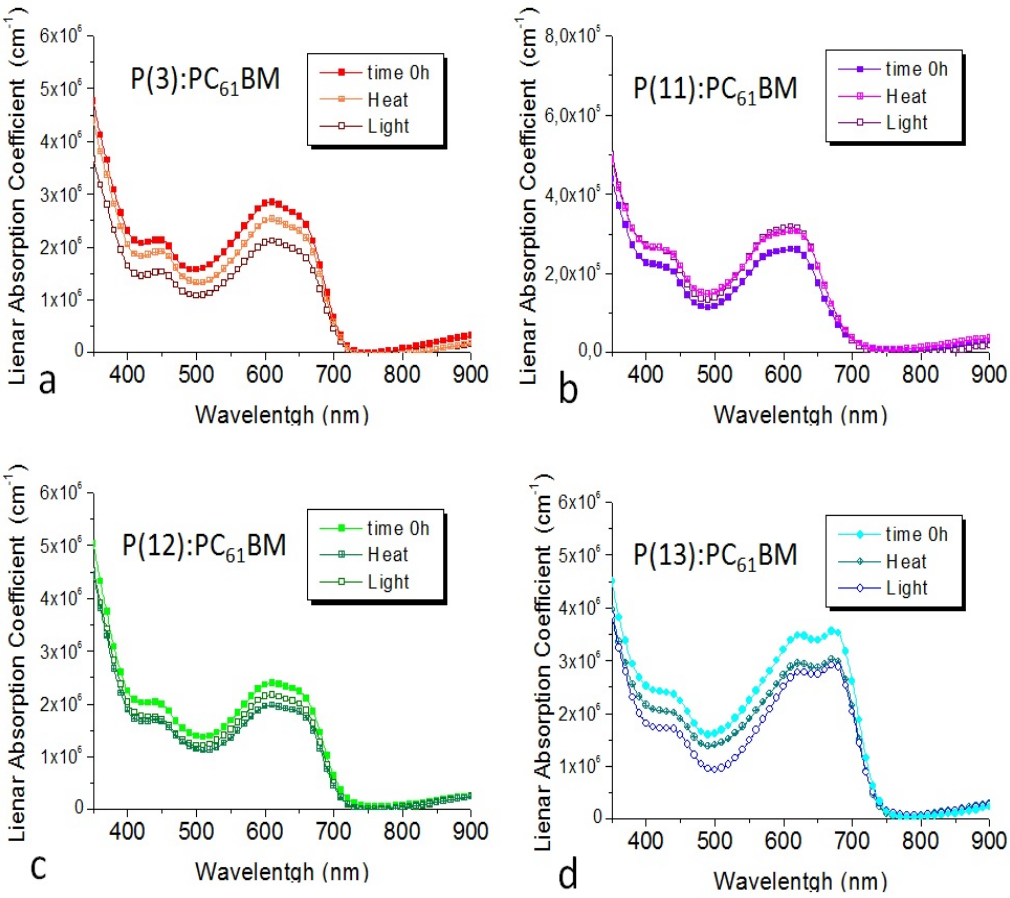

Figure 6.8: Absorption spectra of active layers based on a) P(3), b) P(11), c)P(12) and d) P(13), before ageing, at "Heat" and at "Light" stress in inert atmosphere.

6.4 Influence of the top electrode on the photodegradation

The photodegradation of the active layer is not always the major cause of the OPV degradation [215]. For instance, several groups demonstrated that the cathode interfacial layer has a significant role on the device lifetimes [215] [212] [216]. This observation is valid also for the previous quinoxaline based polymers solar cells. In fact, comparing two similar devices structure ITO/PEDOT:PSS/ActiveLayer/LiF/Al and ITO/PEDT:PSS/ActiveLayer/Al a different photostability is observed, despite processing conditions for devices fabrication are the same. The PCE decay during the "Heat" and the "Light" stress of the two devices structures are reported in Figure 6.9 and 6.10 respectively.
To summarized the percentage of PCE variation from fresh to aged device a corresponding ΔPCE value is reported in Table 6.4.

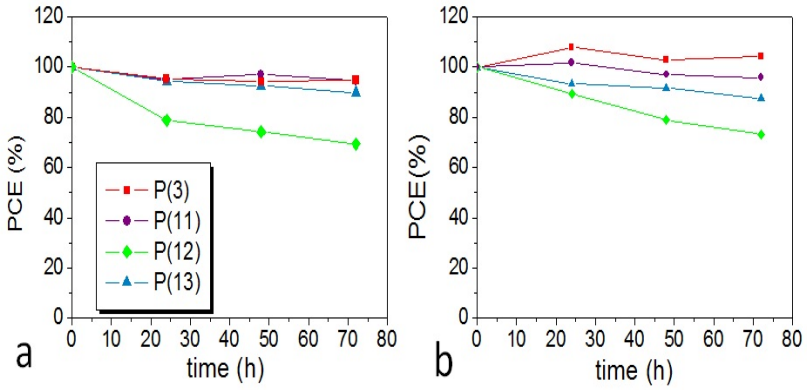

Figure 6.9: PCE decay of P(3)(red), P(11) (purple), P(12) (green), P(13) (blue) based devices heat in dark in inert atmosphere with a) LiF/Al and b) Al as top electrode.

The "Heat" stress has similar effect on the devices when the top electrode LiF/Al is replaced with Al. Probably the temperature reached under illumination is not enough high to induce percolations of atoms from the top electrode into the active layer [156]. Thus the thermal degradation mainly concerns the properties of the other layers.
Diversely the stability under "Light" conditions results worsened for devices where Al is used as top electrode, with a loss in PCE of more than 60% for all devices. This result is not surprising, in fact many research groups [215][212] observed that the photostability of organic solar cells is limited by photo-induced changes that occur at the active organic layer/Al electrode interface. Wang *et al.* [216] suggest, from X-ray photoelectron spectroscopy characteristics, that the interface photodegradation consists of a reduction in bonds associated with organic-metal complexes, with a consequent decrease in organic/metal adhesion. This contact degradation reduces both charge injection (i.e., from the metal to the organic layer) and charge extraction (i.e., from the organic layer to the metal) [216].
However, it has been demonstrated [215] [212] that the presence of a buffer layer, as LiF, can have

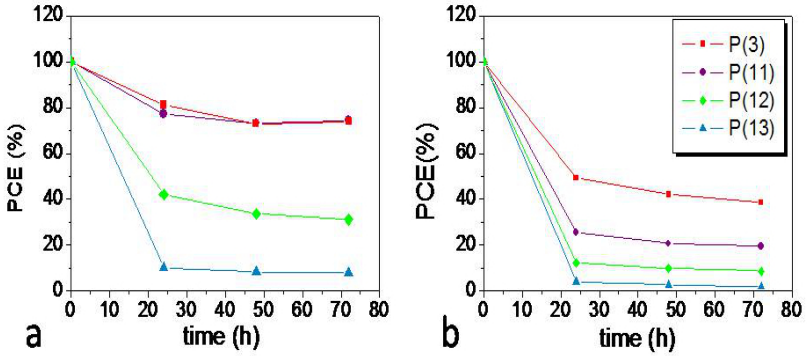

Figure 6.10: PCE decay of P(3)(red), P(11) (purple), P(12) (green), P(13) (blue) based devices under 1 Sun in inert atmosphere with a) LiF/Al and b) Al as top electrode.

significant benefits to minimize this photo-induced degradation and then to improve the photostability.
These considerations, in perfect agreement with the presented results, underline how the organic/metal interface plays a crucial role on the device stability.

6.5 Influence of buffer layers on the photodegradation

A possible strategy to increase the stability of the solar cells is the use of an inverted structure [217] . This configuration is proven to be more stable than the conventional one because no low WF metal electrode is exposed to ambient conditions and therefore its deterioration due to oxidation can be prevented [218]. In inverted structures, to optimize the charge collection at the electrodes, air stable high WF materials e.g. PEDOT:PSS or MoO_3 are typically used as interlayer at the top anode as EBL, while low WFn materials like PFN, PEIE, TiO_x or ZnO are deposited on ITO (cathode) acting as HBL [219]. Among them ZnO is very attractive for its high electron conductivity, good optical transmittance, non toxicity and low cost [220]. In addition, ZnO can be synthesized in the form of nanoparticles (ZnO NPs) which can be deposited from solution generating thin films with high conductivity without the need of strong annealing treatments [221]. ZnO NPs are usually doped with small amounts of metal ions, to increase their electrical properties [222]. The most studied is the aluminum-doped ZnO (AZO) [223], the AZO has the same advantages of ZnO NPs, while having a conductivity which can be three order of magnitude higher [224]. This is a good advantages in the industrial fabrication, where relatively thick layers, in order of 100 nm, are preferred to ensure complete substrate coverage and avoid the risk of defects. Here, the higher conductivity AZO NPs allows to obtained thicker layer maintaining the conductive proprieties necessary for the final device [225].
Despite ZnO shows a variety of suitable properties for photovoltaic applications, one limitation is that its conductivity is negatively affected by chemisorbed oxygen [37]. It is well known that

Active Layer	Top electrode	Δ PCE Heat	Δ PCE Light
P(3):$PC_{61}BM$ (1:1)	LiF/AL	-7%	-27%
	AL	+4%	-61%
P(11):$PC_{61}BM$ (1:1)	LiF/Al	-6%	-28%
	Al	-4%	-79%
P(12):$PC_{61}BM$ (1:1)	LiF/Al	-31%	-70%
	Al	-27%	-91 %
P(13):$PC_{61}BM$ (1:1)	LiF/Al	-15%	-92%
	Al	-13%	-98%

Table 6.4: Variations of PCE under "Heat" and "Light" stress, of devices based on P(3), P(11),P(12), (13) with LiF/Al or Al as top electrode.

O_2 molecules are able to capture electrons from the conduction band of ZnO creating a depletion region near the surface with high resistivity [177]. This process is physically reversible and if ZnO is irradiated with ultraviolet light, oxygen molecules can be released from the ZnO layer leading to an improvement of the ZnO conductivity [220][226]. Although light irradiation could restore the conductivity of ZnO, prolonged illumination could induce irreversible degradation [227][28]. Indeed, UV light soaking in the presence of oxygen triggers the formation of shunts which reduce the n-type behaviour of the ZnO. These shunts are likely p-type defects of the lattice structure that induce an increase of the ZnO WF [5]. As a consequence, the presence of oxygen during the ZnO film processing could represent an issue for the photostability of solar cells.

6.5.1 ZnO characterization

In order to understand how to limit the degradation under prolonged illumination on solar cells, a light soaking test is performed on four devices based on different buffer layer. The formulations of ZnO-based NPs used for the EBLs, are: i) pristine (ZnO) and ii) low (AZO_{low}), iii) medium (AZO_{medium}) and iv) high aluminium-doped (AZO_{high}) [83].
To guarantee a good comparison, all the EBLs are deposited via spin coating in the same condition. The film thickness is intentionally fixed around 40 nm for all ZnO/AZO_x NPs to obtain layers with similar conductivity and avoid the limitations which could occur when using thicker undoped ZnO films. Then, the morphology of each layer is investigated, the AFM images are reported in Figure 6.11. Each samples results very similar between each other, the surfaces are homogeneous and relatively smooth with a RMS of 8 nm, 6 nm, 4 nm and 4 nm for ZnO, AZO_{low}, AZO_{medium} and AZO_{high}, respectively. From an optical point of view, all the ZnO-based layers are characterized

by similar UV-vis spectra with an optical transmittance higher than 80% over the entire visible range and an absorption peak at 345 nm (Figure 6.12). The optical properties, in conjunction with the relatively low surface roughness, make the ZnO-based films compatible for their incorporation in polymer solar cells. Moreover, the energy levels of the Valence band and of the Conductive band are similar for all ZnO (-7,7 eV and -3,6 eV, respectively) and AZO_x (-7,8 eV and -3,7 eV, respectively) layers.

To note, ZnO, AZO_{low}, AZO_{medium} and AZO_{high} are characterized by similar optical, morphological and electronic properties which do not depend on the aluminium concentration in the nanoparticles.

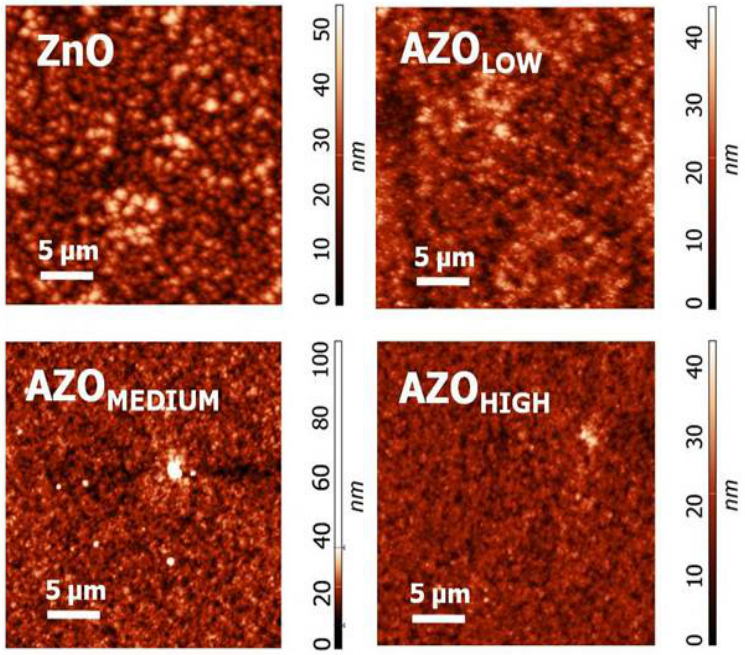

Figure 6.11: AFM images of ZnO, AZO_{low}, AZO_{medium} and AZO_{high} films deposited via spin coater

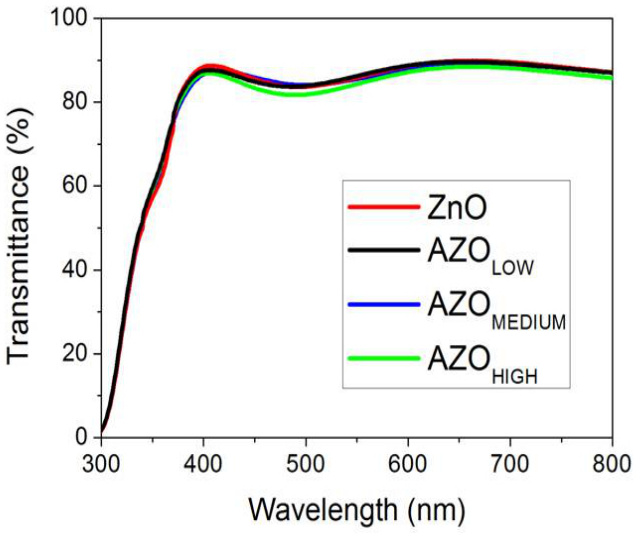

Figure 6.12: Transmittance of ZnO, AZO_{low}, AZO_{medium} and AZO_{high} films with a thickness of 40 nm.

6.5.2 Device Fabrication

The solar cells are based on inverted structure: glass/ITO/EBL/P(1):PC61BM/MoO_3/Ag. Devices have the same active layer based on a D polymer P(14) PFQ2T-BDT with a new chemical structure, similar to the P(3), reported in Chapter 2 Figure 2.2The HOMO and LUMO level, reported in Table 2.1 in Chapter 2, are -3,6 eV and -5,9 eV respectively. The deep HOMO energy levels would result in devices with a high V_{oc} and ensure good air stability [137] [49]. The P(14) is mixed with $PC_{61}BM$ in ratio 1:1 in a solution of ODCB with 3% of DIO.
In order to investigate the effect of the oxygen adsorbed by the ZnO during film processing two groups of devices are fabricated: one with the EBLs deposited in inert atmosphere, and one processed in air.
As reported in Table 6.5, all the Device show nearly identical photovoltaic performances, with initial PCE over 4%, J_{sc} of $\sim$ 8,7 mA/cm^2, V_{oc} of $\sim$ 0,87 V, FF of $\sim$ 55%. Therefore, the OPV parameters of fresh cells are not affected by the Al doping content in the ZnO layer. This is expected since the ZnO, AZO_{low}, AZO_{medium} and AZO_{high} based films show similar optical transmittance, surface roughness and WFs. In addition the photovoltaic response of the solar cells are independent on the processing environment, since it results unvaried if ZnO or AZOx films are either processed in inert atmosphere or in air.

HBL	HBL process conditions	$J_{sc}(mA/cm^2)$	V_{oc} (V)	FF (%)	PCE (%)
ZnO	N_2	8,6 ± 0,3	0,870 ± 0,005	55 ± 2	4,1 ± 0,1
	Air	8,8 ± 0,3	0,870 ± 0,005	55 ± 1	4,2 ± 0,1
AzO_{low}	N_2	8,7 ± 0,1	0,870 ± 0,005	55 ± 1	4,2± 0,1
	Air	8,8 ± 0,3	0,870 ± 0,005	54 ± 2	4,1 ± 0,1
AzO_{medium}	N_2	8,7 ± 0,3	0,870 ± 0,005	55 ± 2	4,2 ± 0,1
	Air	8,7 ± 0,3	0,870 ± 0,005	55 ± 2	4,2 ± 0,1
AzO_{high}	N_2	8,6 ± 0,2	0,860 ± 0,005	56 ± 1	4,1 ± 0,1
	Air	8,8 ± 0,2	0,86 ± 0,01	54 ± 1	4,1 ± 0,1

Table 6.5: PV Parameters of BHJ solar cells based on different HBLs processed in inert atmosphere and in air.)

6.5.3 Devices photodegradation

To study the photodegradation, all devices are kept in a glove box under 1 Sun for 40 hours and their J-V characteristics are measured at defined time intervals.

Figure6.13 a shows the J-V plot of fresh and degraded devices with the ZnO-based HBLs processed in inert atmosphere. After light soaking, the J-V curves result slightly changed in a similar way for all devices (Table 6.6). Indeed, the devices were equally degraded reaching similar OPV parameters (Table 6.6): J_{sc} drops to about 7 mA/cm^2, V_{oc} to 0,81 V, FF to 45% and the PCE decreases from about 4% to 2.5%. A partial decrease of the photovoltaic performance with light soaking can be expected for all devices as observe in the previous section. Despite the P(14) has chemical structure similar to the P(3) the different in the photostability can be related to the presence of DIO in the active layer solution. In any case, since the OPV parameters of all the degraded ZnO-based solar cells are comparable, it is reasonable to assume that the light-induced processes occurring in the four devices are not influenced by the nature of the ZnO-based HBLs when processed in inert atmosphere.

HBL	HBL process conditions	$J_{sc}(mA/cm^2)$	V_{oc} (V)	FF (%)	PCE (%)
ZnO	N_2	7,2 ± 0,3	0,810 ± 0,005	43 ± 1	2,5 ± 0,1
	Air	7,5 ± 0,1	0,660 ± 0,005	35 ± 1	1,7 ± 0,1
AzO_{low}	N_2	6,9 ± 0,5	0,810 ± 0,005	46 ± 1	2,6 ± 0,1
	Air	7,3 ± 0,3	0,810 ± 0,005	43 ± 1	2,5 ± 0,1
AzO_{medium}	N_2	7,0 ± 0,2	0,810 ± 0,005	43 ± 1	2,4 ± 0,1
	Air	6,9 ± 0,2	0,720 ± 0,005	40 ± 1	2,0 ± 0,1
AzO_{high}	N_2	6,9 ± 0,3	0,820 ± 0,005	45 ± 1	2,5 ± 0,1
	Air	6,8 ± 0,1	0,720 ± 0,005	41 ± 1	2,0 ± 0,1

Table 6.6: PV Parameters of BHJ solar cells based on different HBLs processed in inert atmosphere and in air after photodegradation test

On the contrary, the degradation trend observed for the devices based on air processed HBLs is considerably different. As shown in Figure 6.13b and in Table 6.6, degraded devices exhibit different J-V plots. In particular it can be observed that the least stable solar cell is device with undoped ZnO as HBL, while the most stable solar cell is device where the ZnO-based HBL is prepared with the lowest concentration of aluminium dopant. The other formulations of AZO_x show an intermediate behaviour, but still an increased stability as compared to device based on undoped ZnO. Interestingly the degraded device based on ZnO_{low} gives the same photovoltaic response (same J-V curve) irrespective of the AZO processing atmosphere.

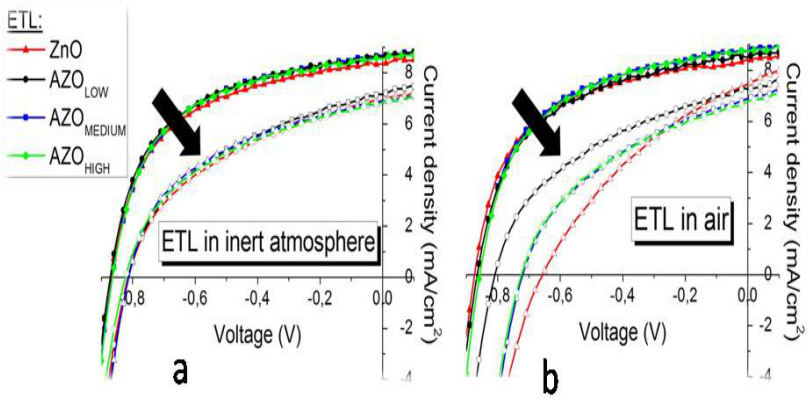

Figure 6.13: J-V plots of fresh (filled symbols) and degraded (empty symbols) solar cells with HBL of i) ZnO (red), ii) AZO_{low} (black), AZO_{medium} (blue) and AZO_{high} (green). The ZnO-based HBLs are processed a)in inert atmosphere, N_2, and b)in air. The black arrows highlight the transition of the J-V curves when passing from fresh to degraded devices.

The degradation processes which involve the HBL of a solar cell usually affect the bulk conductivity and/or its charge selectivity [227][28].

It has been demonstrated that organic solar cells containing a ZnO film which has been previously UV soaked in dry air, suffer of shunting losses [228]. Indeed, during illumination, the UV treatment of oxygen present in dry air causes the introduction in the ZnO lattice of interstitial oxygen atoms which act as p-type defects [229]. As a result, the Fermi level of ZnO decreases, promoting the extraction of holes from the valence band of the D material that affect the V_{oc} and the FF [230], in agreement with the results (Table 6.6). Indeed, oxygen adsorbed on ZnO/AZO_x during processing, when released under illumination, causes of the degradation of the devices through the shunting process.

To verify the occurrence of the UV/oxygen-related degradation process in the present systems, all the devices with air-processed HBLs are degraded under 1 Sun UV-filtered. Since oxygen can degrade ZnO/AZO_x films only under UV irradiation, the use of a filter should hinder the described shunting process. The J-V plots of all the devices before and after degradation with the UV-filtered light are reported in Figure 6.14. As expected all the solar cells are now characterized by the same J-V plot after UV-filtered light-soaking. Indeed as oxygen cannot interact with the ZnO/AZO_x-based HBL, the devices are equally affected by the same degradation processes, which is in this case independent on the HBL nature and which involves the remaining layers of the devices.

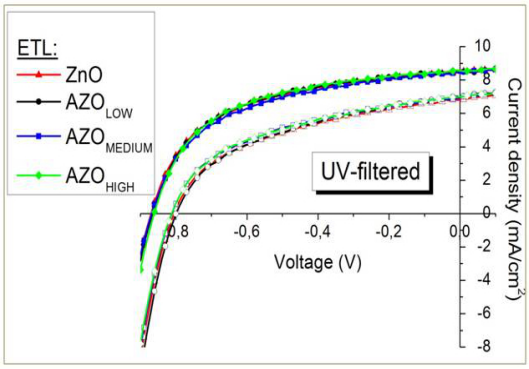

Figure 6.14: J-V plots of fresh (filled symbols) and degraded (empty symbols) solar cells with HBL of i) ZnO (red), ii) AZO_{low} (black), AZO_{medium} (blue) and AZO_{high} (green). The HBLs are processed in air and the light soaking is filtered by an UV filter.

6.6 Conclusion

In conclusion, as observed for the thermal stability, also the photostability of a solar cells depends on many factors. First of all, the reported study demonstrated that: focusing the attention on the photodegradation of a pure D polymer, despite it can provide precious information on the intrinsic properties of different materials, remains rather inconclusive in terms of stability assessments of corresponding OPV devices. Indeed, the introduction of additional variables such as fullerenes molecules, solvent additives, different processing conditions strongly influences the BHJ self-organization, the morphological stability and thus the resulting photodegradation mechanisms. In addition, it has been demonstrated that the interface between the active layer and top electrode is crucial for the degradation. Detrimental interaction with Al is observed under light soaking, that can be prevented adding a buffer layer. However, in order to improve the device lifetime, buffer layers and metal contact have to be chosen carefully. For example, LiF results beneficial for the photostability preventing the photo induced interactions between active layer and Al, however it has a negative effect under thermal stress, due to the percolation of Li atoms into the active layer. Moreover, in view of an industrial product, where all layers are deposited in air, the contamination of oxygen, that can accelerate the photo degradation, has to be considered.
For this reason, the concept of inverted structure has been introduced. This configuration results more stable because no low WF metal electrode is exposed to ambient and therefore oxidation can be prevented. Despite this advantage, also in the inverted structure, as for the standard, the buffer layers can affect the resulting stability. In fact it has been demonstrated that, when ZnO/AZO is used as HBL, the presence of oxygen during the layer deposition can be detrimental for the photostability of the resulting solar cell. In particular the air-processed devices based on undoped ZnO result particularly affected by degradation while, using AZO, the loss of performance ascribed to ZnO-oxygen interaction can be partially or totally prevented.

Conclusions and future work

In the field of Photovoltaic technologies the organic solar cells are particularly attractive because of their ease of processing, mechanical flexibility and potential low cost production techniques. So far, the reported efficiencies are not high enough to allow direct competition against mature photovoltaic technologies, however with the introduction of new photoactive materials, device architectures and light management structures, the power conversion efficiencies, at laboratory scale, has rapidly reached the 12%, showing a great potential and a bright future for organic solar cells. Nevertheless, in view of commercial products, two main problems are still unresolved: the relatively low performance of the modules and their lifetime.

In sight of this, in the first part of this work, particular attention was given to the optimization of the BHJ devices performances, based on different photoactive materials and fabricated with a solution based deposition (doctor blade) technique fully compatible with roll-to-roll production. In particular six different donor polymers based on the same Donor and Acceptor units have been investigated in order to correlate their structure with the corresponding device performance. As a result, promising approaches to further optimize the polymer's optoelectrial properties, and thus the corresponding device performance, are demonstrated.

The second part of the work was focused on the solar cells lifetime, in particular on the thermal and photostability. First, the thermal evolution of active layers based on two standard polymers (P3HT and PTB7) has been investigated. The highly crystalline polymer (P3HT) showed a higher thermal stability than the amorphous one (PTB7). Through a morphological characterization it has been demonstrated that the main degradation process involved was the fullerene aggregation, which is likely facilitated in a soft matrix of an amorphous polymer. Moreover, the devices comparison showed that: despite the initial efficiency of P3HT based solar cell was half then the PTB7 based device, after the thermal stress the two residual performances become comparable, underlining that in view of a commercial product, a correct compromise between stability and efficiency has to be reached before to get into the market.

In this context, an innovative fast capacitance based thermal test has been proposed. This new approach not only identifies the stable device at a particular stress test temperature as a standard thermal test, but it gives additional information regarding the limit operating temperature above which the device becomes thermally unstable. Thus, this new method results as an interesting tools in view of an industrial production. In addition it was demonstrated the potential of the Impedance Spectroscopy technique as a powerful tool to indentify and explain the degradation mechanisms occurring within the device during the ageing process. As future works it would be

interesting to investigate different photoactive materials and device structures in order to establish general guidelines to obtain stable organic solar cells.

In the end, the photostability issue was addressed comparing the behavior of four different photoactive materials. As a result, a discrepancy between the photo degradation of the pure donor polymers and the corresponding devices was found. The reasons of this incongruence are manifold. Firstly the introduction of additional variables such as fullerenes molecules, solvent additives, different processing conditions, strongly influences the BHJ self-organization, the morphological stability and thus the resulting photo degradation mechanisms. In addition, it has been demonstrated that also the buffer layers photostability plays a crucial role on the whole device lifetime. Solutions to limit the device photo degradation are proposed.

For future work it would be interesting to investigate the behavior under light soaking of different device architectures, varying the combination of active and buffer layers, in order to understand and possibly prevent the degradation mechanisms.

Bibliography

[1] URL `http://www.erec.org/fileadmin/erec_docs/Documents/Publications`.

[2] M. Hosenuzzaman, N.A. Rahim, J. Selvaraj, M. Hasanuzzaman, A.B.M.A. Malek, and A. Nahar. Global prospects, progress, policies, and environmental impact of solar photovoltaic power generation. *Renewable and Sustainable Energy Reviews*, 41:284 – 297, 2015.

[3] *Renewable Energy Policy Network for the 21st Century*, 2014.

[4] Seth B. Darling and Fengqi You. The case for organic photovoltaics. *RSC Advanced*, 3: 17633–17648, 2013.

[5] Bradley A. MacLeod, Bertrand J. Tremolet de Villers, Philip Schulz, Paul F. Ndione, Hyungchul Kim, Anthony J. Giordano, Kai Zhu, Seth R. Marder, Samuel Graham, Joseph J. Berry, Antoine Kahn, and Dana C. Olson. Stability of inverted organic solar cells with zno contact layers deposited from precursor solutions. *Energy Environ. Sci.*, 8:592–601, 2015.

[6] Joseph D. Bergesen, Garvin A. Heath, Thomas Gibon, and Sangwon Suh. Thin-film photovoltaic power generation offers decreasing greenhouse gas emissions and increasing environmental co-benefits in the long term. *Environmental Science & Technology*, 48(16):9834–9843, 2014.

[7] Michael Dale and Sally M. Benson. Energy Balance of the Global Photovoltaic (PV) Industry - Is the PV Industry a Net Electricity Producer? *Environmental Science & Technology*, 47 (7):3482–3489, 2013.

[8] Christiane Becker, Tobias Sontheimer, Simon Steffens, Simone Scherf, and Bernd Rech. Polycrystalline silicon thin films by high-rate electronbeam evaporation for photovoltaic applications - influence of substrate texture and temperature. *Energy Procedia*, 10:61 – 65, 2011.

[9] Yukimi Ichikawa, Takashi Yoshida, Toshio Hama, Hiroshi Sakai, and Kouichi Harashima. Production technology for amorphous silicon-based flexible solar cells. *Solar Energy Materials and Solar Cells*, 66:107 – 115, 2001.

[10] D. L. Staebler and C. R. Wronski. Reversible conductivity changes in discharge produced amorphous si. *Applied Physics Letters*, 31(4):292–294, 1977.

[11] V. Plotnikov, X. Liu, N. Paudel, D. Kwon, K.A. Wieland, and A.D. Compaan. Thin-film cdte cells: Reducing the cdte. *Thin Solid Films*, 519(21):7134 – 7137, 2011.

[12] Martin A. Green, Keith Emery, Yoshihiro Hishikawa, Wilhelm Warta, and Ewan D. Dunlop. Solar cell efficiency tables (version 45). *Progress in Photovoltaics: Research and Applications*, 23:1–9, 2015.

[13] Vasilis M. Fthenakis, Hyung Chul Kim, and Erik Alsema. Emissions from photovoltaic life cycles. *Environmental Science & Technology*, 42(6):2168–2174, 2008.

[14] Brian O'Regan and Michael Gratzel. A low-cost, high-efficiency solar cell based on dye-sensitized colloidal TiO2 films,. *Nature*, 353(6346):737–740, 1991.

[15] Martin A. Green, Keith Emery, Yoshihiro Hishikawa, Wilhelm Warta, and Ewan D. Dunlop. Solar cell efficiency tables (version 45). *Progress in Photovoltaics: Research and Applications*, 23(1):1–9, 2015.

[16] Dianyi Liu and Timothy L Kelly. Perovskite solar cells with a planar heterojunction structure prepared using room-temperature solution processing techniques,. *Nature Photonics*, 8(2): 133–38, 2014.

[17] Letian Dou, Jingbi You, Ziruo Hong, Zheng Xu, Gang Li, Robert a Street, and Yang Yang. 25th anniversary article: a decade of organic/polymeric photovoltaic research. *Adv. Mater.*, 25(46):6642–71, 2013.

[18] Frederik C. Krebs, Suren A. Gevorgyan, and Jan Alstrup. roll-to-roll process to flexible polymer solar cells: model studies,, manufacture and operational stability studies. *J. Mater. Chem.*, 19(30):5442–5451, 2009.

[19] T. M. Eggenhuisen, Y. Galagan, a. F. K. V. Biezemans, T. M. W. L. Slaats, W. P. Voorthuijzen, S. Kommeren, S. Shanmugam, J. P. Teunissen, a. Hadipour, W. J. H. Verhees, S. C. Veenstra, M. J. J. Coenen, J. Gilot, R. Andriessen, and W. a. Groen. High efficiency, fully inkjet printed organic solar cells with freedom of design,. *J. Mater. Chem. A*, 3(14):7255–7262, 2015.

[20] P. Sommer-Larsen, M. Jorgensen, R. R. Sondergaard, M. Hoesel, and F. C. Krebs. It is all in the Pattern-High-Efficiency Power Extraction from Polymer Solar Cells through High-Voltage Serial Connection,. *Energy Technol.*, 1(1):15–19, 2013.

[21] Frederik C. Krebs, Nieves Espinosa, Markus Hösel, Roar R. Søndergaard, and Mikkel Jørgensen. 25th Anniversary Article: Rise to Power - OPV-Based Solar Parks,. *Adv. Mater.*, 26(1):29–39, 2014.

[22] Yannick-Serge Zimmermann, Andreas Schä, ffer, Christoph Hugi, Karl Fent, Philippe F.-X. Corvini, and Markus Lenz. Organic photovoltaics: Potential fate and effects in the environment,. *Environ. Int.*, 49:128–140, 2012.

[23] Yinhua Zhou, Canek Fuentes-Hernandez, Talha M Khan, Jen-Chieh Liu, James Hsu, Jae Won Shim, Amir Dindar, Jeffrey P Youngblood, Robert J Moon, and Bernard Kippelen. Recyclable organic solar cells on cellulose nanocrystal substrates. *Sci. Rep.*, 3:1536, 2013.

[24] Marianne Strange, David Plackett, Martin Kaasgaard, and Frederik C. Krebs. Biodegradable polymer solar cells. *Solar Energy Materials and Solar Cells*, 92(7):805 – 813, 2008.

[25] Mihai Irimia-Vladu, Pavel A. Troshin, Melanie Reisinger, Lyuba Shmygleva, Yasin Kanbur, Günther Schwabegger, Marius Bodea, Reinhard Schwödiauer, Alexander Mumyatov, Jeffrey W. Fergus, Vladimir F. Razumov, Helmut Sitter, Niyazi Serdar Sariciftci, and Siegfried Bauer. Biocompatible and biodegradable materials for organic field-effect transistors. *Advanced Functional Materials*, 20(23):4069–4076, 2010.

[26] Anna Posati Tamara Tessarolo Marta Bolognesi Margherita Cavallini Susanna Toffanin Stefano Benfenati Valentina Seri Mirko Ruani Giampiero Muccini Michele Prosa, Mario Sagnella and Roberto Zamboni. Integration of a silk fibroin based film as a luminescent down-shifting layer in ITO-free organic solar cells,. *RSC Advanced*, 4(84):44815–44822, 2014.

[27] Yu-Sheng Hsiao, Wha-Tzong Whang, Chih-Ping Chen, and Yi-Chun Chen. High-conductivity poly(3,4-ethylenedioxythiophene):poly(styrene sulfonate) film for use in ITO-free polymer solar cells. *J. Mater. Chem.*, 18(48):5948, 2008.

[28] Pablo Romero-Gomez, Rafael Betancur, Alberto Martinez-Otero, Xavier Elias, Marina Mariano, Beatriz Romero, Belén Arredondo, Ricardo Vergaz, and Jordi Martorell. Enhanced stability in semi-transparent PTB7/PC71BM photovoltaic cells. *Sol. Energy Mater. Sol. Cells*, 137:44–49, 2015.

[29] Chu-Chen Chueh, Kai Yao, Hin-Lap Yip, Chih-Yu Chang, Yun-Xiang Xu, Kung-Shih Chen, Chang-Zhi Li, Peng Liu, Fei Huang, Yiwang Chen, Wen-Chang Chen, and Alex K.-Y. Jen. Non-halogenated solvents for environmentally friendly processing of high-performance bulk-heterojunction polymer solar cells,. *Energy Environ. Sci.*, 6(11):3241, 2013.

[30] Marta Tessarolo Mario Prosa Giovanni Donati Stefano Toffanin Michele Muccini Margherita Bolognesi, Mirko Seri. Enhanced BHJ stability through environmentally friendly processing: local morphological investigations on complete solar cells using non-invasive microscopy techniques.

[31] T. Posati M. Nocchetti V. Benfenati M. Seri G. Ruani M. Muccini M. Bolognesi, M. Tessarolo. Efficiency enhancement of P3HT: PCBM solar cells containing scattering Zn-Al hydrotalcite nanoparticles in the PEDOT: PSS layer. *Organic Photonics and Photovoltaics*, 1:1–10, 2013.

[32] M.C. Scharber and N.S. Sariciftci. Efficiency of bulk-heterojunction organic solar cells. *Progress in Polymer Science*, 38(12):1929 – 1940, 2013.

[33] Ning Li, Derya Baran, George D. Spyropoulos, Hong Zhang, Stephane Berny, Mathieu Turbiez, Tayebeh Ameri, Frederik C. Krebs, and Christoph J. Brabec. Environmentally printing efficient organic tandem solar cells with high fill factors: A guideline towards 20 *Advanced Energy Materials*, 4(11):1400084, 2014.

[34] Jing-De Chen, Chaohua Cui, Yan-Qing Li, Lei Zhou, Qing-Dong Ou, Chi Li, Yongfang Li, and Jian-Xin Tang. Single-junction polymer solar cells exceeding 10efficiency. *Advanced Materials*, 27(6):1035–1041, 2015.

[35] Abd. Rashid bin Mohd Yusoff, Dongcheon Kim, Hyeong Pil Kim, Fabio Kurt Shneider, Wilson Jose da Silva, and Jin Jang. A high efficiency solution processed polymer inverted triple-junction solar cell exhibiting a power conversion efficiency of 11.83%. *Energy Environ. Sci.*, 8(1):303–316, 2015.

[36] URL `www.nrel.gov`.

[37] Anthony J. Morfa, Brandon I. MacDonald, Jegadesan Subbiah, and Jacek J. Jasieniak. Understanding the chemical origin of improved thin-film device performance from photodoped zno nanoparticles. *Solar Energy Materials and Solar Cells*, 124:211 – 216, 2014.

[38] Christoph Lungenschmiedb Oskar Armbrusterc Siegfried Bauerc H.-J. Egelhaafa Jens Haucha Andrea Seemanna, Tobias Sauermanna. Reversible and irreversible degradation of organic solar cell performance by oxygen. *Solar Energy*, 85:1238 – 1249, 2011.

[39] Andrea Buri Robert Müller Daniele Di Nuzzo-Paul Heremans Eszter Voroshazi, Bregt Verreet. Influence of cathode oxidation via the hole extraction layer in polymer:fullerene solar cells. *Organic Electronics*, 12(5):736 – 744, 2011.

[40] Sabine Bertho, Ilse Haeldermans, Ann Swinnen, Wouter Moons, Tom Martens, Laurence Lutsen, Dirk Vanderzande, Jean Manca, Alessia Senes, and Annalisa Bonfiglio. Influence of thermal ageing on the stability of polymer bulk heterojunction solar cells. *Sol. Energy Mater. Sol. Cells*, 91(5):385–389, 2007.

[41] Roland Steim, F. René Kogler, and Christoph J. Brabec. Interface materials for organic solar cells. *J. Mater. Chem.*, 20:2499, 2010.

[42] Ronn Andriessen Nadia Grossiord, Jan M. Kroon and Paul W.M. Blom. Degradation mechanisms in organic photovoltaic devices. *Org. Electron.*, 13(3):432–456, 2012.

[43] Antonio Facchetti. π-conjugated polymers for organic electronics and photovoltaic cell applications. *Chemistry of Materials*, 23:733, 2011.

[44] URL `www.belectric.com/en/organic-photovoltaics/`.

[45] Roland Steim, Tayebeh Ameri, Pavel Schilinsky, Christoph Waldauf, Gilles Dennler, Markus Scharber, and Christoph J. Brabec. Organic photovoltaics for low light applications. *Sol. Energy Mater. Sol. Cells*, 95(12):3256–3261, 2011.

[46] Christopher J. M. Emmott, Jason A. Rohr, Mariano Campoy-Quiles, Thomas Kirchartz, Antonio Urbina, Nicholas J. Ekins-Daukes, and Jenny Nelson. Organic photovoltaic greenhouses: a unique application for semi-transparent pv? *Energy Environ. Sci.*, 8(4):1317–1328, 2015.

[47] URL `http://eight19.com/company/off-grid-opportunity`.

[48] Hideki Shirakawa, Edwin J. Louis, Alan G. MacDiarmid, Chwan K. Chiang, and Alan J. Heeger. Synthesis of electrically conducting organic polymers: halogen derivatives of polyacetylene $(CH)_x$. *J. Chem. Soc. Chem. Commun.*, pages 578–580, 1977.

[49] Harald Hoppe and Niyazi Serdar Sariciftci. Organic solar cells: An overview. *J. Mater. Res.*, 19(07):1924–1945, 2011.

[50] Barry P. Rand, Jan Genoe, Paul Heremans, and Jef Poortmans. Solar cells utilizing small molecular weight organic semiconductors. *Progress in Photovoltaics: Research and Applications*, 15(8):659–676, 2007.

[51] J. Frenkel. On the transformation of light into heat in solids. i. *Phys. Rev.*, 37:17–44, 1931.

[52] Rui Zhu Gang Li and Yang Yang. Polymer solar cells. *Nature Photonics*, 6:153, 2012.

[53] H. Kallmann and M. Pope. Photovoltaic effect in organic crystals. *The Journal of Chemical Physics*, 30(2):585–586, 1959.

[54] C. W. Tang. Two-layer organic photovoltaic cell. *Applied Physics Letters*, 48:183, 1986.

[55] Hai Wang, Hai-Yu Wang, Bing-Rong Gao, Lei Wang, Zhi-Yong Yang, Xiao-Bo Du, Qi-Dai Chen, Jun-Feng Song, and Hong-Bo Sun. Exciton diffusion and charge transfer dynamics in nano phase-separated P3HT/PCBM blend films. *Nanoscale*, 3:2280–2285, 2011.

[56] A. J. Heeger F. Wudl N. S. Sariciftci, L. Smilowitz. Photoinduced electron transfer from a conducting polymer to buckminsterfullerene. *Science*, 258:1474, 2013.

[57] K. Yoshino S. Morita, A. A. Zakhidov. Doping effect of buckminsterfullerene in conducting polymer: Change of absorption spectrum and quenching of luminescene. *Solid State Communications*, 82:249, 1992.

[58] N. S. Sariciftci A. J. Heeger. Patent us 1992/5331183 a. 1992.

[59] N. C. Greenham E. A. Marseglial R. H. Friend S. C. Moratti J. J. M. Halls, C. A. Walsh and A. B. Holmes. Efficient photodiodes from interpenetrating polymer networks. *Nature*, 376:498, 1995.

[60] J. C. Hummelen F. Wudl A. J. Heeger G. Yu, J. Gao. Polymer photovoltaic cells: Enhanced efficiencies via a network of internal donor-acceptor heterojunctions. *Science*, 376:1789, 1995.

[61] L. J. A. Koster Wp.W.M. Blom, V.D. Mihailetchi and D.E. Markov. Device physics of polymer:fullerene bulk heterojunction solar cells. *Advanced Materials*, 19(12):1551–1556, 2007.

[62] Peter Peumans, Aharon Yakimov, and Stephen R. Forrest. Small molecular weight organic thin-film photodetectors and solar cells. *Journal of Applied Physics*, 93(7):3693–3723, 2003.

[63] André Moliton and Jean-Michel Nunzi. How to model the behaviour of organic photovoltaic cells. *Polymer International*, 55(6):583–600, 2006.

[64] Peter Peumans and Stephen R. Forrest. Separation of geminate charge-pairs at donor-acceptor interfaces in disordered solids. *Chemical Physics Letters*, 398(1):27–31, 2004.

[65] Germà Garcia-Belmonte, Antoni Munar, Eva M. Barea, Juan Bisquert, Irati Ugarte, and Roberto Pacios. Charge carrier mobility and lifetime of organic bulk heterojunctions analyzed by impedance spectroscopy. *Org. Electron.*, 9:847–851, 2008.

[66] Markus Koppe Patrick Denk Christoph Waldauf Alan J. Heeger Markus C. Scharber, David Mühlbacher and Christoph J. Brabec. Design Rules for Donors in Bulk-Heterojunction Solar Cells-Towards 10% Energy-Conversion Efficiency. *Advanced Materials*, 18:789, 2006.

[67] C. J. Brabec, a. Cravino, D. Meissner, N. S. Sariciftci, T. Fromherz, M. T. Rispens, L. Sanchez, and J. C. Hummelen. Origin of the open circuit voltage of plastic solar cells. *Adv. Funct. Mater.*, 11(5):374–380, 2001.

[68] Yong Hyun Kim, Christoph Sachse, Michael L. Machala, Christian May, Lars Ḿuller-Meskamp, and Karl Leo. Highly conductive pedot:pss electrode with optimized solvent and thermal post-treatment for ito-free organic solar cells. *Advanced Functional Materials*, 21(6): 1076–1081, 2011.

[69] X Crispin, F L E Jakobsson, A Crispin, P C M Grim, P Andersson, A Volodin, C Van Haesendonck, M Van Der Auweraer, W R Salaneck, and M Berggren. The Origin of the High Conductivity of of Poly(3,4-ethylenedioxythiophene)-Poly(styrenesulfonate) (PEDOT-PSS) Plastic Electrodes. *Chem. Mater.*, 18(4):4354–4360, 2006.

[70] Aung Ko Ko Kyaw, Dong Hwan Wang, David Wynands, Jie Zhang, Thuc-Quyen Nguyen, Guillermo C. Bazan, and Alan J. Heeger. Improved Light Harvesting and Improved Efficiency by Insertion of an Optical Spacer (ZnO) in Solution-Processed Small-Molecule Solar Cells. *Nano Letters*, 13(8):3796–3801, 2013.

[71] Sadok Ben Dkhil, David Duché, Meriem Gaceur, Anil K. Thakur, Fatima Bencheikh Aboura, Ludovic Escoubas, Jean-Jacques Simon, Antonio Guerrero, Juan Bisquert, GermĠarcia-Belmonte, Qinye Bao, Mats Fahlman, Christine Videlot-Ackermann, Olivier Margeat, and Jörg Ackermann. Interplay of optical, morphological, and electronic effects of zno optical spacers in highly efficient polymer solar cells. *Advanced Energy Materials*, 4(18):1400805, 2014.

[72] P. Schilinsky, C. Waldauf, and C.J.â Brabec. Performance Analysis of Printed Bulk Heterojunction Solar Cells. *Adv. Funct. Mater.*, 16(13):1669–1672, 2006.

[73] "Frederik C. Krebs. Polymer solar cell modules prepared using roll-to-roll methods: Knife-over-edge coating, slot-die coating and screen printing. *Solar Energy Materials and Solar Cells*, 93(4):465 – 475, 2009.

[74] Dechan Angmo, Markus Hö, sel, and Frederik C. Krebs. All solution processing of ito-free organic solar cell modules directly on barrier foil. *Sol. Energy Mater. Sol. Cells*, 107:329–336, 2012.

[75] Margherita Bolognesi, Desta Gedefaw, Dongfeng Dang, Patrik Henriksson, Wenliu Zhuang, Marta Tessarolo, Ergang Wang, Michele Muccini, Mirko Seri, and Mats R. Andersson. 2d π-conjugated benzo$[1,2-b:4,5-b']$dithiophene- and quinoxaline-based copolymers for photovoltaic applications. *RSC Adv.*, 3(46):24543, 2013.

[76] Marta Tessarolo, Antonio Guerrero, Desta Gedefaw, Margherita Bolognesi, Mario Prosa, Xiaofeng Xu, Mahdi Mansour, Ergang Wang, Mirko Seri, Mats R. Andersson, Michele Muccini, and Germá Garcia-Belmonte. Predicting thermal stability of organic solar cells through an easy and fast capacitance measurement. *Solar Energy Materials and Solar Cells*, 141:240 – 247, 2015.

[77] Marta Tessarolo, Desta Gedefaw, Margherita Bolognesi, Fabiola Liscio, Patrik Henriksson, Wenliu Zhuang, Silvia Milita, Michele Muccini, Ergang Wang, Mirko Seri, and Mats R. Andersson. Structural tuning of quinoxaline-benzodithiophene copolymers via alkyl side chain manipulation: synthesis, characterization and photovoltaic properties. *J. Mater. Chem. A*, 2:11162–11170, 2014.

[78] Desta Gedefaw, Marta Tessarolo, Mario Prosa, Margherita Bolognesi, Patrik Henriksson, Wenliu Zhuang, Mirko Seri, Michele Muccini, and Mats R Andersson. Induced photodegradation of quinoxaline based copolymers for photovoltaic applications. *Solar Energy Materials and Solar Cells*, 144:150–158, 2016.

[79] Desta Gedefaw, Marta Tessarolo, Wenliu Zhuang, Renee Kroon, Ergang Wang, Margherita Bolognesi, Mirko Seri, Michele Muccini, and Mats R. Andersson. Conjugated polymers based on benzodithiophene and fluorinated quinoxaline for bulk heterojunction solar cells: thiophene versus thieno[3,2-b]thiophene as π-conjugated spacers. *Polym. Chem.*, 5(6):2083, 2014.

[80] Gang Li, Vishal Shrotriya, Jinsong Huang, Yan Yao, Tom Moriarty, Keith Emery, and Yang Yang. High-efficiency solution processable polymer photovoltaic cells by self-organization of polymer blends. *Nat. Mater.*, 4(11):864–868, 2005.

[81] Jiangbin Xia Szu Ting Tsai Yue Wu Gang Li Claire Ray Yongye Liang, Zheng Xu and Luping Yu. For the bright future-bulk heterojunction polymer solar cells with power conversion efficiency of 7.4%. *Adv. Mater.*, 22(20):135–138, 2010.

[82] S.C. Price, a.C. Stuart, L.G. Yang, H.X. Zhou, and W. You. Fluorine substituted conjugated polymer of medium bandwidth yield 7% efficiency in polymer-fullerine solar cells. *J. Am. Chem. Soc.*, 133:4625–4631, 2011.

[83] Mario Prosa, Marta Tessarolo, Margherita Bolognesi, Olivier Margeat, Desta Gedefaw, Meriem Gaceur, Christine Videlot-Ackermann, Mats R Andersson, Michele Muccini, Mirko

Seri, and Jörg Ackermann. Enhanced ultraviolet stability of air-processed polymer solar cells by al doping of the zno interlayer. *ACS Applied Materials & Interfaces*, 2016.

[84] Jonathan D. Servaites, Mark a. Ratner, and Tobin J. Marks. Organic solar cells: A new look at traditional models. *Energy Environ. Sci.*, 4(11):4410, 2011.

[85] Kevin J. Bergemann and Stephen R. Forrest. Measurement of exciton diffusion lengths in optically thin organic films. *Applied Physics Letters*, 99(24):243303, 2011.

[86] Jonathan D. Servaites, Mark a. Ratner, and Tobin J. Marks. Organic solar cells: A new look at traditional models,. *Energy Environ. Sci.*, 4(11):4410, 2011.

[87] Matthew Wright and Ashraf Uddin. Organic-inorganic hybrid solar cells: A comparative review. *Solar Energy Materials and Solar Cells*, 107:87 – 111, 2012.

[88] P. W. M. Blom, M. J. M. de Jong, and J. J. M. Vleggaar. Electron and hole transport in poly(p-phenylene vinylene) devices. *Appl. Phys. Lett.*, 68(23):3308, 1996.

[89] G. Binnig, C. F. Quate, and Ch. Gerber. Atomic force microscope. *Phys. Rev. Lett.*, 56: 930–933, 1986.

[90] Hans-Jürgen Butt, Brunero Cappella, and Michael Kappl. Force measurements with the atomic force microscope: Technique, interpretation and applications. *Surface Science Reports*, 59:1 – 152, 2005.

[91] Jacob N. Israelachvili. *Intermolecular and Surface Forces*. Academic Press, 2011.

[92] Alisher Maksumov, Ruxandra Vidu, Ahmet Palazoglu, and Pieter Stroeve. Enhanced feature analysis using wavelets for scanning probe microscopy images of surfaces. *Journal of Colloid and Interface Science*, 272(2):365 – 377, 2004.

[93] Maria B. Retschke Stefan A. L. Weber Rudiger Berger, Hans-Jurgen Butt. Electrical modes in scanning probe microscopy. *Macromolecular Rapid Communications*, 30(14):1167–1178, 2009.

[94] Andrea Liscio, Vincenzo Palermo, e Gentilini, Desiré, Fabian Nolde, Klaus Mü, llen, and Paolo Samorì. Quantitative measurement of the local surface potential of π-conjugated nanostructures: A Kelvin probe force microscopy study. *Advanced Functional Materials*, 16: 1407–1416, 2006.

[95] Roland Rösch, David M. Tanenbaum, Mikkel Jørgensen, Marco Seeland, Maik Bärenklau, Martin Hermenau, Eszter Voroshazi, Matthew T. Lloyd, Yulia Galagan, Birger Zimmermann, Uli Würfel, Markus Hösel, Henrik F. Dam, Suren a. Gevorgyan, Suleyman Kudret, Wouter Maes, Laurence Lutsen, Dirk Vanderzande, Ronn Andriessen, Gerardo Teran-Escobar, Monica Lira-Cantu, Agnès Rivaton, Gülsah Y. Uzunoglu, David Germack, Birgitta Andreasen, Morten V. Madsen, Kion Norrman, Harald Hoppe, and Frederik C. Krebs. Investigation of the degradation mechanisms of a variety of organic photovoltaic devices by combination of

imaging techniques the ISOS-3 inter-laboratory collaboration. *Energy Environ. Sci.*, 5(4): 6521, 2012.

[96] Matthieu Manceau, s Rivaton, Agnè, Jean-Luc Gardette, phane Guillerez, Sté, and lla Lemaître, Noë. Light-induced degradation of the P3HT-based solar cells active layer. *Sol. Energy Mater. Sol. Cells*, 95:1315–1325, 2011.

[97] Francisco Fabregat-Santiago, Germa Garcia-Belmonte, Ivan Mora-Sero, and Juan Bisquert. Characterization of nanostructured hybrid and organic solar cells by impedance spectroscopy. *Phys. Chem. Chem. Phys.*, 13(20):9083–9118, 2011.

[98] Thomas Kirchartz, Wei Gong, Steven A. Hawks, Tiziano Agostinelli, Roderick C. I. MacKenzie, Yang Yang, and Jenny Nelson. Sensitivity of the Mott-Schottky Analysis in Organic Solar Cells. *The Journal of Physical Chemistry C*, 116(14):7672–7680, 2012.

[99] Germà Garcia-Belmonte, Antonio Guerrero, and Juan Bisquert. Elucidating Operating Modes of Bulk-Heterojunction Solar Cells from Impedance Spectroscopy Analysis. *J. Phys. Chem. Lett.*, 4(6):877–886, 2013.

[100] Juan Bisquert. A variable series resistance mechanism to explain the negative capacitance observed in impedance spectroscopy measurements of nanostructured solar cells. *Phys. Chem. Chem. Phys.*, 13(10):4679–85, March 2011. ISSN 1463-9084.

[101] *Impedance Spectroscopy: Theory, Experiment, and Applications*. John Wiley & Sons, Inc., 2005.

[102] Antonio Guerrero, Teresa Ripolles-Sanchis, Pablo P. Boix, and Germà Garcia-Belmonte. Series resistance in organic bulk-heterojunction solar devices: Modulating carrier transport with fullerene electron traps. *Org. Electron.*, 13(11):2326–2332, 2012.

[103] Germá Garcia-Belmonte, Pablo P. Boix, Juan Bisquert, Martijn Lenes, Henk J. Bolink, Andrea La Rosa, Salvatore Filippone, and Nazario Martín. Influence of the intermediate density-of-states occupancy on open-circuit voltage of bulk heterojunction solar cells with different fullerene acceptors. *The Journal of Physical Chemistry Letters*, 1(17):2566–2571, 2010.

[104] Chihaya Adachi Wolfgang Brutting. *Physics of Organic Semiconductors*. WILEY-VCH, 2012.

[105] Georg Heimel, Ingo Salzmann, Steffen Duhm, and Norbert Koch. Design of organic semiconductors from molecular electrostatics. *Chemistry of Materials*, 23(3):359–377, 2011.

[106] Chengliang Wang, Huanli Dong, Wenping Hu, Yunqi Liu, and Daoben Zhu. Semiconducting π-conjugated systems in field-effect transistors: A material odyssey of organic electronics. *Chemical Reviews*, 112(4):2208–2267, 2012.

[107] I. I. Fishchuk, V. I. Arkhipov, A. Kadashchuk, P. Heremans, and H. Bässler. Analytic model of hopping mobility at large charge carrier concentrations in disordered organic semiconductors: Polarons versus bare charge carriers. *Phys. Rev. B*, 76:045210, 2007.

[108] Pierre-Luc T. Boudreault, Ahmed Najari, and Mario Leclerc. Processable low-bandgap polymers for photovoltaic applications. *Chemistry of Materials*, 23(3):456–469, 2011.

[109] Ajay A. Virkar, Stefan Mannsfeld, Zhenan Bao, and Natalie Stingelin. Organic semiconductor growth and morphology considerations for organic thin-film transistors. *Advanced Materials*, 22(34):3857–3875, 2010.

[110] S. D. Baranovskii, H. Cordes, F. Hensel, and G. Leising. Charge-carrier transport in disordered organic solids. *Phys. Rev. B*, 62:7934–7938, 2000.

[111] D. A. da Silva Filho Y. Olivier R. Silbey V. Coropceanu, J. Cornil and J.L. Bredas. Charge transport in organic semiconductors. *Chemical Reviews*, 107(4):926–952, 2013.

[112] R J Kline and M D McGehee. Morphology and charge transport in conjugated polymers. *Polym. Rev.*, 46(1):27–45, 2006.

[113] Minh Trung Dang, Lionel Hirsch, Guillaume Wantz, and James D. Wuest. Controlling the Morphology and Performance of Bulk Heterojunctions in Solar Cells. Lessons Learned from the Benchmark Poly(3-hexylthiophene):[6,6]-Phenyl-C61-butyric Acid Methyl Ester System. *Chemical Reviews*, 113(5):3734–3765, 2013.

[114] Zhuping Fei Martin Heeney Scott Himmelberger, Koen Vandewal and Alberto Salleo. Role of molecular weight distribution on charge transport in semiconducting polymers. *Macromolecules*, 47:7151–7157, 2014.

[115] Rodrigo Noriega, Jonathan Rivnay, Koen Vandewal, Felix P V Koch, Natalie Stingelin, Paul Smith, Michael F Toney, and Alberto Salleo. A general relationship between disorder, aggregation and charge transport in conjugated polymers. *Nat. Mater.*, 12(11):1038–44, 2013.

[116] Sameer Vajjala Kesava, Zhuping Fei, Adam D. Rimshaw, Cheng Wang, Alexander Hexemer, John B. Asbury, Martin Heeney, and Enrique D. Gomez. Domain compositions and fullerene aggregation govern charge photogeneration in polymer/fullerene solar cells. *Adv. Energy Mater.*, 4(11):1–10, 2014.

[117] Ian a Howard, Ralf Mauer, Michael Meister, and Frédéric Laquai. Effect of Morphology on Ultrafast Free Carrier Generation in Polythiophene: Fullerene Organic Solar Cells. *J. Am. Chem. Soc.*, 132(42):14866–14876, 2010.

[118] Claudia Piliego and Maria Antonietta Loi. Charge transfer state in highly efficient polymer - fullerene bulk heterojunction solar cells. *J. Mater. Chem.*, 22(10):4141, 2012.

[119] Fred Wudl. The chemical properties of buckminsterfullerene (c60) and the birth and infancy of fulleroids. *Accounts of Chemical Research*, 25(3):157–161, 1992.

[120] Hsiang-Yu Chen, Jianhui Hou, Shaoqing Zhang, Yongye Liang, Guanwen Yang, Yang Yang, Luping Yu, Yue Wu, and Gang Li. Polymer solar cells with enhanced open-circuit voltage and efficiency. *Nat Phot.*, 3(11):649–653, 2009.

[121] Youjun He, Hsiang-Yu Chen, Jianhui Hou, and Yongfang Li. Indene - c60 bisadduct: A new acceptor for high-performance polymer solar cells. *Journal of the American Chemical Society*, 132(4):1377–1382, 2010.

[122] Antonio Facchetti. $\pi-$conjugated polymers for organic electronics and photovoltaic cell applications. *Chemistry of Materials*, 23(3):733–758, 2011.

[123] Seth B. Darling and Fengqi You. The case for organic photovoltaics. *RSC Advances*, 3:17633, 2013.

[124] Ikerne Etxebarria, Jon Ajuria, and Roberto Pacios. Solution-processable polymeric solar cells: A review on materials, strategies and cell architectures to overcome 10%. *Organic Electronics*, 9:34 – 60, 2015.

[125] Martijn M. Wienk, Jan M. Kroon, Wiljan J. H. Verhees, Joop Knol, Jan C. Hummelen, Paul A. van Hal, and René A. J. Janssen. Efficient Methano[70]fullerene/MDMO-PPV Bulk Heterojunction Photovoltaic Cells. *Angewandte Chemie International Edition*, 42(29):3371–3375, 2003.

[126] Pierre M. Beaujuge, Chad M. Amb, and John R. Reynolds. Spectral engineering in $\pi-$conjugated polymers with intramolecular donor-acceptor interactions. *Accounts of Chemical Research*, 43(11):1396–1407, 2010.

[127] Ta-Ya Chu, Salima Alem, Sai-Wing Tsang, Shing-Chi Tse, Salem Wakim, Jianping Lu, Gilles Dennler, David Waller, Russell Gaudiana, and Ye Tao. Morphology control in polycarbazole based bulk heterojunction solar cells and its impact on device performance. *Applied Physics Letters*, 98(25):253301, 2011.

[128] Shinuk Cho, Nelson Coates, Ji Sun Moon, Sung Heum Park, Anshuman Roy, Serge Beaupre, Daniel Moses, Mario Leclerc, Kwanghee Lee, and Alan J Heeger. Bulk heterojunction solar cells with internal quantum efficiency approaching 100%. *Nat. Photonics*, 3:297, 2009.

[129] Hsieh-chih Chen, Ying-hsiao Chen, Chi-chang Liu, Yun-chen Chien, Shang-wei Chou, and Pi-tai Chou. Prominent short-circuit currents of fluorinated quinoxaline-based copolymer solar cells with a power conversion efficiency of 8.0%. *Chem. Mater.*, 24:4766–4772, 2012.

[130] Yong Zhang, Steven K. Hau, Hin-Lap Yip, Ying Sun, Orb Acton, and Alex K.-Y. Jen. Efficient polymer solar cells based on the copolymers of benzodithiophene and thienopyrroledione. *Chemistry of Materials*, 22(9):2696–2698, 2010.

[131] Claudia Piliego, Thomas W. Holcombe, Jessica D. Douglas, Claire H. Woo, Pierre M. Beaujuge, and Jean M. J. Fréchet. Synthetic control of structural order in n-alkylthieno[3,4-c]pyrrole-4,6-dione-based polymers for efficient solar cells. *Journal of the American Chemical Society*, 132(22):7595–7597, 2010.

[132] Xun Huang Wai-YeungWong Hongbin Wu Liwei Chen Shijian Su Yong Cao Zhicai He, Chengmei Zhong. Simultaneous enhancement of open-circuit voltage, short circuit current density, and fill factor in polymer solar cells. *Advanced Materials*, 23(40):4636–4643, 2011.

[133] Zhicai He, Chengmei Zhong, Shijian Su, Miao Xu, Hongbin Wu, and Yong Cao. Enhanced power-conversion efficiency in polymer solar cells using an inverted device structure. *Nat. Photonics*, 6:591–595, 2012.

[134] Jing-De Chen, Chaohua Cui, Yan-Qing Li, Lei Zhou, Qing-Dong Ou, Chi Li, Yongfang Li, and Jian-Xin Tang. Single-junction polymer solar cells exceeding 10% power conversion efficiency. *Advanced Materials*, 27(6):1035–1041, 2015.

[135] Desta Gedefaw, Yi Zhou, Stefan Hellstrom, Lars Lindgren, L. Mattias Andersson, Fengling Zhang, Wendimagegn Mammo, Olle Inganas, and Mats R. Andersson. Alternating copolymers of fluorene and donor-acceptor-donor segments designed for miscibility in bulk heterojunction photovoltaics. *J. Mater. Chem.*, 19:5359–5363, 2009.

[136] Yunzhang Lu, Zhengguo Xiao, Yongbo Yuan, Haimei Wu, Zhongwei An, Yanbing Hou, Chao Gao, and Jinsong Huang. Fluorine substituted thiophene-quinoxaline copolymer to reduce the homo level and increase the dielectric constant for high open-circuit voltage organic solar cells. *J. Mater. Chem. C*, 1(4):630, 2013.

[137] D.M. de Leeuw, M.M.J. Simenon, a.R. Brown, and R.E.F. Einerhand. Stability of n-type doped conducting polymers and consequences for polymeric microelectronic devices. *Synth. Met.*, 87(1):53–59, 1997.

[138] Tae In Ryu, Youngwoon Yoon, Ji-Hoon Kim, Do-Hoon Hwang, Min Jae Ko, Doh-Kwon Lee, Jin Young Kim, Honggon Kim, Nam-Gyu Park, BongSoo Kim, and Hae Jung Son. Simultaneous enhancement of solar cell efficiency and photostability via chemical tuning of electron donating units in diketopyrrolopyrrole-based push-pull type polymers. *Macromolecules*, 47 (18):6270–6280, 2014.

[139] Jie Min, Zhi-guo Zhang, Siyuan Zhang, and Yongfang Li. Conjugated Side-Chain-Isolated D - A Copolymers Based on and Photovoltaic Properties. *Chem. Mater.*, 24:3247–3254, 2012.

[140] Yang Wang, Ying Liu, Shaojie Chen, Ruixiang Peng, and Ziyi Ge. Significant enhancement of polymer solar cell performance via side-chain engineering and simple solvent treatment. *Chemistry of Materials*, 25(15):3196–3204, 2013.

[141] Koen Vandewal, Scott Himmelberger, and Alberto Salleo. Structural Factors That Affect the Performance of Organic Bulk Heterojunction Solar Cells. *Macromolecules*, 46:6379–6387, 2013.

[142] Alessandro Abbotto, Mirko Seri, Milind S. Dangate, Filippo De Angelis, Norberto Manfredi, Edoardo Mosconi, Margherita Bolognesi, Riccardo Ruffo, Matteo M. Salamone, and Michele Muccini. A vinylene-linked benzo[1,2-b:4,5-b']dithiophene-2,1,3-benzothiadiazole

low-bandgap polymer. *Journal of Polymer Science Part A: Polymer Chemistry*, 50(14): 2829–2840, 2012.

[143] Xiaochen Wang, Yeping Sun, Song Chen, Xia Guo, Maojie Zhang, Xiaoyu Li, Yongfang Li, and Haiqiao Wang. Effects of π-conjugated bridges on photovoltaic properties of donor-π-acceptor conjugated copolymers. *Macromolecules*, 45(3):1208–1216, 2012.

[144] Sangwon Ko, Rajib Mondal, Chad Risko, Jung Kyu Lee, Sanghyun Hong, Michael D. McGehee, Jean-Luc Brédas, and Zhenan Bao. Tuning the optoelectronic properties of vinylene-linked donorâacceptor copolymers for organic photovoltaics. *Macromolecules*, 43(16):6685–6698, 2010.

[145] Mirko Seri, Assunta Marrocchi, Diego Bagnis, Rocio Ponce, Aldo Taticchi, Tobin J. Marks, and Antonio Facchetti. Molecular-shape-controlled photovoltaic performance probed via soluble Ï-conjugated arylacetylenic semiconductors. *Advanced Materials*, 23(33):3827–3831, 2011.

[146] Yang Dong, Wanzhu Cai, Ming Wang, Qingduan Li, Lei Ying, Fei Huang, and Yong Cao. [1,2,5]thiadiazolo[3,4-f]benzotriazole based narrow band gap conjugated polymers with photocurrent response up to 1.1 μm. *Organic Electronics*, 14(10):2459 – 2467, 2013.

[147] Letian Dou, Wei-Hsuan Chang, Jing Gao, Chun-Chao Chen, Jingbi You, and Yang Yang. A selenium-substituted low-bandgap polymer with versatile photovoltaic applications. *Advanced Materials*, 25(6):825–831, 2013.

[148] Ting Lei, Yue Cao, Xu Zhou, Yang Peng, Jiang Bian, and Jian Pei. Systematic investigation of isoindigo-based polymeric field-effect transistors: Design strategy and impact of polymer symmetry and backbone curvature. *Chemistry of Materials*, 24(10):1762–1770, 2012.

[149] Ying Sun, Baoping Lin, Hong Yang, and Xiaohui Gong. Improved bulk-heterojunction polymer solar cell performance through optimization of the linker groupin donorâacceptor conjugated polymer. *Polymer*, 53:1535–1542, 2012.

[150] Xia Guo, Maojie Zhang, Lijun Huo, Feng Xu, Yue Wu, and Jianhui Hou. Design, synthesis and photovoltaic properties of a new D-π-A polymer with extended $\pi-$bridge units. *J. Mater. Chem.*, 22:21024–21031, 2012.

[151] Badrou Réda Aïch, Jianping Lu, Serge Beaupré, Mario Leclerc, and Ye Tao. Control of the active layer nanomorphology by using co-additives towards high-performance bulk heterojunction solar cells. *Org. Electron.*, 13(9):1736–1741, 2012.

[152] Matthew O. Reese, Suren a. Gevorgyan, Mikkel Jørgensen, Eva Bundgaard, Sarah R. Kurtz, David S. Ginley, Dana C. Olson, Matthew T. Lloyd, Pasquale Morvillo, Eugene a. Katz, Andreas Elschner, Olivier Haillant, Travis R. Currier, Vishal Shrotriya, Martin Hermenau, Moritz Riede, Kiril R. Kirov, Gregor Trimmel, Thomas Rath, Olle Inganäs, Fengling Zhang, Mattias Andersson, Kristofer Tvingstedt, Monica Lira-Cantu, Darin Laird, Christine McGuiness, Srinivas Gowrisanker, Michael Pannone, Min Xiao, Jens Hauch, Roland Steim, Dean M.

DeLongchamp, Roland Rösch, Harald Hoppe, Nieves Espinosa, Antonio Urbina, Gülsah Yaman-Uzunoglu, Jörg-Bernd Bonekamp, Albert J.J.M. van Breemen, Claudio Girotto, Eszter Voroshazi, and Frederik C. Krebs. Consensus stability testing protocols for organic photovoltaic materials and devices. *Sol. Energy Mater. Sol. Cells*, 95(5):1253–1267, 2011.

[153] Sylvain Chambon, Agnès Rivaton, Jean L. Gardette, and Muriel Firon. Durability of MDMO-PPV and MDMO-PPV: PCBM blends under illumination in the absence of oxygen. *Sol. Energy Mater. Sol. Cells*, 92:785–792, 2008.

[154] Antonio Guerrero, Pablo P. Boix, Luís F. Marchesi, Teresa Ripolles-Sanchis, Ernesto C. Pereira, and Germà Garcia-Belmonte. Oxygen doping-induced photogeneration loss in P3HT:PCBM solar cells. *Sol. Energy Mater. Sol. Cells*, 100:185–191, 2012.

[155] Suren Gevorgyan Kion Norrman and Frederik C. Krebs. Water-induced degradation of polymer solar cells studied by H2(18)O labeling. *ACS Appl. Mater. Interfaces*, 1(1):102–112, 2009.

[156] Dong Liu, Tatsuya Nagamori, Masaki Yabusaki, Takeshi Yasuda, Liyuan Han, and Kazuhiro Marumoto. Dramatic enhancement of fullerene anion formation in polymer solar cells by thermal annealing: Direct observation by electron spin resonance. *Applied Physics Letters*, 104(24):243903, 2014.

[157] C.W.T. Bulle-Lieuwma, W.J.H. van Gennip, J.K.J. van Duren, P. Jonkheijm, R.A.J. Janssen, and J.W. Niemantsverdriet. Characterization of polymer solar cells by tof-sims depth profiling. *Applied Surface Science*, 203:547 – 550, 2003.

[158] Hyo Jung Kim, Hyun Hwi Lee, and Jang-Joo Kim. Real Time Investigation of the Interface between a P3HT:PCBM Layer and an Al Electrode during Thermal Annealing. *Macromolecular Rapid Communications*, 30(14):1269–1273, 2009.

[159] Dmitry Poplavskyy Jenny Nelson Donal D.C. Bradley James R. Durrant Kenji Kawano, Roberto Pacios. Degradation of organic solar cells due to air exposure. *Solar Energy Materials and Solar Cells*, 90(20):3520 – 3530, 2006.

[160] I. T. Sachs-Quintana, Thomas Heumüller, William R. Mateker, Darian E. Orozco, Rongrong Cheacharoen, Sean Sweetnam, Christoph J. Brabec, and Michael D. McGehee. Electron barrier formation at the organic-back contact interface is the first step in thermal degradation of polymer solar cells. *Advanced Functional Materials*, 24(25):3978–3985, 2014.

[161] Assaf Manor, Eugene A. Katz, Thomas Tromholt, and Frederik C. Krebs. Electrical and photo-induced degradation of zno layers in organic photovoltaics. *Advanced Energy Materials*, 1(5):836–843, 2011.

[162] Christoph J Schaffer, Claudia M Palumbiny, Martin a Niedermeier, Christian Jendrzejewski, Gonzalo Santoro, Stephan V Roth, and Peter Müller-Buschbaum. A direct evidence of morphological degradation on a nanometer scale in polymer solar cells. *Adv. Mater.*, 25(46): 6760–4, 2013.

[163] Fortunato Piersimoni, Giedrius Degutis, Sabine Bertho, Koen Vandewal, Donato Spoltore, Tim Vangerven, Jeroen Drijkoningen, Marlies K. Van Bael, An Hardy, Jan D Haen, Wouter Maes, Dirk Vanderzande, Milos Nesladek, and Jean Manca. Influence of fullerene photodimerization on the PCBM crystallization in polymer: Fullerene bulk heterojunctions under thermal stress. *J. Polym. Sci. Part B Polym. Phys.*, 51(16):1209–1214, 2013.

[164] Christian Müller. On the glass transition of polymer semiconductors and its impact on polymer solar cell stability. *Chemistry of Materials*, 27(8):2740–2754, 2015.

[165] Bert Conings, Sabine Bertho, Koen Vandewal, Alessia Senes, Jan D Haen, Jean Manca, and René A. J. Janssen. Modeling the temperature induced degradation kinetics of the short circuit current in organic bulk heterojunction solar cells. *Applied Physics Letters*, 96:163301, 2010.

[166] S. Schuller, P. Schilinsky, J. Hauch, and C. J. Brabec. Determination of the degradation constant of bulk heterojunction solar cells by accelerated lifetime measurements. *Applied Physics A*, 79(1):37–40, 2004.

[167] Ilaria Cardinaletti, Jurgen Kesters, Sabine Bertho, Bert Conings, Fortunato Piersimoni, Jan D Haen, Laurence Lutsen, Milos Nesladek, Bruno Van Mele, Guy Van Assche, Koen Vandewal, Alberto Salleo, Dirk Vanderzande, Wouter Maes, and Jean V. Manca. Toward bulk heterojunction polymer solar cells with thermally stable active layer morphology. *J. Photonics Energy*, 4:040997, 2014.

[168] A. Tapponnier, I. Biaggio, and P. Günter. Ultrapure c60 field-effect transistors and the effects of oxygen exposure. *Applied Physics Letters*, 86(11):112114, 2005.

[169] Matthias A. J. Michels Xiaoniu Yang, Alexander Alexeev and Joachim Loos. Effect of spatial confinement on the morphology evolution of thin poly(p-phenylenevinylene)/methanofullerene composite films. *Macromolecules*, 38(10):4289–4295, 2005.

[170] Him Cheng Wong, Zhe Li, Ching Hong Tan, Hongliang Zhong, Zhenggang Huang, Hugo Bronstein, Iain McCulloch, Joao T. Cabral, and James R. Durrant. Morphological stability and performance of polymer-fullerene solar cells under thermal stress: The impact of photoinduced pc60bm oligomerization. *ACS Nano*, 8(2):1297–1308, 2014.

[171] Tao Wang, Andrew J. Pearson, Alan D. F. Dunbar, Paul a. Staniec, Darren C. Watters, Hunan Yi, Anthony J. Ryan, Richard a. L. Jones, Ahmed Iraqi, and David G. Lidzey. Correlating Structure with Function in Thermally Annealed PCDTBT:PC70BM Photovoltaic Blends. *Adv. Funct. Mater.*, 22(7):1399–1408, 2012.

[172] Andrew J Dunbar Alan D F Staniec Paul a Watters Darren C Coles David Yi Hunan Iraqi Ahmed Lidzey David G Jones Richard a L Wang, Tao Pearson. Competition between substrate-mediated π-π stacking and surface-mediated T_g depression in ultrathin conjugated polymer films. *Eur. Phys. J. E. Soft Matter*, 35(12):9807, 2012.

[173] Sabine Bertho, Griet Janssen, Thomas J. Cleij, Bert Conings, Wouter Moons, Abay Gadisa, Jan D Haen, Etienne Goovaerts, Laurence Lutsen, Jean Manca, and Dirk Vanderzande. Effect of temperature on the morphological and photovoltaic stability of bulk heterojunction polymer:fullerene solar cells. *Sol. Energy Mater. Sol. Cells*, 92(7):753–760, 2008.

[174] Gang Li, Vishal Shrotriya, Jinsong Huang, Yan Yao, Tom Moriarty, Keith Emery, and Yang Yang. High-efficiency solution processable polymer photovoltaic cells by self-organization of polymer blends. *Nat. Mater.*, 4(11):864–868, 2005.

[175] Luyao Lu and Luping Yu. Understanding low bandgap polymer ptb7 and optimizing polymer solar cells based on it. *Advanced Materials*, 26(26):4413–4430, 2014.

[176] Aurélien Tournebize, Agnés Rivaton, Heiko Peisert, and Thomas Chassé. The Crucial Role of Confined Residual Additives on the Photostability of P3HT:PCBM Active Layers. *The Journal of Physical Chemistry C*, 119(17):9142–9148, 2015.

[177] Yizheng Jin, Jianpu Wang, Baoquan Sun, James C. Blakesley, and Neil C. Greenham. Solution-processed ultraviolet photodetectors based on colloidal zno nanoparticles. *Nano Letters*, 8(6):1649–1653, 2008.

[178] Pavel Schilinsky, Udom Asawapirom, Ullrich Scherf, Markus Biele, , and Christoph J. Brabec. Influence of the molecular weight of poly(3-hexylthiophene) on the performance of bulk heterojunction solar cells. *Chemistry of Materials*, 17(8):2175–2180, 2005.

[179] Amy M. Ballantyne, Lichun Chen, Justin Dane, Thomas Hammant, Felix M. Braun, Martin Heeney, Warren Duffy, Iain McCulloch, Donal D. C. Bradley, and Jenny Nelson. The effect of poly(3-hexylthiophene) molecular weight on charge transport and the performance of polymer:fullerene solar cells. *Advanced Functional Materials*, 18(16):2373–2380, 2008.

[180] Feng Liu, Wei Zhao, John R. Tumbleston, Cheng Wang, Yu Gu, Dong Wang, Alejandro L. Briseno, Harald Ade, and Thomas P. Russell. Understanding the morphology of PTB7:PCBM blends in organic photovoltaics. *Adv. Energy Mater.*, 4(5):1–9, 2014.

[181] Bofei Xue, Ben Vaughan, Chung-How Poh, Kerry B. Burke, Lars Thomsen, Andrew Stapleton, Xiaojing Zhou, Glenn W. Bryant, Warwick Belcher, and Paul C. Dastoor. Vertical Stratification and Interfacial Structure in P3HT:PCBM Organic Solar Cells. *The Journal of Physical Chemistry C*, 114(37):15797–15805, 2010.

[182] Wei Chen, Tao Xu, Feng He, Wei Wang, Cheng Wang, Joseph Strzalka, Yun Liu, Jianguo Wen, Dean J. Miller, Jihua Chen, Kunlun Hong, Luping Yu, and Seth B. Darling. Hierarchical nanomorphologies promote exciton dissociation in polymer/fullerene bulk heterojunction solar cells. *Nano Letters*, 11(9):3707–3713, 2011.

[183] Chun-Guey Wu, Chien-Hung Chiang, and Hsieh-Cheng Han. Manipulating the horizontal morphology and vertical distribution of the active layer in BHJ-PSC with a multi-functional solid organic additive. *J. Mater. Chem. A*, 2(15):5295–5303, 2014.

[184] Jae Kwan Lee, Wan Li Ma, Christoph J Brabec, Jonathan Yuen, Ji Sun Moon, Jin Young Kim, Kwanghee Lee, Guillermo C Bazan, and Alan J Heeger. Processing additives for improved efficiency from bulk heterojunction solar cells. *J. Am. Chem. Soc.*, 130(11):3619–3623, 2008.

[185] Sarah T. Turner, Patrick Pingel, Robert Steyrleuthner, Edward J. W. Crossland, Sabine Ludwigs, and Dieter Neher. Quantitative analysis of bulk heterojunction films using linear absorption spectroscopy and solar cell performance. *Advanced Functional Materials*, 21(24): 4640–4652, 2011.

[186] P. Samorí A. Liscio, V. Palermo. Nanoscale quantitative measurement of the potential of charged nanostructures by electrostatic and Kelvin probe force microscopy: Unraveling electronic processes in complex materials. *Accounts of Chemical Research*, 43(4):541–550, 2010.

[187] Dan Liu, Rodrigo Osuna Orozco, and Tao Wang. Deviations of the glass transition temperature in amorphous conjugated polymer thin films. *Phys. Rev. E*, 88(2):022601, 2013.

[188] Ivan Litzov, Hamed Azimi, Gebhard Matt, Peter Kubis, Tobias Stubhan, Georgi Popov, and Christoph J. Brabec. Accelerated degradation of Al_3^+ doped ZnO thin films using damp heat test. *Org. Electron.*, 15(2):569–576, 2014.

[189] S.C. Price, a.C. Stuart, L.G. Yang, H.X. Zhou, and W. You. Fluorine substituted conjugated polymer of medium bandwidth yield 7% efficiency in polymer-fullerine solar cells. *J. Am. Chem. Soc.*, 133:4625–4631, 2011.

[190] Craig H Peters, I T Sachs-Quintana, William R Mateker, Thomas Heumueller, Jonathan Rivnay, Rodigo Noriega, Zach M Beiley, Eric T Hoke, Alberto Salleo, and Michael D McGehee. The mechanism of burn-in loss in a high efficiency polymer solar cell. *Adv. Mater.*, 24 (5):663–668, 2012.

[191] Christoph Lungenschmied, Siegfried Bauer, Reinhard Schwödiauer, Sheila Rodman, Darcy Fournier, Gilles Dennler, and Christoph J. Brabec. Real-time in-situ observation of morphological changes in organic bulk-heterojunction solar cells by means of capacitance measurements. *J. Appl. Phys.*, 109(4):044503, 2011.

[192] Tao Wang, Andrew J. Pearson, David G. Lidzey, and Richard a. L. Jones. Evolution of Structure, Optoelectronic Properties, and Device Performance of Polythiophene:Fullerene Solar Cells During Thermal Annealing. *Adv. Funct. Mater.*, 21(8):1383–1390, 2011.

[193] B Bernardo, D Cheyns, B Verreet, R D Schaller, B P Rand, and N C Giebink. Delocalization and dielectric screening of charge transfer states in organic photovoltaic cells. *Nat. Commun.*, 5:3245, 2014.

[194] Sameer Vajjala Kesava, Zhuping Fei, Adam D. Rimshaw, Cheng Wang, Alexander Hexemer, John B. Asbury, Martin Heeney, and Enrique D. Gomez. Domain compositions and fullerene

aggregation govern charge photogeneration in polymer/fullerene solar cells. *Adv. Energy Mater.*, 4(11):1–10, 2014.

[195] Andrew J. Pearson, Tao Wang, Richard A. L. Jones, David G. Lidzey, Paul A. Staniec, Paul E. Hopkinson, and Athene M. Donald. Rationalizing phase transitions with thermal annealing temperatures for p3ht:pcbm organic photovoltaic devices. *Macromolecules*, 45(3): 1499–1508, 2012.

[196] Antonio Guerrero, Luís F. Marchesi, Pablo P. Boix, Sonia Ruiz-Raga, Teresa Ripolles-Sanchis, Germá Garcia-Belmonte, and Juan Bisquert. How the charge-neutrality level of interface states controls energy level alignment in cathode contacts of organic bulk-heterojunction solar cells. *ACS Nano*, 6(4):3453–3460, 2012.

[197] Antonio Guerrero, Bernhard Dörling, Teresa Ripolles-Sanchis, Mahdieh Aghamohammadi, Esther Barrena, Mariano Campoy-Quiles, and Germà Garcia-Belmonte. Interplay between fullerene surface coverage and contact selectivity of cathode interfaces in organic solar cells. *ACS Nano*, 7(5):4637–46, 2013.

[198] Antonio Guerrero, Núria F. Montcada, Jon Ajuria, Ikerne Etxebarria, Roberto Pacios, Germà Garcia-Belmonte, and Emilio Palomares. Charge carrier transport and contact selectivity limit the operation of PTB7-based organic solar cells of varying active layer thickness. *J. Mater. Chem. A*, 1(39):12345, 2013.

[199] Antonio Guerrero, Luis F. Marchesi, Pablo P. Boix, Juan Bisquert, and Germa Garcia-Belmonte. Recombination in organic bulk heterojunction solar cells: Small dependence of interfacial charge transfer kinetics on fullerene affinity. *The Journal of Physical Chemistry Letters*, 3(10):1386–1392, 2012.

[200] Agnès Rivaton, Aurélien Tournebize, Julien Gaume, Pierre-Olivier Bussière, Jean-Luc Gardette, and Sandrine Therias. Photostability of organic materials used in polymer solar cells. *Polym. Int.*, 63(November):1335–1345, 2014.

[201] H. Santos Silva, a. Tournebize, D. Bégué, H. Peisert, T. Chassé, J.-L. Gardette, S. Therias, a. Rivaton, and R. C. Hiorns. A universal route to improving conjugated macromolecule photostability. *RSC Adv.*, 4:54919–54923, 2014.

[202] Sylvain Chambon, Agnès Rivaton, Jean L. Gardette, and Muriel Firon. Photo and thermal degradation of MDMO-PPV:PCBM blends. *Sol. Energy Mater. Sol. Cells*, 91:394–398, 2007.

[203] Matthieu Manceau, Eva Bundgaard, Jon E. Carle, Ole Hagemann, Martin Helgesen, Roar Sondergaard, Mikkel Jorgensen, and Frederik C. Krebs. Photochemical stability of π-conjugated polymers for polymer solar cells: a rule of thumb. *J. Mater. Chem.*, 21:4132–4141, 2011.

[204] Jon E. Carlé, Martin Helgesen, Natalia K. Zawacka, Morten V. Madsen, Eva Bundgaard, and Frederik C. Krebs. A comparative study of fluorine substituents for enhanced stability

of flexible and ITO-free high-performance polymer solar cells. *J. Polym. Sci. Part B Polym. Phys.*, 52:893–899, 2014.

[205] H. Neugebauer, C. Brabec, J. C. Hummelen, and N. S. Sariciftci. Stability and photodegradation mechanisms of conjugated polymer/fullerene plastic solar cells. *Sol. Energy Mater. Sol. Cells*, 61:35–42, 2000.

[206] Andreas Distler, Peter Kutka, Tobias Sauermann, Hans Joachim Egelhaaf, Dirk M. Guldi, Daniele Di Nuzzo, Stefan C J Meskers, and René a J Janssen. Effect of PCBM on the photodegradation kinetics of polymers for organic photovoltaics. *Chem. Mater.*, 24:4397–4405, 2012.

[207] Fabrizia Negri John R. Morton and Keith F. Preston. Addition of free radicals to c60. *Accounts of Chemical Research*, 31(2):63–69, 1998.

[208] Chin Pang Yau, Sarah Wang, Neil D. Treat, Zhuping Fei, Bertrand J. Tremolet de Villers, Michael L. Chabinyc, and Martin Heeney. Investigation of radical and cationic cross-linking in high-efficiency, low band gap solar cell polymers. *Advanced Energy Materials*, 5(5):1401228, 2015.

[209] Lijun Huo, Shaoqing Zhang, Xia Guo, Feng Xu, Yongfang Li, and Jianhui Hou. Replacing alkoxy groups with alkylthienyl groups: A feasible approach to improve the properties of photovoltaic polymers. *Angewandte Chemie International Edition*, 50(41):9697–9702, 2011.

[210] E Vitoratos, S Sakkopoulos, E Dalas, N Paliatsas, D Karageorgopoulos, F Petraki, S Kennou, and S Choulis. Thermal degradation mechanisms of PEDOT:PSS. *Org. Electron.*, 10(1):61–66, 2009.

[211] Christian Müller, Ergang Wang, L. Mattias Andersson, Kristofer Tvingstedt, Yi Zhou, Mats R. Andersson, and Olle Inganäs. Influence of molecular weight on the performance of organic solar cells based on a fluorene derivative. *Advanced Functional Materials*, 20(13): 2124–2131, 2010.

[212] Williams Graeme, Wang Qi, and Aziz Hany. The photo-stability of polymer solar cells: Contact photo-degradation and the benefits of interfacial layers. *Adv. Funct. Mater.*, 23: 2239–2247, 2013.

[213] Thomas Heumueller, Timothy M. Burke, William R. Mateker, Isaac T. Sachs-Quintana, Koen Vandewal, Christoph J. Brabec, and Michael D. McGehee. Disorder-induced open-circuit voltage losses in organic solar cells during photoinduced burn-in. *Advanced Energy Materials*, 5(14):1500111, 2015.

[214] D. F. Swinehart. The beer-lambert law. *Journal of Chemical Education*, 39(7):333, 1962.

[215] Kyung Geun Lim, Mi Ri Choi, Ji Hoon Kim, Dong Hun Kim, Gwan Ho Jung, Yongsup Park, Jong Lam Lee, and Tae Woo Lee. Role of ultrathin metal fluoride layer in organic photovoltaic cells: Mechanism of efficiency and lifetime enhancement. *ChemSusChem*, 7: 1125–1132, 2014.

[216] Qi Wang, Graeme Williams, Ting Tsui, and Hany Aziz. Photochemical deterioration of the organic/metal contacts in organic optoelectronic devices. *Journal of Applied Physics*, 112 (6):064502, 2012.

[217] Steven K. Hau, Hin-Lap Yip, Nam Seo Baek, Jingyu Zou, Kevin O Malley, and Alex K.Y. Jen. Air-stable inverted flexible polymer solar cells using zinc oxide nanoparticles as an electron selective layer. *Applied Physics Letters*, 92(25):253301, 2008.

[218] Hye Rim Yeom, Jungwoo Heo, Gi-Hwan Kim, Seo-Jin Ko, Seyeong Song, Yimhyun Jo, Dong Suk Kim, Bright Walker, and Jin Young Kim. Optimal top electrodes for inverted polymer solar cells. *Phys. Chem. Chem. Phys.*, 17:2152–2159, 2015.

[219] Riccardo Po, Chiara Carbonera, Andrea Bernardi, and Nadia Camaioni. The role of buffer layers in polymer solar cells. *Energy Environ. Sci.*, 4:285–310, 2011.

[220] Yanming Sun, Jung Hwa Seo, Christopher J. Takacs, Jason Seifter, and Alan J. Heeger. Inverted Polymer Solar Cells Integrated with a Low-Temperature-Annealed Sol-Gel-Derived ZnO Film as an Electron Transport Layer. *Advanced Materials*, 23(14):1679–1683, 2011.

[221] Il Jeon, James W. Ryan, Tafu Nakazaki, Kee Sheng Yeo, Yuichi Negishi, and Yutaka Matsuo. Air-processed inverted organic solar cells utilizing a 2-aminoethanol-stabilized zno nanoparticle electron transport layer that requires no thermal annealing. *J. Mater. Chem. A*, 2: 18754–18760, 2014.

[222] Sungeun Park, Sung Ju Tark, Joon Sung Lee, Heejin Lim, and Donghwan Kim. Effects of intrinsic ZnO buffer layer based on P3HT/PCBM organic solar cells with Al-doped ZnO electrode . *Solar Energy Materials and Solar Cells*, 93(6):1020 – 1023, 2009.

[223] Lethy Krishnan Jagadamma, Mohammed Al-Senani, Abdulrahman El-Labban, Issam Gereige, Guy O. Ngongang Ndjawa, Jorge C. D. Faria, Taesoo Kim, Kui Zhao, Federico Cruciani, Dalaver H. Anjum, Martyn A. McLachlan, Pierre M. Beaujuge, and Aram Amassian. Polymer Solar Cells with Efficiency >10% Enabled via a Facile Solution-Processed Al-Doped ZnO Electron Transporting Layer. *Advanced Energy Materials*, 5(12):1500204, 2015.

[224] Hyunchul Oh, Johannes Krantz, Ivan Litzov, Tobias Stubhan, Luigi Pinna, and Christoph J. Brabec. Comparison of various sol-gel derived metal oxide layers for inverted organic solar cells. *Solar Energy Materials and Solar Cells*, 95(8):2194 – 2199, 2011.

[225] Tobias Stubhan, Ivan Litzov, Ning Li, Michael Salinas, Matthias Steidl, Gerhard Sauer, Karen Forberich, Gebhard J. Matt, Marcus Halik, and Christoph J. Brabec. Overcoming interface losses in organic solar cells by applying low temperature, solution processed aluminum-doped zinc oxide electron extraction layers. *J. Mater. Chem. A*, 1:6004–6009, 2013.

[226] Sara Trost, Kirill Zilberberg, Andreas Behrendt, Andreas Polywka, Patrick Görrn, Philip Reckers, Julia Maibach, Thomas Mayer, and Thomas Riedl. Overcoming the "light-soaking"

issue in inverted organic solar cells by the use of al:zno electron extraction layers. *Advanced Energy Materials*, 3(11):1437–1444, 2013.

[227] Hanxiao Liu, Zhenghui Wu, Jianqiao Hu, Qunliang Song, Bo Wu, Hoi Lam Tam, Qingyi Yang, Wing Hong Choi, and Furong Zhu. Efficient and ultraviolet durable inverted organic solar cells based on an aluminum-doped zinc oxide transparent cathode. *Applied Physics Letters*, 103(4):043309, 2013.

[228] Qinye Bao, Xianjie Liu, Yuxin Xia, Feng Gao, Louis-Dominique Kauffmann, Olivier Margeat, Jorg Ackermann, and Mats Fahlman. Effects of ultraviolet soaking on surface electronic structures of solution processed zno nanoparticle films in polymer solar cells. *J. Mater. Chem. A*, 2:17676–17682, 2014.

[229] Prajwal Adhikary, Swaminathan Venkatesan, Nirmal Adhikari, Purna P. Maharjan, Olusegun Adebanjo, Jihua Chen, and Qiquan Qiao. Enhanced charge transport and photovoltaic performance of PBDTTT-C-T/PC70BM solar cells via UV-ozone treatment. *Nanoscale*, 5: 10007–10013, 2013.

[230] Zhiming Kam, Xizu Wang, Jie Zhang, and Jishan Wu. Elimination of burn-in open-circuit voltage degradation by zno surface modification in organic solar cells. *ACS Applied Materials & Interfaces*, 7(3):1608–1615, 2015.

Acknowledgements

I am grateful for the financial support to this thesis from the European Commission FP7 collaborative project SUNFLOWER (FP7-ICT-2011-7, Grant no. 287594).
I would really like to thank my advisor, Prof. Beatrice Fraboni, who followed me through my carrier and who supported me in all my working choices.
I am grateful to my supervisor Dr. Mirko Seri who was involved in directing my work, for his continuous help and inspiration in my research job, for his patience and kindness. I express my thanks to Dr. Michele Muccini, Director of "Consiglio Nazionale delle Ricerche - Istituto per lo Studio dei Materiali Nanostrutturati" where I carried out my PhD research.
I want to give sincere thanks to my colleagues Mario Prosa and Margherita Bolognesi, first of all for their friendship, and then for their precious contributions on the many scientific discussions and on the experimental work, and also for their support and encouragement that gave to me. A special thanks also to all the other colleagues from the CNR (just few names): Simone, Anna, Tanja, Federico, Vincenzo...
I wish to thank Prof. Germá Garcia Belmonte and Dr. Antonio Guerrero and all my colleagues from the "Photovoltaic and Optoelectronic Devices Group" in Castellon de la Plana for the precious and instructive experience.
A big thank to all other people with which I collaborated during these years: Desta Gedefaw, Wenliu Zhuang, Ergang Wang for the synthesis of hundreds of new polymers, Jörg Ackermann Olivier Margeat for their ZnO nanoparticles and Tobias Cramer for his precious help with the AFM and KPFM measurements.
Last but not least, thanks to my Mum, my Dad, my sister Valentina, her housband Filippo, my wonderful nephew Andrea, my cousin Claudia and all my family. Thanks to all my good friends (just few names): Anna, Susanna, Laura, Daniela, Giulio, Alberto, Francesca, Elisabetta, Elisa, Nicoletta, Alessia, Davide, Gianluca, Luisa etc... A special and loving thank to Riccardo.